

Leibniz-Institut für Katalyse e.V. an der Universität Rostock

**Surface Structure, Stability and Activity of Molybdenum Carbides Supported Transition Metal Catalysts**

Kumulative Dissertation  
zur Erlangung des akademischen Grades  
**Doctor rerum naturalium (Dr. rer. nat.)**  
der Mathematisch-Naturwissenschaftlichen Fakultät  
der Universität Rostock

vorgelegt von

**Fan Wang**

geb. am 12.03.1990 in P. R. China

Rostock, 16.07.2021

Universität  
Rostock



Traditio et Innovatio



Die vorliegende Arbeit entstand in der Zeit von Dezember 2017 bis Juni 2021 am Leibniz-Institut für Katalyse e.V. an der Universität Rostock.

1. Gutachter:

Dr. Habil. Haijun Jiao

Leibniz-Institut für Katalyse e.V. an der Universität Rostock

Albert-Einstein-Str. 29a, 18059 Rostock, Germany

2. Gutachter:

Prof. Dr. Ralf Ludwig

Institut für Chemie, Universität Rostock

Dr.-Lorenz-Weg 2, 18059 Rostock, Germany

**Tag der Einreichung: 16.07.2021**

**Tag der Verteidigung: 19.10.2021**

### Acknowledgments

First of all, I thank my supervisor, *Dr. Habil. Haijun Jiao*, for offering me the opportunity to do my doctoral studies. During my studies, I benefited greatly from his proper instruction, great patience, valuable suggestions, detailed discussions and warm consideration. His supervision and scientific guidance guarantee the publication of my work and the collaboration with other researchers. His knowledge in structural and physical chemistry not only helps me to complete my current studies but will also guide me in my future scientific work. In addition to the academic part, his wife (Ms. Yihua Zhang) is very kind and has looked after me and my family very much in everyday life.

I thank Prof. Dr. Matthias Beller, director of LIKAT, for the warm working atmosphere. It is a great pleasure for me to be part of the big team.

I thank Prof. Dr. Noritatsu Tsubaki and Dr. Li Tan for giving me the opportunity to collaborate on a joint work that has taught me a lot.

I thank my theoretical group members; Dr. Zhihong Wei, Nan Zhang, Dr. Teng Li, Dr. Yun Zhao, Dr. Xinxin Tian and Chunli Liu; for their help in work and life. We do not just work together; we hang out a lot in our free time.

Many thanks also go to my Chinese colleagues at LIKAT, Dr. Yuya Hu, Dr. Rui Sang, Dr. Delong Han, Dr. Shaoke Zhang, Dr. Jiawang Liu, Dr. Xin Liu, Xuwen Guo, Dr. Zhiping Yin, Dr. Ji Yang and Dr. Wei Zhou.

I thank my friends in Rostock: Xin Wang, Jiawei Yan, Shanshan Song, Dan Wang, Predko and Jarecka.

I appreciate China Scholarship Council (CSC) for scholarship.

Due to the massive Covid-19 pandemic problem, I and my families have to face separation for a long time. Special thanks to my parents for their unconditional love and support throughout my life.

Finally, I would like to thank my dear wife (Lingling Zhao) and daughter (Maimai). Even if they are missing in the final phase of my doctoral studies, they are always my powerful supporters and my mostly emotional nourishment.

### **Abstract**

The central point of this dissertation is a computational investigation into the structure, stability, and activity of transition metals (Fe, Co, Ni, Cu, Pd and Pt) supported on the different terminations of the hexagonal  $\beta$ -Mo<sub>2</sub>C and cubic- $\delta$ -MoC phases. The idea behind is that both transition metals and molybdenum carbides are active catalysts in many reactions, and their proper combination will show some synergistic effects and open a new field for the development of novel catalysts whose activity differs from that of only metals and carbides. Both adsorption and substitution model catalysts have been investigated. It is found that the structure and stability of supported catalysts are determined by the nature of the transition metals and their interaction with the carbide surfaces and are dependent on the metal loading; and this in turn determines the activity of the catalytic reactions.

### **Zusammenfassung**

Der zentrale Punkt dieser Dissertation ist eine theoretische Untersuchung der Struktur, Stabilität und Aktivität von Übergangsmetallen (Fe, Co, Ni, Cu, Pd und Pt), die auf den unterschiedlichen Oberflächen der hexagonalen  $\beta$ -Mo<sub>2</sub>C und kubischen- $\delta$ -MoC Phasen abgelagert sind. Die Idee dahinter ist, dass sowohl Übergangsmetalle als auch Molybdäncarbide in vielen Reaktionen aktive Katalysatoren sind, und ihre richtige Kombination wird einige synergistische Effekte zeigen und ein neues Feld für die Entwicklung neuer Katalysatoren eröffnen, deren Aktivität sich von der nur von Metallen und Carbiden unterscheidet. Sowohl Adsorptions- als auch Substitutionsmodellkatalysatoren wurden untersucht. Es zeigt sich, dass Struktur und Stabilität von Trägerkatalysatoren durch die Eigenschaften der Übergangsmetalle und deren Wechselwirkung mit den Carbidoberflächen bestimmt werden und von der Metallbeladung abhängig sind; und dies wiederum bestimmt die Aktivität der katalytischen Reaktionen.



## Table of Contents

<b>Acknowledgments</b> .....	I
<b>Abstract</b> .....	II
<b>1. Introduction</b> .....	1
1.1 Supported heterogeneous catalysis and catalysts .....	1
1.1.1 Preparation methods of supported catalysts .....	2
1.1.2 Interaction between supports and metals.....	5
1.2 Mo <sub>x</sub> C and transition metals combined catalysts .....	5
1.2.1 Structural and electronic properties of Mo <sub>x</sub> C .....	6
1.2.2 Transition metals modified Mo <sub>x</sub> C in heterogeneous catalysis.....	8
1.2.3 Structures of transition metals modified Mo <sub>x</sub> C .....	10
1.3 Theoretical studies .....	11
1.4 References.....	24
<b>2. Objectives of this work</b> .....	30
<b>3. Summary of publications</b> .....	31
3.1 Adsorption of CO, H <sub>2</sub> , H <sub>2</sub> O, and CO <sub>2</sub> on Fe-, Co-, Ni-, Cu-, Pd-, and Pt-Doped Mo <sub>2</sub> C(101) Surfaces .....	31
3.2 Molybdenum Carbide Supported Metal Catalysts (M <sub>n</sub> /Mo <sub>x</sub> C; M = Co, Ni, Cu, Pd, Pt) – Metal and Surface Dependent Structure and Stability .....	45
3.3 Nitridation of the metallic Mo <sub>2</sub> C(001) surface from NH <sub>3</sub> dissociative adsorption—A DFT study .....	64
3.4 Design of a core–shell catalyst: an effective strategy for suppressing side reactions in syngas for direct selective conversion to light olefins .....	73
<b>Curriculum Vitae</b> .....	83
<b>Selbstständigkeitserklärung</b> .....	86

## 1. Introduction

### 1.1 Supported heterogeneous catalysis and catalysts

Since Davy's discovery in 1817 that catalytic oxidation between two gas molecules can occur on platinum surface,<sup>1</sup> the underlying background has been discussed extensively. In 1835, Berzelius realized that many independent and similar observations at the beginning of the 19th century could be identified as the so-called catalytic force.<sup>1-2</sup> This is probably the first time in the development of catalysis as a concept for a far-reaching natural phenomenon. Since then, catalytic processes of accelerating and modifying chemical transformations are at the heart of many modern industrial processes, i.e., production of fuels, commodity chemicals, pharmaceuticals, agrochemicals, fine chemicals and consumables.<sup>3</sup> In the field of catalysis, especially heterogeneous catalysis occurring usually at the interface between solid and gas or liquid phases plays a central role in modern chemical industry and technology.<sup>4-5</sup>

In catalysis, catalysts are the key contributors to chemical reactions and can form and break chemical bonds during the reactions. These events occur repeatedly and usually without any significant consumption of catalysts. Without catalysts these chemical conversions would either not occur or would occur with slower rates or lower efficiencies. Generally, catalysis can be divided into homogeneous and heterogeneous, and biocatalysis belongs to its class. Homogeneous catalysis typically works in one phase, while heterogeneous catalysis works in two or three phases. Homogeneous catalysis has the problem of separating catalysts from the reaction media and limited activity due to their low stability, while heterogeneous catalysis has the advantage of separating and recovering catalysts from the reaction mixture and has become more obvious and plays a great role in industry. In fact, heterogeneous catalysis makes up about 80% of all catalytic processes currently used in industry.<sup>6</sup> The global catalysts market was valued at 1536.58 Million USD in 2020 and will grow with a CAGR of 5.48% from 2020 to 2027, based on newly published report.<sup>7</sup>

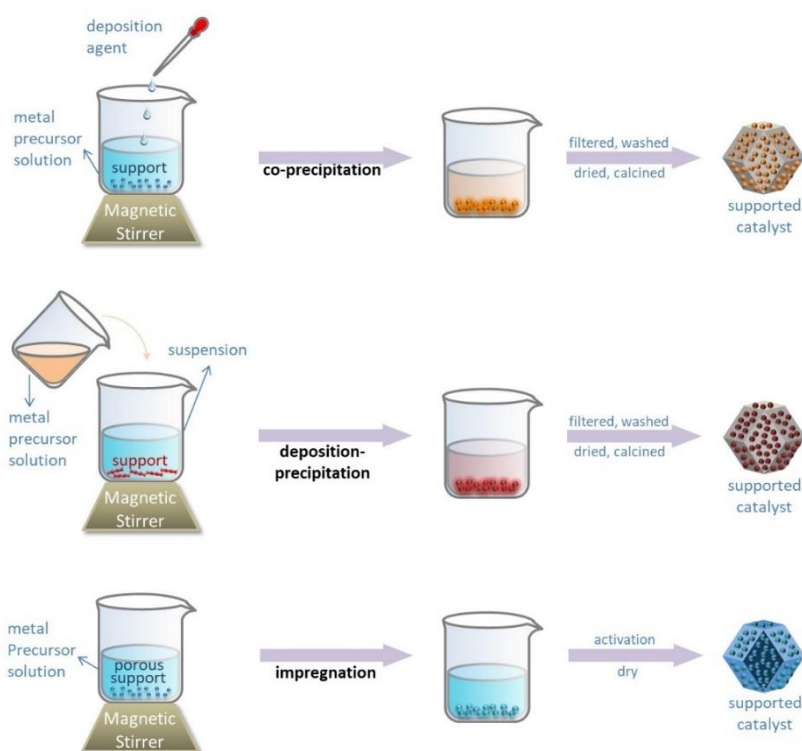
To date, heterogeneous catalysis has been studied in detail not only experimentally but also theoretically along with the development of analytical techniques and quantum chemical methods. Modern density functional theory (DFT) of the electronic structures of molecules and solids has played a growing role in heterogeneous catalysis for over 30 years. Systematic DFT computations can play a supplementary and decisive role in understanding the intrinsic nature of an experimental work. By comparing, or better, combining experiment and theory, it is possible to unravel the details of the intrinsic nature of the experimental phenomena, and so rationally develop more effective and novel catalysts.

In early stage of heterogeneous catalysis, transition metals were usually used as the unique active phases and this is now recognized as unsupported metal catalysts; such as iron catalysts for ammonia synthesis<sup>8-9</sup> and Fischer–Tropsch synthesis (FTS) to produce fuels,<sup>10-11</sup> or mixed metal oxide catalysts for the production of acrylonitrile from ammonia and propylene.<sup>12-13</sup> With the growing development of supports, usually solids having large surface area and being catalytically inert,<sup>14</sup> the use of supported metal catalysts over unsupported metals has been found for various chemical conversions. Particularly, supports can not only facilitate the formation of extremely small metal particles with high proportion and uniform dispersion but also enhance the thermal stability of metal particles on support surfaces. Benefiting from the large surface area of graphene and their strong interaction to metal, for example, Wang *et al.*,<sup>15</sup> successfully prepared graphene-supported Au-Pd bimetallic nanoparticles with uniform dispersion and found excellent catalytic activity in methanol selective

oxidation with 90.2% conversion and 100% selectivity of methyl formate at 70 °C. In addition, supports also enable the incorporation of useful additives, usually known as promoter. For example, Ma *et al.*,<sup>16</sup> investigated the promotion effect of Mo (0-12 wt%) on activated-carbon supported Fe-Cu-K catalysts for FTS and found that 6% Mo can improve the catalyst stability without sacrificing activity on one hand and greatly enhances the secondary reactions of olefins on the other hand, leading to a large amount of internal olefins in the products. Furthermore, supports can also participate in chemical reaction by combining supported metals as an effective strategy to promote catalytic processes. For example, Zheng *et al.*,<sup>17</sup> found that the Ti(III)-O-Pd interface of the atomically dispersed Pd<sub>1</sub>/TiO<sub>2</sub> catalyst can activate O<sub>2</sub> into superoxide (O<sub>2</sub><sup>-</sup>) and promote oxidation reaction, where not only supported metal atoms but also the oxide support are the active sites.

### 1.1.1 Preparation methods of supported catalysts

Generally, two main synthetic methods are used to prepare supported catalysts: precipitation and impregnation (Scheme 1). In both cases, a metal precursor, usually an inorganic salt, is the starting point for depositing active metal on support.



**Scheme 1.** Schematic diagram of the process of precipitation and impregnation methods.

The common precipitation technique is co-precipitation and deposition precipitation. In co-precipitation, salt of active metal and support are dissolved in a precursor solution, leading to the nucleation and growth of solid precursor. During this process, various factors, i.e., temperature gradient, sufficient mixing and stirring, or concentration gradient, should be considered and careful attention should be paid to avoid local fluctuations. All these factors can cause an unexpected nucleation, different or uneven growth patterns, or precipitation of different phases. Using co-precipitation technique, a Fe-Cu-K catalyst for FTS was prepared successfully from a sulfate precursor,<sup>18</sup> and the pretreated catalysts show significantly different activity in CO hydrogenation.

Compared to co-precipitation, deposition precipitation occurs in the presence of a support, which either

reduces surface free energy of tiny nuclei or stabilizes the precipitate, thereby reducing the barrier of nucleation. Similar to co-precipitation, factors such pH value (acidity or basicity), temperature or evaporation for deposit precipitation are sensitive to the deposition in a precursor solution. Deposition precipitation has been used frequently and successfully to produce finely dispersed metal nanoparticles with low loading. For example, Moreau *et al.*,<sup>19</sup> synthesized Au/TiO<sub>2</sub> catalysts via deposit precipitation by manipulating the pH value of the solution using NaOH followed by the addition of the support with vigorous stirring. By increasing the pH value from 2 to 9, the catalytic performance improves as the gold nanoparticle becomes smaller. In addition, temperature is another important factor in catalyst synthesis.

In addition to precipitation, impregnation is another common and most popular method for the synthesis of supported catalysts due to its ease use and low waste stream. This procedure begins by immersing a porous support in an aqueous solution of a metal precursor such as metal sulfates, carbonates, chlorides and acetates due to their high solubility in water. Normally, the concentration of the solution below (super) saturation is required to avoid premature deposition of the metal precursor. Depending on the amount of solution, the process can be mainly divided into wet impregnation, solution exceeding the capacity of adsorption of support, or dry impregnation, in which the impregnated material retains a dry character on a macroscopic scale.

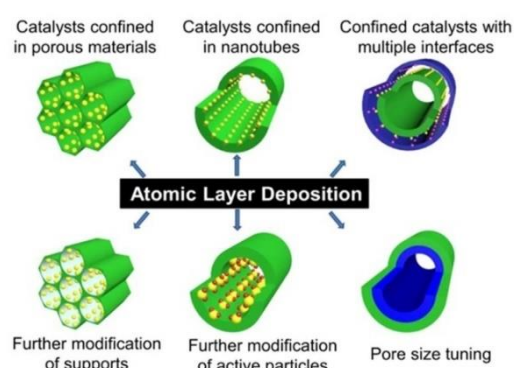
Generally, adsorption of metal ion from an aqueous solution onto a support is an important step during the impregnation process, especially when low metal loading is used. In order to complete the adsorption process, wet impregnation is usually used, which is carried out in an excessive solution, a low concentration of the precursor at a given pH value. In addition, adsorption is an important factor in metal distribution on support on a macroscopic scale,<sup>20-21</sup> and equilibrium between adsorbed and solvated species can determine the degree of distribution. Within a rapid equilibrium, metal precursor complex is mostly adsorbed on the outer shell of the support, leading to eggshell distribution. For slow equilibrium, metal complex prefers diffusion into the center of the support body, eventually developing into a homogeneous distribution.

The drying step normally follows the adequate distribution of metal and the subsequent separation of the solvent and pre-catalyst. It is known that the drying step has a strong influence on the finished catalysts.<sup>21-22</sup> Typically, an entire drying process has three stages, i.e., increasing rate, constant rate and decreasing rate. The increasing rate period is accompanied by an increase in drying temperature until the equilibrium is reached, at which the pre-catalyst is normally placed in a Muffle furnace or vacuum furnace. In the constant rate period, the drying temperature is stable and drying takes place mainly on the outer surface of the pre-catalyst. While a continuous liquid is still present in the entire sample, the solvent can be transported to the outer surface of the pre-catalyst via capillary force. Natural cooling could normally be performed during the decreasing rate period and the final catalyst is ready for catalytic evaluation or application when it cools to room temperature.

Although precipitation and impregnation methods are widely used, their disadvantages are also evident, i.e., they usually result in nanoparticles with broad size distributions and compositional inhomogeneity. Recently, capping agent-free synthesis protocols with excellent control of alloy nanoparticles have been developed by regulating the adsorption of metal precursor on silica support.<sup>23</sup> The synthesis protocol is based on strong electrostatic adsorption (SEA), a special case of wet impregnation in which the charged metal precursor is strongly adsorbed on the oppositely charged oxide or carbon surfaces by controlling the pH value relative to the surface point of zero charge (PZC). By comparing monometallic and bimetallic nanoparticles

made by SEA and impregnation method, it is found that the SEA-made nanoparticles have stronger support interaction and require typically higher reduction temperature than the impregnated nanoparticles. In addition, the simultaneous SEA process can be potentially extended to other surfaces such as alumina, titania and carbon, as long as oppositely charged metal precursors are available.

To better control the process and outcome of chemical reactions, confined catalysts which enclose the active catalysts in a nanospace offer a powerful strategy. The limitation of metal nanoparticles within a nanosized space can inhibit their sintering, aggregation, detachment and poisoning.<sup>24-25</sup> To prepare such catalysts, traditional methods including impregnation, self-assembly and hydrothermal synthesis are used,<sup>24, 26-27</sup> however, further strategies are needed to remove excess metal or unwanted solvents. On the contrary, atomic layer deposition (ALD) technique has proven to be powerful for the synthesis of confined catalysts because of its precise control at the atomic level and its excellent uniformity (Scheme 2).<sup>28-30</sup>



**Scheme 2.** Application of ALD in the synthesis of different types of confined catalysts.<sup>31</sup>

ALD is a thin film deposition technique based on the sequential use of a chemical vapor phase process and during this process unreacted precursors and by-products are removed by a rinsing step. There are two routes for the synthesis of confined catalysts using ALD. In the first route, active nanoparticles can be deposited directly onto various forms of substrates, particularly porous materials, to form highly dispersed confined catalysts. Qin *et al.*,<sup>32</sup> successfully deposited Pt nanoparticles with precisely controlled size ( $\sim 0.8$  nm) and high dispersion into the KL zeolite channels. Various characterization techniques, including  $N_2$  sorption isotherms, infrared spectroscopy of adsorbed CO and DFT calculations, show that most of the Pt is in the KL channels, while a small part of Pt is in the pore opening or the outer surface. The strong interaction between Pt and the KL zeolite results in an electron-enriched state of Pt. The produced Pt/KL catalyst shows a highly efficient performance in *n*-heptane reforming to aromatics with a high toluene selectivity of up to 67.3% (toluene/total aromatics = 97.8%) and a low methane selectivity (0.9%) despite an extremely low Pt loading (0.21% by weight). In addition, the small size and high dispersion of the Pt nanoparticles inhibit the hydrogenolysis. The second route provided by Qin *et al.*,<sup>33</sup> is based on a template assistance. Using this protocol, they successfully prepared sharp-edged (less than 5 nm radius of curvature) and crescent-shaped half-nanotubes. The catalyst is initially prepared based on the creation of crescent-shaped nanochannels in an anodic aluminum oxide (AAO) template by adding ZnO and  $Al_2O_3$  (as sacrificial and filling materials, respectively), then was selectively removed from the pore walls. The subsequent galvanic deposition of metal in the nanochannels creates the desired

nanostructures. This method offers a high degree of freedom in controlling edge sharpness, gap size and wall thickness.

### 1.1.2 Interaction between supports and metals

In catalytic reactions, active phase usually disperses on support having large surface area, such as metal oxides, carbon materials and zeolites, to provide a satisfactory reaction rate and to prevent the aggregation of metal nanoparticles. Supports not only offer a high loading and good distribution of metal nanoparticles but in some cases also take part directly in the catalytic cycle and contribute to the overall catalytic activity, although they are themselves catalytically inert. Hence, understanding the interaction and charge transfer mechanisms between metal nanoparticles and supports is of great importance for the design and synthesis of high performance catalysts. In addition, surface defects (e.g., oxygen vacancies and impurities) and surface steps of supports can also be the anchoring sites that can work better against sintering at high reaction temperatures.<sup>34</sup> In this view, the stability of metal nanoparticles can be enhanced by fine-tuning the surface structures of supports.

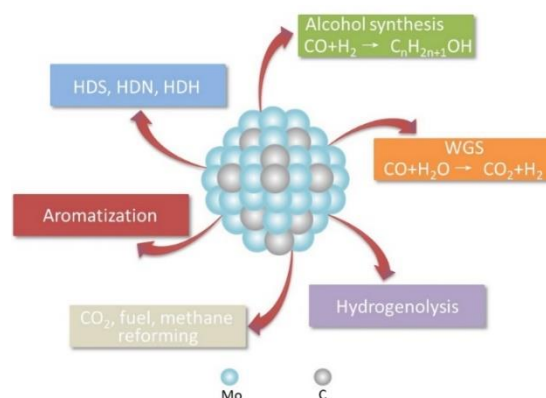
Strong metal-support interaction (SMSI), firstly introduced by Tauster *et al.*, at the end of the 1970s,<sup>35</sup> has been studied in detail for various support materials modifying the catalytic properties of supported metals. Although some SMSI mechanisms were proposed, all have ambiguities. For example, the dramatically suppressed chemisorption of H<sub>2</sub> and CO on TiO<sub>2</sub>-supported noble metals (Pd, Ru, Pt, Rh, Os, Ir) after high-temperature (500 °C) reduction<sup>35</sup> can be ascribed to the charge transfer between metal and support,<sup>35-38</sup> but this cannot explain the effect for metal nanoparticles larger than 10 nm, since the electronic interference on the entire particle is negligible.<sup>39-40</sup> With the development of spectroscopic techniques such as SEM and TEM, direct visual evidences of the spreading of metal oxides over metal surface are observed,<sup>41</sup> i.e., the reduced metal oxide species migrates onto the metal surface during high temperature reduction and blocks the active sites. Although the accurate mechanisms are controversial for decades, a significant role of SMSI in some reactions, such as CO<sub>2</sub> selective reduction,<sup>42</sup> cannot be denied. This effect is characterized by the strongly bound adsorbates (HCO<sub>x</sub>) on the reducible oxide supports (TiO<sub>2</sub> and Nb<sub>2</sub>O<sub>5</sub>), inducing oxygen vacancy formation in the support, causing HCO<sub>x</sub> functionalized encapsulation of Rh nanoparticles by the support. The encapsulation layer, permeable to reactants and stable under the reaction conditions, strongly influences the catalytic properties of Rh, e.g., a selectivity switch in CO<sub>2</sub> reduction from 100% CH<sub>4</sub> production on the bare Rh surface to 90% CO production in the HCO<sub>x</sub>-mediated SMSI state.

Charge transfer between supported metal and support at the interface results in electron deficient or rich configuration of the active sites. This directly influences the adsorption and desorption behaviors of adsorbed species on the active sites. Campbell proposed the electronic metal-supported interaction (EMSI) to explain the electronic perturbations between Pt cluster and ceria.<sup>43</sup> Rodriguez *et al.*,<sup>44</sup> found that strong electronic perturbation of small Pt nanoparticles on ceria enhances significantly H<sub>2</sub>O dissociation activity, particularly the Pt/CeO<sub>2</sub>(111) surface can dissociate water efficiently. On the other hand, support and metal nanoparticles can work cooperatively, proposed as synergistic metal support interaction, to alter and enhance the activity and selectivity. By comparing the performance of Cu/ZnO, Cu/CeO<sub>2</sub> and Cu/ZnO–CeO<sub>2</sub> catalysts in CO<sub>2</sub> hydrogenation to CH<sub>3</sub>OH, Hensen *et al.*,<sup>45</sup> investigated the synergistic metal support interaction and found that the higher CH<sub>3</sub>OH selectivity can be explained by the synergistic Cu–CeO<sub>2</sub> and Cu–ZnO interaction.

### 1.2 Mo<sub>x</sub>C and transition metals combined catalysts

Since the report by Levy and Boudart in 1973 that tungsten carbide exhibits platinum-like catalytic activity in the isomerization of hydrocarbons,<sup>46</sup> transition metal carbides (TMC) have attracted great attention as they are possibly cheap alternative to noble metal catalysts in various chemical reactions, particularly in C-H activation in hydrocarbons (dehydrogenation,<sup>47</sup> hydrogenation,<sup>48</sup> and hydrogenolysis<sup>49</sup>). Structurally, TMC are a class of compounds incorporating carbon atoms into the interstitial sites of their parent metals, which are typically group IV–VI metals.<sup>50</sup> Generally, carbides of early transition metals possess unique physical and chemical properties such as extreme hardness, high melting point and outstanding electric conductivity,<sup>51–52</sup> and therefore, they have been applied as cutting tools<sup>53</sup> and hard-coating materials.<sup>54</sup> For the electronic and chemical properties of TMC surfaces, studies indicate that carbon in TMC can induce both electronic and structural modifications at least on three aspects: (1) electronic interaction between the valence states of carbon and parent metal modifies the density of states (DOS) near the Fermi level; (2) incoming carbon typically increases the metal-metal distance as compared to that of the parent metal, resulting in a tensile strain in the metal lattice for additional modification of the metal *d*-band center<sup>55</sup> and (3) the number of surface metal sites, which are available as adsorption sites for reaction species, decreases with carbon atoms in/on the surface of TMC.

As one of the well-known TMC, molybdenum carbides, utilized in various chemical reactions,<sup>56–63</sup> have been extensively studied experimentally and theoretically. In the early stage, molybdenum carbides themselves were applied in heterogeneous catalysis as active phases for reactions originally catalyzed by noble metals such as CO hydrogenation,<sup>64–65</sup> water-gas shift (WGS) reaction,<sup>66–67</sup> hydrogenolysis,<sup>68</sup> methane reforming,<sup>69–71</sup> aromatization,<sup>72–73</sup> hydrodesulfurization (HDS),<sup>74–75</sup> hydrodenitrogenation (HDN)<sup>76–77</sup> and dehalogenation (Scheme 3).<sup>78–81</sup>



**Scheme 3.** Molybdenum carbides involved chemical transformations.

With the development of supports for catalysis, molybdenum carbides are used as an alternative candidate. Since pure molybdenum carbides are active phase in many reactions, combining molybdenum carbides as supports and other catalytically active transition metals could show promise to produce more active and novel catalysts to meet the demands of the modern chemical industry and environmental problems.

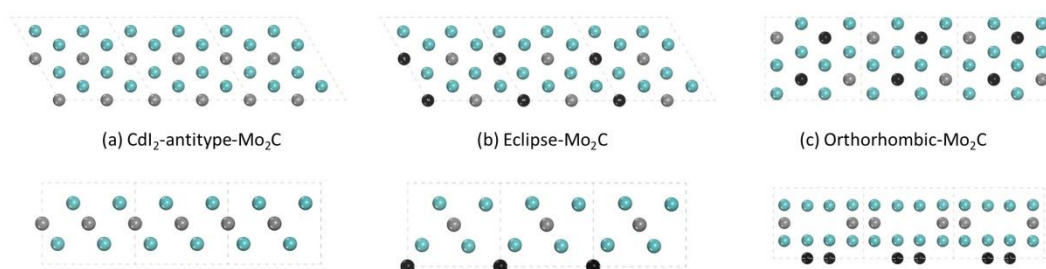
### 1.2.1 Structural and electronic properties of $\text{Mo}_x\text{C}$

Studying the structural and electronic properties is important and necessary to understand the interaction and the synergy between supported metals and molybdenum carbides. The first determination of  $\text{Mo}_2\text{C}$  crystal

structure was reported by Westgren and Phragmen in 1926.<sup>82</sup> Structurally, Mo<sub>2</sub>C is divided into hexagonal ( $\beta$ -Mo<sub>2</sub>C) and orthorhombic ( $\alpha$ -Mo<sub>2</sub>C) phases (Scheme 4), although hexagonal phase as  $\alpha$  and orthorhombic phase as  $\beta$  are also used in literature. Therefore, it is better to use hexagonal and orthorhombic phases for clarity.

In the hexagonal ( $\beta$ -Mo<sub>2</sub>C) phase, Mo atoms are hexagonal close-packed and carbon atoms are arranged statistically in the octahedral holes (the number of holes is twice the number of C atoms). The lattice parameters of the hexagonal ( $\beta$ -Mo<sub>2</sub>C) phase were reported as  $a = 3.002 \text{ \AA}$  and  $c = 4.724 \text{ \AA}$  by Kuo and Hägg in 1952,<sup>83</sup> and  $a = 3.00292 \text{ \AA}$  and  $c = 4.72895 \text{ \AA}$  by Fries and Kempter in 1960.<sup>84</sup> According to the different arrangement of carbon atoms,<sup>85</sup> the hexagonal ( $\beta$ -Mo<sub>2</sub>C) phase can be divided into two types, i.e.; the C6-type with space group of P3m1, where carbon atoms arrange only in one layer and it is also called Cdl<sub>2</sub>-antitype since it is similar with the Cdl<sub>2</sub> structure; and the L'3-type with space group of P63/mmc, where carbon atoms are arranged randomly on all possible sites but systematically in both layers. Experimental and theoretical studies<sup>86-87</sup> identified the eclipsed configuration of the random carbon atoms in the hexagonal L'3-type as thermodynamically most stable, representing the most possible candidate for the disordered hexagonal structure.

In the orthorhombic ( $\alpha$ -Mo<sub>2</sub>C) phase, Mo atoms are also hexagonal close-packed but deformed to an orthorhombic symmetry and carbon atoms orderly occupy half of the octahedral holes. The lattice parameters were reported as  $a = 4.724$ ,  $b = 6.004$  and  $c = 5.199 \text{ \AA}$  by Parthe *et al.*,<sup>85</sup> in 1963, and  $a = 4.732$ ,  $b = 6.037$  and  $c = 5.204 \text{ \AA}$  by Christensen in 1977.<sup>88</sup>

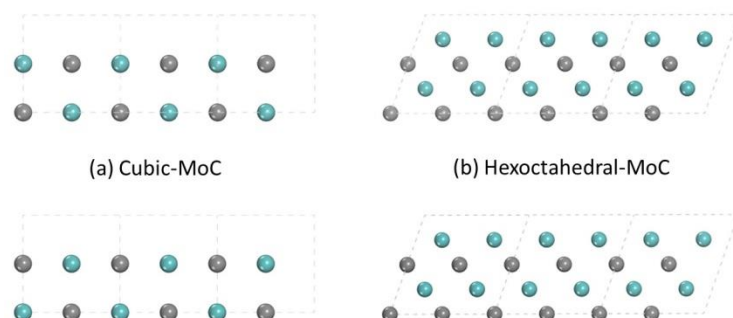


**Scheme 4.** Top (top) and side (bottom) views of Mo<sub>2</sub>C cells (Mo: cyan, first layer C: gray, second layer C: black).

In industrial synthesis, Mo precursors (mostly metal powder, hydrides or oxides) are mixed with certain amount of carbon and then heated to a high temperature up to 1500 K under an inert or reducing atmosphere; and the products obtained are mainly the thermodynamically stable hexagonal ( $\beta$ -Mo<sub>2</sub>C) phase with a relatively small surface area. In 1985, Boudart *et al.*,<sup>89</sup> proposed the temperature-programmed carburization process to increase the surface area. In this process, Mo precursors (normally molybdenum oxides) are introduced into the flow of a hydrocarbon/H<sub>2</sub> mixture. With the gradual increase in temperature, hydrocarbon decomposes and then the generated carbon is incorporated into the reduced Mo lattice to form the specific molybdenum carbides. This process not only increases the surface area of the carbide materials but also can load molybdenum carbides onto various supports. On the basis of the developed synthesis, Dubois *et al.*,<sup>90</sup> and Epicier *et al.*,<sup>91</sup> systematically studied the transformation of the hexagonal ( $\beta$ -Mo<sub>2</sub>C) and orthorhombic ( $\alpha$ -Mo<sub>2</sub>C) phases at high temperatures. They found that the orthorhombic ( $\alpha$ -Mo<sub>2</sub>C) phase is most stable below 1350°C and turns to the hexagonal ( $\beta$ -Mo<sub>2</sub>C) (Cdl<sub>2</sub>-antitype) at 1350-1960°C, while the hexagonal ( $\beta$ -Mo<sub>2</sub>C) (L'3-type) is most stable at temperature higher than 1960°C.



In addition to the Mo<sub>2</sub>C phases, the MoC phase has also been widely studied in experiment and theory.<sup>92-95</sup> Two types of the MoC phase are often utilized: cubic-MoC and hexoctahedral-MoC (Scheme 5), and the space group for both is  $Fm\bar{3}m$ . The cubic phase is referred as  $\delta$ -MoC by the group of Illas<sup>92-93</sup> and the hexoctahedral phase is referred as  $\alpha$ -MoC by the group of Ma.<sup>94-95</sup> The lattice parameters of the cubic  $\delta$ -MoC cell are 4.278 Å from experiment<sup>96</sup> as well as 4.444<sup>97</sup> and 4.373 Å<sup>92</sup> from computation. For the hexoctahedral  $\alpha$ -MoC cell, the parameters are 4.3318 Å from experiment and 4.270 Å from computation.<sup>94</sup>



**Scheme 5.** Top (top) and side (bottom) views of MoC cells (Mo: cyan, C: gray).

### 1.2.2 Transition metals modified Mo<sub>x</sub>C in heterogeneous catalysis

With the development of molybdenum carbides as functional supports, exploring the synthesis of doping second transition metal onto carbides were carried out and two common methods were used. The first one is to introduce metal precursor by impregnation or other deposition processes directly via pre-synthesized carbides, and the second one is to precipitate metal precursor with molybdenum compounds (usually ammonium heptamolybdate) to form metal-Mo-oxide composite. In recent years, the later strategy for the synthesis of metal doped molybdenum carbides has been frequently used. By using a mixture of an aqueous solution of metal nitrate and ammonium heptamolybdate to form the metal-Mo-oxide composite, Nagai *et al.*,<sup>98</sup> prepared Ni-Mo and Co-Mo carbides, which show satisfactory reactivity in WGS reaction at low temperature.

Utilizing pure Mo<sub>2</sub>C in methanol reforming reaction, Széchenyi and Solymosi found high methanol conversion with high activity and selectivity of H<sub>2</sub> at 623 K,<sup>99</sup> but significant deactivation of the catalyst after 10 h. In comparison with pure hexagonal  $\beta$ -Mo<sub>2</sub>C, Guan *et al.*,<sup>58-59</sup> tested supported transition metals (Pt, Fe, Co and Cu) on hexagonal  $\beta$ -Mo<sub>2</sub>C in steam reforming of methanol and found that the supported transition metal catalysts show higher conversion of methanol and higher yield of H<sub>2</sub>, and the supported Pt catalyst exhibits the highest activity and selectivity with 100% methanol conversion even at low temperature (200 °C). In addition, phase transition of molybdenum carbide, depending on metal loading, is found for supported Pt and Cu catalysts, e.g., more cubic  $\alpha$ -Mo<sub>2</sub>C<sub>1-x</sub> phase with the increasing of Cu or Pt loading is observed by XRD characterization.

In reactions catalyzed by molybdenum carbides, such as hydrocarbon isomerization, dehydrogenation and ammonia synthesis, cubic  $\alpha$ -MoC commonly does not exhibit excellent activity as hexagonal  $\beta$ -Mo<sub>2</sub>C due its less metallic properties. As a result, cubic  $\alpha$ -MoC has been not as much studied as hexagonal  $\beta$ -Mo<sub>2</sub>C both experimentally and theoretically. Ma *et al.*,<sup>94</sup> have systematically investigated cubic  $\alpha$ -MoC as support and the interaction with Pt nanoparticles as well as their performance in aqueous methanol reforming. It is found that the Pt/ $\alpha$ -MoC catalyst exhibits extraordinary performance with an average turnover frequency of 18046 mol of H<sub>2</sub> (mol of Pt)<sup>-1</sup> h<sup>-1</sup> at 463 K, which is 2 orders of magnitude higher than those of the traditional Pt/oxide

catalysts and H<sub>2</sub> production rate is 32-fold higher than that of pure cubic  $\alpha$ -MoC catalyst. Moreover, the mass specific activity of 2% Pt/ $\alpha$ -MoC catalyst is over 10 times higher than that of Pt/ $\beta$ -Mo<sub>2</sub>C with the same loading, suggesting that  $\alpha$ -MoC exhibits much stronger interaction than hexagonal  $\beta$ -Mo<sub>2</sub>C with Pt species.

In the process of steam reforming of alcohols, an obvious and serious issue is the inevitable CO impurity, which is required to be less than 10 ppm in hydrogen economy, since further purification and separation of H<sub>2</sub> from impurities will consume a large amount of energy and cost. In this regard, WGS reaction ( $\text{CO} + \text{H}_2\text{O} = \text{H}_2 + \text{CO}_2$ ) is a candidate to remove CO and produce H<sub>2</sub> at the same time. Usually, industrial WGS reaction is conducted in two temperature regions: high temperature region (583-723 K) using Fe-based catalysts (e.g., Fe<sub>2</sub>O<sub>3</sub>/Cr<sub>2</sub>O<sub>3</sub>/MgO)<sup>100</sup> and low temperature region (473-523K) using Cu-based catalysts (e.g., CuO/ZnO/Al<sub>2</sub>O<sub>3</sub>).<sup>101</sup> Various transition metals catalysts such as Co, Ni, Pd, Pt, Ru and Rh are also found active for WGS reaction under different conditions.<sup>102-104</sup>

Thermodynamically WGS reaction is moderately exothermic, equilibrium-limited and favors low temperature, and therefore reducing temperature is beneficial for CO conversion. However, current industrial catalysts either require a mobile CO removal system due to their high temperature and poor stability or bad activity at low temperature with poor conversion. In this regard, molybdenum carbide catalysts show the potential to improve the low temperature activity of WGS reaction. For example, Patt *et al.*,<sup>66</sup> reported that Mo<sub>2</sub>C is highly active for WGS reaction compared to the commercial catalysts (Cu–Zn–Al) at low temperature (493-568 K). Since both Mo<sub>2</sub>C and transition metals are active for WGS reaction, adding transition metals into Mo<sub>2</sub>C system to form bimetallic carbides and dispersing metal nanoparticles on Mo<sub>2</sub>C surfaces to form supported catalysts were studied extensively. Ribeiro *et al.*,<sup>105</sup> investigated the promotion effect of hexagonal  $\beta$ -Mo<sub>2</sub>C supported Pt, Pd, Au, Ni, Cu and Ag catalysts in WGS kinetics. Compared with the commercial catalyst (Cu/ZnO/Al<sub>2</sub>O<sub>3</sub>), the supported Au, Pd and Ni catalysts are at least 4 times higher active, and the Pt/ $\beta$ -Mo<sub>2</sub>C catalyst is nearly 8 times more active at ultralow operation temperature (393 K). Among other reported transition metals doped catalysts tested in WGS reaction,<sup>106-108</sup> moreover, the Pt/ $\beta$ -Mo<sub>2</sub>C catalyst is much more active at 473 K.

A number of Au/ $\alpha$ -MoC catalysts were synthesized and tested in WGS reaction by Ma *et al.*,<sup>95</sup> It is found that 2% Au/ $\alpha$ -MoC, which reaches 1.05 mol of CO/(mol of Au/s) at 423 K and is more than 25 times higher active than the precedent catalysts, is probably the most active WGS catalyst known so far. Structure characterization indicates that Au nanoparticles are anchored with fine dispersion over cubic  $\alpha$ -MoC even after 2h treatment at 863 K, revealing a strong interaction between Au nanoparticles and cubic  $\alpha$ -MoC. High-resolution STEM images and EDS element mappings show two types of Au species on the surface of cubic  $\alpha$ -MoC: small Au clusters (1–2 nm average diameter) and atomically dispersed Au atoms. A NaCN leaching proves that the layered Au clusters rather than Au single atoms are active for WGS reaction at ultralow temperature. Temperature-programmed surface reaction shows that the entire water dissociation step takes place on the cubic  $\alpha$ -MoC surface, while the strong interaction between Au cluster and support enhances the reaction rate for surface OH and CO.

Inspired by these results, Ma *et al.*,<sup>109</sup> successfully developed a one-pot tandem process combining FTS and WGS reaction in aqueous phase to produce liquid fuels with a highly efficient tandem Pt–Mo<sub>2</sub>C/C and Ru/C system. In this system, Pt–Mo<sub>2</sub>C/C is active for WGS reaction, and Ru/C is the active FTS catalyst, where a high formation rate of liquid hydrocarbons (up to 8.7 mol<sub>-CH<sub>2</sub></sub>·mol<sub>Ru</sub><sup>-1</sup> h<sup>-1</sup>) is achieved at 200 °C and the selectivity for

C<sub>5+</sub> hydrocarbons is up to 68.4%.

All these studies demonstrate the synergy of transition metals and molybdenum carbide supports, resulting in exceptional catalytic performance superior to pure transition metals or pure molybdenum carbides as active catalysts. Comparing the structures and behavior of metals involved in cubic  $\alpha$ -MoC and hexagonal  $\beta$ -Mo<sub>2</sub>C indicates that the structural variation of the carbides would significantly change the catalytic behavior of these systems and further investigation into the structure-performance relationship in molybdenum carbide-based catalysts is important for advanced catalyst development.

### 1.2.3 Structures of transition metals modified Mo<sub>x</sub>C

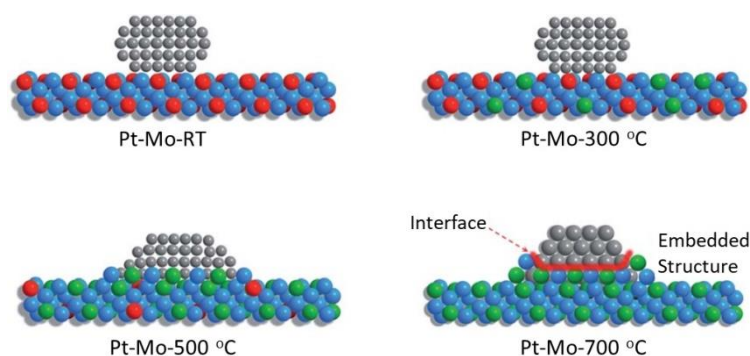
Despite different synthetic methods to incorporate transition metals into molybdenum carbide to form functionalized catalysts, there are mainly three structures for the prepared catalysts; supported, doped and embedded, depending on the factors such as metal properties, metal loadings and carburization temperature. Zhao *et al.*,<sup>110</sup> synthesized molybdenum carbide supported cobalt catalyst on modified activated carbon (Co-Mo<sub>2</sub>C/AC) for the chemo-selective reduction of aromatic nitro compounds. They found that Co is successfully introduced into the Mo<sub>2</sub>C matrix as observed from XRD analysis. Chen *et al.*,<sup>62</sup> prepared several copper-doped molybdenum carbide (Cu/Mo<sub>2</sub>C) nanomaterials for the hydrogenation of dimethyl oxalate to ethanol. At high Cu/Mo atomic ratio, the peak of Cu(111) lattice plane is found from XRD analysis, while at Cu/Mo atomic ratio lower than 0.04:1, the diffraction peak of Cu is not detected. It may be due to the well dispersion of Cu on the Mo<sub>2</sub>C surface or incorporation of Cu into the Mo<sub>2</sub>C lattice.

For the supported metal catalyst, which is either metal clusters or single metal atoms, there is a correlation between the reactivity, the size of supported Pt domains, the Pt-Mo interaction and the percentage of cubic  $\alpha$ -MoC in the support. Using X-ray-absorption fine-structure (EXAFS) technique, Ma *et al.*,<sup>94</sup> found a high percentage of atomically dispersed Pt<sub>1</sub> for Pt loading in the range of 0.2 to 2 wt %. When the Pt loading decreases to 0.2 wt %, both EXFAS and STEM analysis show that the Pd-Pd coordination number drops to 0, proving that Pt disperses atomically on  $\alpha$ -MoC and the nanoparticles disappear with the decrease of Pt loading. Similarly, atomically dispersed Au on cubic  $\alpha$ -MoC for WGS reaction has also been detected and confirmed by XANES and XPS characterization.

Varying metal/Mo molar ratio can lead to phase transformation. For Cu doped molybdenum carbide catalyst (Cu/Mo<sub>x</sub>C<sub>y</sub>) prepared from carburization of Cu doped molybdenum oxide (Cu/MoO<sub>3</sub>) using temperature-programmed reaction with a 20% CH<sub>4</sub>/H<sub>2</sub> mixture at 700 °C by Guan *et al.*,<sup>59</sup> XRD analysis does not show any peaks corresponding to metallic Cu in all as-prepared samples, suggesting the absence of metallic Cu nanoparticles. With the increasing of the Cu/Mo molar ratio from 1.6/98.4 to 10/90, the signal of cubic  $\alpha$ -MoC<sub>1-x</sub> phase increases but starts to decrease with the continued increase of the Cu/Mo molar ratio at 15/85. At the Cu/Mo molar ratio of 25/75, the  $\alpha$ -MoC<sub>1-x</sub> phase was barely observed and mainly the hexagonal  $\beta$ -Mo<sub>2</sub>C phase was found. Phase transformation of Mo<sub>2</sub>C is related not only to the varying amount but also the intrinsic nature of the metals. For instance, the hexagonal  $\beta$ -Mo<sub>2</sub>C phase was formed for supported Fe, Co, or Cu catalysts, while supported Ni, Pd or Pt facilitate the formation of the cubic  $\alpha$ -MoC phase.<sup>58-59, 111</sup>

In practical application, supported catalysts are inevitably confronted with metal agglomeration during the reactions, especially at high temperatures.<sup>112</sup> In addition, much attention was paid to the development of novel synthetic methods for the preparation of nanostructured catalysts with higher activity and thermal stability,

limited by the uncertainty of the preparation of the doped structure. An alternative embedding approach, which typically involves embedding metal nanoparticles in an inorganic matrix or support, is proposed.<sup>113-115</sup> Using temperature-programmed reaction method, Guan *et al.*,<sup>60</sup> synthesized for the first time Pt embedded molybdenum carbide catalysts, which have excellent and stable catalytic activity in WGS reaction at low temperatures. XRD analysis shows that as the degree of carburization (temperature) increases, 3 wt% Pt-modified molybdenum carbide catalyst is formed along with the gradual transfer from  $\text{MoO}_3$  to  $\text{MoO}_x\text{C}_y$ , and full carburization at 700 °C, whereby multiple molybdenum carbide phases (i.e.,  $\beta\text{-Mo}_2\text{C}$  and  $\alpha\text{-MoC}_{1-x}$ ) coexist. XRD analysis also shows that the intensity of the Pt peak becomes weaker after the carburization process, indicating either the size or the morphology changes of Pt nanoparticles into platelet-shaped (Scheme 6).



**Scheme 6.** Embedded structure of Pt on molybdenum carbide surface during the carburization process (blue ball: molybdenum, red ball: oxygen, green ball: carbon, grey ball: platinum).<sup>60</sup>

Further HR-TEM and XPS analysis shows that the Pt nanoparticles in full carburized catalyst ( $\text{Pt}/\text{Mo}_x\text{C}_y$ ) are surrounded by molybdenum carbides, indicating the formation of the embedded structure. This novel structuralized catalyst utilized into WGS reaction gives a CO conversion of 100 and 90% in the reaction time of 50 h at 150 and 400 °C, respectively. Importantly, the XRD pattern of the spent catalyst is not changed compared to the fresh one, indicating the excellent stability of the embedded  $\text{Pt}/\text{Mo}_x\text{C}_y$  catalyst. Thus, understanding the structure, stability and activity relationship in molybdenum carbide and molybdenum carbide supported metal catalysts is significant for studying reaction mechanisms and design of novel catalysts.

### 1.3 Theoretical studies

Since pure molybdenum carbides are active in many chemical reactions, there are extensive theoretical studies about the structures, stability and adsorption properties on small molecules of hexagonal  $\beta\text{-Mo}_2\text{C}$  and orthorhombic  $\alpha\text{-Mo}_2\text{C}$  phases. For the hexagonal  $\beta\text{-Mo}_2\text{C}$  phase, the facet stability based on the computed surface energy<sup>116</sup> in Table 1 has the decreasing order of (101) > (011) > (201) > (001) > (100) > (112) > (111) > (010) > (103) > (102) > (110), in agreement with the experimentally determined XRD pattern and intensity.<sup>117</sup>

**Table 1.** Surface energies ( $\text{J}/\text{m}^2$ ) of different terminations (ter) of hexagonal  $\beta\text{-Mo}_2\text{C}$  by using graphite bulk energy as carbon chemical potential ( $\mu_{\text{C}}$ ).<sup>a</sup>

Facet	Mo-ter <sup>b</sup>	C-ter	Mo/C-ter
001	2.76	2.67	—
010	3.32, 3.18	3.01	—

011	2.87	–	2.57
100	3.27, 2.93	3.40	–
101	2.52, 3.32	–	2.19
102	3.05	3.28	–
103	3.12	3.05	–
110	3.42	–	3.09
111	2.99	3.05	–
112	3.21	–	2.96
201	–	2.67	2.65

(a) Smaller value indicates higher stability. (b) Multiple terminations for some facets.

The (101) surface with Mo/C mixed termination has the lowest surface energy (2.19 J/m<sup>2</sup>) and is therefore most stable. The Wulff construction based on the calculated surface free energies suggests that with increasing temperature the equilibrium ratio of the (101) surface increases, while that of (001) decreases. The (101) facet represents the largest surface area of hexagonal  $\beta$ -Mo<sub>2</sub>C, in good accordance with the HRTEM results.<sup>98, 118</sup> Next, the adsorption properties of CO, H<sub>2</sub> and H<sub>2</sub>O on hexagonal  $\beta$ -Mo<sub>2</sub>C surfaces have been investigated, and these molecules and their adsorption intermediates are involved in many catalytic reactions, i.e., WGS reaction, FTS and alcohol synthesis from CO hydrogenation. First, the (001), (101) and (201) surfaces of the hexagonal  $\beta$ -Mo<sub>2</sub>C phase have been used to study their surface properties by investigating CO adsorption under the consideration of temperature and CO partial pressure.<sup>119</sup> It is reported that the most stable (101) surface has lower saturated monolayer coverage (9.64/nm<sup>-2</sup>; 8 CO) than the less stable (001) (10.85/nm<sup>-2</sup>; 16 CO) and (201) (11.74/nm<sup>-2</sup>; 10 CO) surfaces on the calculated stepwise CO adsorption energy. The relationship among CO coverage, temperature and CO partial pressure has been revealed by calculating surface Gibbs free energies; and the resulted phase diagram provides a theoretical basis for estimating the stable CO coverage by balancing temperature and CO partial pressure as well as for identifying the active surface and the initial states under given conditions for the reactions. Qualitatively, raising temperature lowers CO coverage at given CO partial pressure and raising CO partial pressure increases CO coverage at given temperature. Quantitatively, the calculated CO desorption temperature agrees perfectly with the experimentally determined results from the temperature-programmed desorption measurement.

To better understand the behaviors of hexagonal  $\beta$ -Mo<sub>2</sub>C in chemical reactions, the mechanisms of H<sub>2</sub>, O<sub>2</sub>, H<sub>2</sub>O, CO<sub>2</sub>, CO, CH<sub>4</sub> and C<sub>2</sub>H<sub>x</sub> dissociative adsorption on metallic Mo<sub>2</sub>C(001) surface and the Mo<sub>2</sub>C(101) surface with Mo/C = 1/1 surface ratio have been computed.<sup>120</sup> It is found that on both surfaces the dissociative adsorption of these small molecules is exothermic and has low barrier; and the Mo<sub>2</sub>C(001) surface has much stronger dissociative adsorption than the Mo<sub>2</sub>C(101) surface. On both surfaces, the dissociative adsorption of H<sub>2</sub>O under high oxygen coverage has also been considered along with gaseous H<sub>2</sub> evolution and high coverage carbon adsorption using carbon atom as carburization agent. Both surfaces can be easily oxidized with H<sub>2</sub>O and high oxygen coverage can be expected, and these surfaces can also be carburized by using CH<sub>4</sub>.

Hydrogen adsorption on the Mo-terminated (001) and (100) as well as Mo/C-terminated (101) and (201) surfaces of hexagonal  $\beta$ -Mo<sub>2</sub>C at different coverage has also been studied.<sup>121</sup> With the exception of the (001)

surface, which has barrier-free  $\text{H}_2$  dissociative adsorption, molecular  $\text{H}_2$  adsorption is found on the (100), (101) and (201) surfaces, and  $\text{H}_2$  dissociative adsorption has rather low barrier of 0.14, 0.34 and 0.20 eV, respectively. On these surfaces,  $\text{H}_2$  dissociative adsorption is exothermic by  $-2.15$ ,  $-1.09$ ,  $-0.64$  and  $-1.14$  eV, respectively, indicating their ability to activate  $\text{H}_2$ . As in case of CO adsorption, the resulted phase diagram based on the computed surface Gibbs free energies reveals the dependence of hydrogen coverage on temperature and partial pressure, i.e., at given  $\text{H}_2$  partial pressure, raising temperature decreases the coverage, while at given temperature, raising partial pressure increases the coverage.

To explore the oxidation process,  $\text{H}_2\text{O}$  dissociative adsorption on the hexagonal  $\beta\text{-Mo}_2\text{C}(101)$  surface has been computed.<sup>122</sup> At coverage up to 0.5 ML ( $n = 1-4$ ), all  $\text{H}_2\text{O}$  molecules adsorb on the top of surface Mo atoms, and further  $\text{H}_2\text{O}$  adsorption ( $n = 5-8$ ) relies only on hydrogen bonding. At coverage up to 0.5 ML,  $\text{H}_2\text{O}$  dissociation into surface OH and O is favorable kinetically and thermodynamically, and OH dissociation into O and H can have equilibrium. At higher coverage ( $> 0.5$  ML), the adsorbed  $\text{H}_2\text{O}$  molecules prefer desorption instead of dissociation due to their weak hydrogen bonding. Therefore, surface OH is the most abundant oxygene species during  $\text{H}_2\text{O}$  dissociation, and surface OH rather than surface O atom should play an essential role in WGS reaction. Liu *et al.*,<sup>63</sup> studied the kinetics of WGS reaction on the Mo- and C-terminated hexagonal  $\text{Mo}_2\text{C}(001)$  and  $\text{Cu}(111)$  surfaces and found the decrease of WGS activity in the order of  $\text{Cu} > \text{C-Mo}_2\text{C}(001) > \text{Mo-Mo}_2\text{C}(001)$ , due to the too strong bonding of surface oxygen to surface C or Mo sites, which suppresses the removal of surface oxygen.

Apart from the hexagonal  $\beta\text{-Mo}_2\text{C}$  phase, the structure, stability and surface adsorption properties of the orthorhombic  $\alpha\text{-Mo}_2\text{C}$  phase have also been systematically computed (Table 2).<sup>123</sup>

**Table 2.** Surface energies ( $\text{J/m}^2$ ) of different terminations (ter) of orthorhombic  $\alpha\text{-Mo}_2\text{C}$  by using graphite bulk energy as carbon chemical potential ( $\mu_{\text{C}}$ ).<sup>a</sup>

Facet	Mo-ter <sup>b</sup>	C-ter <sup>b</sup>	Mo/C-ter <sup>b</sup>
001	3.32, 3.16	3.05	–
010	–	–	3.15, 2.94
011	3.20	3.26, 3.28	3.26, 3.11, 3.20
100	3.11	3.08	–
101	–	–	2.70
110	3.57	2.63	3.07, 2.38
111	3.50,	–	2.42, 2.66, 2.97

(a) Smaller value indicates higher stability. (b) Multiple terminations for some facets.

The calculated surface energy (Table 2) has the decreasing order of  $(110) > (111) > (101) > (010) > (001) > (100) > (011)$ . However, the most stable surface is different at different  $\mu_{\text{C}}$ . For the twenty-two terminations of the seven low-Miller index orthorhombic  $\alpha\text{-Mo}_2\text{C}$  surfaces, the surface stability follows the order of  $(100) > (111) \approx (110)$  at  $\mu_{\text{C}} = -10.4$  eV, while it changes to  $(111) > (100) > (110)$  at  $\mu_{\text{C}} = -10.1$  eV, in good accordance with the available X-ray diffraction results. Similar to hexagonal  $\beta\text{-Mo}_2\text{C}$ , the adsorption, dissociation and desorption of CO on the Mo and C terminations of the orthorhombic  $\alpha\text{-Mo}_2\text{C}(100)$  surface have been explored at

different coverage.<sup>124</sup> On the Mo terminated surface (16 surface Mo atoms), the saturated coverage has  $n_{\text{CO}} = 16$  and the most stable adsorption configurations vary from the 3-fold hollow site to the coexisted bridge and 3-fold hollow sites, as well as to the atop site from coverage ranges of  $n_{\text{CO}} = 1-4$ ,  $n_{\text{CO}} = 5-9$  and  $n_{\text{CO}} = 10-16$ , respectively. On the C termination having 8 surface C atoms and 16 Mo atoms exposed, diverse molecular CO adsorption configurations at different coverage are found, i.e., the adsorbed CO molecules are located on surface C atoms for  $n_{\text{CO}} = 1-8$ , and two adsorption configurations on the surface C and Mo sites coexist for  $n_{\text{CO}} = 9-16$ . These results are supported by the agreement between the computed and recorded C-O stretching frequencies from the high-resolution electron energy loss spectroscopy studies. According to the computed CO stepwise adsorption energies and dissociation barriers, equilibrium between molecular and dissociative adsorption has been proposed. On the Mo termination, mixed molecular and dissociative CO adsorption is found for  $n_{\text{CO}} = 8$ ; pure dissociative CO adsorption and molecular CO adsorption are found for  $n_{\text{CO}} < 8$  and  $n_{\text{CO}} > 8$ , respectively. On the contrary, the C termination favors only molecular CO adsorption at all coverages.

On the contrary to the orthorhombic  $\text{Mo}_2\text{C}(100)$ ,<sup>124</sup> and eclipsed  $\text{Mo}_2\text{C}(001)$ ,<sup>119</sup> the  $\text{CdI}_2$ -antitype  $\text{Mo}_2\text{C}(001)$  surface has much weaker ability in CO adsorption and activation based on the computed CO adsorption energy and dissociation barrier at low coverage.<sup>125</sup> Due to the different surface structures, CO adsorption has coverage dependent configurations at the top, bridge and 3-fold hollow sites on the orthorhombic  $\text{Mo}_2\text{C}(100)$  and eclipsed  $\text{Mo}_2\text{C}(001)$  surfaces, while only adsorption configuration at the top site on the  $\text{CdI}_2$ -antitype  $\text{Mo}_2\text{C}(001)$  surface. In addition, Mo atoms on the orthorhombic  $\text{Mo}_2\text{C}(100)$  and eclipsed  $\text{Mo}_2\text{C}(001)$  surfaces are coordinatively unsaturated, while those on the  $\text{CdI}_2$ -antitype  $\text{Mo}_2\text{C}(001)$  surface are saturated. This might rationalize their different activity in the adsorption and activation of CO and  $\text{H}_2$ . All these investigations on those  $\text{Mo}_2\text{C}$  surfaces provide the basis for further systematic studies on the reaction mechanisms and are also of great importance for not only practical industry applications but also future catalysts design.

For the MoC with the ratio of  $\text{Mo}/\text{C} = 1/1$ , Jin *et al.*,<sup>126</sup> have systematically computed the structure and stability of seven  $\delta$ -MoC surfaces, and found that the most stable surface changes from the carbon deficit metallic (311)-Mo termination to mixed Mo/C termination of (100) surface with the increase of the carbon chemical potential ( $\mu_{\text{C}}$ ), eventually to carbon rich (311)-C termination. On the basis of calculated surface energy and Wulff construction,  $\delta$ -MoC has different morphologies at different carburization conditions, i.e., only (311) surface is exposed at  $\text{CH}_4/\text{H}_2$  gas mixture; (100) and (210) surfaces are exposed at  $\mu_{\text{C}}$  comparable with graphite bulk energy; while (100), (210) and (311) surfaces are exposed at  $\text{CO}/\text{CO}_2$  gas mixture.

Extensive studies of the cubic  $\delta$ -MoC phase have been reported by Illas and co-workers. The geometric and electronic structure of  $\delta$ -MoC and its low Miller-index surfaces, (001), (111) and (011), have been computed.<sup>92</sup> It is found that  $\delta$ -MoC has a large ionic contribution. The (001) surface is computed as most stable and the polar (111) surface is also stable and exhibits a reduced work function, while the unreconstructed (011) surface is highly unstable. In addition to investigating the interaction between metal atoms and carbide surfaces, they investigated  $\text{H}_2$  dissociative adsorption.<sup>127</sup> It is found that  $\text{H}_2$  dissociative adsorption is strongly exothermic on all three surfaces and the dissociation barrier with van der Waals correction is essentially zero on both termination of hexagonal  $\beta$ - $\text{Mo}_2\text{C}(001)$ , while a small but noticeable (0.60 eV) barrier on cubic  $\delta$ - $\text{MoC}(001)$  suggests the desorption instead of dissociation.

In addition to the pure surfaces of molybdenum carbides, decorated surfaces with transition metals have

attracted increasing interests from experiment and theory. Computationally, the most common model is supported and has simply single metal atom or metal nanoparticles adsorbed on surface. For example, Illas *et al.*,<sup>128</sup> found that the interaction between transition metal atoms and transition metal carbides is rather strong. They further studied the interaction of Au, Cu and Ni metal atoms with the  $\delta$ -MoC(001) surface with the respect of adsorption energy, equilibrium geometry, work function, atomic charge, projected density of states (PDOS) and shifts of the transition metal d-band center.<sup>129</sup> They found the interaction strength following the order Ni > Cu > Au, and it turns to be coverage dependent. In addition, PDOS analysis shows that a higher atomic coverage produces a shift of the d-band center closer to the Fermi level, in line with the decrease of the calculated adsorption energy, and the calculated d-band center proposes the decrease of the activity in the order Ni > Cu > Au. They further investigated and compared the atomic structure and electronic properties of Cu<sub>n</sub> nanoclusters ( $n = 4, 6, 7$  and 10) on  $\delta$ -MoC(001) and orthorhombic  $\beta$ -Mo<sub>2</sub>C(001) with C- and Mo-terminations.<sup>93</sup> They found that the Cu nanoparticles on hexagonal  $\beta$ -Mo<sub>2</sub>C(001), either Mo- or C-terminated, prefer two-dimensional structure, while a three-dimensional geometry is preferred on cubic  $\delta$ -MoC(001), indicating that Mo/C ratio and surface polarity play a key role in determining the structure of supported clusters.

Besides, Ma and coworkers applied a supported model with one Pt atom adsorbed on the cubic  $\alpha$ -MoC(111) surface (Pt/ $\alpha$ -MoC) as a bifunctional catalyst for H<sub>2</sub> generation from aqueous methanol reforming.<sup>94</sup> It is found that cubic  $\alpha$ -MoC(111) is active for H<sub>2</sub>O dissociation and the atomically dispersed Pt atom is active for C–H bond activation, while the Pt and  $\alpha$ -MoC interface is the active site for the generation of CO<sub>2</sub> and H<sub>2</sub>.

For WGS reaction at low temperature, they utilized cubic  $\alpha$ -MoC(111) supported monolayer Au and Au<sub>15</sub> cluster catalysts.<sup>95</sup> On the cubic  $\alpha$ -MoC(111) supported monolayer catalyst, Au/ $\alpha$ -MoC(111), H<sub>2</sub>O dissociation [H<sub>2</sub>O → OH + H] has high barrier of 1.66 eV and is endothermic by 1.55 eV, and is favored neither kinetically nor thermodynamically. On the  $\alpha$ -MoC(111) supported Au<sub>15</sub> cluster, Au<sub>15</sub>/ $\alpha$ -MoC(111), on the contrary, H<sub>2</sub>O dissociation has lower barrier of 0.77 eV and is exothermic by 1.06 eV. As a result, the low barrier of H<sub>2</sub>O dissociation results in the presence of high OH coverage and the rate limiting step (CO + OH → CO<sub>2</sub> + H) has also low barrier of 0.52 eV. These results on the supported Au<sub>15</sub> nanoparticle model agree with the experiment.

In addition to the supported model, the substitution model, in which one or more parent surface metal atoms are substituted by other transition metal atoms, is also frequently used to modify the surface properties. To study the kinetics of surface oxygen removal, Zhou *et al.*,<sup>130</sup> used six different models on the basis of the orthorhombic  $\alpha$ -Mo<sub>2</sub>C(001) surface, i.e.; the clean surface with both Mo- and C-termination, T<sub>Mo</sub>-Mo<sub>2</sub>C(001) and T<sub>C</sub>-Mo<sub>2</sub>C(001), the surface with Ni substitution, in which one Mo atom of the top Mo surface is substituted by one Ni atom, T<sub>Mo</sub>-NiMo<sub>2</sub>C(001) and T<sub>C</sub>-NiMo<sub>2</sub>C(001), and the surface with Ni adsorption, in which one Ni atom is chemisorbed on the surface, Ni-T<sub>Mo</sub>-Ni/Mo<sub>2</sub>C(001) and T<sub>C</sub>-Ni/Mo<sub>2</sub>C(001). It is found that the Ni adsorbed T<sub>Mo</sub>-Ni/Mo<sub>2</sub>C(001) and T<sub>C</sub>-Ni/Mo<sub>2</sub>C(001) surfaces as well as the Ni substituted T<sub>Mo</sub>-NiMo<sub>2</sub>C(001) surface can destabilize the adsorption of surface O and OH species, and thus promote the removal process, and the Ni-adsorbed T<sub>C</sub>-Ni/Mo<sub>2</sub>C(001) is most active in surface O removal. These results are supported by the temperature-programmed reduction profiles of Mo<sub>2</sub>C and Ni-doped Mo<sub>2</sub>C catalysts. Recently, Hu *et al.*,<sup>131</sup> prepared a Ni-doped Mo<sub>2</sub>C electrocatalyst with nanoflower clusters on carbon fiber paper via a molten salt synthesis protocol for hydrogen evolution reaction. The XRD analysis shows that the Ni atoms are successfully doped into the crystal lattice of Mo<sub>2</sub>C. Based on the XRD results, a DFT model was used in which a Mo atom was replaced by a Ni atom



in the hexagonal  $\beta$ -Mo<sub>2</sub>C model to simulate the Ni doping. For both pure and Ni-doped hexagonal  $\beta$ -Mo<sub>2</sub>C models, PDOS was calculated. Compared to pure  $\beta$ -Mo<sub>2</sub>C, the lower d-band center of the Ni-doped  $\beta$ -Mo<sub>2</sub>C (−0.69 vs. −1.66 eV) shows the property of better balancing the adsorption and desorption of H of the Ni doping; this agrees well with the experimental results.

In addition to adsorption and substitution models, embedding model has also been used in modifying surface structures and properties. Similar with the substitution model, in which on surface atom is normally substituted, embedding model can be considered as the substitution of several surface atoms by a transition metal cluster. For example, Orazi *et al.*,<sup>132</sup> embedded a Ni<sub>4</sub> cluster in graphene surface with multivacancy, i.e., three, four and six order vacancies were modeled by removing carbon atoms on the graphene surface. For all optimized structures, the hydrogen adsorption stability, geometry, electronic structure and mechanism have been investigated. In terms of Mo<sub>2</sub>C, the structures and properties with metal doping in multivacancy need further systematic investigations.

In addition to the activation of small molecules, catalytic reactions of large and functionalized substrates on the surfaces of molybdenum carbides have been carried out computationally. For example, Jiao *et al.*,<sup>133</sup> computed formic acid (HCO<sub>2</sub>H) dissociation into CO<sub>2</sub> and H<sub>2</sub> on the clean hexagonal  $\beta$ -Mo<sub>2</sub>C(101) surface by considering formic acid as hydrogen storage materials. The adsorption configurations and energies of the surface intermediates (HCO<sub>2</sub>H, CO<sub>2</sub>, CO, H<sub>2</sub>O, HCO<sub>2</sub>, CO<sub>2</sub>H, CHO, OH, O and H) have been systematically characterized. Among the different dissociation steps considered, the minimum energy path follows the sequence of the formate route (HCO<sub>2</sub>H → H + HCO<sub>2</sub>; HCO<sub>2</sub> → H + CO<sub>2</sub>). In addition to the  $\beta$ -Mo<sub>2</sub>C(101) surface with mixed Mo/C termination, Logsdai *et al.*,<sup>134</sup> computed the dehydration and dehydrogenation of formic acid on the Mo-terminated orthorhombic  $\beta$ -Mo<sub>2</sub>C(100) surface. To determine the most stable orientations and sites for each molecule to study the dehydration and dehydrogenation pathways of the conversion, different adsorption orientations of formic acid, CO, CO<sub>2</sub> and H<sub>2</sub>O on the surface at different sites were calculated. Thermodynamically, the conversion of the HCOOH is most likely to proceed by the breaking of H–COOH bond to yield CO as the dehydration product; however, the desorption energy for CO from the surface is high (2.74 eV), which suggests that the surface is susceptible to CO poisoning. Microkinetic analysis shows slow adsorption of formic acid on the surface and most of the surface sites were vacant and the conversion was inefficient. The concentration profile shows that the appearance of gas phase CO<sub>2</sub> will be kinetically faster than gas phase CO. CO formation will saturate the surface as the CO desorption step is very slow, and therefore rate limiting, in agreement with the computed CO adsorption energy. At 10 % and 40 % formic acid coverage, HCOOH conversion occurs at low temperature; CO<sub>2</sub> desorption is most favorable at 320 K, reaching a steady state at 370 K. All other species start desorbing from the surface after 400 K. This shows a temperature and concentration dependent formic acid dehydrogenation and dehydration; and this was not considered in computations.

To understand the catalytic role of molybdenum carbides in the conversion of biomass to chemicals and fuel additives, Jiao *et al.*,<sup>135</sup> computed the conversion of furfural into 2-methylfuran and furan on the clean and 4H pre-covered Mo<sub>2</sub>C(101) surfaces. The clean Mo<sub>2</sub>C(101) surface has two distinct surface sites: unsaturated C and Mo sites for the adsorption of H and furfural, respectively. The selectivity comes from the different preference of furfural hydrogenation and dissociation (F-CHO+H = F-CH<sub>2</sub>O vs. F-CHO = F-CO+H) under the variation of H<sub>2</sub> partial pressure. On the basis of the computed minimum energy path on the clean surface, micro-kinetic

analysis shows that high  $H_2$  partial pressure can promote 2-methylfuran formation and suppress furan formation. To verify this proposed selectivity trend of 2-methylfuran at high  $H_2$  partial pressure, the 4H pre-covered  $Mo_2C(101)$  surface (0.25 monolayer H coverage), which provides neighboring hydrogen to promote furfural hydrogenation and blocks the active sites for suppressing furfural dissociation, has been used. The computed results are in full agreement with the experimentally observed selective formation of 2-methylfuran and the half  $H_2$  reaction order as well as rationalize the need of high  $H_2$ /furfural ratio (400 to 1). On the basis of these results, a new two-step protocol for experiment is proposed, i.e., the first step is the pre-treatment of the catalyst with hydrogen and the second step is furfural hydrogenation on H pre-covered catalysts.

To understand the conversion mechanism of fatty acids to long-chain alkanes using molybdenum carbides as catalysts, Jiao *et al.*,<sup>136</sup> computed the hydrogenation of butyric acid to butane on the H-pre-covered hexagonal  $Mo_2C(101)$  surface. The first step is butyric acid dissociation into surface OH and acyl  $[R-COOH+H = R-CO+OH+H]$ , and the successive step is the formation of butanal from acyl hydrogenation  $[R-CO+OH+H = R-CHO+OH]$ . The second step of the reaction is butanal hydrogenation into butanol via surface butoxyl intermediate  $[R-CHO+H+OH = R-CH_2O+OH; R-CH_2O+H+OH = R-CH_2OH+OH]$ . The third step is butanol dissociation into surface OH and butyl  $[R-CH_2OH+H = R-CH_2+OH+H]$ , which is further hydrogenated into butane  $[R-CH_2+H+OH = R-CH_3+OH]$ . The formation of butanal and butanol as intermediates in equilibrium as well as butane as the final product is in full agreement with the experiment of stearic acid hydrodeoxygenation into octadecane. Within the conversion, butanol dissociation  $[R-CH_2OH+H = R-CH_2+OH+H]$  has the highest barrier and represents the rate-determining step. It is noted that metallic  $Mo_2C(001)$  surface can bind surface  $H_2O$ , OH and O much more strongly than the  $Mo_2C(101)$  surface with exposed Mo and C atoms ( $C/Mo = 1$ ). It is noted that obtained results are only from the most stable  $Mo_2C(101)$  surface and cannot directly correlate with the whole experimentally observed reactivity and selectivity of different  $Mo_2C$  phases in different surface terminations. These results provide the basis for exploring the intrinsic nature of  $Mo_2C$  catalysts in deoxygenation of oxygenates involved in the refining of biomass-derived oils.

Very recently, Ge *et al.*,<sup>137</sup> carried out  $CH_4$  activation vs. C-C coupling on the Mo-terminated  $\beta$ - $Mo_2C$  surfaces. It is found that the less carburized  $\beta$ - $Mo_2C(100)$  exhibits a superior reactivity toward  $CH_4$  dissociation and can completely dissociate  $CH_4$ . In addition, the surface can be carburized by inserting the carbon adatoms from  $CH_4$  dissociation into the interstitial face-centered cubic sites in the subsurface layer. Such carburization occurs more readily, producing surface layer similar to that of MoC. Consequently, the carburized  $\beta$ - $Mo_2C(100)$  exhibits a similar reactivity to that of MoC, favoring the dimerization of the surface  $CH^*$  species through the C-C coupling and resulting in surface acetylene  $HCCH^*$ . This study demonstrates a dynamic nature of the carburization under the condition of  $CH_4$  activation on the  $MoC_x$  surfaces, which may play an important role in determining the activity and selectivity of methane aromatization.

In addition, Rodriguez and Illas carried out combined experimental and computational investigation into  $CO_2$  hydrogenation on  $MoC_x$  nanoclusters supported on an inert Au(111) support.<sup>138</sup> This is different from all other reported studies, where  $MoC_x$  were used as supports and transition metals were used as catalysts. It is found that both carbon-poor ( $MoC_{0.6}$ ) and carbon-rich ( $MoC_{1.1}$ ) nanoparticles of molybdenum carbides supported on Au(111) are active for  $CO_2$  hydrogenation. On the carbon-poor surface,  $CO_2$  molecule can dissociate partially ( $CO_2 \rightarrow CO + O$ ) and fully ( $CO_2 \rightarrow C + 2O$ ). However, it is found that this surface is highly active but unstable

under CO<sub>2</sub> hydrogenation conditions, producing CO and CH<sub>4</sub> as main product with a very minor amount of CH<sub>3</sub>OH. On the carbon-rich surface, on the contrary, CO<sub>2</sub> has reversible adsorption and desorption. Under H<sub>2</sub> atmosphere, CO<sub>2</sub> is mainly converted to CO with a significant amount of methanol, however, neither CH<sub>4</sub> nor other hydrocarbons are formed. Compared to the corresponding to bulk  $\delta$ -MoC (17 kcal/mol) and a Cu(111) benchmark system (25 kcal/mol), the apparent activation energy for this supported system is lower (14 kcal/mol), demonstrating the superior ability of MoC<sub>1.1</sub>/Au(111) to bind and dissociate H<sub>2</sub>. To understand this trend, DFT calculations for free or supported Mo<sub>12</sub>C<sub>12</sub> nanoparticles were carried out. Without H<sub>2</sub> adsorption, CO<sub>2</sub> direct dissociation needs to overcome rather high barrier, in agreement with the experiment. With the adsorption of H<sub>2</sub> on Mo<sub>12</sub>C<sub>12</sub> nanoparticles, on the contrary, the barrier of CO<sub>2</sub> dissociation to CO and surface OH is largely reduced, and it is also noted that carboxylate as intermediate was not observed. However, the authors pointed out that the energy barriers predicted with the present models featuring different hydrogen coverages have to be taken as an indication of the overall effect and should not be directly compared to experimentally derived values. For high H coverage, the present model calculations suggest that the pathway to methanol is likely to involve an Eley–Rideal mechanism leading to a formate intermediate, which can be hydrogenated in a stepwise way.

In addition to all these stable phases and terminations, the relative stabilities of different metastable phases for Mo and W carbides with varying synthesis conditions and particle sizes have been also computed since such metastable phases during particle growth cannot be described by traditional phase diagrams. On the basis of Wulff constructions and neural network assisted screening of high-index facets, Paolucci *et al.*,<sup>139</sup> found several facets with significant area fraction for phases that are underrepresented in the literature. It shows that specific higher index facets with large area fraction for commonly synthesized carbides have been experimentally reported but are often neglected in computational studies. The authors found that reported particle sizes for different phases, extract from a large body of experimental synthesis literature, are generally consistent with the trends predicted by computation, which suggests that particle size is an important factor when determining the product phase resulting from a wide variety of synthesis protocols. There are some commonalities between Mo and W carbides; the face-centered cubic phases ( $\gamma$ -WC and  $\delta$ -MoC) are prevalent at small particle sizes, and hexagonal phases tend to dominate the large particle size regions ( $\delta$ -WC,  $\gamma$ -MoC, and  $\beta$ -Mo<sub>2</sub>C). For commonly observed phases, one notable outlier is plasma-based syntheses of  $\gamma$ -WC, which yields nanoparticles at much larger sizes than that predicted by present computation and produced by non-plasma syntheses. In contrast, there are very few reports for the synthesis of  $\delta$ -MoC at large particle sizes; similar plasma-based synthesis routes, or promotion of carbon vacancy formation to lower the bulk energy of  $\delta$ -MoC, may be useful for the synthesis of large  $\delta$ -MoC nanoparticles. The predicted crystallization pathways for Mo and W carbides are consistent with available literature, and in addition, the computed results also predicted several interphase transitions ( $\gamma$ -WC to  $\epsilon$ -W<sub>2</sub>C and  $\alpha$ -Mo<sub>2</sub>C/ $\beta$ -Mo<sub>2</sub>C to  $\gamma$ -MoC) that have not yet been experimentally demonstrated, which could be used to crystallize difficult to synthesize carbide phases. More broadly, these computational findings underscore the importance of particle size and synthesis conditions in determining the phase stability of transition metal carbides and the need for computational models that provide a framework to explore nano-scale and metastable energy landscapes.

In addition, C-H activation of CH<sub>4</sub>, C<sub>2</sub>H<sub>6</sub> and C<sub>2</sub>H<sub>4</sub> on metastable and most stable molybdenum carbide

( $\text{Mo}_2\text{C}_6$ ) nanoclusters have been computed and compared.<sup>140</sup> It is found that the metastable nanocluster, which is very close in energy to the lowest-energy structure, is much more active kinetically than the global minimum isomer. While the metastable isomer is calculated to have a significantly lower statistical probability at 700 °C, its weighted contribution is observed to be maximal in the ensemble average expression for  $\text{CH}_4$  activation. Similar effects are also observed for  $\text{C}_2\text{H}_6$  and  $\text{C}_2\text{H}_4$  activation, wherein the activation energies are also observed to be significantly reduced on the metastable isomer compared to the lowest-energy nanocluster. This shows that the metastable species is likely to contribute more to the reaction than the most stable nanostructure, as previously thought. This significantly enhanced kinetics is attributed to the nearly planar geometrical overlap of the orbitals between the Mo center and the carbon atoms undergoing C–H bond activation.

In this context, this dissertation mainly focused on the structure and stability of transition metal catalysts adsorbed on or doped in the surfaces of molybdenum carbides as supports. Since both molybdenum carbides and transition metals are active catalysts in many reactions, their combination could open new opportunity for rational design of promising catalysts with different activities. The structure and stability of supported catalysts are determined by the nature and strength of the interaction between metal and support and are also dependent on metal loading.

First, the author has computed the structures and stability of metal catalysts ( $\text{M}_n/\text{Mo}_x\text{C}$ ;  $\text{M} = \text{Co}, \text{Ni}, \text{Cu}, \text{Pd}, \text{Pt}$ ) adsorbed on the surfaces of molybdenum carbides.<sup>141</sup> With respect of size and shape-dependent catalysis of supported metal catalysts, the adsorption structure and stability of  $\text{M}_n$  ( $\text{M} = \text{Co}, \text{Ni}, \text{Cu}, \text{Pd}, \text{Pt}$ ) on the hexagonal  $\text{Mo}_2\text{C}(001)$  and  $\text{Mo}_2\text{C}(101)$  as well as the cubic non-polar  $\delta\text{-MoC}(001)$  surfaces using spin-polarized density functional theory method were computed systematically. On all three surfaces, surface morphology of monolayer dispersion, monolayer aggregation and three-dimensional cluster are compared and discussed. These results provide the basis for studying catalytic reactions on supported metal catalysts with different sizes and shapes (single atom, nanoclusters and nanoparticles) and for the design of catalysts.

On the Mo-terminated  $\text{Mo}_2\text{C}(001)$  surface, Co and Ni prefer dispersion at very low loading and aggregation at high coverage. The dispersion of Pd and Pt is possible at relative higher loading, and Cu prefers aggregation from low to high loading. For all five metals, monolayer adsorption structures are more stable than the corresponding three-dimensional clusters ( $n = 4$  and  $5$ ). On the Mo/C-mixed  $\text{Mo}_2\text{C}(101)$  surface, all metals prefer dispersion adsorption for  $n = 1$ -8 and aggregation appears from  $n = 9$  up to full monolayer. Three-dimensional clusters become possible for metal loading over full monolayer coverage. On the Mo/C-mixed  $\text{MoC}(001)$  surface, only single atom prefers dispersion and aggregation can be stable from low ( $n = 2$ ) to medium coverage. Three-dimensional clusters become stable at high coverage.

On all three surfaces (Figure 1), the adsorption energy of Pt is strongest and that of Cu is lowest, while those of Co, Ni and Pd are in between. In addition, the adsorption energy of metals increases with metal coverage increase. The average adsorption energy further verifies the order of adsorption energies. For Pd and Pt, the average adsorption energy decreases dramatically with the coverage increase from low to medium and marginally up to high coverage. For Co, Ni and Cu, the average adsorption energy increases marginally on the metallic  $\text{Mo}_2\text{C}(001)$  and the Mo/C-mixed  $\text{MoC}(001)$  surfaces and is constant on the Mo/C-mixed  $\text{Mo}_2\text{C}(101)$  surface from  $n = 1$ -8 and decreases slightly with coverage increase. The calculated stepwise adsorption energy can further realize the difference of adsorption energy up on coverage increase. Except single atom of Pd and Pt,

the stepwise adsorption energies of all five metals are regular change while some exceptional increase or decrease at given coverage appears due to surface reconstruction.

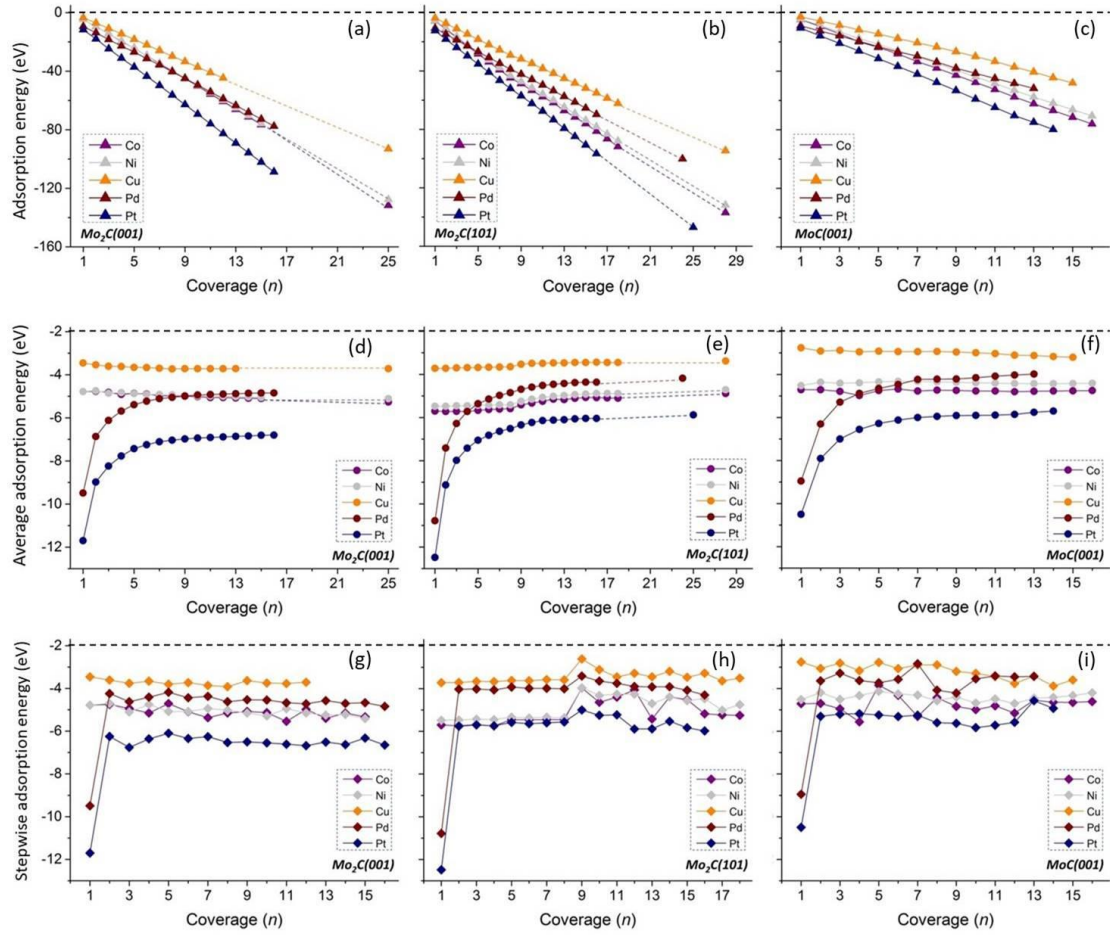


**Figure 1.** Adsorption energy (a-c), average adsorption energy (e-f) and stepwise adsorption energy (g-i) for  $\text{M}_n$  ( $\text{M} = \text{Co}, \text{Ni}, \text{Cu}, \text{Pd}, \text{Pt}$ ) on  $\text{Mo}_2\text{C}(001)$ ,  $\text{Mo}_2\text{C}(101)$  and  $\text{MoC}(001)$ .<sup>141</sup>

In addition to the structures and energies, electron transfer between surface and the adsorbed atoms are found (Table 3). On the Mo-terminated  $\text{Mo}_2\text{C}(001)$  surface, all adsorbed atoms become negatively charged, indicating electron transfer from surface to the adsorbed atoms. On the Mo/C-mixed  $\text{Mo}_2\text{C}(101)$  and  $\text{MoC}(001)$ , the adsorbed Co, Ni and Cu atoms are positively charged, and the adsorbed Pt atoms are negatively charged, while the adsorbed Pd atoms are nearly neutral; and this demonstrates electron transfer from the adsorbed Co, Ni and Cu atoms to surface, while from surface to the adsorbed Pt atoms. For single atom adsorption, the order of the computed adsorption correlates with the quantity of electron transfer. However, neither the adsorption energy nor the quantity of electron transfer correlates with the electronegativity of the atoms and their respective ionization potential as well as electron affinity.

**Table 3.** Electronegativity ( $\chi$ ), ionization potential (IP, eV), electro affinity (EA, eV), and calculated Bader charge ( $q$ ) for adsorbed single atom.<sup>141</sup>

M	$\chi$	IP	EA	$q$		
				M/ $\text{Mo}_2\text{C}(001)$	M/ $\text{Mo}_2\text{C}(101)$	M/ $\text{MoC}(001)$
Mo	1.47	7.09	0.75	0.45 <sup>a</sup> / $\text{Mo}_A$ ; 0.23 <sup>a</sup> / $\text{Mo}_B$	0.79 <sup>a</sup> / $\text{Mo}_A$ ; 0.89 <sup>a</sup> / $\text{Mo}_B$	1.32 <sup>a</sup> / $\text{Mo}$

## Introduction

Co	1.84	7.88	0.66	-0.44	0.20	0.21
Ni	1.88	7.64	1.16	-0.44	0.18	0.18
Cu	1.85	7.73	1.24	-0.32	0.26	0.25
Pd	1.59	8.34	0.56	-0.57	-0.01	-0.05
Pt	1.72	8.96	2.13	-0.79	-0.25	-0.27

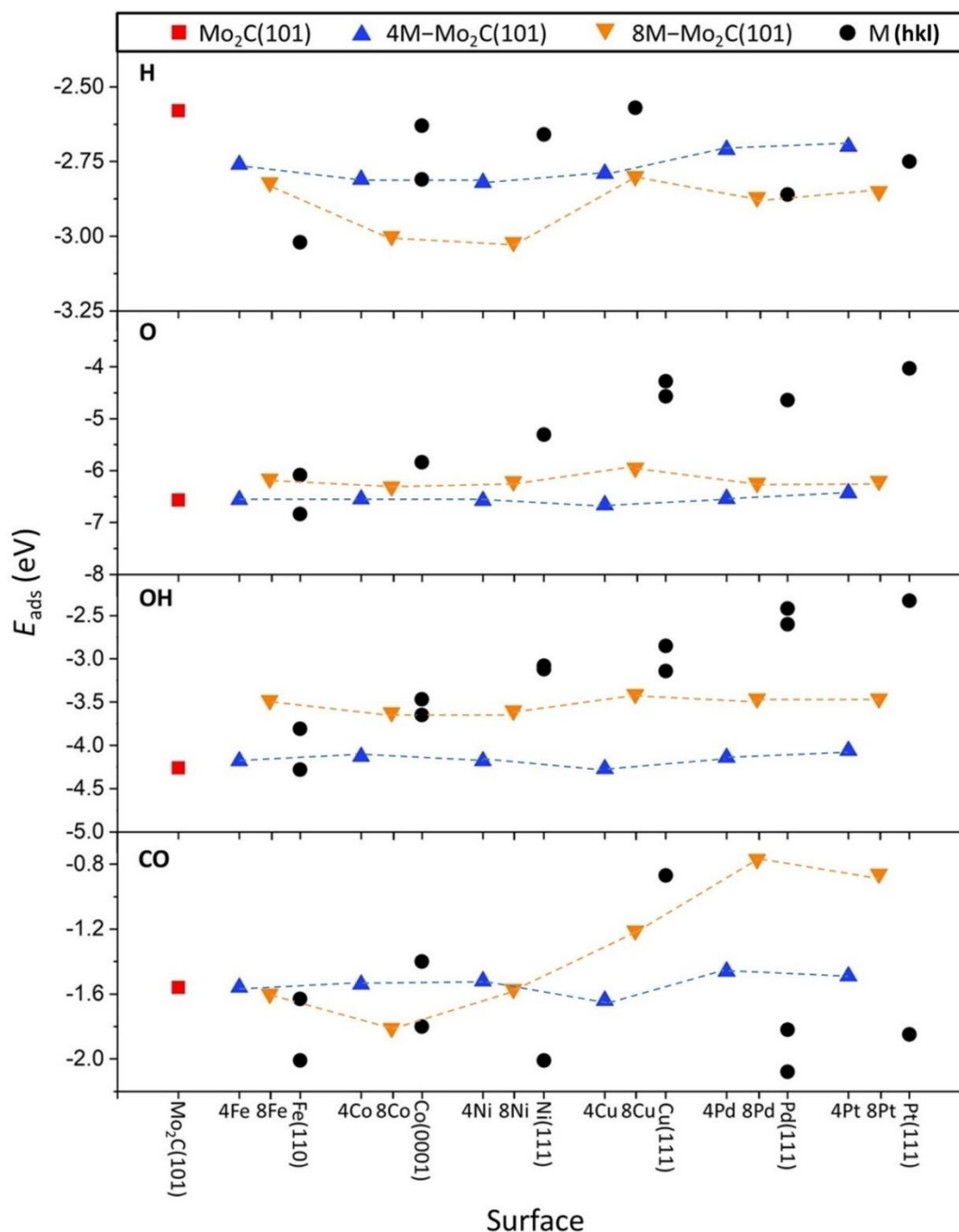
a) The value stands for the average Bader charge of surface Mo atoms on corresponding bare slab.

In addition to the adsorption model catalysts, the structure and energy of substitution model catalysts were computed, in which the outermost surface molybdenum atoms of the most stable hexagonal Mo<sub>2</sub>C(101) surface are gradually replaced by Fe, Co, Ni, Cu, Pd and Pt for investigating the adsorption of CO, H<sub>2</sub>, H<sub>2</sub>O and CO<sub>2</sub> as well as OH, H and O.<sup>142</sup> Experimentally, supported transition metal catalysts in heterogeneous catalysis show different activity from only metals and pure supports due to their enhanced mutual and synergistic interaction. To understand these effects, we computed transition metal doping on the hexagonal Mo<sub>2</sub>C(101) surface by substituting the less coordinated and more active surface Mo<sub>A</sub> atoms with Fe, Co, Ni, Cu, Pd and Pt in 4M (25%) and 8M (50%) metal loading.

It is found that metal doping affects the surface electronic properties based on the analysis of projected density states and creates more adsorption sites by changing coordination environment for surface metal and carbons atoms. Strong electron transfer from metal to surface has been found for Fe, Co, Ni and Cu, resulting positive Bader charge on doping metal, and this agrees with the experimentally observed effect for Cu-doped Mo<sub>2</sub>C. On the contrary, much less electron transfer from Pd to surface or from surface to Pt has been found. Consequently, not only surface metal atoms but also surface carbon atoms become active in adsorption of surface species.

On the pure and 4M (25%) doped surfaces, surface Mo<sub>A</sub> atoms are most preferred sites for the adsorption of H<sub>2</sub>, H<sub>2</sub>O, OH and O, and surface carbon (C<sub>A</sub>) atoms are responsible for the adsorption of H atoms, while surface Mo<sub>A</sub> and C<sub>A</sub> are co-responsible for the adsorption of CO and CO<sub>2</sub>. On the 8M (50%) doped surfaces, the less active surface Mo<sub>B</sub> and surface C<sub>B</sub> becomes active for the adsorption of CO and CO<sub>2</sub>, and the adsorption energy depends on the doping metals. It is also found that molecular H<sub>2</sub> has physisorption preferring the top of doping metal, while atomic H prefers the top of surface C<sub>A</sub> atom forming C-H bond. The adsorption of H<sub>2</sub>O and OH prefers the top and bridge site, respectively, while atomic O prefers the top site of surface C<sub>A</sub> atom forming C-O bond. Depending on doping metals and adsorption sites, the adsorption of each surface species can become more or less exothermic compared to pure surface.

On the basis of these results, the dissociative adsorption of H<sub>2</sub>O and CO<sub>2</sub> was explored, and it is found that the potential energy surfaces depend on metal and loading. Full H<sub>2</sub>O dissociative adsorption is favored thermodynamically on the 4M doped surfaces and more exothermic compared to the pure surface, while less exothermic and doping metal dependent on the 8M doped surfaces apart from Co. CO<sub>2</sub> dissociative adsorption is favored thermodynamically on the 4M doped surfaces, while becomes endothermic on the 8M doped surface, preferring molecular instead dissociative adsorption for Co, Ni, Cu, Pd and Pt as well as equilibrium between molecular and dissociative adsorption for Co. Comparing the adsorption of CO, OH, O and H on the pure and doped Mo<sub>2</sub>C(101) surfaces and the corresponding metallic M(*hkl*) surfaces reveals their similarity and difference (Scheme 7), and these should also be found in the reaction kinetic and thermodynamics.



**Scheme 7.** Comparative adsorption energies of CO, OH, O and H on Mo<sub>2</sub>C(101), 4M-Mo<sub>2</sub>C(101), 8M-Mo<sub>2</sub>C(101) and the corresponding metallic low-index surfaces (M = Fe, Co, Ni, Cu, Pd and Pt).<sup>142</sup>

The adsorption and sequential decomposition of ammonia on the metallic Mo<sub>2</sub>C(001) surface have been also systematically computed.<sup>143</sup> Density functional theory computations were carried out to study the adsorption and sequential decomposition of ammonia on the hexagonal metallic Mo<sub>2</sub>C(001) surface. The ultimate goal of this study is the nitridation degree of the Mo<sub>2</sub>C(001) surface by using NH<sub>3</sub> as environment agent. The metallic Mo<sub>2</sub>C(001) surface has two types of Mo atoms differentiated by the local carbon environment, the Mo atom with two carbon atoms has higher NH<sub>3</sub> adsorption energy than that with one carbon atom; and each type has eight expose Mo atoms.

The adsorption of  $\text{NH}_3$  prefers the top site via the nitrogen lone pair electrons in the entire coverage range, and the saturation coverage is 0.75 monolayer on the basis of exposed surface Mo atoms. There is no hydrogen bonding among the adsorbed  $\text{NH}_3$  molecules. It is found that  $\text{NH}_3$  prefers decomposition instead of desorption, and all three elementary decomposition steps have low barriers and are exothermic; and this shows that full decomposition into surface N and H atoms are favored kinetically and thermodynamically.

The adsorption of  $\text{NH}_2$  is coverage-dependent, i.e., at low coverage  $\text{NH}_3$  adsorption at both bridge and hollow sites have close energies, and bridge sites are preferred at high coverage up to saturation; and the saturation coverage is 1.0 monolayer. In contrast, the adsorption of NH and N is coverage independent, and only hollow sites are preferred in the entire coverage range. The saturation coverage for NH and N is 1.0 and 0.5 monolayer, respectively. The dissociative adsorption of ammonia among other metals and molybdenum nitrides has been categorized and compared. Our results provide the basis for studying the surface properties and catalytic reaction of nitrated  $\text{Mo}_2\text{C}$  surfaces.

These results of both adsorption and substitution models provide the basis for the investigation of catalysts made of single atoms, nanoclusters and nanoparticles either adsorbed on the surfaces or doped into the surfaces and the respective catalysis. These results, in comparison or combination with experiment, can help the characterization to identify the forms of the active catalysts and in turn to understand the catalytic activity for catalytic reactions, such as water-gas shift reaction, methane dry and steam reforming, reforming of methyl formate dimethyl ether, ammonia synthesis and hydrogenation reactions as well as photo- and electrocatalysis.



#### 1.4 References

- (1) Roberts, M. Birth of the Catalytic Concept (1800-1900). *Catal. Lett.* **2000**, 67, 1–4.
- (2) Robertson, A. The Early History of Catalysis. *Platinum Met. Rev.* **1975**, 19, 64–69.
- (3) Armor, J. N. A History of Industrial Catalysis. *Catal. Today* **2011**, 163, 3–9.
- (4) Burwell Jr, R. L. Heterogeneous Catalysis before 1934. **1983**.
- (5) Robertson, A. The Development of Ideas on Heterogeneous Catalysis. *Platinum Met. Rev.* **1983**, 27, 31–39.
- (6) Li, J.; Stephanopoulos, M. F.; Xia, Y., Introduction: Heterogeneous Single-Atom Catalysis. *Chem. Rev.* **2020**, 120, 11699–11702.
- (7) 2021–2027 Global and Regional Catalysts Industry Status and Prospects Professional Market Research Report Standard Version. <https://www.researchreportsworld.com/2021-2027-global-and-regional-catalysts-industry-status-and-prospects-professional-market-18125957>.
- (8) Oudart, M.; Löffler, D. Surface Structure of Iron Catalysts for Ammonia Synthesis. *J. Phys. Chem.* **1984**, 88, 5763–5763.
- (9) Herzog, B.; Herein, D.; Schlögl, R. In Situ X-Ray Powder Diffraction Analysis of the Microstructure of Activated Iron Catalysts for Ammonia Synthesis. *Appl. Catal., A* **1996**, 141, 71–104.
- (10) Dry, M. E. Fischer-Tropsch Synthesis over Iron Catalysts. *Catal. Lett.* **1990**, 7, 241–251.
- (11) Jung, H.; Thomson, W. J. Dynamic X-Ray Diffraction Study of an Unsupported Iron Catalyst in Fischer-Tropsch Synthesis. *J. Catal.* **1992**, 134, 654–667.
- (12) Brazdil, J. F. Acrylonitrile. *Ullmann's Encyclopedia of Industrial Chemistry* **2000**.
- (13) Schönbeck, R.; König, H.; Krzemicki, K.; Kahofer, L. Acrylonitrile from Propylene, Ammonia, and Atmospheric Oxygen. *Angew. Chem. Int. Ed.* **1966**, 5, 642–646.
- (14) Robert, L.; Burwell, J. Manual of Symbols and Terminology for Physicochemical Quantities and Units—Appendix II. *Pure Appl. Chem.* **1976**, 46, 71–90.
- (15) Wang, R.; Wu, Z.; Chen, C.; Qin, Z.; Zhu, H.; Wang, G.; Wang, H.; Wu, C.; Dong, W.; Fan, W. Graphene-Supported Au–Pd Bimetallic Nanoparticles with Excellent Catalytic Performance in Selective Oxidation of Methanol to Methyl Formate. *Chem. Commun.* **2013**, 49, 8250–8252.
- (16) Ma, W.; Kugler, E. L.; Wright, J.; Dadyburjor, D. B. Mo–Fe Catalysts Supported on Activated Carbon for Synthesis of Liquid Fuels by the Fischer–Tropsch Process: Effect of Mo Addition on Reducibility, Activity, and Hydrocarbon Selectivity. *Energy Fuels* **2006**, 20, 2299–2307.
- (17) Liu, P.; Zhao, Y.; Qin, R.; Gu, L.; Zhang, P.; Fu, G.; Zheng, N. A Vicinal Effect for Promoting Catalysis of Pd<sub>1</sub>/TiO<sub>2</sub>: Supports of Atomically Dispersed Catalysts Play More Roles Than Simply Serving as Ligands. *Sci. Bull.* **2018**, 63, 675–682.
- (18) Shroff, M. D.; Kalakkad, D. S.; Coulter, K. E.; Kohler, S. D.; Harrington, M. S.; Jackson, N. B.; Sault, A. G.; Datye, A. K. Activation of Precipitated Iron Fischer-Tropsch Synthesis Catalysts. *J. Catal.* **1995**, 156, 185–207.
- (19) Moreau, F.; Bond, G. C. Gold on Titania Catalysts, Influence of Some Physicochemical Parameters on the Activity and Stability for the Oxidation of Carbon Monoxide. *Appl. Catal., A* **2006**, 302, 110–117.
- (20) Lee, S.-Y.; Aris, R. The Distribution of Active Ingredients in Supported Catalysts Prepared by Impregnation. *Catal. Rev. Sci. Eng.* **1985**, 27, 207–340.
- (21) Neimark, A. V.; Kheifets, L.; Fenelonov, V. Theory of Preparation of Supported Catalysts. *Ind. Eng. Chem. Res.* **1981**, 20, 439–450.
- (22) Lekhal, A.; Glasser, B. J.; Khinast, J. G. Impact of Drying on the Catalyst Profile in Supported Impregnation Catalysts. *Chem. Eng. Sci.* **2001**, 56, 4473–4487.
- (23) Wong, A.; Liu, Q.; Griffin, S.; Nicholls, A.; Regalbuto, J. Synthesis of Ultrasmall, Homogeneously Alloyed, Bimetallic Nanoparticles on Silica Supports. *Science* **2017**, 358, 1427–1430.
- (24) Otto, T.; Zones, S. I.; Iglesia, E. Challenges and Strategies in the Encapsulation and Stabilization of Monodisperse Au Clusters within Zeolites. *J. Catal.* **2016**, 339, 195–208.
- (25) Wang, P.; Wang, H.; Chen, X.; Liu, Y.; Weng, X.; Wu, Z. Novel Scr Catalyst with Superior Alkaline Resistance Performance: Enhanced Self-Protection Originated from Modifying Protonated Titanate Nanotubes. *J. Mater. Chem. A* **2015**, 3, 680–690.
- (26) Pan, X.; Bao, X. The Effects of Confinement inside Carbon Nanotubes on Catalysis. *Acc. Chem. Res.* **2011**, 44, 553–562.
- (27) Yang, X.; Yu, X.; Long, L.; Wang, T.; Ma, L.; Wu, L.; Bai, Y.; Li, X.; Liao, S. Pt Nanoparticles Entrapped in Titanate Nanotubes (Tnt) for Phenol Hydrogenation: The Confinement Effect of Tnt. *Chem. Commun.* **2014**, 50, 2794–2796.
- (28) Lu, J.; Elam, J. W.; Stair, P. C. Synthesis and Stabilization of Supported Metal Catalysts by Atomic Layer Deposition. *Acc. Chem. Res.* **2013**, 46, 1806–1815.

- (29) O'Neill, B. J.; Jackson, D. H.; Lee, J.; Canlas, C.; Stair, P. C.; Marshall, C. L.; Elam, J. W.; Kuech, T. F.; Dumesic, J. A.; Huber, G. W. Catalyst Design with Atomic Layer Deposition. *ACS Catal.* **2015**, *5*, 1804–1825.
- (30) Lu, J.; Fu, B.; Kung, M. C.; Xiao, G.; Elam, J. W.; Kung, H. H.; Stair, P. C. Coking-and Sintering-Resistant Palladium Catalysts Achieved through Atomic Layer Deposition. *Science* **2012**, *335*, 1205–1208.
- (31) Gao, Z.; Qin, Y. Design and Properties of Confined Nanocatalysts by Atomic Layer Deposition. *Acc. Chem. Res.* **2017**, *50*, 2309–2316.
- (32) Xu, D.; Wu, B.; Ren, P.; Wang, S.; Huo, C.; Zhang, B.; Guo, W.; Huang, L.; Wen, X.; Qin, Y. Controllable Deposition of Pt Nanoparticles into a KI Zeolite by Atomic Layer Deposition for Highly Efficient Reforming of N-Heptane to Aromatics. *Catal. Sci. Technol.* **2017**, *7*, 1342–1350.
- (33) Qin, Y.; Pan, A.; Liu, L.; Moutanabbir, O.; Yang, R. B.; Knez, M. Atomic Layer Deposition Assisted Template Approach for Electrochemical Synthesis of Au Crescent-Shaped Half-Nanotubes. *ACS Nano* **2011**, *5*, 788–794.
- (34) Lopez, N.; Nørskov, J. K.; Janssens, T.; Carlsson, A.; Puig-Molina, A.; Clausen, B.; Grunwaldt, J.-D. The Adhesion and Shape of Nanosized Au Particles in a Au/TiO<sub>2</sub> Catalyst. *J. Catal.* **2004**, *225*, 86–94.
- (35) Tauster, S.; Fung, S.; Garten, R. L. Strong Metal-Support Interactions. Group 8 Noble Metals Supported on Titanium Dioxide. *J. Am. Chem. Soc.* **1978**, *100*, 170–175.
- (36) Tauster, S. Strong Metal-Support Interactions. *Acc. Chem. Res.* **1987**, *20*, 389–394.
- (37) Belzunegui, J. P.; Sanz, J.; Rojo, J. M. Contribution of Physical Blocking and Electronic Effect to Establishment of Strong Metal-Support Interaction in Rhodium/Titanium Dioxide Catalysts. *J. Am. Chem. Soc.* **1992**, *114*, 6749–6754.
- (38) Xu, B.; Yang, H.; Zhou, G.; Wang, X. Strong Metal-Support Interaction in Size-Controlled Monodisperse Palladium-Hematite Nano-Heterostructures During a Liquid-Solid Heterogeneous Catalysis. *Sci. China Mater.* **2014**, *57*, 34–41.
- (39) Santos, J.; Phillips, J.; Dumesic, J. Metal-Support Interactions between Iron and Titania for Catalysts Prepared by Thermal Decomposition of Iron Pentacarbonyl and by Impregnation. *Journal of Catalysis* **1983**, *81*, 147–167.
- (40) Fung, S. C. Xps Studies of Strong Metal-Support Interactions (Smsi)-Pt/Tio/Sub 2. *J. Catal. (United States)* **1982**, *76*.
- (41) Liu, J. Advanced Electron Microscopy of Metal-Support Interactions in Supported Metal Catalysts. *ChemCatChem* **2011**, *3*, 934–948.
- (42) Matsubu, J. C.; Zhang, S.; DeRita, L.; Marinkovic, N. S.; Chen, J. G.; Graham, G. W.; Pan, X.; Christopher, P. Adsorbate-Mediated Strong Metal-Support Interactions in Oxide-Supported Rh Catalysts. *Nat. Chem.* **2017**, *9*, 120–127.
- (43) Campbell, C. T. Electronic Perturbations. *Nat. Chem.* **2012**, *4*, 597–598.
- (44) Bruix, A.; Rodriguez, J. A.; Ramirez, P. J.; Senanayake, S. D.; Evans, J.; Park, J. B.; Stacchiola, D.; Liu, P.; Hrbek, J.; Illas, F. A New Type of Strong Metal-Support Interaction and the Production of H<sub>2</sub> through the Transformation of Water on Pt/CeO<sub>2</sub> (111) and Pt/CeO<sub>x</sub>/TiO<sub>2</sub> (110) Catalysts. *J. Am. Chem. Soc.* **2012**, *134*, 8968–8974.
- (45) Zhu, J.; Ciolca, D.; Liu, L.; Parastaev, A.; Kosinov, N.; Hensen, E. J. Flame Synthesis of Cu/ZnO–CeO<sub>2</sub> Catalysts: Synergistic Metal-Support Interactions Promote CH<sub>3</sub>OH Selectivity in CO<sub>2</sub> Hydrogenation. *ACS Catal.* **2021**, *11*, 4880–4892.
- (46) Levy, R. B.; Boudart, M. Platinum-Like Behavior of Tungsten Carbide in Surface Catalysis. *Science* **1973**, *181*, 547–549.
- (47) Kelly, T. G.; Chen, J. G. Controlling C–O, C–C and C–H Bond Scission for Deoxygenation, Reforming, and Dehydrogenation of Ethanol Using Metal-Modified Molybdenum Carbide Surfaces. *Green Chem.* **2014**, *16*, 777–784.
- (48) Perret, N.; Wang, X.; Delannoy, L.; Potvin, C.; Louis, C.; Keane, M. A. Enhanced Selective Nitroarene Hydrogenation over Au Supported on B-Mo<sub>2</sub>C and B-Mo<sub>2</sub>C/Al<sub>2</sub>O<sub>3</sub>. *J. Catal.* **2012**, *286*, 172–183.
- (49) Ji, N.; Zhang, T.; Zheng, M.; Wang, A.; Wang, H.; Wang, X.; Chen, J. G. Direct Catalytic Conversion of Cellulose into Ethylene Glycol Using Nickel-Promoted Tungsten Carbide Catalysts. *Angew. Chem.* **2008**, *120*, 8638–8641.
- (50) Chen, J. G. Carbide and Nitride Overlayers on Early Transition Metal Surfaces: Preparation, Characterization, and Reactivities. *Chem. Rev.* **1996**, *96*, 1477–1498.
- (51) Hwu, H. H.; Chen, J. G. Surface Chemistry of Transition Metal Carbides. *Chem. Rev.* **2005**, *105*, 185–212.
- (52) Wan, W.; Tackett, B. M.; Chen, J. G. Reactions of Water and C1 Molecules on Carbide and Metal-Modified Carbide Surfaces. *Chemical Society Reviews* **2017**, *46*, 1807–1823.
- (53) Toth, L., *Transition Metal Carbides and Nitrides*; Elsevier, **2014**.

- (54) Gubanov, V. A.; Ivanovsky, A. L.; Zhukov, V. P., *Electronic Structure of Refractory Carbides and Nitrides*; Cambridge University Press, **2005**.
- (55) Mavrikakis, M.; Hammer, B.; Nørskov, J. K. Effect of Strain on the Reactivity of Metal Surfaces. *Phys. Rev. Lett.* **1998**, *81*, 2819.
- (56) Széchenyi, A.; Solymosi, F. Production of Hydrogen in the Decomposition of Ethanol and Methanol over Unsupported Mo<sub>2</sub>C Catalysts. *J. Phys. Chem. C* **2007**, *111*, 9509–9515.
- (57) Barthos, R.; Széchenyi, A.; Solymosi, F. Efficient H<sub>2</sub> Production from Ethanol over Mo<sub>2</sub>C/C Nanotube Catalyst. *Catal. Lett.* **2008**, *120*, 161–165.
- (58) Ma, Y.; Guan, G.; Shi, C.; Zhu, A.; Hao, X.; Wang, Z.; Kusakabe, K.; Abudula, A. Low-Temperature Steam Reforming of Methanol to Produce Hydrogen over Various Metal-Doped Molybdenum Carbide Catalysts. *Int. J. Hydrog. Energy* **2014**, *39*, 258–266.
- (59) Ma, Y.; Guan, G.; Hao, X.; Zuo, Z.; Huang, W.; Phanthong, P.; Kusakabe, K.; Abudula, A. Highly-Efficient Steam Reforming of Methanol over Copper Modified Molybdenum Carbide. *Rsc Adv.* **2014**, *4*, 44175–44184.
- (60) Ma, Y.; Guan, G.; Hao, X.; Zuo, Z.; Huang, W.; Phanthong, P.; Li, X.; Kusakabe, K.; Abudula, A. Embedded Structure Catalyst: A New Perspective from Noble Metal Supported on Molybdenum Carbide. *Rsc Adv.* **2015**, *5*, 15002–15005.
- (61) Wan, C.; Leonard, B. M. Iron-Doped Molybdenum Carbide Catalyst with High Activity and Stability for the Hydrogen Evolution Reaction. *Chem. Mater.* **2015**, *27*, 4281–4288.
- (62) Liu, Y.; Ding, J.; Bi, J.; Sun, Y.; Zhang, J.; Liu, K.; Kong, F.; Xiao, H.; Chen, J. Effect of Cu-Doping on the Structure and Performance of Molybdenum Carbide Catalyst for Low-Temperature Hydrogenation of Dimethyl Oxalate to Ethanol. *Appl. Catal., A* **2017**, *529*, 143–155.
- (63) Liu, P.; Rodriguez, J. A. Water-Gas-Shift Reaction on Molybdenum Carbide Surfaces: Essential Role of the Oxycarbide. *J. Phys. Chem. B* **2006**, *110*, 19418–19425.
- (64) Zaman, S.; Smith, K. J. A Review of Molybdenum Catalysts for Synthesis Gas Conversion to Alcohols: Catalysts, Mechanisms and Kinetics. *Catalysis Reviews* **2012**, *54*, 41–132.
- (65) Saito, M.; Anderson, R. The Activity of Several Molybdenum Compounds for the Methanation of CO. *Journal of catalysis* **1980**, *63*, 438–446.
- (66) Patt, J.; Moon, D. J.; Phillips, C.; Thompson, L. Molybdenum Carbide Catalysts for Water–Gas Shift. *Catal. Lett.* **2000**, *65*, 193–195.
- (67) Tominaga, H.; Nagai, M. Density Functional Theory of Water–Gas Shift Reaction on Molybdenum Carbide. *J. Phys. Chem. B* **2005**, *109*, 20415–20423.
- (68) Lee, J. S.; Locatelli, S.; Oyama, S.; Boudart, M. Molybdenum Carbide Catalysts 3. Turnover Rates for the Hydrogenolysis of N-Butane. *J. Catal.* **1990**, *125*, 157–170.
- (69) Naito, S.; Tsuji, M.; Miyao, T. Mechanistic Difference of the CO<sub>2</sub> Reforming of CH<sub>4</sub> over Unsupported and Zirconia Supported Molybdenum Carbide Catalysts. *Catal. Today* **2002**, *77*, 161–165.
- (70) Darujati, A. R.; LaMont, D. C.; Thomson, W. J. Oxidation Stability of Mo<sub>2</sub>C Catalysts under Fuel Reforming Conditions. *Appl. Catal., A* **2003**, *253*, 397–407.
- (71) Darujati, A. R.; Thomson, W. J. Kinetic Study of a Ceria-Promoted Mo<sub>2</sub>C/γ-Al<sub>2</sub>O<sub>3</sub> Catalyst in Dry-Methane Reforming. *Chem. Eng. Sci.* **2006**, *61*, 4309–4315.
- (72) Solymosi, F.; Cserényi, J.; Szöke, A.; Bánsági, T.; Oszko, A. Aromatization of Methane over Supported and Unsupported Mo-Based Catalysts. *J. Catal.* **1997**, *165*, 150–161.
- (73) Barthos, R.; Bánsági, T.; Zakar, T. S.; Solymosi, F. Aromatization of Methanol and Methylation of Benzene over Mo<sub>2</sub>C/ZSM-5 Catalysts. *J. Catal.* **2007**, *247*, 368–378.
- (74) Lee, J. S.; Boudart, M. Hydrodesulfurization of Thiophene over Unsupported Molybdenum Carbide. *Appl. Catal.* **1985**, *19*, 207–210.
- (75) McCrea, K. R.; Logan, J. W.; Tarbuck, T. L.; Heiser, J. L.; Bussell, M. E. Thiophene Hydrodesulfurization over Alumina-Supported Molybdenum Carbide and Nitride Catalysts: Effect of Mo Loading and Phase. *J. Catal.* **1997**, *171*, 255–267.
- (76) Nelson, N.; Levy, R. B. Organic Chemistry of Hydrodenitrogenation. *J. Catal. (United States)* **1979**, *58*.
- (77) Al-Megren, H. A.; González-Cortés, S. L.; Xiao, T.; Green, M. L. A Comparative Study of the Catalytic Performance of Co-Mo and Co (Ni)-W Carbide Catalysts in the Hydrodenitrogenation (HDN) Reaction of Pyridine. *Appl. Catal., A* **2007**, *329*, 36–45.
- (78) Delannoy, L.; Giraudon, J.-M.; Granger, P.; Leclercq, L.; Leclercq, G. Group VI Transition Metal Carbides as Alternatives in the Hydrodechlorination of Chlorofluorocarbons. *Catal. Today* **2000**, *59*, 231–240.
- (79) Delannoy, L.; Giraudon, J.-M.; Granger, P.; Leclercq, L.; Leclercq, G. Hydrodechlorination of CCl<sub>4</sub> over Group VI Transition Metal Carbides. *Appl. Catal. B* **2002**, *37*, 161–173.

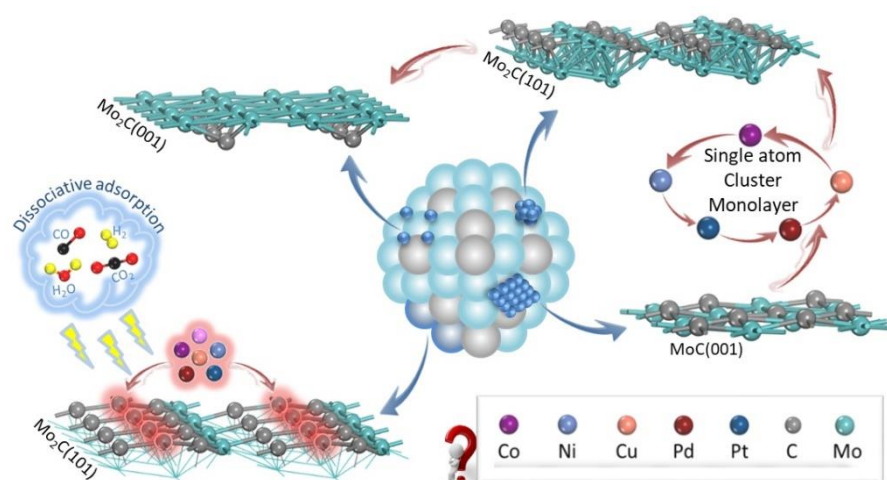
- (80) Jujjuri, S. T., *Catalytic Hydrodechlorination of Chloroarenes over Novel Transition Metal and Carbide Catalysts*; University of Kentucky, **2006**.
- (81) Jujjuri, S.; Cárdenas-Lizana, F.; Keane, M. A. Synthesis of Group VI Carbides and Nitrides: Application in Catalytic Hydrodechlorination. *J Mater. Sci.* **2014**, *49*, 5406–5417.
- (82) Westgren, A.; Phragmén, G. Röntgenanalyse Der Systeme Wolfram-Kohlenstoff Und Molybdän-Kohlenstoff. *Z. Anorg. Allg. Chem.* **1926**, *156*, 27–36.
- (83) Kuo, K.; Hägg, G. A New Molybdenum Carbide. *Nature* **1952**, *170*, 245–246.
- (84) Fries, R.; Kempter, C. P. 195. Dimolybdenum Carbide. *Anal. Chem.* **1960**, *32*, 1898–1898.
- (85) Parthé, E.; Sadogopan, V. The Structure of Dimolybdenum Carbide by Neutron Diffraction Technique. *Acta Crystallogr.* **1963**, *16*, 202–205.
- (86) Haines, J.; Leger, J.; Chateau, C.; Lowther, J. Experimental and Theoretical Investigation of Mo<sub>2</sub>C at High Pressure. *J. Phys.: Condens. Matter* **2001**, *13*, 2447.
- (87) Shi, X.-R.; Wang, S.-G.; Wang, H.; Deng, C.-M.; Qin, Z.; Wang, J. Structure and Stability of  $\beta$ -Mo<sub>2</sub>C Bulk and Surfaces: A Density Functional Theory Study. *Surf. Sci.* **2009**, *603*, 852–859.
- (88) Christensen, A. A Neutron Diffraction Investigation on a Crystal of Alpha-Mo<sub>2</sub>C. **1977**.
- (89) Volpe, L.; Boudart, M. Topotactic Preparation of Powders with High Specific Surface Area. *Catal. Rev. Sci. Eng.* **1985**, *27*, 515–538.
- (90) Dubois, J.; Epicier, T.; Esnouf, C.; Fantozzi, G.; Convert, P. Neutron Powder Diffraction Studies of Transition Metal Hemiacarbides M<sub>2</sub>C<sub>1-x</sub>—I. Motivation for a Study on W<sub>2</sub>C and Mo<sub>2</sub>C and Experimental Background for an *in Situ* Investigation at Elevated Temperature. *Acta Metall.* **1988**, *36*, 1891–1901.
- (91) Epicier, T.; Dubois, J.; Esnouf, C.; Fantozzi, G.; Convert, P. Neutron Powder Diffraction Studies of Transition Metal Hemiacarbides M<sub>2</sub>C<sub>1-x</sub>—II. *In Situ* High Temperature Study on W<sub>2</sub>C<sub>1-x</sub> and Mo<sub>2</sub>C<sub>1-x</sub>. *Acta Metall.* **1988**, *36*, 1903–1921.
- (92) dos Santos Politi, J. R.; Vines, F.; Rodriguez, J. A.; Illas, F. Atomic and Electronic Structure of Molybdenum Carbide Phases: Bulk and Low Miller-Index Surfaces. *Phys. Chem. Chem. Phys.* **2013**, *15*, 12617–12625.
- (93) Posada-Pérez, S.; Viñes, F.; Rodríguez, J. A.; Illas, F. Structure and Electronic Properties of Cu Nanoclusters Supported on Mo<sub>2</sub>C(001) and MoC(001) Surfaces. *J. Chem. Phys.* **2015**, *143*, 114704.
- (94) Lin, L.; Zhou, W.; Gao, R.; Yao, S.; Zhang, X.; Xu, W.; Zheng, S.; Jiang, Z.; Yu, Q.; Li, Y.; Shi, C.; Wen, X.; Ma, D. Low-Temperature Hydrogen Production from Water and Methanol Using Pt/ $\alpha$ -MoC Catalysts. *Nature* **2017**, *544*, 80–83.
- (95) Yao, S.; Zhang, X.; Zhou, W.; Gao, R.; Xu, W.; Ye, Y.; Lin, L.; Wen, X.; Liu, P.; Chen, B.; Crumlin, E.; Guo, J.; Zuo, Z.; Li, W.; Xie, J.; Lu, L.; Kiely, C. J.; Gu, L.; Shi, C.; Rodriguez, J. A.; Ma, D. Atomic-Layered Au Clusters on  $\alpha$ -MoC as Catalysts for the Low-Temperature Water-Gas Shift Reaction. *Science* **2017**, *357*, 389–393.
- (96) Guillermet, A. F.; Häglund, J.; Grimvall, G. Cohesive Properties of 4d-Transition-Metal Carbides and Nitrides in the NaCl-Type Structure. *Phys Rev B* **1992**, *45*, 11557.
- (97) Vojvodic, A. Steam Reforming on Transition-Metal Carbides from Density-Functional Theory. *Catal. Lett.* **2012**, *142*, 728–735.
- (98) Nagai, M.; Zahidul, A. M.; Matsuda, K. Nano-Structured Nickel–Molybdenum Carbide Catalyst for Low-Temperature Water-Gas Shift Reaction. *Appl. Catal., A* **2006**, *313*, 137–145.
- (99) Szechenyi, A.; Solymosi, F. Production of Hydrogen in the Decomposition of Ethanol and Methanol over Unsupported Mo<sub>2</sub>C Catalysts. *J. Phys. Chem. C* **2007**, *111*, 9509–9515.
- (100) Newsome, D. S. The Water-Gas Shift Reaction. *Catal. Rev.* **1980**, *21*, 275–318.
- (101) Callaghan, C. A. Kinetics and Catalysis of the Water-Gas Shift Reaction: A Microkinetic and Graph Theoretic Approach. **2006**.
- (102) Panagiotopoulou, P.; Kondarides, D. I. Effect of the Nature of the Support on the Catalytic Performance of Noble Metal Catalysts for the Water–Gas Shift Reaction. *Catal. Today* **2006**, *112*, 49–52.
- (103) Saw, E. T.; Oemar, U.; Tan, X. R.; Du, Y.; Borgna, A.; Hidajat, K.; Kawi, S. Bimetallic Ni–Cu Catalyst Supported on CeO<sub>2</sub> for High-Temperature Water–Gas Shift Reaction: Methane Suppression Via Enhanced CO Adsorption. *J. Catal.* **2014**, *314*, 32–46.
- (104) Kubacka, A.; Fernández-García, M.; Martínez-Arias, A. Catalytic Hydrogen Production through WGS or Steam Reforming of Alcohols over Cu, Ni and Co Catalysts. *Appl. Catal., A* **2016**, *518*, 2–17.
- (105) Sabnis, K. D.; Cui, Y.; Akatay, M. C.; Shekhar, M.; Lee, W.-S.; Miller, J. T.; Delgass, W. N.; Ribeiro, F. H. Water–Gas Shift Catalysis over Transition Metals Supported on Molybdenum Carbide. *J. Catal.* **2015**, *331*, 162–171.
- (106) Schweitzer, N. M.; Schaidle, J. A.; Ezekoye, O. K.; Pan, X.; Linic, S.; Thompson, L. T. High Activity Carbide Supported Catalysts for Water Gas Shift. *J. Am. Chem. Soc.* **2011**, *133*, 2378–2381.

- (107) Rodriguez, J. A.; Ramírez, P. J.; Gutierrez, R. A. Highly Active Pt/MoC and Pt/TiC Catalysts for the Low-Temperature Water-Gas Shift Reaction: Effects of the Carbide Metal/Carbon Ratio on the Catalyst Performance. *Catal. Today* **2017**, *289*, 47–52.
- (108) Wang, G.; Schaidle, J. A.; Katz, M. B.; Li, Y.; Pan, X.; Thompson, L. T. Alumina Supported Pt–Mo<sub>2</sub>C Catalysts for the Water–Gas Shift Reaction. *Journal of Catalysis* **2013**, *304*, 92–99.
- (109) Xu, Y.; Li, J.; Li, W.; Li, W.; Zhang, X.; Zhao, Y.; Xie, J.; Wang, X.; Liu, X.; Li, Y. Xiao, D.; Yin, Z.; Cao, Y.; Ma, D. Direct Conversion of CO and H<sub>2</sub>O into Liquid Fuels under Mild Conditions. *Nat. Commun.* **2019**, *10*, 1–7.
- (110) Zhao, Z.; Yang, H.; Li, Y.; Guo, X. Cobalt-Modified Molybdenum Carbide as an Efficient Catalyst for Chemoselective Reduction of Aromatic Nitro Compounds. *Green Chem.* **2014**, *16*, 1274–1281.
- (111) Jung, K. T.; Kim, W. B.; Rhee, C. H.; Lee, J. S. Effects of Transition Metal Addition on the Solid-State Transformation of Molybdenum Trioxide to Molybdenum Carbides. *Chem. Mater.* **2004**, *16*, 307–314.
- (112) Cao, A.; Lu, R.; Vesper, G. Stabilizing Metal Nanoparticles for Heterogeneous Catalysis. *Phys. Chem. Chem. Phys.* **2010**, *12*, 13499–13510.
- (113) Montini, T.; Condò, A.; Hickey, N.; Lovey, F.; De Rogatis, L.; Fornasiero, P.; Graziani, M. Embedded Rh (1 wt.%)@ Al<sub>2</sub>O<sub>3</sub>: Effects of High Temperature and Prolonged Aging under Methane Partial Oxidation Conditions. *Appl. Catal. B* **2007**, *73*, 84–97.
- (114) Montini, T.; De Rogatis, L.; Gombac, V.; Fornasiero, P.; Graziani, M. Rh(1%)@Ce<sub>x</sub>Zr<sub>1-x</sub>O<sub>2</sub>–Al<sub>2</sub>O<sub>3</sub> Nanocomposites: Active and Stable Catalysts for Ethanol Steam Reforming. *Appl. Catal. B* **2007**, *71*, 125–134.
- (115) De Rogatis, L.; Montini, T.; Casula, M. F.; Fornasiero, P. Design of Rh@Ce<sub>0.2</sub>Zr<sub>0.8</sub>O<sub>2</sub>–Al<sub>2</sub>O<sub>3</sub> Nanocomposite for Ethanol Steam Reforming. *J. Alloys Compd.* **2008**, *451*, 516–520.
- (116) Wang, T.; Liu, X.; Wang, S.; Huo, C.; Li, Y.-W.; Wang, J.; Jiao, H. Stability of  $\beta$ -Mo<sub>2</sub>C Facets from Ab Initio Atomistic Thermodynamics. *J. Phys. Chem. C* **2011**, *115*, 22360–22368.
- (117) Hanif, A.; Xiao, T.; York, A. P.; Sloan, J.; Green, M. L. Study on the Structure and Formation Mechanism of Molybdenum Carbides. *Chem. Mater.* **2002**, *14*, 1009–1015.
- (118) Wang, X.-H.; Hao, H.-L.; Zhang, M.-H.; Li, W.; Tao, K.-Y. Synthesis and Characterization of Molybdenum Carbides Using Propane as Carbon Source. *J. Solid State Chem.* **2006**, *179*, 538–543.
- (119) Wang, T.; Wang, S.; Li, Y.-W.; Wang, J.; Jiao, H. Adsorption Equilibria of Co Coverage on  $\beta$ -Mo<sub>2</sub>C Surfaces. *J. Phys. Chem. C* **2012**, *116*, 6340–6348.
- (120) Shi, Y.; Yang, Y.; Li, Y.-W.; Jiao, H. Activation Mechanisms of H<sub>2</sub>, O<sub>2</sub>, H<sub>2</sub>O, CO<sub>2</sub>, CO, CH<sub>4</sub> and C<sub>2</sub>H<sub>x</sub> on Metallic Mo<sub>2</sub>C (001) as Well as Mo/C Terminated Mo<sub>2</sub>C (101) from Density Functional Theory Computations. *Appl. Catal., A* **2016**, *524*, 223–236.
- (121) Wang, T.; Li, Y.-W.; Wang, J.; Beller, M.; Jiao, H. Dissociative Hydrogen Adsorption on the Hexagonal Mo<sub>2</sub>C Phase at High Coverage. *J. Phys. Chem. C* **2014**, *118*, 8079–8089.
- (122) Tian, X.; Wang, T.; Jiao, H. Oxidation of the Hexagonal Mo<sub>2</sub>C(101) Surface by H<sub>2</sub>O Dissociative Adsorption. *Catal. Sci. Technol.* **2017**, *7*, 2789–2797.
- (123) Wang, T.; Luo, Q.; Li, Y.-W.; Wang, J.; Beller, M.; Jiao, H. Stable Surface Terminations of Orthorhombic Mo<sub>2</sub>C Catalysts and Their Co Activation Mechanisms. *Appl. Catal., A* **2014**, *478*, 146–156.
- (124) Wang, T.; Li, Y.-W.; Wang, J.; Beller, M.; Jiao, H. High Coverage Co Adsorption and Dissociation on the Orthorhombic Mo<sub>2</sub>C (100) Surface. *J. Phys. Chem. C* **2014**, *118*, 3162–3171.
- (125) Wang, T.; Tian, X.; Yang, Y.; Li, Y.-W.; Wang, J.; Beller, M.; Jiao, H. Coverage Dependent Adsorption and Co-Adsorption of CO and H<sub>2</sub> on the CdI<sub>2</sub>-Antitype Metallic Mo<sub>2</sub>C(001) Surface. *Phys. Chem. Chem. Phys.* **2015**, *17*, 1907–1917.
- (126) Cheng, L.; Yu, X.; Zhang, J.; Li, W.; Zhao, C.; Wang, Z.; Jin, L. DFT Investigations into Surface Stability and Morphology of  $\delta$ -MoC Catalyst. *Appl. Surf. Sci.* **2019**, *497*, 143790.
- (127) Posada-Pérez, S.; Viñes, F.; Valero, R.; Rodriguez, J. A.; Illas, F. Adsorption and Dissociation of Molecular Hydrogen on Orthorhombic  $\beta$ -Mo<sub>2</sub>C and Cubic  $\delta$ -MoC (001) Surfaces. *Surf. Sci.* **2017**, *656*, 24–32.
- (128) Gómez, T.; Florez, E.; Rodriguez, J. A.; Illas, F. Theoretical Analysis of the Adsorption of Late Transition-Metal Atoms on the (001) Surface of Early Transition-Metal Carbides. *J. Phys. Chem. C* **2010**, *114*, 1622–1626.
- (129) Asara, G. G.; Viñes, F.; Ricart, J. M.; Rodriguez, J. A.; Illas, F. When Reconstruction Comes Around: Ni, Cu, and Au Adatoms on  $\delta$ -MoC (001). *Surf. Sci.* **2014**, *624*, 32–36.
- (130) Zhou, M.; Cheng, L.; Choi, J.-S.; Liu, B.; Curtiss, L. A.; Assary, R. S. Ni-Doping Effects on Oxygen Removal from an Orthorhombic Mo<sub>2</sub>C (001) Surface: A Density Functional Theory Study. *J. Phys. Chem. C* **2018**, *122*, 1595–1603.
- (131) Hu, Z.; Zhang, L.; Huang, J.; Feng, Z.; Xiong, Q.; Ye, Z.; Chen, Z.; Li, X.; Yu, Z. Self-Supported Nickel-Doped Molybdenum Carbide Nanoflower Clusters on Carbon Fiber Paper for an Efficient Hydrogen Evolution Reaction. *Nanoscale* **2021**, *13*, 8264–8274.

- (132) Orazi, V.; Ambrusi, R. E.; Marchetti, J. M.; Pronsato, M. E. DFT Study of the Hydrogen Adsorption and Storage on Ni<sub>4</sub> Cluster Embedded in Multivacancy Graphene. *Int. J. Hydrog. Energy* **2020**, *45*, 30805–30817.
- (133) Luo, Q.; Wang, T.; Walther, G.; Beller, M.; Jiao, H. Molybdenum carbide catalysed hydrogen production from formic acid — A density functional theory study. *J. Power Sources* **2014**, *246*, 548–555.
- (134) Agrawal, K.; Roldan, A.; Kishore, N.; Logsdail, A. J. Dehydrogenation and dehydration of formic acid over orthorhombic molybdenum carbide. *Catal. Today* **2021**, *X*, XXX–XXX. DOI: 10.1016/j.cattod.2021.04.011
- (135) Shi, Y.; Yang, Y.; Li, Y. W.; Jiao, H. Mechanisms of Mo<sub>2</sub>C(101)-Catalyzed Furfural Selective Hydrodeoxygenation to 2-Methylfuran from Computation. *ACS Catal.* **2016**, *6*, 6790–6803.
- (136) Shi, Y.; Yang, Y.; Li, Y. W.; Jiao, H. Theoretical study about Mo<sub>2</sub>C(101)-catalyzed hydrodeoxygenation of butyric acid to butane for biomass conversion. *Catal. Sci. Technol.* **2016**, *6*, 4923–4936.
- (137) Zhang, T.; Yang, X.; Ge, Q. A DFT study of methane conversion on Mo-terminated Mo<sub>2</sub>C carbides: Carburization vs C–C coupling. *Catal. Today* **2021**, *368*, 140–147.
- (138) Figueras, M.; Gutiérrez, R. A.; Viñes, F.; Ramírez, P. J.; Rodríguez, J. A.; Illas, F. Supported Molybdenum Carbide Nanoparticles as an Excellent Catalyst for CO<sub>2</sub> Hydrogenation. *ACS Catal.* **2021**, *11*, 9679–9687.
- (139) Shrestha, A.; Gao, X.; Hicks, J. C.; Paolucci, C. Nanoparticle Size Effects on Phase Stability for Molybdenum and Tungsten Carbides. *Chem. Mater.* **2021**, *33*, 4606–4620.
- (140) Balyan, S.; Saini, S.; Khan, T. S.; Pant, K. K.; Gupta, P.; Bhattacharya, S.; Haider, M. A. Unravelling the reactivity of metastable molybdenum carbide nanoclusters in the C–H bond activation of methane, ethane and ethylene. *Nanoscale* **2021**, *13*, 4451–4466.
- (141) Wang, F.; Li, T.; Shi, Y.; Jiao, H. Molybdenum Carbide Supported Metal Catalysts (M<sub>n</sub>/Mo<sub>x</sub>C; M= Co, Ni, Cu, Pd, Pt)–Metal and Surface Dependent Structure and Stability. *Catal. Sci. Technol.* **2020**, *10*, 3029–3046.
- (142) Wang, F.; Tian, X.; Jiao, H. Adsorption of CO, H<sub>2</sub>, H<sub>2</sub>O, and CO<sub>2</sub> on Fe-, Co-, Ni-, Cu-, Pd-, and Pt-Doped Mo<sub>2</sub>C(101) Surfaces. *J. Phys. Chem. C* **2021**, *125*, 11419–11431.
- (143) Wang, F.; Li, T.; Jiao, H. Nitridation of the Metallic Mo<sub>2</sub>C(001) Surface from NH<sub>3</sub> Dissociative Adsorption— a DFT Study. *Surf. Sci.* **2019**, *689*, 121466.

## 2. Objectives of this work

Since molybdenum carbides and transition metals are active catalysts in many chemical reactions, it is interesting to investigate their mutual interaction and synergy in structure, stability and activity in molybdenum carbide-supported transition metals as novel catalysts. Depending on the synthetic methods and procedures there are mainly three types of structures of transition metal catalysts on different molybdenum carbides as supports: adsorption, substitution, and embedding. Depending on the metal loading, the supported metal can have atomically dispersed metal atoms as single-atom catalysts, small clusters in two- and three-dimensional forms as nanoparticles, as well as large clusters that resemble metallic catalysts. Experimentally, it is found that molybdenum carbide-supported transition metal catalysts have astonishing stability, activity and selectivity in many reactions. However, the detailed structures of these supported catalysts are not well investigated and understood, and the extraordinary catalytic activity is not rationalized.



**Scheme 8.** Surface structural models for molybdenum carbide supported transition metal catalysts.

Objectives of this dissertation are density functional theory investigations into the metal loading dependent structures, stability and activity of Fe, Co, Ni, Cu, Pd and Pt on different molybdenum carbides surfaces (Scheme 8). In our study, we used both adsorption and substitution models. Depending on metal loading, dispersed single atoms, aggregated small two-dimensional surface models and large three-dimensional clusters have been found; and the stability has been investigated on the basis of the computed adsorption energy and the mutual interaction has been analyzed on the basis of difference in electronic negativity, resulting in electronic perturbation between support and metal. To better understand the mutual interaction and synergy between transition metals and molybdenum carbides, the adsorption of CO, H<sub>2</sub>, H<sub>2</sub>O, and CO<sub>2</sub> and their dissociative intermediates (OH, H, and O), which are involved in many catalytic reactions, are investigated.

These results form a basis for the investigation of the mechanisms of various reactions with size-dependent transition metal catalysts on molybdenum carbides as well as for designing novel catalysts and catalytic reactions. These results are also interesting and promising for other supports such as metal oxides, carbides, nitrides, phosphides as well as functionalized carbon materials, zeolites and organometallic frameworks.

### 3. Summary of publications

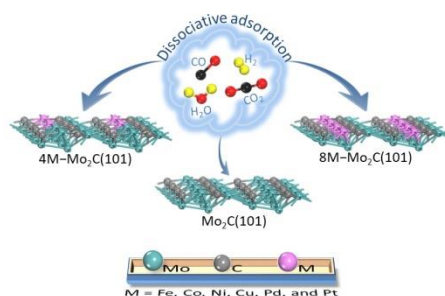
#### 3.1 Adsorption of CO, H<sub>2</sub>, H<sub>2</sub>O, and CO<sub>2</sub> on Fe-, Co-, Ni-, Cu-, Pd-, and Pt-Doped Mo<sub>2</sub>C(101) Surfaces

Fan Wang, Xinxin Tian, Haijun Jiao\*

*J. Phys. Chem. C* **2021**, 125, 11419–11431.

DOI: 10.1021/acs.jpcc.1c03372

**Summary:** The less coordinated and more active surface Mo<sub>A</sub> atoms in hexagonal Mo<sub>2</sub>C(101) were substituted with Fe, Co, Ni, Cu, Pd, and Pt doping atoms for investigating the adsorption of CO, H<sub>2</sub>, H<sub>2</sub>O, and CO<sub>2</sub> as well as OH, H, and O. Metal loading affects the surface electronic structure. For the adsorption of those species, on the pure Mo<sub>2</sub>C(101) surface and surfaces doped with four metal atoms (4M, 25%), surface Mo<sub>A</sub> atoms are most preferred adsorption sites. By replacing all surface Mo<sub>A</sub> atoms with eight doping atoms (8M, 50%), the more coordinated and less active surface Mo<sub>B</sub> atoms become active. Depending on doping metals, the adsorption of surface species can become slightly more or less exothermic. Full H<sub>2</sub>O dissociative adsorption is favored thermodynamically on the 4M-doped surfaces and more exothermic than on the pure surface while doping metal-dependent on the 8M-doped surfaces. CO<sub>2</sub> dissociative adsorption is thermodynamically favored on the 4M-doped surfaces, while it becomes endothermic on the 8M-doped surfaces.



#### Author contributions

In this work I designed and performed all calculations and analyzed all the results. I completed writing and proofreading based on the suggestions and comments of all co-authors. My scientific contribution as the first author of this paper is more than 95%.



# Adsorption of CO, H<sub>2</sub>, H<sub>2</sub>O, and CO<sub>2</sub> on Fe-, Co-, Ni-, Cu-, Pd-, and Pt-Doped Mo<sub>2</sub>C(101) Surfaces

Fan Wang, Xinxin Tian, and Haijun Jiao\*

Cite This: *J. Phys. Chem. C* 2021, 125, 11419–11431

Read Online

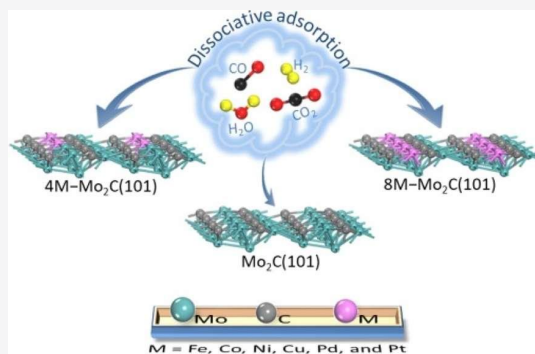
ACCESS |

Metrics & More

Article Recommendations

Supporting Information

**ABSTRACT:** To understand the mutual interaction and synergistic effect of transition metals and supports in heterogeneous catalysis, the less coordinated and more active surface Mo<sub>A</sub> atoms were substituted with Fe, Co, Ni, Cu, Pd, and Pt doping atoms for investigating the adsorption of CO, H<sub>2</sub>, H<sub>2</sub>O, and CO<sub>2</sub> as well as OH, H, and O. Metal loading affects the surface electronic structure. On these surfaces, Fe, Co, Ni, Cu, and Pd doping atoms are positively charged, indicating electron transfer from the metal to the surface, while Pt doping atoms are slightly negatively charged, revealing electron transfer from the surface to the metal. On the pure surfaces and surfaces doped with four metal atoms (4M, 25%), surface Mo<sub>A</sub> atoms are most preferred adsorption sites. By replacing all surface Mo<sub>A</sub> atoms with eight doping atoms (8M, 50%), the more coordinated and less active surface Mo<sub>B</sub> atoms become active. Not only surface metal atoms but also surface carbon atoms are active for the adsorption of surface species. Depending on doping metals, the adsorption of surface species can become slightly more or less exothermic. Exploring the dissociative adsorption of H<sub>2</sub>O and CO<sub>2</sub> reveals metal- and loading-dependent potential energy surfaces. Full H<sub>2</sub>O dissociative adsorption is favored thermodynamically on the 4M-doped surfaces and more exothermic than on the pure surface while doping metal-dependent on the 8M-doped surfaces. CO<sub>2</sub> dissociative adsorption is thermodynamically favored on the 4M-doped surfaces, while it becomes endothermic on the 8M-doped surfaces, which prefer either molecular adsorption or equilibrium between molecular and dissociative adsorption. Comparing the adsorption of CO, OH, O, and H on the pure and doped Mo<sub>2</sub>C(101) surfaces as well as the corresponding metallic low-index M(*hkl*) surfaces reveals their similarity and difference. These results provide a basis for studying the mechanisms of reactions involving these surface species.



## INTRODUCTION

In supported heterogeneous catalysis, enormous efforts have been devoted toward improving the catalytic performance by designing and controlling the loading, shape, and size of active catalysts.<sup>1–4</sup> However, one problem of supported catalysts is the agglomeration of metal particles during the reactions, especially at high temperatures,<sup>5</sup> and great attention has been paid to thermal stabilization of nanostructures. Alternatively, structurally embedded catalysts, normally embedding metal nanoparticles in an inorganic matrix or supports, have attracted great interest due to their stable catalytic activity and capacity for limiting the sintering of metal nanoparticles at high temperatures.<sup>6</sup>

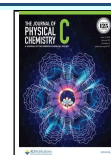
To prepare a promising metal-atom-embedded catalyst, choosing suitable materials as matrixes (or supports) is of great significance as they could play multiple roles in specific chemical reactions. Among various supports, group IV–VI transition-metal carbides are intriguing as they possess strong interactions with doping metals and exhibit a non-negligible influence on the geometric and electronic structures of metal species.<sup>7</sup> As one of the most frequently studied transition-metal carbides, molybdenum carbides have been reported to have

excellent catalytic activities in various chemical transformations, that is, Mo<sub>2</sub>C-catalyzed methanol reforming gave a high H<sub>2</sub> yield (75%) and selectivity at 723 K.<sup>8</sup> In addition, ethanol decomposition to H<sub>2</sub> and hydrocarbons catalyzed by Mo<sub>2</sub>C deposited on silica showed almost 100% conversion at 623–673 K.<sup>9</sup> Recently, Ma *et al.*<sup>10</sup> doped various transition metals (Pt, Fe, Co, and Ni) into molybdenum carbides by *in situ* carburization of metal-doped molybdenum oxide and found that the β-Mo<sub>2</sub>C phase was formed in most of the cases and metal-doped molybdenum carbides showed higher methanol conversion and H<sub>2</sub> yield compared to pure molybdenum carbides, and Pt-doped molybdenum carbide had the highest catalytic activity and selectivity among the prepared catalysts and methanol conversion reached 100% even at a temperature

Received: April 14, 2021

Revised: May 6, 2021

Published: May 19, 2021



as low as 473 K and a long-time stability with a stable methanol conversion. By preparing Cu-doped molybdenum carbide ( $\text{Cu@Mo}_x\text{C}_y$ ) catalysts from the carburization of Cu-doped molybdenum oxide, Ma *et al.*<sup>11</sup> found that Cu loading-dependent phase transition and these carbides ( $\text{Cu@Mo}_x\text{C}_y$ ) exhibited promising activity for methane decomposition and long-term stability at 473–673 K. It is reported that noble metal Pt-embedded molybdenum carbides can hinder Pt sintering at high temperature and promote the interaction between Pt and molybdenum carbide,<sup>12</sup> and this catalyst exhibited excellent and stable catalytic activity for water-gas shift reaction at low temperature. By doping Fe and Ni into the lattice of molybdenum carbide, Wan and Leonard,<sup>13</sup> reported that Fe-doped  $\beta\text{-Mo}_2\text{C}$  are more active electrocatalysts than pure  $\beta\text{-Mo}_2\text{C}$  in  $\text{H}_2$  evolution reaction, while Ni-doped  $\beta\text{-Mo}_2\text{C}$  are less active due to not only the electronic structure but also particle size. Very recently, Chen *et al.*<sup>14</sup> reported that incorporation of copper species in  $\text{Mo}_2\text{C}$  plays a crucial role in modifying the morphologic structure of  $\text{Cu-Mo}_2\text{C}$  as well as tuning the electronic state of Mo active sites, resulting in an important enhancement in the catalytic performance. They also observed a strong synergistic effect between Cu and  $\text{Mo}_2\text{C}$  in hydrogenation of dimethyl oxalate (DMO) to achieve a higher ethanol yield over the pure catalyst (67.2 vs 13.7%) at 673 K as well as excellent catalytic stability during the hydrogenation of DMO to ethanol for longer than 300 h.

Using periodic density functional theory (DFT) methods, Liu and Rodriguez<sup>15</sup> studied water-gas shift reaction on Mo- and C-terminated  $\beta\text{-Mo}_2\text{C}(001)$  surfaces. Our group studied the activation mechanisms of various intermediates on different  $\text{Mo}_2\text{C}$  surfaces.<sup>16,17</sup> Recently, we systematically studied the coverage-dependent adsorption structure and stability of Co, Ni, Cu, Pd, and Pt on the hexagonal  $\text{Mo}_2\text{C}(001)$  and  $\text{Mo}_2\text{C}(101)$  surfaces as well as the cubic non-polar  $\delta\text{-MoC}(001)$  surface. Compared to pure  $\text{Mo}_2\text{C}$  surfaces, theoretical investigations into the structures of metal-doped molybdenum carbides are rather limited. By investigating the transition-metal-atom-embedded graphene, Krasheninnikov *et al.*<sup>18</sup> found that the bonding between the transition-metal atom and neighboring carbon atoms determines the magnetic and electronic properties. By substituting one surface Mo atom with one Ni atom on the Mo- and C-terminated orthorhombic  $\text{Mo}_2\text{C}(001)$  surfaces, Assary *et al.*<sup>19</sup> found that the Ni-doped Mo-terminated surface destabilizes the adsorption of surface  $\text{O}^*$  and  $\text{OH}^*$  and promotes the reaction associated with the removal of surface oxygen. Chen *et al.*<sup>20</sup> studied the promotion effect in water-gas shift reaction on  $\text{M/MoS}_2$  by substituting one surface Mo atom ( $\text{M} = \text{Fe}, \text{Co}, \text{Ni}$ ) and found that Ni has the largest promotion effect in reducing the effective barrier (0.72 eV), followed by Co (0.45 eV), whereas Fe has the smallest effect (0.04 eV) compared with pure  $\text{MoS}_2$  (2.45 eV).

Since metal-doped or embedded molybdenum carbides are promising in various catalysis processes as shown above, it is interesting and worth to systematically investigate the structures of metal-doped molybdenum carbides and their adsorption properties of valuable chemical intermediates involved in various important chemical reactions. In this present study, therefore, we selected the hexagonal  $\text{Mo}_2\text{C}(101)$  surface for doping Fe, Co, Ni, Cu, Pd, and Pt atoms at different degrees; this is because not only the hexagonal  $\text{Mo}_2\text{C}$  phase was widely detected in the preparation of metal-doped molybdenum carbide catalysts but also the (101) surface with

a  $\text{Mo/C} = 1/1$  ratio and a surface energy of  $2.19 \text{ J m}^{-2}$  was reported to be most stable.<sup>21–23</sup> The aim of this work is to shed light on the surface morphology and adsorption properties of these doped catalysts and provide a basis for understanding the catalytic properties of many chemical transformations involving transition-metal-doped molybdenum carbides.

## ■ COMPUTATIONAL METHODS AND MODELS

**Methods.** All calculations were performed using the plane-wave-based periodic DFT method implemented in the Vienna ab initio simulation package (VASP),<sup>24,25</sup> where the ionic cores are described by the projector augmented wave (PAW) method.<sup>26</sup> The exchange and correlation energies are computed using the Perdew, Burke, and Ernzerhof functional (PBE).<sup>27</sup> To achieve accurate energies with errors of less than 1 meV per atom, the cutoff energy was set at 400 eV. The Gaussian electron smearing method with  $\sigma = 0.10 \text{ eV}$  and  $\text{ISMEAR} = 0$  were used. Geometric optimization converged until the forces acting on the atoms were smaller than  $0.02 \text{ eV \AA}^{-1}$ , whereas the energy threshold-defining self-consistency of the electron density was set to  $10^{-4} \text{ eV}$ . Spin polarization was included to correctly describe magnetic properties, which is essential for an accurate description of all energetic data. All transition-state structures were optimized by using the climbing image nudged elastic band method,<sup>28</sup> and the frequency analysis was also processed to verify an authentic transition state having only one imaginary frequency. For bulk optimization, the lattice parameters for the hexagonal  $\text{Mo}_2\text{C}$  phase are determined by minimizing the total energy of the unit cell by using a conjugated gradient algorithm to relax the ions, and a  $5 \times 5 \times 5$  Monkhorst–Pack  $k$ -point grid<sup>29</sup> is used for sampling the Brillouin zone.

**Models.** Generally,  $\text{Mo}_2\text{C}$  has orthorhombic<sup>30</sup> and hexagonal<sup>31,32</sup> crystalline phases. In this work, we used the hexagonal phase with an eclipsed configuration as the unit cell.<sup>16,17,21,33</sup> The calculated lattice parameters of the unit cell are  $2a = 6.079$ ,  $2b = 6.073$ , and  $c = 4.722 \text{ \AA}$ , in good agreement with the experimental values ( $a = b = 3.002$ ,  $c = 4.724 \text{ \AA}$ ).<sup>34</sup> Among all hexagonal  $\text{Mo}_2\text{C}$  surfaces, the (101) surface with a  $\text{Mo/C} = 1/1$  ratio and a surface energy of  $2.19 \text{ J/m}^2$  was reported to be most stable.<sup>21–23,35</sup> Hence, we used  $\text{Mo}_2\text{C}(101)$  to execute our study, and it was modeled by a periodic slab with  $p(2 \times 2)$  super cells having a surface area of  $14.2 \text{ \AA} \times 12.1 \text{ \AA}$ . We applied a four-layer model with the top two layers relaxed and the bottom two layers fixed in their bulk positions. The vacuum layer between the periodically repeated slabs was set at  $15 \text{ \AA}$  to avoid significant interactions between slabs. Surface structural relaxation and total energy calculations were performed with  $3 \times 3 \times 1$  Monkhorst–Pack  $k$ -point sampling. For the relevant gas-phase species, we used a cubic box with a side length of  $10 \text{ \AA}$  to calculate the structures and total energies.

The adsorption energy ( $E_{\text{ads}}$ ) is defined according to  $E_{\text{ads}} = E(\text{X/slab}) - [E(\text{X}) + E(\text{slab})]$ , where  $E(\text{X/slab})$  is the total energy of the slab with one X molecule,  $E(\text{slab})$  is the total energy of the bare slab, and  $E(\text{X})$  is the total energy of a free X molecule in the gas phase, and therefore, the more negative the  $E_{\text{ads}}$ , the stronger the adsorption. For the adsorption of atomic H or O, half of the total energy of gas-phase molecular  $\text{H}_2$  or  $\text{O}_2$  was used. The barrier ( $E_a$ ) and reaction energy ( $\Delta E_r$ ) are calculated according to  $E_a = E_{\text{TS}} - E_{\text{IS}}$  and  $\Delta E_r = E_{\text{FS}} - E_{\text{IS}}$ , where  $E_{\text{IS}}$ ,  $E_{\text{FS}}$ , and  $E_{\text{TS}}$  are the energies of the corresponding

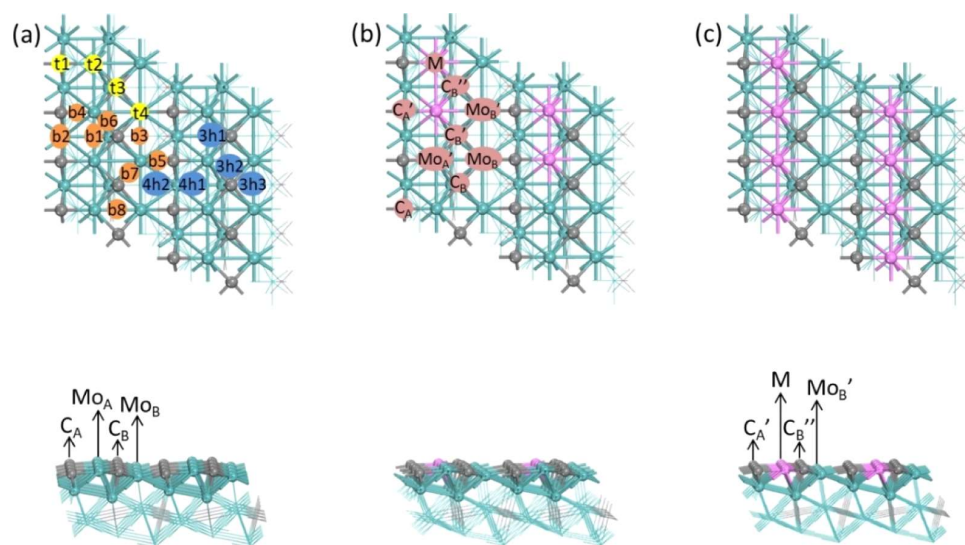


**Figure 1.** Top (top) and side (bottom) views of the (a)  $\text{Mo}_2\text{C}(101)$ , (b)  $4\text{M}-\text{Mo}_2\text{C}(101)$ , and (c)  $8\text{M}-\text{Mo}_2\text{C}(101)$  surface structures and possible adsorption sites (t: top, b: bridge, 3h: threefold hollow, and 4h: fourfold hollow sites; C: gray, Mo: cyan, M: pink).

initial state (IS), final state (FS), and transition state (TS), respectively. All reported energetic data included zero-point energy (ZPE) correction through processing the frequency analysis. In our previous work, we used PBE to compute the high coverage adsorption and desorption of CO on the orthorhombic  $\text{Mo}_2\text{C}(100)$  surface<sup>36</sup> and the hexagonal eclipsed  $\text{Mo}_2\text{C}(001)$  surface<sup>37</sup> and found that the estimated desorption temperatures agree with the experimental values, and this in turn validates the PBE functional and also the calculated adsorption energies. The same is also found for the high coverage co-adsorption of CO and  $\text{H}_2$  on the  $\text{CdI}_2$ -antitype metallic  $\text{Mo}_2\text{C}(001)$  surface.<sup>38</sup> On the contrary, the computed adsorption energies including dispersion correction<sup>39</sup> are in the range of 0.25–0.54 eV stronger than those from only PBE and should be overestimated. Therefore, we used only PBE for energy calculations.

Figure 1 shows the top and side views of the  $\text{Mo}_2\text{C}(101)$ ,  $4\text{M}-\text{Mo}_2\text{C}(101)$ , and  $8\text{M}-\text{Mo}_2\text{C}(101)$  surfaces. For  $\text{Mo}_2\text{C}(101)$ , there are totally 16 surface Mo and 16 surface C atoms. Four types of surface atoms with different coordination patterns are exposed. The surface  $\text{C}_\text{A}$  atom interacts with four Mo atoms and has two dangling bonds (saturated bulk Mo coordinating with three C atoms), and the surface  $\text{C}_\text{B}$  atom interacts with five Mo atoms and has one dangling bond. The surface  $\text{Mo}_\text{A}$  atom interacts with seven Mo atoms, and the surface  $\text{Mo}_\text{B}$  atom interacts with eight Mo atoms. These four different surface atoms build four top sites (t1–t4), eight bridge sites (b1–b8), three threefold hollow sites (3h1–3h3), and two fourfold hollow sites (4h1 and 4h2) for adsorption. The t1–t4 sites are on the  $\text{C}_\text{A}$ ,  $\text{Mo}_\text{A}$ ,  $\text{C}_\text{B}$ , and  $\text{Mo}_\text{B}$ , respectively. The b1 ( $\text{Mo}_\text{A}-\text{Mo}_\text{A}$ ) site has two  $\text{Mo}_\text{A}$  atoms; the b2 ( $\text{C}_\text{A}-\text{C}_\text{A}$ ) site has two  $\text{C}_\text{A}$  atoms; the b3 ( $\text{Mo}_\text{B}-\text{Mo}_\text{B}$ ) site has two  $\text{Mo}_\text{B}$  atoms; the b4 ( $\text{Mo}_\text{A}-\text{C}_\text{A}$ ) site has one  $\text{Mo}_\text{A}$  atom and one  $\text{C}_\text{A}$  atom; the b5 ( $\text{Mo}_\text{B}-\text{C}_\text{A}$ ) site has one  $\text{Mo}_\text{B}$  atom and one  $\text{C}_\text{A}$  atom; the b6 ( $\text{Mo}_\text{A}-\text{C}_\text{B}$ ) site has one  $\text{C}_\text{B}$  atom and one  $\text{Mo}_\text{A}$  atom; the b7 ( $\text{Mo}_\text{B}-\text{C}_\text{B}$ ) site has one  $\text{C}_\text{B}$  atom and one  $\text{Mo}_\text{B}$  atom; the b8 ( $\text{Mo}_\text{A}-\text{Mo}_\text{B}$ ) site has one  $\text{Mo}_\text{A}$  atom and one  $\text{Mo}_\text{B}$  atom. The 3h1 ( $2\text{Mo}_\text{A}-\text{C}_\text{B}$ ) site has two  $\text{Mo}_\text{A}$  atoms and one  $\text{C}_\text{B}$  atom; the 3h2 ( $\text{Mo}_\text{A}-\text{Mo}_\text{B}-\text{C}_\text{B}$ ) site has one  $\text{Mo}_\text{A}$  atom, one  $\text{Mo}_\text{B}$  atom, and one  $\text{C}_\text{B}$  atom; and the 3h3 ( $2\text{Mo}_\text{B}-$

$\text{C}_\text{B}$ ) site has two  $\text{Mo}_\text{B}$  atoms and one  $\text{C}_\text{B}$  atom. The 4h1 ( $2\text{Mo}_\text{A}-2\text{C}_\text{A}$ ) site has two  $\text{Mo}_\text{A}$  atoms and two  $\text{C}_\text{A}$  atoms, while the 4h2 ( $2\text{Mo}_\text{B}-2\text{C}_\text{A}$ ) site has two  $\text{Mo}_\text{B}$  atoms and two  $\text{C}_\text{A}$  atoms. The total supercell contains a  $\text{Mo}_{64}\text{C}_{32}$  unit.

The  $4\text{M}-\text{Mo}_2\text{C}(101)$  surface, formed by substituting 4 surface  $\text{Mo}_\text{A}$  atoms on the pure  $\text{Mo}_2\text{C}(101)$  surface with 4 doping metal atoms, has 12 surface Mo, 4 doping metal, and 16 surface C atoms. As shown in Figure 1b, nine types of surface atoms can be recognized with different coordination environments. The surface M atom interacts with six Mo atoms and one M atom. The surface  $\text{C}_\text{A}$  atom interacts with four Mo atoms; surface  $\text{C}_\text{A}'$  interacts with three Mo atoms and one M atom; the surface  $\text{C}_\text{B}$  atom interacts with five Mo atoms; the surface  $\text{C}_\text{B}'$  atom interacts with four Mo atoms and one M atom; the surface  $\text{C}_\text{B}''$  atom interacts with three Mo atoms and two M atoms. Surface  $\text{Mo}_\text{A}'$  interacts with six Mo atoms and one M atom; the surface  $\text{Mo}_\text{B}$  atom interacts with eight Mo atoms; the surface  $\text{Mo}_\text{B}'$  atom interacts with seven Mo atoms and one M atom.

On the  $8\text{M}-\text{Mo}_2\text{C}(101)$  surface (Figure 1c), all surface  $\text{Mo}_\text{A}$  atoms on the pure  $\text{Mo}_2\text{C}(101)$  surface are replaced with doping metal atoms. Therefore, this surface has totally 8 surface  $\text{Mo}_\text{B}$  atoms, 8 surface doping M atoms, and 16 surface C atoms. There are four types of surface atoms with different coordination environments. The surface M atom interacts with five Mo and two M atoms. Surface  $\text{C}_\text{A}'$  interacts with three Mo atoms and one M atom, the surface  $\text{C}_\text{B}''$  atom interacts with three Mo and two M atoms, and the surface  $\text{Mo}_\text{B}'$  atom interacts with seven Mo atoms and one M atom.

## RESULTS AND DISCUSSION

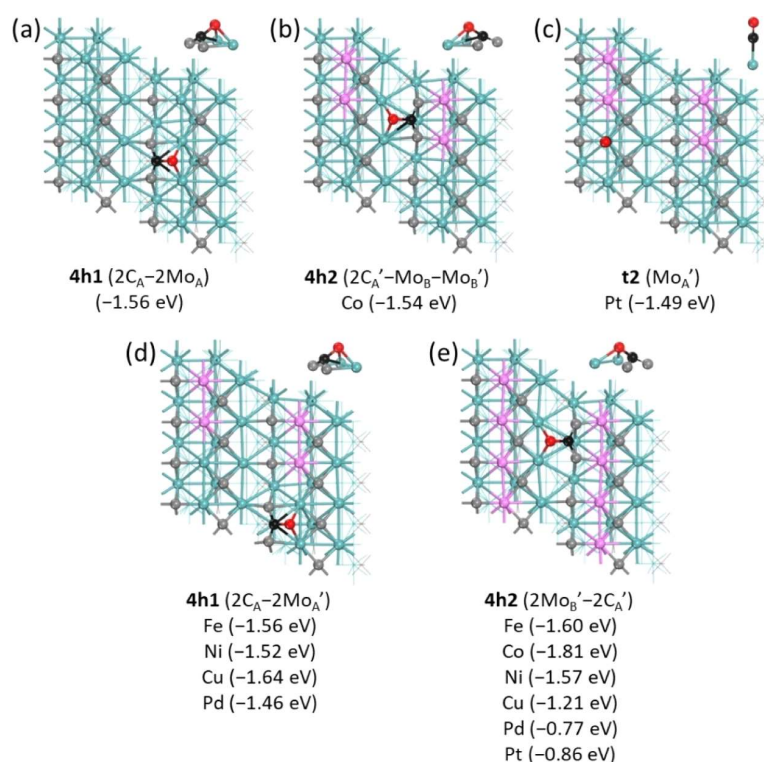
Since doping metals have different electronic configurations, it is meaningful to investigate the changes in geometric, electronic, and adsorption properties with the respect of catalysis. At first, we analyzed the projected density of states (PDOS) of the d-orbitals of all these doped surfaces. We compared our results with those reported previously<sup>40</sup> and found good accordance. On pure  $\text{Mo}_2\text{C}(101)$ , the PDOS shows that the d-orbitals of  $\text{Mo}_\text{A}$  with sevenfold coordination is closer to the Fermi level than  $\text{Mo}_\text{B}$  with eightfold coordination



**Table 1.** Average Bader Charge for Surface Metal Atoms on Pure Mo<sub>2</sub>C(101), 4M–Mo<sub>2</sub>C(101), and 8M–Mo<sub>2</sub>C(101) (M = Fe, Co, Ni, Cu, Pd, and Pt)

site	Mo <sub>2</sub> C(101)	4M–Mo <sub>2</sub> C(101)						8M–Mo <sub>2</sub> C(101)					
		Fe	Co	Ni	Cu	Pd	Pt	Fe	Co	Ni	Cu	Pd	Pt
Mo <sub>A</sub> <sup>a</sup>	0.79	0.85	0.88	0.89	0.88	0.91	0.91						
Mo <sub>B</sub> <sup>b</sup>	0.89	0.86	0.86	0.87	0.89	0.90	0.90	0.86	0.85	0.90	0.93	0.93	0.92
C <sub>A</sub>	–1.14	–1.13	–1.12	–1.12	–1.13	–1.10	–1.08	–1.10	–1.08	–1.06	–1.10	–1.02	–0.99
C <sub>B</sub>	–1.32	–1.29	–1.25	–1.24	–1.25	–1.20	–1.17	–1.23	–1.14	–1.12	–1.16	–1.03	–0.98
M		0.51	0.32	0.27	0.33	0.04	–0.12	0.54	0.36	0.27	0.37	0.10	–0.03

<sup>a</sup>Average Bader charge of surface Mo<sub>A</sub> atoms in 4M–Mo<sub>2</sub>C(101). <sup>b</sup>Average Bader charge of surface Mo<sub>B</sub> and Mo<sub>B</sub>' atoms in 4M–Mo<sub>2</sub>C(101) or surface Mo<sub>B</sub>' atoms in 8M–Mo<sub>2</sub>C(101).

**Figure 2.** Most stable adsorption configurations and energies (in parentheses) of CO on (a) pure Mo<sub>2</sub>C(101), (b–d) 4M–Mo<sub>2</sub>C(101), and (e) 8M–Mo<sub>2</sub>C(101) (M = Fe, Co, Ni, Cu, Pd, and Pt; O: red, C in CO: black, C in Mo<sub>2</sub>C: gray, Mo: cyan, M: pink).

and surface Mo<sub>A</sub> atoms are more active than Mo<sub>B</sub> atoms. For 8M–Mo<sub>2</sub>C(101), with all surface Mo<sub>A</sub> atoms replaced with doping metals (Figure S1), surface Mo<sub>B</sub> has no obvious change in PDOS, while the PDOSs of Fe and Co are closer to the Fermi level compared to those of Ni, Cu, Pd, and Pt. The same situation has also been found on the fourM–Mo<sub>2</sub>C(101) surfaces (Figure S2).

In addition to PDOS, we have analyzed the electronic effect (Bader charge analysis<sup>41</sup>) of different doping metals (Table 1). On pure Mo<sub>2</sub>C(101), both Mo<sub>A</sub> and Mo<sub>B</sub> are positively charged. On both 4M–Mo<sub>2</sub>C(101) and 8M–Mo<sub>2</sub>C(101) for 3d metals, the positive Bader charge of the doping metal is in the order of Fe (0.51) > Cu (0.33) ≈ Co (0.32) > Ni (0.27) and Fe (0.54) > Cu (0.37) ≈ Co (0.36) > Ni (0.27), respectively, in line with the order of the Allen electronegativity of Fe (1.80) < Co (1.84) ≈ Cu (1.85) < Ni (1.88).<sup>42</sup> Comparatively, Pd atoms are slightly positively charged for 4M– and 8M–Mo<sub>2</sub>C(101) (0.04 and 0.10, respectively), while Pt atoms are slightly negatively charged (–0.12 and –0.03,

respectively), although the electronegativities of Pd and Pt are 1.59 and 1.72, respectively. The difference among Ni, Pd, and Pt might be associated with their different electronic configurations, that is, 3d<sup>8</sup>4s<sup>2</sup> for Ni, 4d<sup>10</sup>5s<sup>0</sup> for Pd, and 5d<sup>9</sup>6s<sup>1</sup> for Pt. In all cases, surface C<sub>A</sub> and C<sub>B</sub> are negatively charged due to the much larger electronegativity (2.544), and C<sub>A</sub> is more negatively charged than C<sub>B</sub>. However, both C<sub>A</sub> and C<sub>B</sub> become less negatively charged upon transition-metal doping, and the largest change is C<sub>B</sub> on the 8M-doped surface. That the doped Cu atoms are positively charged agrees with the X-ray photoelectron spectroscopy analysis,<sup>11</sup> and these positively charged Cu species could result in high activity for methanol conversion and high stability, which might result from the strong interaction between Cu and the Mo<sub>2</sub>C support. Having these results in hand, we computed the adsorption properties of CO, H<sub>2</sub>O, H<sub>2</sub>, and CO<sub>2</sub>.

**CO Adsorption.** First, we studied CO adsorption. Figure 2 shows the most stable adsorption configurations, while the less stable adsorption configurations are given in Figure S3. On

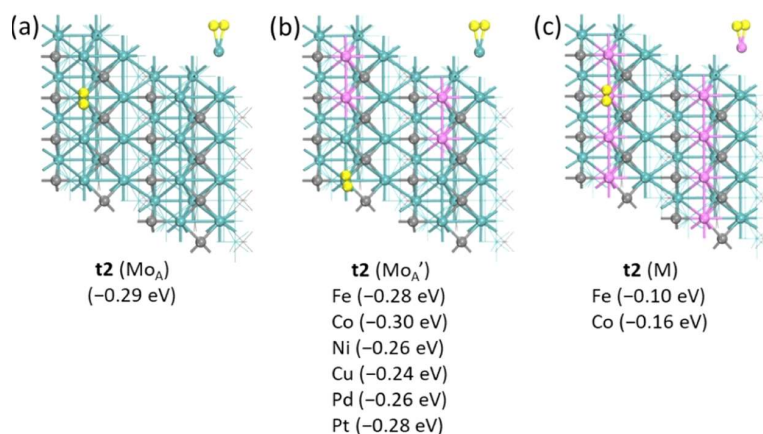


**Figure 3.** Most stable adsorption configurations and energies (in parentheses) of  $H_2$  on (a) pure  $Mo_2C(101)$ , (b)  $4M-Mo_2C(101)$ , and (c)  $8M-Mo_2C(101)$  ( $M = Fe, Co, Ni, Cu, Pd$ , and  $Pt$ ;  $H$ : yellow,  $C$ : gray,  $Mo$ : cyan,  $M$ : pink).

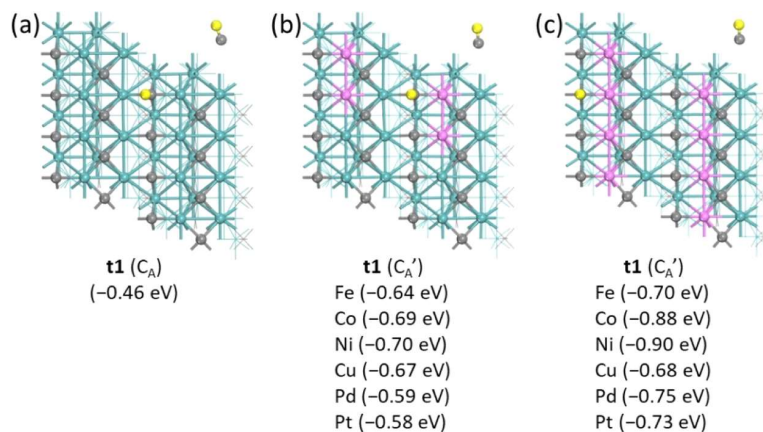


**Figure 4.** Most stable adsorption configurations and energies (in parentheses) of  $H$  on (a) pure  $Mo_2C(101)$ , (b)  $4M-Mo_2C(101)$ , and (c)  $8M-Mo_2C(101)$  ( $M = Fe, Co, Ni, Cu, Pd$ , and  $Pt$ ;  $H$ : yellow,  $C$ : gray,  $Mo$ : cyan,  $M$ : pink; using gaseous  $H_2$  as a reference).

pure  $Mo_2C(101)$ , CO prefers the  $4h1$  ( $2C_A-2Mo_A$ ) site with the strongest adsorption energy of  $-1.56$  eV, followed by the  $t2$  ( $Mo_A$ ) site ( $-1.53$  eV), indicating their competition, while the  $t4$  ( $Mo_B$ ) and  $4h2$  ( $2C_A-2Mo_B$ ) sites have much lower adsorption energies ( $-0.96$  and  $-0.67$  eV, respectively, Figure S3). At the  $4h1$  site ( $2C_A-2Mo_A$ ), the C atom of CO interacts with two surface  $C_A$  atoms and the O atom interacts with two surface  $Mo_A$  atoms. At the  $4h2$  ( $2C_A-2Mo_B$ ) site, the C atom of CO interacts with two surface  $C_A$  atoms and the O atom interacts with two surface  $Mo_B$  atoms. The stronger adsorption at  $4h1$  than at  $4h2$  shows that  $Mo_A$  is more active than  $Mo_B$ . These results match well with those reported previously.<sup>16,37</sup>

On  $4M-Mo_2C(101)$ , where half surface  $Mo_A$  atoms on  $Mo_2C(101)$  are replaced with doping metals, CO prefers the  $4h1$  ( $2C_A-2Mo_A'$ ) site for  $M = Fe, Ni, Cu$ , and  $Pd$  with adsorption energies of  $-1.56$ ,  $-1.52$ ,  $-1.64$ , and  $-1.46$  eV, respectively. For  $M = Co$  and  $Pt$ , CO prefers the  $4h2$  ( $2C_A'-Mo_B-Mo_B'$ ) and  $t2$  ( $Mo_A'$ ) sites with adsorption energies of  $-1.54$  and  $-1.49$  eV, respectively, while the  $4h1$  ( $2C_A-2Mo_A'$ ) site has lower adsorption energies ( $-1.45$  and  $-1.42$  eV, respectively). It is noted that CO adsorption at the top site of doping metal  $t2$  ( $M$ ) at the  $t4$  ( $Mo_B'$ ) site and at the  $4h1$  ( $2M-2C_A'$ ) site (vertically at the  $2C_A'$  bridge site) for  $Pd$  and  $Pt$  is less or much less stable (Figure S3). This shows that the doping metal does not significantly affect CO adsorption at the

$4h1$  ( $2C_A-2Mo_A'$ ) site but increases CO adsorption energy at the  $4h2$  ( $2C_A'-Mo_B-Mo_B'$ ) and  $t2$  ( $Mo_A'$ ) sites. However, CO adsorption around the doping metal is not competitive and favorable.

On  $8M-Mo_2C(101)$ , CO prefers the  $4h2$  ( $2Mo_B'-2C_A'$ ) site for  $M = Fe, Co, Ni, Cu$ , and  $Pt$  with adsorption energies of  $-1.60$ ,  $-1.81$ ,  $-1.57$ ,  $-1.21$ , and  $-0.86$  eV, respectively. For  $M = Pd$ , both  $4h2$  ( $2Mo_B'-2C_A'$ ) and  $t4$  ( $Mo_B'$ ) sites have the same CO adsorption energy ( $-0.77$  eV). On the contrary, CO adsorption at the top site of doping metal  $t2$  ( $M$ ), at the  $t4$  ( $Mo_B'$ ) site, and at the  $4h1$  ( $2M-2C_A$ ) site is less or much less stable (Figure S3). This shows that the doping metal promotes CO adsorption at the  $4h2$  ( $2Mo_B'-2C_A'$ ) site, while CO adsorption around the doping metal is not competitive and favorable.

In addition to the adsorption configurations and energies, we computed CO stretching frequencies (Table S1). It is found that CO stretching frequencies at fourfold hollow sites are in the range of  $1000-1300$   $cm^{-1}$ , while those at the top sites are in the range of  $1900-2100$   $cm^{-1}$ . However, CO stretching frequency does not correlate with the adsorption energy since CO has close adsorption energy at fourfold hollow and top sites, that is, at  $4h1$  ( $2C_A-2Mo_A$ ) and  $t2$  ( $Mo_A$ ) sites on pure  $Mo_2C(101)$  ( $-1.56$  and  $-1.53$  eV, respectively), at  $4h1$  ( $2C_A-2Mo_A'$ ) and  $t2$  ( $M$ ) sites on  $4Fe-Mo_2C(101)$  ( $-1.56$

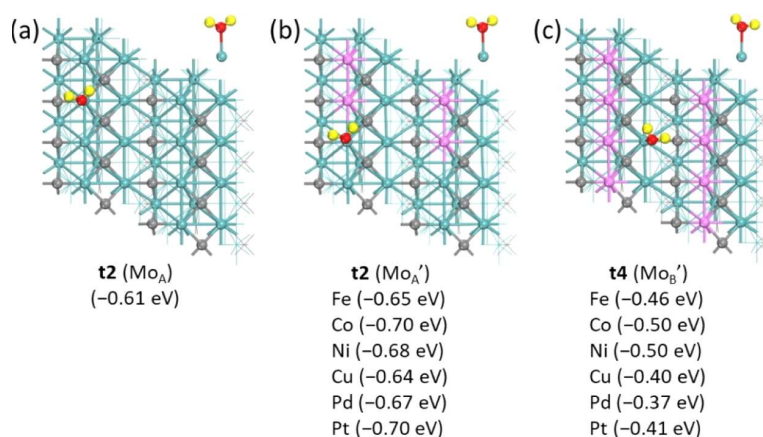


**Figure 5.** Most stable adsorption configurations and energies (in parentheses) of H<sub>2</sub>O on (a) pure Mo<sub>2</sub>C(101), (b) 4M–Mo<sub>2</sub>C(101), and (c) 8M–Mo<sub>2</sub>C(101) (M = Fe, Co, Ni, Cu, Pd, and Pt; H: yellow, O: red, C: gray, Mo: cyan, M: pink).

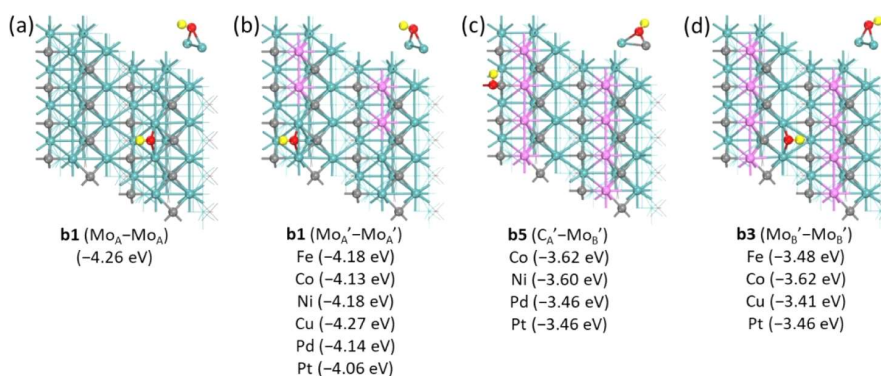


**Figure 6.** Most stable adsorption configurations and energies (in parentheses) of OH on (a) pure Mo<sub>2</sub>C(101), (b) 4M–Mo<sub>2</sub>C(101), and (c,d) 8M–Mo<sub>2</sub>C(101) (M = Fe, Co, Ni, Cu, Pd, and Pt; H: yellow, O: red, C: gray, Mo: cyan, M: pink).

and −1.55 eV, respectively), and at **4h2** (2Mo<sub>B</sub>'–2C<sub>A</sub>') and **t4** (Mo<sub>B</sub>') sites on 8Pd–Mo<sub>2</sub>C(101) (−0.77 and −0.77 eV, respectively). These results should provide theoretical reference for assigning specific adsorption sites with the corresponding stretching frequencies.

**Hydrogen Adsorption.** As reported previously,<sup>29</sup> molecular H<sub>2</sub> can occupy the top site of the surface Mo atom vertically and horizontally, and the former is slightly more stable than the latter; thus, we only considered the vertical type in the present study.

On pure Mo<sub>2</sub>C(101) (Figure 3a), H<sub>2</sub> adsorption at the **t2** (Mo<sub>A</sub>) site is exothermic (−0.29 eV), while at the **t4** (Mo<sub>B</sub>) site, it is endothermic (0.13 eV) (Figure S4). On 4M–Mo<sub>2</sub>C(101), H<sub>2</sub> prefers the **t2** (Mo<sub>A</sub>') site with adsorption energies of −0.28, −0.30, −0.26, −0.24, −0.26, and −0.28 eV for M = Fe, Co, Ni, Cu, Pd, and Pt, respectively (Figure 3b), close to that on the pure surface. On the contrary, H<sub>2</sub> adsorption at the **t2** (M) site has either very low or negligible adsorption energy (Figure S4). On the **t4** (Mo<sub>B</sub> or Mo<sub>B</sub>') sites, H<sub>2</sub> has adsorption energies close to 0 (Figure S4). These show that on 4M–Mo<sub>2</sub>C(101), the doping metal does not significantly affect H<sub>2</sub> adsorption at the **t2** (Mo<sub>A</sub>') site, and H<sub>2</sub> adsorption around the doping metal is not favored and competitive. On 8M–Mo<sub>2</sub>C(101), H<sub>2</sub> adsorption at the **t2** (M) site has very low adsorption energies (−0.10 and −0.16 eV, respectively) for M = Fe and Co (Figure 3c) and negligible

adsorption energy for M = Ni, Cu, Pd, and Pt (Figure S4), indicating the complete suppression of H<sub>2</sub> adsorption.

As H<sub>2</sub> prefers dissociation adsorption (−0.92 eV) on the pure Mo<sub>2</sub>C(101) surface with a very low barrier (0.31 eV),<sup>16</sup> we computed the adsorption of a H atom for H<sub>2</sub> dissociative adsorption. The most stable adsorption configurations are listed in the Figure 4, and other less stable adsorption configurations and energies are summarized in Figure S5.

As shown in Figure 4, the H atom prefers the C<sub>A</sub> (or C<sub>A</sub>') sites on pure and metal-doped surfaces. On pure Mo<sub>2</sub>C(101), the adsorption energy at the C<sub>A</sub> site is −0.46 eV (Figure 4a), much stronger than that at the other adsorption sites (Figure S5). Based on the results on pure Mo<sub>2</sub>C(101), we mainly considered the different top sites for H adsorption on the 4M– and 8M–Mo<sub>2</sub>C(101) surfaces. On 4M–Mo<sub>2</sub>C(101), it is interesting to note that H adsorption has stronger adsorption energy at the top of C<sub>A</sub>' site than at the C<sub>A</sub> site (−0.64 vs −0.43 eV, −0.69 vs −0.43 eV, −0.70 vs −0.42 eV, −0.67 vs −0.43 eV, −0.59 vs −0.41 eV, and −0.58 vs −0.41 eV for M = Fe, Co, Ni, Cu, Pd, and Pt, respectively), while H does not adsorb at all other sites. On 8M–Mo<sub>2</sub>C(101), the adsorption energies at the top of the C<sub>A</sub>' site for M = Fe, Co, Ni, Cu, Pd, and Pt are −0.70, −0.88, −0.90, −0.68, −0.75, and −0.73 eV, respectively. These results show that the doping metal promotes hydrogen atom adsorption at the top site of the surface carbon atom. On the contrary, the adsorption of the



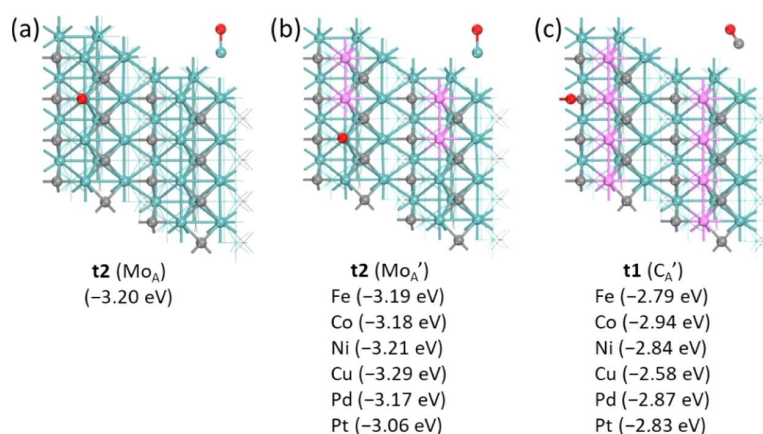


**Figure 7.** Most stable adsorption configurations and energies (in parentheses) of O on (a) pure Mo<sub>2</sub>C(101), (b) 4M–Mo<sub>2</sub>C(101), and (c) 8M–Mo<sub>2</sub>C(101) (M = Fe, Co, Ni, Cu, Pd, and Pt; O: red, C: gray, Mo: cyan, M: pink; using gaseous O<sub>2</sub> as a reference).

**Table 2.** Dissociation Barrier ( $E_a$ , eV) and Reaction Energy ( $\Delta E_r$ , eV) as Well as the Critical O–H Distance ( $d$ , Å) in the Transition State

surfaces	H <sub>2</sub> O → TS1 → OH + H			OH + H → TS2 → O + 2H		
	$E_a$	$\Delta E_r$	$d$ (TS1)	$E_a$	$\Delta E_r$	$d$ (TS2)
Mo <sub>2</sub> C(101)	0.23	−0.94	1.307	0.72	−0.30	1.314
4Fe–Mo <sub>2</sub> C(101)	0.28	−0.79	1.311	0.77	−0.38	1.325
4Co–Mo <sub>2</sub> C(101)	0.31	−0.87	1.312	0.80	−0.40	1.316
4Ni–Mo <sub>2</sub> C(101)	0.30	−0.75	1.306	0.79	−0.39	1.319
4Cu–Mo <sub>2</sub> C(101)	0.27	−0.90	1.304	0.77	−0.40	1.321
4Pd–Mo <sub>2</sub> C(101)	0.31	−0.73	1.318	0.81	−0.39	1.325
4Pt–Mo <sub>2</sub> C(101)	0.36	−0.62	1.326	0.81	−0.37	1.316
8Fe–Mo <sub>2</sub> C(101)	0.10	−0.48	1.313	0.65	−0.58	1.354
8Co–Mo <sub>2</sub> C(101)	0.08	−0.72	1.265	0.60	−0.70	1.326
8Ni–Mo <sub>2</sub> C(101)	0.05	−0.61	1.278	0.68	−0.64	1.360
8Cu–Mo <sub>2</sub> C(101)	0.05	−0.53	1.307	0.73	−0.49	1.388
8Pd–Mo <sub>2</sub> C(101)	0.18	−0.40	1.307	0.87	−0.55	1.410
8Pt–Mo <sub>2</sub> C(101)	0.21	−0.40	1.302	0.85	−0.51	1.388

hydrogen atom around the doping metal has either negligible or endothermic adsorption energies.

**H<sub>2</sub>O Dissociative Adsorption.** Figure 5 shows the most stable H<sub>2</sub>O adsorption configurations on all these surfaces, and the less stable adsorption configurations are listed in Figure S6. On pure Mo<sub>2</sub>C(101), H<sub>2</sub>O prefers the t2 (Mo<sub>A</sub>) site with an adsorption energy of −0.61 eV,<sup>16</sup> while adsorption on the t4 (Mo<sub>B</sub>) site is less stable (−0.31 eV, Figure S6). For 4M–Mo<sub>2</sub>C(101), H<sub>2</sub>O also prefers the t2 (Mo<sub>A</sub>') site for all doped surfaces with adsorption energies of −0.65, −0.70, −0.68, −0.64, −0.67, and −0.70 eV for M = Fe, Co, Ni, Cu, Pd, and Pt, respectively (Figure 5b), while adsorption at other top sites, t2 (Mo), t4 (Mo<sub>B</sub>), and t4 (Mo<sub>B</sub>'), is much less stable. It is also to note that metal doping increases slightly the adsorption energy.

On 8M–Mo<sub>2</sub>C(101), H<sub>2</sub>O prefers the t4 (Mo<sub>B</sub>') site with adsorption energies of −0.46, −0.50, −0.50, −0.40, −0.37, and −0.41 eV for M = Fe, Co, Ni, Cu, Pd, and Pt, respectively (Figure 5c), while H<sub>2</sub>O adsorption at the top of the t2 (M) doping metal is less stable with adsorption energies of −0.40, −0.38, −0.27, −0.28, −0.15, and −0.10 eV for M = Fe, Co, Ni, Cu, Pd, and Pt, respectively (Figure S6).

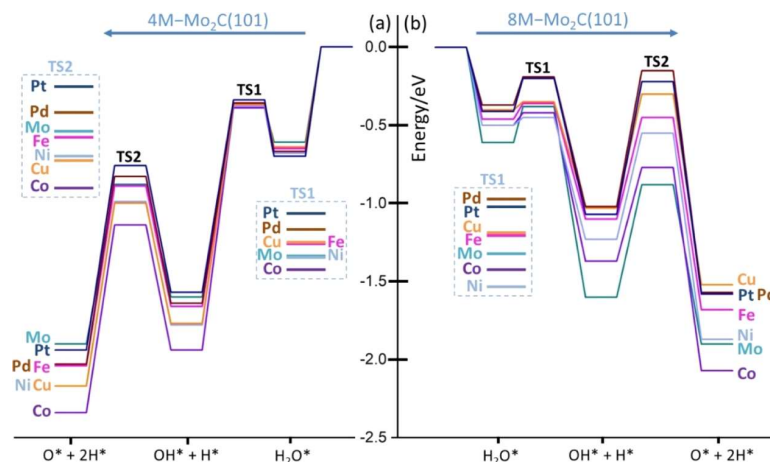
Next, we computed the adsorption of OH and O, the intermediates of H<sub>2</sub>O dissociative adsorption. For OH, the most stable adsorption configurations are shown in Figure 6,

and the other less stable adsorption configurations are listed in Figure S7.

On pure Mo<sub>2</sub>C(101) (Figure 6a), OH prefers the b1 (Mo<sub>A</sub>–Mo<sub>A</sub>) site with an adsorption energy of −4.26 eV, followed by that at the t2 (Mo<sub>A</sub>) site (−3.85 eV), while adsorption at other sites (t4, b4, b3, and t3) is much less stable. On 4M–Mo<sub>2</sub>C(101), OH also prefers the b1 (Mo<sub>A</sub>'–Mo<sub>A</sub>') site with adsorption energies of −4.18, −4.13, −4.18, −4.27, −4.14, and −4.06 eV for M = Fe, Co, Ni, Cu, Pd, and Pt, respectively (Figure 6b). Since OH prefers the bridge sites over the top sites, we also computed other bridge sites, b1 (M–Mo<sub>A</sub>') and b1 (M–M) as well as b3 (Mo<sub>B</sub>–Mo<sub>B</sub>), b3 (Mo<sub>B</sub>'–Mo<sub>B</sub>), and b3 (Mo<sub>B</sub>'–Mo<sub>B</sub>'), and all these sites have lower OH adsorption energies (Figure S7).

On 8M–Mo<sub>2</sub>C(101), dramatic changes have been found. For M = Co and Pt (Figure 6c,d), b5 (C<sub>A</sub>'–Mo<sub>B</sub>') and b3 (Mo<sub>B</sub>'–Mo<sub>B</sub>') sites have the same adsorption energy (−3.62 and −3.46 eV, respectively). For M = Ni and Pd, the b5 (C<sub>A</sub>'–Mo<sub>B</sub>') site has a stronger adsorption energy than the b3 (Mo<sub>B</sub>'–Mo<sub>B</sub>') site (−3.60 vs −3.42 eV for Ni and −3.46 vs −3.39 eV for Pd). For M = Fe and Cu, the b3 (Mo<sub>B</sub>'–Mo<sub>B</sub>') and b5 (C<sub>A</sub>'–Mo<sub>B</sub>') sites have close adsorption energies (−3.48 vs −3.46 eV for Fe and −3.41 vs −3.37 eV for Cu). On the contrary, the b1 (M–M) site has much lower OH adsorption energy (Figure S7). It shows that metal doping can

**Scheme 1.** Potential Energy Surface of H<sub>2</sub>O Dissociative Adsorption on (a) 4M–Mo<sub>2</sub>C(101), Left, and (b) 8M–Mo<sub>2</sub>C(101), Right (M = Mo, Fe, Co, Ni, Cu, Pd, and Pt; the Magnified Surface in the Dash Line Square)



lower OH adsorption energy to a large extent on the 8M–Mo<sub>2</sub>C(101) surfaces by about 15–20%, and this might affect the reactions associated with surface OH.

Next, we computed surface oxygen adsorption (Figure 7). On pure Mo<sub>2</sub>C(101), O prefers the t2 (Mo<sub>A</sub>) site with an adsorption energy of –3.20 eV. Similarly, O also prefers the t2 (Mo<sub>A</sub>') site on 4M–Mo<sub>2</sub>C(101) with adsorption energies close to that on the pure surface. On 8M–Mo<sub>2</sub>C(101), however, O prefers the t1 (C<sub>A</sub>') site with adsorption energies of –2.79, –2.94, –2.84, –2.58, –2.87, and –2.83 eV for M = Fe, Co, Ni, Cu, Pd, and Pt, respectively. The t4 (Mo<sub>B</sub>') site is the second most stable site with adsorption energies of –2.44, –2.49, –2.54, –2.35, –2.52, and –2.53 eV for M = Fe, Co, Ni, Cu, Pd, and Pt, respectively. It is also noted that O adsorption at the t2 (M) site has a very low or even positive adsorption energy and therefore not favored. It shows that metal doping can lower the adsorption energy to a large extent on the 8M–Mo<sub>2</sub>C(101) surfaces by about 10–20%, and this might affect the reactions associated with surface O.

On the basis of these most stable adsorption sites of H<sub>2</sub>O, OH, O, and H, we explored H<sub>2</sub>O sequential dissociation on these surfaces. The barriers, reaction energies, and breaking bond distances are listed in Table 2, and the adsorption structures of the IS, TS, and FS are summarized in Figures S9 and S10. The simplified potential energy surfaces are shown in Scheme 1.

On the pure Mo<sub>2</sub>C(101) and 4M–Mo<sub>2</sub>C(101) surfaces, the adsorption configurations of the first H<sub>2</sub>O dissociation step (H<sub>2</sub>O → OH + H) are very similar since they start at the Mo<sub>A</sub> or Mo<sub>A</sub>' sites, and the potential energy surfaces are also very similar (Scheme 1a, left). Compared to the pure Mo<sub>2</sub>C(101) surface (0.23 and –0.94 eV), the dissociation barrier becomes higher, while the dissociation energy becomes less exothermic, and the largest change has been found for Pt doping (0.36 and –0.62 eV). In addition, the corresponding transition states also have similar breaking O–H distances (Table 2).

For the second dissociation step (OH + H → O + 2H), their configurations in IS, TS, and FS are also similar on both pure and 4M–Mo<sub>2</sub>C(101) surfaces (Figure S10) but vary in H atom migration. After the first dissociation step, the H atom migrates to the more stable remote site (C<sub>A</sub> or C<sub>A</sub>') which is also the most stable adsorption site for the pure single H atom (Figure 4). Compared to the pure Mo<sub>2</sub>C(101) surface (0.72

and –0.30 eV), the dissociation barrier increases slightly (0.81 eV for Pd and Pt) and the dissociation energy becomes slightly more exothermic (–0.40 eV for Cu and Co). In addition, the corresponding transition states have similar breaking O–H distances (Table 2).

On the 8M–Mo<sub>2</sub>C(101) surface, where all Mo<sub>A</sub> atoms are replaced with doping metal atoms, H<sub>2</sub>O adsorbs at the t4 (Mo<sub>B</sub>') sites (Figure S9). The adsorption configuration of the first H<sub>2</sub>O dissociation step (H<sub>2</sub>O → OH + H) is similar compared to pure and 4M–Mo<sub>2</sub>C(101) but with different orientation for O–H bond breaking. As shown in Scheme 1b (right), H<sub>2</sub>O has not only lower adsorption energy but also a much lower barrier for the first-step H<sub>2</sub>O dissociation (H<sub>2</sub>O → OH + H), as compared to the 4M–Mo<sub>2</sub>C(101) and pure Mo<sub>2</sub>C surfaces. In addition, the first dissociation step on 8M–Mo<sub>2</sub>C(101) is also much less exothermic than that on the 4M–Mo<sub>2</sub>C(101) and pure Mo<sub>2</sub>C surfaces. Compared to the 4M–Mo<sub>2</sub>C(101) surface, the barrier of the second dissociation step (OH + H → O + 2H) is lower for M = Fe, Co, Ni, and Cu but higher for M = Pd and Pt, while the reaction is more exothermic.

In addition to the individual steps, the general trend of H<sub>2</sub>O dissociative adsorption over 4M- and 8M-doped surfaces in comparison with the pure surface can be seen in Scheme 1. Due to the similar or same adsorption site of the 4M-doped surface (Mo<sub>A</sub>' vs Mo<sub>A</sub>) and the pure surface (Scheme 1, left), the same trend has been found, that is, the first H<sub>2</sub>O dissociation step has a barrier lower than the H<sub>2</sub>O adsorption energy and the dissociation is very exothermic, indicating that dissociation is more preferred than desorption. Next, the second dissociation step has a higher barrier and is less exothermic than the first dissociation step. Compared to the pure surface, the total reaction on the 4M-doped surface is more exothermic, indicating the enhanced thermodynamic trend. This shows that the 4M-doped surface can bind surface intermediates more strongly than the pure surface. On the 8M-doped surface with Mo<sub>B</sub>' as the favored adsorption site, the first H<sub>2</sub>O dissociation step also has a barrier lower than the H<sub>2</sub>O adsorption energy, and the dissociation is very exothermic, indicating that dissociation is more preferred than desorption, and the dissociation is less exothermic than that on the pure surface. All these changes are to a lesser extent than those on the corresponding 4M-doped surfaces. Different



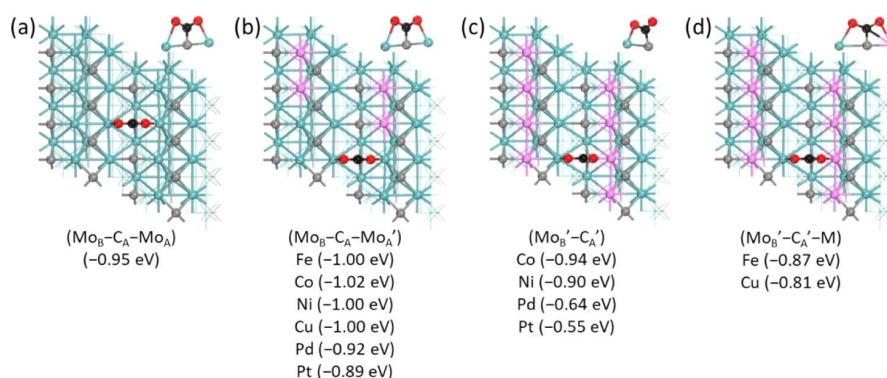


**Figure 8.** Most stable adsorption configurations and energies (in parentheses) of CO<sub>2</sub> on (a) pure Mo<sub>2</sub>C(101), (b) 4M-Mo<sub>2</sub>C(101), and (c,d) 8M-Mo<sub>2</sub>C(101) (M = Fe, Co, Ni, Cu, Pd, and Pt; O: red, C in CO<sub>2</sub>: black, C in Mo<sub>2</sub>C: gray, Mo: cyan, M: pink).

from the 4M-doped surface, the transition state of the second dissociation step is higher in energy for M = Cu and Pd and lower in energy for M = Fe, Co, Ni, and Pt than that of the first dissociation step, indicating that surface OH can be a stable intermediate for M = Cu and Pd. Next, the second dissociation step has a higher barrier than the first dissociation step, and the reaction energy is close to the first dissociation step. Compared to the pure surface, the total reaction on the 8M-doped surface is less exothermic apart from M = Co, indicating the doping metal dependence.

**CO<sub>2</sub> Dissociative Adsorption.** The adsorption of CO<sub>2</sub> on the pure and metal doping surfaces is computed, and the most stable adsorption configurations are listed in Figure 8, while the less stable configurations and energies are listed in Figure S11.

On pure Mo<sub>2</sub>C(101), the most stable adsorption configuration of CO<sub>2</sub> has a tridentate mode, in which the C atom interacts with surface C<sub>A</sub> and the O atoms interact with surface Mo<sub>A</sub> and Mo<sub>B</sub>, and the adsorption energy is -0.95 eV, followed by that at the b1 (Mo<sub>A</sub>-Mo<sub>A</sub>) site (Figure S11, -0.90 eV), and the b3 (Mo<sub>B</sub>-Mo<sub>B</sub>) site has a positive adsorption energy (Figure S11, 0.45 eV). On the 4M-Mo<sub>2</sub>C(101) surface (Figure 8b), the most stable CO<sub>2</sub> adsorption has the same configuration and similar energy as on the pure surface, while CO<sub>2</sub> adsorption at the Mo<sub>B</sub>-C<sub>A</sub>'-M site is less stable (Figure S11). In addition, CO<sub>2</sub> adsorption at other bridge sites also becomes less stable or has a positive adsorption energy. On 8M-Mo<sub>2</sub>C(101), the most stable CO<sub>2</sub> adsorption has a bidentate mode for M = Co, Ni, Pd, and Pt, in which the C atom interacts with surface C<sub>A</sub>' and one O atom interacts with Mo<sub>B</sub>' and another O atom does not interact with the doping atom, and a tridentate mode for M = Fe and Cu; also, the adsorption energies are lower than those on 4M-Mo<sub>2</sub>C(101). Besides, their corresponding C-O stretching frequencies are also calculated (Table S2). The stretching frequencies are similar between the 4M-Mo<sub>2</sub>C(101) and pure Mo<sub>2</sub>C(101) surfaces due to their similar adsorption configurations. On the 8M-Mo<sub>2</sub>C(101) surfaces, significant differences in C-O stretching frequencies between the bidentate modes (Fe and Cu) compared to tridentate (Co, Ni, Pd, and Pt) adsorption configurations are found.

On the basis of the most stable adsorption configurations of CO<sub>2</sub>, CO (Figure 2), and O (Figure 7), we computed CO<sub>2</sub> dissociation on these surfaces. The barriers, reaction energies, and breaking C-O bond distances are listed in Table 3, and the adsorption structures of the IS, TS, and FS are given in

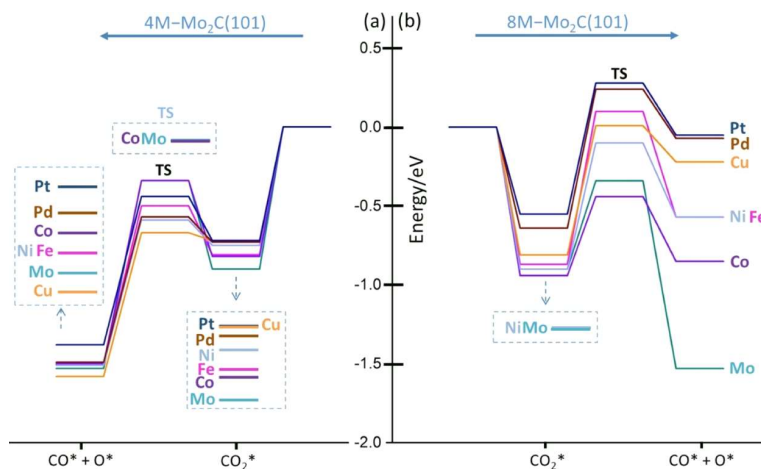
Figure S12. The simplified potential energy surfaces are shown in Scheme 2.

**Table 3.** Dissociation Barrier ( $E_a$ , eV), Reaction Energy ( $\Delta E_r$ , eV), and Critical C-O Distance ( $d$ , Å) in the Transition State

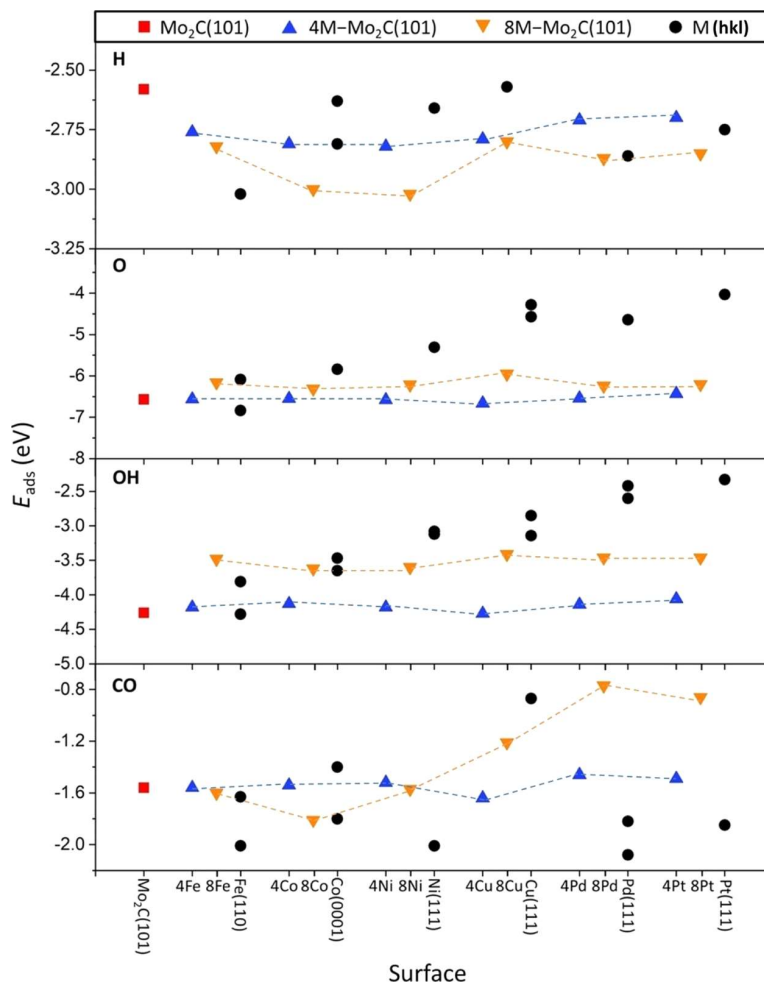
surfaces	CO <sub>2</sub> → TS → CO + O		
	$E_a$	$\Delta E_r$	$d$ (TS)
Mo <sub>2</sub> C(101)	0.56	-0.63	1.602
4Fe-Mo <sub>2</sub> C(101)	0.31	-0.70	1.640
4Co-Mo <sub>2</sub> C(101)	0.48	-0.68	1.648
4Ni-Mo <sub>2</sub> C(101)	0.16	-0.76	1.660
4Cu-Mo <sub>2</sub> C(101)	0.05	-0.86	1.665
4Pd-Mo <sub>2</sub> C(101)	0.16	-0.76	1.661
4Pt-Mo <sub>2</sub> C(101)	0.28	-0.66	1.660
8Fe-Mo <sub>2</sub> C(101)	0.97	0.30	1.917
8Co-Mo <sub>2</sub> C(101)	0.50	0.09	1.620
8Ni-Mo <sub>2</sub> C(101)	0.80	0.33	1.717
8Cu-Mo <sub>2</sub> C(101)	0.82	0.56	1.652
8Pd-Mo <sub>2</sub> C(101)	0.88	0.57	1.700
8Pt-Mo <sub>2</sub> C(101)	0.83	0.50	1.694

On the pure surface, CO<sub>2</sub> dissociation has a barrier (0.56 eV) lower than the adsorption energy (-0.95 eV) and is exothermic (-0.63 eV), and the same trend is found on 4M-Mo<sub>2</sub>C(101) with a lower barrier and the dissociation is more exothermic, indicating that the doping metal can promote CO<sub>2</sub> dissociation, although it does not participate in CO<sub>2</sub> dissociation directly. On 8M-Mo<sub>2</sub>C(101), totally different results have been found, that is, CO<sub>2</sub> dissociation becomes endothermic compared to that on the pure and 4M-doped surfaces, indicating the doping effect. In addition to these individual values, the general trend can be seen in Scheme 2. It shows that on pure and 4M-doped surfaces, CO<sub>2</sub> dissociation barriers are lower than their adsorption energy, indicating that dissociation is favored over desorption. In addition, the dissociated state is in close energy to that on the pure surface for M = Fe, Co, Ni, and Pd but less stable for M = Pt and more stable for M = Cu. On 8M-Mo<sub>2</sub>C(101), the CO<sub>2</sub> dissociation barrier is higher than the adsorption energy for M = Fe, Pd, and Pt, close to that of Cu, and lower than that for M = Ni and Co. This indicates that at an elevated temperature, CO<sub>2</sub> desorption is more preferred than dissociation for M = Fe, Pd, and Pt, while molecular and dissociative adsorption might have equilibrium for M = Ni, Cu, and Co.

Scheme 2. Potential Energy Surface of CO<sub>2</sub> Dissociative Adsorption on (a) 4M–Mo<sub>2</sub>C(101), Left, and (b) 8M–Mo<sub>2</sub>C(101), Right (M = Mo, Fe, Co, Ni, Cu, Pd, and Pt; the Magnified Surface in the Dash Line Square)



Scheme 3. Comparative Adsorption Energies of CO, OH, O, and H on Mo<sub>2</sub>C(101), 4M–Mo<sub>2</sub>C(101), and 8M–Mo<sub>2</sub>C(101) and the Corresponding Metallic Low-Index Surfaces (M = Fe, Co, Ni, Cu, Pd, and Pt)



Since both metals and supports play decisive and unique roles in heterogeneous catalysis, we compared the adsorption properties of surface CO, OH, O, and H species, which are intermediates of many catalytic reactions, on the pure and

metal-doped Mo<sub>2</sub>C(101) surfaces as well as on the corresponding metallic low-index Fe(110),<sup>43–47</sup> Co(0001),<sup>43,48–50</sup> Ni(111),<sup>43,51–54</sup> Cu(111),<sup>43,54–56</sup> Pd(111),<sup>43,54,57,58</sup> and Pt(111)<sup>43,54,59–61</sup> surfaces. For making

as close comparison as possible, we compiled all these reported data using the same or nearly the same methodology despite their different adsorption sites and configurations (Table S3); and the general trend is shown in Scheme 3.

For CO adsorption, the adsorption energy on the pure and 4M-doped  $\text{Mo}_2\text{C}(101)$  surfaces varies only slightly but strongly on the 8M-doped  $\text{Mo}_2\text{C}(101)$  surfaces. The CO adsorption energies on these surfaces are lower than that of the metallic low-index surfaces apart from  $\text{Cu}(111)$ , which has lower adsorption than the pure M-doped  $\text{Mo}_2\text{C}(101)$  surfaces. For the adsorption of surface OH and O species, the adsorption energies on the pure and 4M-doped  $\text{Mo}_2\text{C}(101)$  surfaces are more or less the same but stronger than those on the 8M-doped  $\text{Mo}_2\text{C}(101)$  surfaces, and all these adsorption energies are stronger than those on the metallic low-index surfaces. For the adsorption of atomic hydrogen, the adsorption energies on the 4M- and 8M-doped surfaces are stronger than that on the pure surface, and the 8M-doped surfaces have stronger adsorption energies than the 4M-doped surface apart from 4Cu- and 8Cu-doped surfaces which have nearly the same adsorption energies. Compared to the pure and M-doped  $\text{Mo}_2\text{C}(101)$  surfaces,  $\text{Fe}(110)$  has stronger adsorption energy, while  $\text{Co}(0001)$ ,  $\text{Ni}(111)$ , and  $\text{Cu}(111)$  have weaker adsorption energies. Pd(111)- and 8Pd-doped surfaces have similar adsorption energies, and Pt(111) has adsorption energy between 4Pt- and 8Pt-doped surfaces. All these show their similarity and differences in adsorption, which should also be reflected in their catalytic kinetics and thermodynamics.

## CONCLUSIONS

Experimentally, supported transition-metal catalysts in heterogeneous catalysis show different activity from only metals and pure supports due to their enhanced mutual and synergistic interaction. To understand these effects, we computed transition-metal doping on the hexagonal  $\text{Mo}_2\text{C}(101)$  surface by substituting the less coordinated and more active surface  $\text{Mo}_\text{A}$  atoms with Fe, Co, Ni, Cu, Pd, and Pt in 4M (25%) and 8M (50%) metal loading.

It is found that metal doping affects the surface electronic properties based on the analysis of PDOS and creates more adsorption sites by changing the coordination environment for surface metal and carbons atoms. Strong electron transfer from the metal to the surface has been found for Fe, Co, Ni, and Cu, resulting in a positive Bader charge on the doping metal, and this agrees with the experimentally observed effect for Cu-doped  $\text{Mo}_2\text{C}$ . On the contrary, much less electron transfer from Pd to the surface or from the surface to Pt has been found. Consequently, not only surface metal atoms but also surface carbon atoms become active in adsorption of surface species.

On the pure and 4M (25%)-doped surfaces, surface  $\text{Mo}_\text{A}$  atoms are most preferred sites for the adsorption of  $\text{H}_2$ ,  $\text{H}_2\text{O}$ , OH, and O, and surface carbon ( $\text{C}_\text{A}$ ) atoms are responsible for the adsorption of H atoms, while surface  $\text{Mo}_\text{A}$  and  $\text{C}_\text{A}$  are co-responsible for the adsorption of CO and  $\text{CO}_2$ . On the 8M (50%)-doped surfaces, the less active surface  $\text{Mo}_\text{B}$  and surface  $\text{C}_\text{B}$  become active for the adsorption of CO and  $\text{CO}_2$ , and the adsorption energy depends on the doping metals. It is also found that molecular  $\text{H}_2$  has physisorption preferring the top of the doping metal, while atomic H prefers the top of the surface  $\text{C}_\text{A}$  atom forming the C–H bond. The adsorption of  $\text{H}_2\text{O}$  and OH prefers the top and bridge sites, respectively,

while atomic O prefers the top site of the surface  $\text{C}_\text{A}$  atom forming the C–O bond. Depending on doping metals and adsorption sites, the adsorption of each surface species can become more or less exothermic compared to the pure surface.

On the basis of these results, we explored the dissociative adsorption of  $\text{H}_2\text{O}$  and  $\text{CO}_2$  and found potential energy surfaces depending on the metal and loading. Full  $\text{H}_2\text{O}$  dissociative adsorption is favored thermodynamically on the 4M-doped surfaces and more exothermic compared to that on the pure surface but less exothermic and doping-metal-dependent on the 8M-doped surfaces apart from Co.  $\text{CO}_2$  dissociative adsorption is thermodynamically favored on the 4M-doped surfaces but becomes endothermic on the 8M-doped surface, preferring molecular instead of dissociative adsorption for Co, Ni, Cu, Pd, and Pt as well as equilibrium between molecular and dissociative adsorption for Co. Comparing the adsorption of CO, OH, O, and H on the pure and doped  $\text{Mo}_2\text{C}(101)$  surfaces and the corresponding metallic M(*hkl*) surfaces reveals their similarity and difference, and these should also be found in the reaction kinetics and thermodynamics. These results provide a basis for studying the mechanisms of reactions involving these surface species, for example, the reported promotion effect in water-gas reaction, methanol reforming, and evolution reaction of hydrogen and oxygen.

## ASSOCIATED CONTENT

### Supporting Information

The Supporting Information is available free of charge at <https://pubs.acs.org/doi/10.1021/acs.jpcc.1c03372>.

PDOS; adsorption configurations and energies; energy barriers and structural parameters of IS, TS, and FS involved in  $\text{H}_2\text{O}$  and  $\text{CO}_2$  dissociation; stretching frequency of CO; and bond distance (PDF)

## AUTHOR INFORMATION

### Corresponding Author

Haijun Jiao – Leibniz-Institut für Katalyse e.V. an der Universität Rostock, Rostock 18059, Germany; [orcid.org/0000-0002-2947-5937](https://orcid.org/0000-0002-2947-5937); Email: [haiju.jiao@catalysis.de](mailto:haiju.jiao@catalysis.de)

### Authors

Fan Wang – Leibniz-Institut für Katalyse e.V. an der Universität Rostock, Rostock 18059, Germany

Xinxin Tian – Leibniz-Institut für Katalyse e.V. an der Universität Rostock, Rostock 18059, Germany; Institute of Molecular Science, Key Laboratory of Materials for Energy Conversion and Storage of Shanxi Province, Shanxi University, Taiyuan 030006, China

Complete contact information is available at: <https://pubs.acs.org/doi/10.1021/acs.jpcc.1c03372>

### Notes

The authors declare no competing financial interest.

## ACKNOWLEDGMENTS

F.W. thanks the support of the China Scholarship Council (CSC), and X.T. thanks the financial support from the National Natural Science Foundation of China (no. 21903049). The general financial support from the BMBF and the state of Mecklenburg–Vorpommern, Germany, is acknowledged.



## REFERENCES

- (1) Valden, M.; Lai, X.; Goodman, D. W. Onset of Catalytic Activity of Gold Clusters on Titania with the Appearance of Nonmetallic Properties. *science* **1998**, *281*, 1647–1650.
- (2) Navlani-García, M.; Salinas-Torres, D.; Mori, K.; Kuwahara, Y.; Yamashita, H. Tailoring the Size and Shape of Colloidal Noble Metal Nanocrystals as a Valuable Tool in Catalysis. *Catal. Surv. Asia* **2019**, *23*, 127–148.
- (3) Ruditskiy, A.; Peng, H.-C.; Xia, Y. Shape-Controlled Metal Nanocrystals for Heterogeneous Catalysis. *Annu. Rev. Chem. Biomol. Eng.* **2016**, *7*, 327–348.
- (4) Lane, M. K. M.; Zimmerman, J. B. Controlling Metal Oxide Nanoparticle Size and Shape with Supercritical Fluid Synthesis. *Green Chem.* **2019**, *21*, 3769–3781.
- (5) Cao, A.; Lu, R.; Vesper, G. Stabilizing Metal Nanoparticles for Heterogeneous Catalysis. *Phys. Chem. Chem. Phys.* **2010**, *12*, 13499–13510.
- (6) De Rogatis, L.; Cargnello, M.; Gombac, V.; Lorenzuti, B.; Montini, T.; Fornasiero, P. Embedded Phases: A Way to Active and Stable Catalysts. *ChemSusChem* **2010**, *3*, 24–42.
- (7) dos Santos Politi, J. R.; Viñes, F.; Rodríguez, J. A.; Illas, F. Atomic and Electronic Structure of Molybdenum Carbide Phases: Bulk and Low Miller-Index Surfaces. *Phys. Chem. Chem. Phys.* **2013**, *15*, 12617–12625.
- (8) Széchenyi, A.; Solymosi, F. Production of Hydrogen in the Decomposition of Ethanol and Methanol over Unsupported Mo<sub>2</sub>C Catalysts. *J. Phys. Chem. C* **2007**, *111*, 9509–9515.
- (9) Barthos, R.; Széchenyi, A.; Solymosi, F. Efficient H<sub>2</sub> Production from Ethanol over Mo<sub>2</sub>C/C Nanotube Catalyst. *Catal. Lett.* **2008**, *120*, 161–165.
- (10) Ma, Y.; Guan, G.; Shi, C.; Zhu, A.; Hao, X.; Wang, Z.; Kusakabe, K.; Abudula, A. Low-Temperature Steam Reforming of Methanol to Produce Hydrogen over Various Metal-Doped Molybdenum Carbide Catalysts. *Int. J. Hydrogen Energy* **2014**, *39*, 258–266.
- (11) Ma, Y.; Guan, G.; Hao, X.; Zuo, Z.; Huang, W.; Phanthong, P.; Kusakabe, K.; Abudula, A. Highly-Efficient Steam Reforming of Methanol over Copper Modified Molybdenum Carbide. *RSC Adv.* **2014**, *4*, 44175–44184.
- (12) Ma, Y.; Guan, G.; Hao, X.; Zuo, Z.; Huang, W.; Phanthong, P.; Li, X.; Kusakabe, K.; Abudula, A. Embedded Structure Catalyst: A New Perspective from Noble Metal Supported on Molybdenum Carbide. *RSC Adv.* **2015**, *5*, 15002–15005.
- (13) Wan, C.; Leonard, B. M. Iron-Doped Molybdenum Carbide Catalyst with High Activity and Stability for the Hydrogen Evolution Reaction. *Chem. Mater.* **2015**, *27*, 4281–4288.
- (14) Liu, Y.; Ding, J.; Bi, J.; Sun, Y.; Zhang, J.; Liu, K.; Kong, F.; Xiao, H.; Chen, J. Effect of Cu-Doping on the Structure and Performance of Molybdenum Carbide Catalyst for Low-Temperature Hydrogenation of Dimethyl Oxalate to Ethanol. *Appl. Catal., A* **2017**, *529*, 143–155.
- (15) Liu, P.; Rodríguez, J. A. Water-Gas-Shift Reaction on Molybdenum Carbide Surfaces: Essential Role of the Oxycarbide. *J. Phys. Chem. B* **2006**, *110*, 19418–19425.
- (16) Shi, Y.; Yang, Y.; Li, Y.-W.; Jiao, H. Activation Mechanisms of H<sub>2</sub>, O<sub>2</sub>, H<sub>2</sub>O, CO<sub>2</sub>, CO, CH<sub>4</sub> and C<sub>2</sub>H<sub>4</sub> on Metallic Mo<sub>2</sub>C(001) as Well as Mo/C Terminated Mo<sub>2</sub>C(101) from Density Functional Theory Computations. *Appl. Catal., A* **2016**, *524*, 223–236.
- (17) Wang, F.; Li, T.; Jiao, H. Nitridation of the Metallic Mo<sub>2</sub>C(001) Surface from NH<sub>3</sub> Dissociative Adsorption—a Dft Study. *Surf. Sci.* **2019**, *689*, 121466.
- (18) Krashennikov, A. V.; Lehtinen, P. O.; Foster, A. S.; Pyykkö, P.; Nieminen, R. M. Embedding Transition-Metal Atoms in Graphene: Structure, Bonding, and Magnetism. *Phys. Rev. Lett.* **2009**, *102*, 126807.
- (19) Zhou, M.; Cheng, L.; Choi, J.-S.; Liu, B.; Curtiss, L. A.; Assary, R. S. Ni-Doping Effects on Oxygen Removal from an Orthorhombic Mo<sub>2</sub>C(001) Surface: A Density Functional Theory Study. *J. Phys. Chem. C* **2018**, *122*, 1595–1603.
- (20) Chen, Y.-Y.; Dong, M.; Wang, J.; Jiao, H. Mechanisms and Energies of Water Gas Shift Reaction on Fe-, Co-, and Ni-Promoted MoS<sub>2</sub> Catalysts. *J. Phys. Chem. C* **2012**, *116*, 25368–25375.
- (21) Wang, T.; Liu, X.; Wang, S.; Huo, C.; Li, Y.-W.; Wang, J.; Jiao, H. Stability of  $\beta$ -Mo<sub>2</sub>C Facets from Ab Initio Atomistic Thermodynamics. *J. Phys. Chem. C* **2011**, *115*, 22360–22368.
- (22) Haines, J.; Léger, J. M.; Chateau, C.; Lowther, J. E. Experimental and Theoretical Investigation of Mo<sub>2</sub>C at High Pressure. *J. Phys.: Condens. Matter* **2001**, *13*, 2447–2454.
- (23) Wang, X.-H.; Hao, H.-L.; Zhang, M.-H.; Li, W.; Tao, K.-Y. Synthesis and Characterization of Molybdenum Carbides Using Propane as Carbon Source. *J. Solid State Chem.* **2006**, *179*, 538–543.
- (24) Kresse, G.; Furthmüller, J. Efficiency of Ab-Initio Total Energy Calculations for Metals and Semiconductors Using a Plane-Wave Basis Set. *Comput. Mater. Sci.* **1996**, *6*, 15–50.
- (25) Kresse, G.; Furthmüller, J. Efficient Iterative Schemes for Ab Initio Total-Energy Calculations Using a Plane-Wave Basis Set. *Phys. Rev. B: Condens. Matter Mater. Phys.* **1996**, *54*, 11169–11186.
- (26) Blöchl, P. E. Projector Augmented-Wave Method. *Phys. Rev. B: Condens. Matter Mater. Phys.* **1994**, *50*, 17953–17979.
- (27) Perdew, J. P.; Burke, K.; Ernzerhof, M. Generalized Gradient Approximation Made Simple. *Phys. Rev. Lett.* **1996**, *77*, 3865–3868.
- (28) Henkelman, G.; Uberuaga, B. P.; Jónsson, H. A Climbing Image Nudged Elastic Band Method for Finding Saddle Points and Minimum Energy Paths. *J. Chem. Phys.* **2000**, *113*, 9901–9904.
- (29) Wang, T.; Li, Y.-W.; Wang, J.; Beller, M.; Jiao, H. Dissociative Hydrogen Adsorption on the Hexagonal Mo<sub>2</sub>C Phase at High Coverage. *J. Phys. Chem. C* **2014**, *118*, 8079–8089.
- (30) CHRISTENSEN, A. N.; Kvande, H.; Wahlbeck, P. G.; Näsäkkälä, E. A Neutron Diffraction Investigation on a Crystal of  $\alpha$ -Mo<sub>2</sub>C. *Acta Chem. Scand., Ser. A* **1977**, *31*, 509–511.
- (31) Dubois, J.; Epicier, T.; Esnouf, C.; Fantozzi, G.; Convert, P. Neutron Powder Diffraction Studies of Transition Metal Hemiacarbides M<sub>2</sub>C<sub>1-x</sub>—I. Motivation for a Study on W<sub>2</sub>C and Mo<sub>2</sub>C and Experimental Background for an in Situ Investigation at Elevated Temperature. *Acta Metall.* **1988**, *36*, 1891–1901.
- (32) Epicier, T.; Dubois, J.; Esnouf, C.; Fantozzi, G.; Convert, P. Neutron Powder Diffraction Studies of Transition Metal Hemiacarbides M<sub>2</sub>C<sub>1-x</sub>—II. In Situ High Temperature Study on W<sub>2</sub>C<sub>1-x</sub> and Mo<sub>2</sub>C<sub>1-x</sub>. *Acta Metall.* **1988**, *36*, 1903–1921.
- (33) Shi, Y.; Yang, Y.; Li, Y.-W.; Jiao, H. Theoretical Study About Mo<sub>2</sub>C(101)-Catalyzed Hydrodeoxygenation of Butyric Acid to Butane for Biomass Conversion. *Catal. Sci. Technol.* **2016**, *6*, 4923–4936.
- (34) Fries, R. J.; Kemper, C. P. 195. Dimolybdenum Carbide. *Anal. Chem.* **1960**, *32*, 1898.
- (35) Miyao, T.; Shishikura, I.; Matsuoka, M.; Nagai, M.; Oyama, S. T. Preparation and Characterization of Alumina-Supported Molybdenum Carbide. *Appl. Catal., A* **1997**, *165*, 419–428.
- (36) Wang, T.; Li, Y.-W.; Wang, J.; Beller, M.; Jiao, H. High Coverage Co Adsorption and Dissociation on the Orthorhombic Mo<sub>2</sub>C(100) Surface. *J. Phys. Chem. C* **2014**, *118*, 3162–3171.
- (37) Wang, T.; Wang, S.; Li, Y.-W.; Wang, J.; Jiao, H. Adsorption Equilibria of Co Coverage on  $\beta$ -Mo<sub>2</sub>C Surfaces. *J. Phys. Chem. C* **2012**, *116*, 6340–6348.
- (38) Wang, T.; Tian, X.; Yang, Y.; Li, Y.-W.; Wang, J.; Beller, M.; Jiao, H. Coverage Dependent Adsorption and Co-Adsorption of Co and H<sub>2</sub> on the CdI<sub>2</sub>-Antitype Metallic Mo<sub>2</sub>C(001) Surface. *Phys. Chem. Chem. Phys.* **2015**, *17*, 1907–1917.
- (39) Grimme, S. Semiempirical GGA-Type Density Functional Constructed with a Long-Range Dispersion Correction. *J. Comput. Chem.* **2006**, *27*, 1787–1799.
- (40) Hugosson, H. W.; Eriksson, O.; Jansson, U.; Johansson, B. Phase Stabilities and Homogeneity Ranges in 4d-Transition-Metal Carbides: A Theoretical Study. *Phys. Rev. B: Condens. Matter Mater. Phys.* **2001**, *63*, 134108.
- (41) Henkelman, G.; Arnaldsson, A.; Jónsson, H. A Fast and Robust Algorithm for Bader Decomposition of Charge Density. *Comput. Mater. Sci.* **2006**, *36*, 354–360.

- (42) Allen, L. C. Electronegativity Is the Average One-Electron Energy of the Valence-Shell Electrons in Ground-State Free Atoms. *J. Am. Chem. Soc.* **1989**, *111*, 9003–9014.
- (43) Abild-Pedersen, F.; Andersson, M. P. Co Adsorption Energies on Metals with Correction for High Coordination Adsorption Sites—a Density Functional Study. *Surf. Sci.* **2007**, *601*, 1747–1753.
- (44) Xu, L.; Kirvassilis, D.; Bai, Y.; Mavrikakis, M. Atomic and Molecular Adsorption on Fe(110). *Surf. Sci.* **2018**, *667*, 54–65.
- (45) Liu, S.; Li, Y.-W.; Wang, J.; Jiao, H. Reactions of CO, H<sub>2</sub>O, CO<sub>2</sub>, and H<sub>2</sub> on the Clean and Precovered Fe(110) Surfaces—a Dft Investigation. *J. Phys. Chem. C* **2015**, *119*, 28377–28388.
- (46) Chakrabarty, A.; Bouhali, O.; Mousseau, N.; Becquart, C. S.; El-Mellouhi, F. Insights on Finite Size Effects in Ab Initio Study of Co Adsorption and Dissociation on Fe 110 Surface. *J. Appl. Phys.* **2016**, *120*, 055301.
- (47) Liu, S.; Tian, X.; Wang, T.; Wen, X.; Li, Y.-W.; Wang, J.; Jiao, H. Coverage Dependent Water Dissociative Adsorption on Fe(110) from Dft Computation. *Phys. Chem. Chem. Phys.* **2015**, *17*, 8811–8821.
- (48) Luo, W.; Asthagiri, A. Density Functional Theory Study of Methanol Steam Reforming on Co(0001) and Co(111) Surfaces. *J. Phys. Chem. C* **2014**, *118*, 15274–15285.
- (49) Ma, Y.; Hernández, L.; Guadarrama-Pérez, C.; Balbuena, P. B. Ethanol Reforming on Co(0001) Surfaces: A Density Functional Theory Study. *J. Phys. Chem. A* **2012**, *116*, 1409–1416.
- (50) Gunasooriya, G. T. K. K.; van Bavel, A. P.; Kuipers, H. P. C. E.; Saey, M. Co Adsorption on Cobalt: Prediction of Stable Surface Phases. *Surf. Sci.* **2015**, *642*, L6–L10.
- (51) Eichler, A. Co Adsorption on Ni(111)—a Density Functional Theory Study. *Surf. Sci.* **2003**, *526*, 332–340.
- (52) Zhu, L.; Liu, C.; Wen, X.; Li, Y.-W.; Jiao, H. Coverage-Dependent Water Dissociative Adsorption Properties on Nickel Surfaces. *J. Phys. Chem. C* **2020**, *124*, 25835–25845.
- (53) Mohsenzadeh, A.; Bolton, K.; Richards, T. Dft Study of the Adsorption and Dissociation of Water on Ni(111), Ni(110) and Ni(100) Surfaces. *Surf. Sci.* **2014**, *627*, 1–10.
- (54) Phatak, A. A.; Delgass, W. N.; Ribeiro, F. H.; Schneider, W. F. Density Functional Theory Comparison of Water Dissociation Steps on Cu, Au, Ni, Pd, and Pt. *J. Phys. Chem. C* **2009**, *113*, 7269–7276.
- (55) Wang, J.; Wang, G.-C. Promotion Effect of Methane Activation on Cu(111) by the Surface-Active Oxygen Species: A Combination of Dft and Reaxff Study. *J. Phys. Chem. C* **2018**, *122*, 17338–17346.
- (56) Jiang, Z.; Fang, T. Dissociation Mechanism of H<sub>2</sub>O on Clean and Oxygen-Covered Cu(111) Surfaces: A Theoretical Study. *Vacuum* **2016**, *128*, 252–258.
- (57) Martin, N. M.; Van den Bossche, M.; Grönbeck, H.; Hakanoglu, C.; Zhang, F.; Li, T.; Gustafson, J.; Weaver, J. F.; Lundgren, E. Co Adsorption on Clean and Oxidized Pd(111). *J. Phys. Chem. C* **2014**, *118*, 1118–1128.
- (58) Tian, P.; Ouyang, L.; Xu, X.; Xu, J.; Han, Y.-F. Density Functional Theory Study of Direct Synthesis of H<sub>2</sub>O<sub>2</sub> from H<sub>2</sub> and O<sub>2</sub> on Pd(111), Pd(100), and Pd(110) Surfaces. *Chin. J. Catal.* **2013**, *34*, 1002–1012.
- (59) Lakshmikanth, K. G.; Kundappaden, I.; Chatanathodi, R. A Dft Study of Co Adsorption on Pt(111) Using Van Der Waals Functionals. *Surf. Sci.* **2019**, *681*, 143–148.
- (60) Jinnouchi, R.; Kodama, K.; Morimoto, Y. Dft Calculations on H, Oh and O Adsorbate Formations on Pt(111) and Pt(332) Electrodes. *J. Electroanal. Chem.* **2014**, *716*, 31–44.
- (61) Offermans, W. K.; Jansen, A. P. J.; van Santen, R. A.; Novell-Leruth, G.; Ricart, J. M.; Pérez-Ramírez, J. Ammonia Dissociation on Pt{100}, Pt{111}, and Pt{211}: A Comparative Density Functional Theory Study. *J. Phys. Chem. C* **2007**, *111*, 17551–17557.

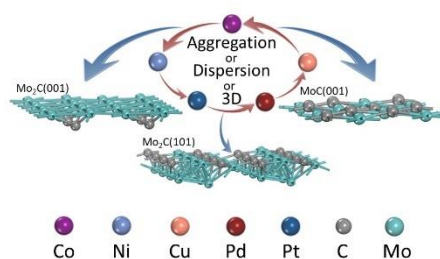
### 3.2 Molybdenum Carbide Supported Metal Catalysts ( $M_n/\text{Mo}_x\text{C}$ ; $M = \text{Co, Ni, Cu, Pd, Pt}$ ) – Metal and Surface Dependent Structure and Stability

Fan Wang, Teng Li, Yun Shi, Haijun Jiao\*

*Catal. Sci. Technol.* **2020**, *10*, 3029–3046.

DOI: 10.1039/d0cy00504e

**Summary:** The surface and metal-dependent morphologies and energies of molybdenum carbide supported metal catalysts ( $M_n/\text{Mo}_x\text{C}$ ;  $M = \text{Co, Ni, Cu, Pd, Pt}$ ) have been systematically investigated on the basis of periodic density functional theory computations. On all three surfaces, hexagonal  $\text{Mo}_2\text{C}(001)$  and  $\text{Mo}_2\text{C}(101)$  as well as cubic  $\text{MoC}(101)$ , the adsorption of these metals is favored thermodynamically. On the hexagonal  $\text{Mo}_2\text{C}$  phase, metallic  $\text{Mo}_2\text{C}(001)$  prefers dispersion at very low loading for Co and Ni, up to high loading for Pd and Pt, but only aggregation for Cu. On  $\text{Mo}/\text{C}$ -mixed  $\text{Mo}_2\text{C}(101)$ , all metals prefer dispersion up to high loading and aggregation with very high loading. On cubic  $\text{Mo}/\text{C}$ -mixed  $\delta\text{-MoC}(001)$ , all metals prefer aggregation up to high loading and three-dimensional clusters with very high loading. The electron transfer between the surface and the adsorbed metals has also been computed, while neither the adsorption energy nor the quantity of electron transfer correlates with the electronegativity of the atoms and their respective ionization potential or their electron affinity. Our study provides a basis of size-dependent supported catalysts with respect to single atoms, nanoclusters and nanoparticles for understanding the exceptional catalytic effect of specific metals and to provide insights into catalyst design in heterogeneous catalysis.



#### Author contributions

In this work I designed and performed most of the calculations and analyzed all the results. I completed writing and proofreading based on suggestions and comments of all co-authors. My scientific contribution as the first author of this paper is about 90%.

## PAPER

View Article Online

View Journal | View Issue

Cite this: *Catal. Sci. Technol.*, 2020,  
10, 3029Molybdenum carbide supported metal catalysts  
( $M_n/\text{Mo}_x\text{C}$ ;  $M = \text{Co}, \text{Ni}, \text{Cu}, \text{Pd}, \text{Pt}$ ) – metal and  
surface dependent structure and stability†Fan Wang,<sup>a</sup> Teng Li,<sup>b</sup> Yun Shi <sup>\*c</sup> and Haijun Jiao <sup>\*a</sup>

The surface and metal-dependent morphologies and energies of molybdenum carbide supported metal catalysts ( $M_n/\text{Mo}_x\text{C}$ ;  $M = \text{Co}, \text{Ni}, \text{Cu}, \text{Pd}, \text{Pt}$ ) have been systematically investigated on the basis of periodic density functional theory computations. On the hexagonal  $\text{Mo}_2\text{C}$  phase, metallic  $\text{Mo}_2\text{C}(001)$  prefers dispersion at very low loading for Co and Ni, up to high loading for Pd and Pt; but only aggregation for Cu. On  $\text{Mo}/\text{C}$ -mixed  $\text{Mo}_2\text{C}(101)$ , all metals prefer dispersion up to high loading and aggregation at very high loading. On cubic  $\text{Mo}/\text{C}$ -mixed  $\delta\text{-MoC}(001)$ , all metals prefer aggregation up to high loading and three-dimensional clusters at very high loading. On  $\text{Mo}_2\text{C}(001)$ , all adsorbed metals are negatively charged, while on  $\text{Mo}_2\text{C}(101)$  and  $\text{MoC}(001)$ , Co, Ni and Cu are positively charged, and Pt is negatively charged, while Pd is nearly neutral. On all three surfaces, the adsorption of these metals is favored thermodynamically. Although correlation between electron transfer and adsorption energy has been found, no correlations between the adsorption energy (and electron transfer) and electronegativity (and ionization potential and electron affinity) of the atoms can be estimated. These results provide a basis for the study and design of size- and shape-dependent (single-atom, nanocluster and nanoparticle) catalysts and their respective associated catalytic processes.

Received 12th March 2020,  
Accepted 9th April 2020

DOI: 10.1039/d0cy00504e

rsc.li/catalysis

## 1. Introduction

In heterogeneous catalysis, supported metal catalysts have found wide applications in the chemical industry and academia, and attracted growing interest in recent years due to their promising size- and shape-dependent (single-atom, nanocluster and nanoparticle) activity and selectivity in various chemical reactions.<sup>1</sup> In supported metal catalysts, not only the metals but also the supports play decisive roles in their catalytic behaviors and the most important aspect is their synergistic effect in creating novel and exciting chemistry. Among various supports, group IV–VI transition metal carbides (TMCs) are intriguing, not only because of their being stable supports but also because of their Pt-like behavior in various catalytic reactions<sup>2</sup> as well as their abundance and low cost.<sup>3–6</sup> This is why TMCs have been considered as potential alternatives to noble metals in many reactions, such as the water-gas shift (WGS) reaction,<sup>7</sup> hydrogen

evolution reaction (HER),<sup>8–11</sup> oxygen reduction reaction (ORR)<sup>12,13</sup> and methanol oxidation reaction.<sup>14</sup> As functionalized supports TMCs also have achieved significant breakthroughs, especially in low-temperature domains, including the WGS reaction,<sup>15–17</sup> hydrosulfurization,<sup>18,19</sup> CO oxidation<sup>20,21</sup> and  $\text{CO}_2$  hydrogenation.<sup>22–24</sup>

As an important member of TMCs, molybdenum carbides and metal doped molybdenum carbides have attracted special interest in supported metal catalysis. In 2004, Lee *et al.*<sup>25</sup> studied  $\text{MoO}_3$  direct conversion to molybdenum carbides using a temperature-programmed reaction in the presence of Co, Ni, Cu, Pd and Pt, and found that the supported metals can not only lower the  $\text{MoO}_3$  reduction temperature but also alter the phase and specific surface area of the carbides. With an increase in the amount of Cu from a Cu/Mo molar ratio of 1.6/98.4 to 25/75, Abudula *et al.*<sup>26</sup> found that the  $\alpha\text{-MoC}_{1-x}$  phase gradually disappeared and the  $\beta\text{-Mo}_2\text{C}$  phase was mainly formed. Besides, noble and base metal supported  $\text{Mo}_2\text{C}$  and  $\text{MoC}$  catalysts have also been widely reported. For example, Leclercq *et al.*<sup>27</sup> found that a catalyst of  $\text{Mo}_2\text{C}$  and 1 wt% dispersed Co exhibited better catalytic activity and a higher yield of heavy hydrocarbons than bulk  $\text{Mo}_2\text{C}$  in the Fischer–Tropsch synthesis. Schweitzer *et al.*<sup>17</sup> employed high surface area  $\text{Mo}_2\text{C}$  as a support for Pt nanoparticles ( $\text{Pt}/\text{Mo}_2\text{C}$ ) in the WGS reaction and found a higher reaction rate than for most active  $\text{Pt}/\text{CeO}_2$  and  $\text{Pt}/\text{TiO}_2$  catalysts. Moreover, Ribeiro<sup>16</sup>

<sup>a</sup> Leibniz-Institut für Katalyse e.V. an der Universität Rostock, Albert-Einstein-Str. 29a, 18059 Rostock, Germany. E-mail: haijun.jiao@catalysis.de

<sup>b</sup> State Key Laboratory of Coal Conversion, Institute of Coal Chemistry, Chinese Academy of Sciences, Taiyuan, 030001, China

<sup>c</sup> School of Chemistry & Chemical Engineering, Linyi University, Linyi 276000, China. E-mail: shiyun@lyu.edu.cn

† Electronic supplementary information (ESI) available. See DOI: 10.1039/d0cy00504e



reported that the WGS reaction rate for supported M/Mo<sub>2</sub>C (M = Pt, Au, Pd, Ni) catalysts was 4–8 times higher than that of a commercial Cu/ZnO/Al<sub>2</sub>O<sub>3</sub> catalyst. Most interestingly, Xu *et al.*<sup>28</sup> prepared a supported M/Mo<sub>2</sub>C (M = Co, Ni, Cu) catalyst for CO<sub>2</sub> hydrogenation and found that Cu/Mo<sub>2</sub>C displayed high selectivity in CO and methanol production, and that Ni/Mo<sub>2</sub>C and Co/Mo<sub>2</sub>C were most active for the activation and full conversion of CO<sub>2</sub> with high selectivity by Ni/Mo<sub>2</sub>C for methane and by Co/Mo<sub>2</sub>C for hydrocarbon C<sub>n</sub>H<sub>2n+2</sub> (*n* > 2). Posada-Pérez *et al.* investigated CO<sub>2</sub> conversion on bare β-Mo<sub>2</sub>C and Cu/β-Mo<sub>2</sub>C (ref. 29) as well as on Cu/δ-MoC and Au/δ-MoC (ref. 22) catalysts, and found that the supported metals improved methanol production. Moreover, the metal/carbon ratio governs the chemical behavior of the carbide and the properties of the supported metals, up to the point of being able to switch the rate and mechanism of CO<sub>2</sub> conversion. Ma *et al.* studied Pt/α-MoC (ref. 30) and Au/α-MoC (ref. 31) catalysts for methanol reforming and a low-temperature WGS reaction, and found that α-MoC exhibits stronger interaction with Pt and Au than common oxide supports or β-Mo<sub>2</sub>C, and Au and Pt prefer atomic dispersion over α-MoC and exhibit great catalytic performance. Most recently, Tong *et al.*<sup>32</sup> successfully synthesized an atomic scale Ni/β-Mo<sub>2</sub>C electrocatalyst that exhibited remarkable catalytic activity for HER at all pH values.

Computationally, Illas *et al.*<sup>33</sup> studied the interaction of Group 9, 10, and 11 (Co, Rh, Ir, Ni, Pd, Pt, Cu, Ag and Au) atoms with the (001) surface of δ-MoC, based on periodic density functional theory (DFT) calculations, and found that many of the supported admetals are electronically perturbed upon interaction with the carbide surface. By analyzing the adsorption energies and equilibrium geometries, work functions, atomic charges, projected density of states (PDOS) and shifts of the d-band center of Au, Cu and Ni atoms with the δ-MoC(001) surface,<sup>34</sup> they found that atomic adsorption can cause an in-plane distortion of the surface and the interaction strength turns out to be coverage dependent. By investigating the atomic structures and electronic properties of Cu<sub>n</sub> nanoclusters (*n* = 4, 6, 7, 10) supported on cubic non-polar δ-MoC(001) and orthorhombic C/Mo-terminated polar β-Mo<sub>2</sub>C(001) surfaces,<sup>35</sup> they found that the Cu adsorption prefers two-dimensional structures on β-Mo<sub>2</sub>C(001), but three-dimensional (3D) structures on δ-MoC(001), indicating that the Mo/C ratio and the surface polarity play a key role in determining the structure of the supported clusters. Tian *et al.* investigated the surface morphology of Cu<sub>n</sub> clusters on Fe(110) and Fe<sub>3</sub>C(001)<sup>36</sup> surfaces as well as the different terminations of the Hägg iron carbide (χ-Fe<sub>5</sub>C<sub>2</sub>) phase,<sup>37</sup> and found a thermodynamically favored adsorption mode of Cu<sub>n</sub> clusters on specific coverage. The computed results of Cu favoring either dispersion or mono-layer adsorption at low coverage are supported by a recent experimental investigation into the influence of a Cu promoter on the carburization of Fe-based precursors,<sup>38</sup> where the characteristic X-ray diffraction patterns of metallic Cu have not been identified, which indicates the dispersion of Cu on χ-Fe<sub>5</sub>C<sub>2</sub> surfaces. He

*et al.*<sup>39</sup> studied the surface morphology of Pt<sub>n</sub> clusters on Fe<sub>5</sub>C<sub>2</sub>(100) and Fe<sub>5</sub>C<sub>2</sub>(111) surfaces using *ab initio* molecular dynamics and found the collapse of the initial 3D structure of Pt<sub>12</sub> to the monolayer configurations.

All these studies show that different metal/Mo<sub>x</sub>C<sub>y</sub> systems exhibit large variations in activity and selectivity towards the corresponding catalytic transformations, and the interplay between metals and supports plays an irreplaceable role as the surface metals possess a novel coordination environment with special electronic properties, which may enhance the synergistic effect between metal and carbide. Inspired by all these results, we selected the hexagonal Mo<sub>2</sub>C(001) and Mo<sub>2</sub>C(101) as well as the cubic non-polar δ-MoC(001) surfaces to systematically study the interaction of Co, Ni, Cu, Pd and Pt metals with the surfaces to analyze the adsorption energies and equilibrium geometries from low to high metal loading. The aim of this work is to build a basis of size-dependent supported catalysts with respect to single atoms, nanoclusters and nanoparticles for understanding the exceptional catalytic effect of specific metals and to provide insights into catalyst design in heterogeneous catalysis.

## 2. Computational methods and models

### 2.1. Methods

All calculations were performed using the plane-wave based periodic DFT method implemented in the Vienna *ab initio* simulation package (VASP, version 5.3.5),<sup>40,41</sup> where the ionic cores are described by the projector augmented wave (PAW) method.<sup>42</sup> The exchange and correlation energies are computed using the Perdew, Burke and Ernzerhof functional (PBE).<sup>43</sup> To achieve accurate energies with errors of less than 1 meV per atom, the cutoff energy was set at 400 eV. The Gaussian electron smearing method with  $\sigma = 0.10$  eV was used. Geometric optimization converged until the forces acting on the atoms were smaller than 0.02 eV Å<sup>-1</sup>, whereas the energy threshold-defining self-consistency of the electron density was set to 10<sup>-4</sup> eV. Spin-polarization was included to obtain the energies of metal clusters in gas phase and adsorption systems, but it has no effect on the adsorption systems. For bulk optimization, the lattice parameters for the hexagonal Mo<sub>2</sub>C and cubic δ-MoC phases are determined by minimizing the total energy of the unit cell by using a conjugated gradient algorithm to relax the ions, and a 5 × 5 × 5 Monkhorst-Pack *k*-point grid<sup>44</sup> is used for sampling the Brillouin zone. To validate the PBE results, calculations with PBE including van der Waals dispersion with Becke-Jonson damping<sup>45,46</sup> (PBE+D3) and the RPBE functional on some selected M<sub>n</sub> clusters in the gas phase were carried out.

### 2.2. Models

Generally, Mo<sub>2</sub>C has orthorhombic<sup>47</sup> and hexagonal<sup>48,49</sup> crystalline phases. In this work, we used the hexagonal phase with an eclipsed configuration as the unit cell.<sup>50–53</sup> The



calculated lattice parameters of the unit cell are  $2a = 6.079 \text{ \AA}$ ,  $2b = 6.073 \text{ \AA}$  and  $c = 4.722 \text{ \AA}$ , in good agreement with the experimental values ( $a = b = 3.002 \text{ \AA}$ ,  $c = 4.724 \text{ \AA}$ ).<sup>54</sup> Among all the hexagonal  $\text{Mo}_2\text{C}$  surfaces, the (101) surface with ratio  $\text{Mo/C} = 1/1$  and surface energy of  $2.19 \text{ J m}^{-2}$  was reported to be the most stable,<sup>53,55–57</sup> and the metallic  $\text{Mo}_2\text{C}(001)$  surface was proved to be stable and representative with a surface energy of  $2.76 \text{ J m}^{-2}$  from theoretical<sup>57</sup> and experimental studies.<sup>56,58,59</sup> Hence, we used  $\text{Mo}_2\text{C}(101)$  and  $\text{Mo}_2\text{C}(001)$  to execute our study, and they were modeled by periodic slabs with  $p(2 \times 2)$  super cells having surface areas of  $12.2 \text{ \AA} \times 12.1 \text{ \AA}$  and  $15.4 \text{ \AA} \times 12.1 \text{ \AA}$ , respectively. For  $\text{Mo}_2\text{C}(101)$ , we applied a four-layer model with the top two layers relaxed and the bottom two layers fixed in their bulk positions. For  $\text{Mo}_2\text{C}(001)$ , we used a six-layer model with the top three layers relaxed and the bottom three layers fixed in their bulk positions. For the cubic  $\delta\text{-MoC}$  phase, the calculated lattice parameter of the unit cell is  $4.360 \text{ \AA}$ , in agreement with the experimental ( $4.278 \text{ \AA}$ )<sup>60</sup> and computational ( $4.444$  (ref. 61) and  $4.373 \text{ \AA}$  (ref. 62)) values. Since the  $\delta\text{-MoC}(001)$  surface is the most stable and is used in many studies,<sup>22,33–35</sup> we used this surface to carry out our study. The  $\delta\text{-MoC}(001)$  surface was modeled by a periodic slab with a  $p(2 \times 2)$  super cell having a surface area of  $8.72 \text{ \AA} \times 8.72 \text{ \AA}$ . We applied a four-layer model with the top two layers relaxed and the bottom two layers fixed in their bulk positions. The vacuum layer between the periodically repeated slabs was set at  $10 \text{ \AA}$  to avoid significant interactions between slabs. Dipole correction was applied to decouple the slabs and to avoid the effect of dipolar interaction on the total energy. Surface structural relaxation and total energy calculation were performed with  $3 \times 3 \times 1$  Monkhorst-Pack  $k$ -point sampling. For the relevant gas phase species, we used a cubic box with side length  $15 \text{ \AA}$  to calculate the structures and total energies.

Metallic  $\text{Mo}_2\text{C}(001)$  has sixteen surface Mo atoms and two top (**t1–t2**), four bridge (**b1–b4**) and four 3-fold hollow (**3h1–3h4**) adsorption sites (Fig. 1a). On **t1**, the  $\text{Mo}_\text{A}$  atom coordinates with two C atoms in the sublayer and has one dangling bond (saturated bulk Mo coordinating with three C atoms, saturated bulk C atom coordinating with six Mo atoms). On **t2**, the  $\text{Mo}_\text{B}$  atom coordinates with one C atom in the sublayer and has two dangling bonds. The **b1** site links two  $\text{Mo}_\text{A}$  atoms; the **b2** site links one  $\text{Mo}_\text{A}$  and one  $\text{Mo}_\text{B}$  atom sharing one sublayer C atom; the **b3** site links two  $\text{Mo}_\text{B}$  atoms; while the **b4** site links one  $\text{Mo}_\text{A}$  and one  $\text{Mo}_\text{B}$ . The **3h1** site has one  $\text{Mo}_\text{A}$  atom and two  $\text{Mo}_\text{B}$  atoms as well as one carbon vacancy in the sublayer. The **3h2** site has two  $\text{Mo}_\text{A}$  atoms as well as one  $\text{Mo}_\text{B}$  atom and one third-layer Mo atom. The **3h3** site has two  $\text{Mo}_\text{A}$  atoms and one  $\text{Mo}_\text{B}$  atom as well as one sublayer carbon atom. The **3h4** site has one  $\text{Mo}_\text{A}$  atom and two  $\text{Mo}_\text{B}$  atoms as well as one third-layer Mo atom. The total supercell contains an  $\text{Mo}_{48}\text{C}_{24}$  unit.

The Mo/C-mixed  $\text{Mo}_2\text{C}(101)$  has sixteen surface Mo and sixteen surface C atoms as well as four top (**t1–t4**), eight bridge (**b1–b8**), three 3-fold hollow (**3h1–3h3**) and two 4-fold

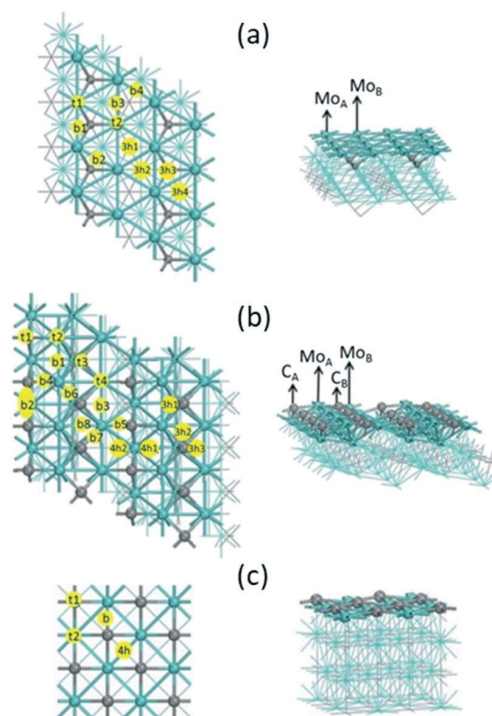


Fig. 1 Top (left) and side (right) views of the (a)  $\text{Mo}_2\text{C}(001)$ , (b)  $\text{Mo}_2\text{C}(101)$  and (c)  $\text{MoC}(001)$  surface structures and possible adsorption sites (t: top, b: bridge, 3h: 3-fold hollow and 4h: 4-fold hollow sites; C: gray, Mo: cyan).

hollow (**4h1** and **4h2**) adsorption sites (Fig. 1b). Four types of surface atoms with different coordination patterns are exposed: the surface  $\text{C}_\text{A}$  atom on the **t1** site coordinates with four Mo atoms and has two dangling bonds; and the surface  $\text{C}_\text{B}$  atom on the **t3** site coordinates with five Mo atoms and has one dangling bond. The Mo atoms on the **t2** and **t4** sites coordinate with three C atoms to form a saturated coordination and differ in the numbers of their coordinated Mo atoms. On the **t2** site, the  $\text{Mo}_\text{A}$  atom coordinates with seven Mo atoms, and the  $\text{Mo}_\text{B}$  atom on the **t4** site coordinates with eight Mo atoms. For the bridge sites, the **b1** site has two  $\text{Mo}_\text{A}$  atoms; the **b2** site has two  $\text{C}_\text{A}$  atoms; the **b3** site has two  $\text{Mo}_\text{B}$  atoms; the **b4** site has one  $\text{Mo}_\text{A}$  atom and one  $\text{C}_\text{A}$  atom; the **b5** site has one  $\text{Mo}_\text{B}$  atom and one  $\text{C}_\text{A}$  atom; while the **b6** site has one  $\text{C}_\text{B}$  atom and one  $\text{Mo}_\text{A}$  atom; the **b7** site has one  $\text{C}_\text{B}$  atom and one  $\text{Mo}_\text{B}$  atom; the **b8** site has one  $\text{Mo}_\text{A}$  atom and one  $\text{Mo}_\text{B}$  atom. With respect to the 3-fold hollow sites, the **3h1** site has two  $\text{Mo}_\text{A}$  atoms and one  $\text{C}_\text{B}$  atom, the **3h2** site has one  $\text{Mo}_\text{A}$  atom, one  $\text{Mo}_\text{B}$  atom and one  $\text{C}_\text{B}$  atom, and the **3h3** site has two  $\text{Mo}_\text{B}$  atoms and one  $\text{C}_\text{B}$  atom. In addition, there are two 4-fold hollow sites: the **4h1** site has two  $\text{Mo}_\text{A}$  atoms and two  $\text{C}_\text{A}$  atoms; while the **4h2** site has two  $\text{Mo}_\text{B}$  atoms and two  $\text{C}_\text{A}$  atoms. The total supercell contains an  $\text{Mo}_{64}\text{C}_{32}$  unit.

The Mo/C-mixed  $\delta\text{-MoC}(001)$  has eight surface Mo and eight surface C atoms as well as four possible adsorption sites (Fig. 1c): the **t1** and **t2** sites are the top sites of surface C

and Mo atoms, respectively; the **b** site is the bridge site of C and Mo atoms, while the **4h** site is the 4-fold hollow site, which links two surface C and two surface Mo atoms. The total supercell contains an  $\text{Mo}_{32}\text{C}_{32}$  unit.

### 3. Results

#### 3.1. $M_n$ ( $M = \text{Co}, \text{Ni}, \text{Cu}, \text{Pd}, \text{Pt}$ ) clusters in the gas phase

The most stable gas phase structures of  $M_n$  are shown in Fig. 2. For  $M_3$ , the most stable structure is a triangle; for  $M_4$ , the most stable structure of  $\text{Co}_4$ ,  $\text{Ni}_4$  and  $\text{Pd}_4$  is tetrahedral, while that of  $\text{Cu}_4$  and  $\text{Pt}_4$  is rhombic. For  $M_5$ , the most stable structure of  $\text{Co}_5$ ,  $\text{Ni}_5$  and  $\text{Pd}_5$  is trigonal bipyramidal, while that of  $\text{Cu}_5$  is a fused bicyclic triangle and that of  $\text{Pt}_5$  has fused bicyclic tri- and tetra-angles. For  $M_6$ , the most stable structure of  $\text{Co}_6$ ,  $\text{Ni}_6$  and  $\text{Pd}_6$  is octahedral, while that  $\text{Cu}_6$  and  $\text{Pt}_6$  is fused star-like. These calculated structures are in good agreement with previous results.<sup>63–71</sup> For  $M_7$ ,  $\text{Cu}_7$  and  $\text{Pt}_7$  the most stable structure is pentagonal bipyramidal, while  $\text{Pt}_7$  has a fused planar structure, and these structures agree well with previous results.<sup>36,39,72–78</sup>

In addition to the structural changes, average aggregation and stepwise growth energies are used to describe the energetics of clusters in the gas phase and on surfaces.<sup>36,37,79</sup> For  $M_n$  clusters in the gas phase, the average aggregation energy [ $E_{\text{agg}}(M_{\text{gas}})$ ] is calculated on the basis of eqn (1)<sup>36</sup> and the stepwise growth energy [ $E_{\text{growth}}(M_{\text{gas}})$ ] is defined

according to eqn (2),<sup>36</sup> where  $E(M_{n/\text{gas}})$  and  $E(M_{\text{gas}})$  are the total energies of an  $M_n$  cluster and an isolated  $M$  atom in the gas phase, respectively, and  $n$  is the number of  $M$  atoms. Minus  $E_{\text{agg}}(M_{\text{gas}})$  actually equates to the average binding energy.<sup>75,80</sup> The stepwise growth energy stands for the formation reaction of  $M_{n-1} + M_1 = M_n$ , and the more negative the growth energy, the easier the  $M_n$  formation.

$$E_{\text{agg}}(M_{\text{gas}}) = [E(M_{n/\text{gas}}) - nE(M_{\text{gas}})]/n \quad (1)$$

$$E_{\text{growth}}(M_{\text{gas}}) = E(M_{n/\text{gas}}) - E(M_{n-1/\text{gas}}) - E(M_{\text{gas}}) \quad (2)$$

In addition, the computed negatives of  $E_{\text{agg}}(M_{\text{gas}})$  (*i.e.*, the binding energies),  $E_{\text{growth}}(M_{\text{gas}})$  of  $M_n$  in the gas phase, the magnetic moment and the average M–M distance of all five metal clusters (Table S1†) are in agreement with previous results.<sup>39,63–65,68,70,78,81–85</sup> The binding energies increase as the size increases, indicating the higher stability of a larger aggregated  $M_n$  cluster. For  $\text{Cu}_n$  ( $n = 2–7$ ), our computed binding energies are in the range of the experimental values derived from the collision-induced dissociation of anionic copper clusters by Spasov *et al.*,<sup>86</sup> and are in agreement with previous computational work.<sup>36</sup> Due to electron pairing in the highest occupied molecular orbital, the computed  $E_{\text{growth}}(\text{Cu}_{\text{gas}})$  exhibits an oscillating behavior: *i.e.*, each odd-numbered cluster has a lower binding energy than its two neighboring even-numbered clusters, and the oscillator

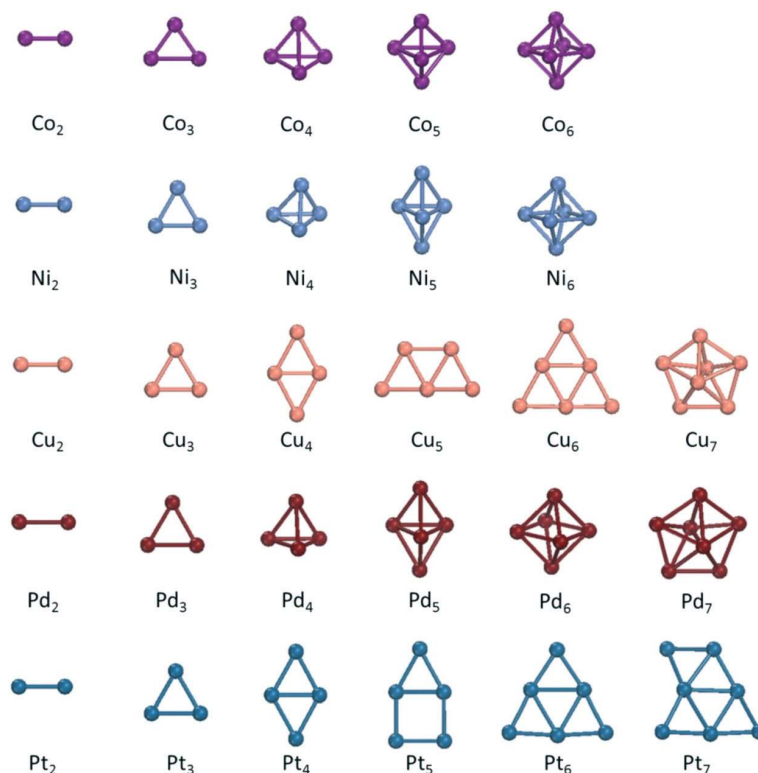


Fig. 2 The most stable gas phase structures for Co, Ni, Cu, Pd and Pt clusters (Co: purple, Ni: gray blue, Cu: orange, Pd: brown, Pt: blue).

strength decreases as the size increases and the differences in stability between odd- and even-membered clusters also decrease accordingly.

It is also interesting to note the change in the binding energy from Co to Ni and Cu as well as from Ni to Pd and Pt. Since they have the same most stable structures (Table S1†), the binding energies of  $\text{Co}_3$ ,  $\text{Ni}_3$  and  $\text{Cu}_3$  are in the order 1.91, 1.87 and 1.22 eV, respectively, and the binding energies of  $\text{Ni}_3$ ,  $\text{Pd}_3$  and  $\text{Pt}_3$  are in the order 1.87, 1.28 and 2.53 eV, respectively. Although  $\text{M}_6$  does not have the same most stable structure, the binding energies are in decreasing order 3.33, 3.05, 2.67, 1.96 and 1.92 eV, respectively, for  $\text{Pt}_6$ ,  $\text{Co}_6$ ,  $\text{Ni}_6$ ,  $\text{Pd}_6$  and  $\text{Cu}_6$ . All these indicate that Pt has the strongest aggregation ability, followed by Co and Ni, while Pd and Cu have rather low aggregation ability; and this will determine their adsorption morphology on a surface, especially at low loading. In addition to the binding energy, the intrinsic properties of the metals, for example, the electronegativity and atomic radii of the metals, also play a decisive role in the stability and morphology of metal clusters on surfaces.

With respect to the reliability of the computational methods and the computed results, we checked other methods in calculating the average aggregation energies of some selected metal clusters (Table S1†). Previously, Wei *et al.*<sup>87</sup> computed the stability of 13-atom metal clusters of 3d, 4d and 5d (group B) elements using the local density approximation (LDA), and the generalized gradient approximation (GGA) with PW91 as well as with PBE. For all 44 metallic 13-atom clusters, both PW91 and PBE show great consistency. Isaev *et al.*<sup>100</sup> computed the binding energies of linear monoatomic nanowires, dimers and bulk of Cu, Ag, Au, Ni, Pd and Pt using LDA, PW91 and PBE; and they found that both PW91 and PBE values are very close, while those of LDA differ strongly. In a previous study of  $\text{Cu}_n$  ( $n = 2-7$ ) clusters,<sup>36</sup> Tian *et al.* found that the PBE computed average aggregation energies agree with the available experimental results within the standard deviations as well as with the results from B3PW91 and HSE06. Taking  $\text{Cu}_4$  as an example, the computed average aggregation energies of PBE, PBE+D3, HSE06 and RPBE are 1.59, 1.63, 1.32 and 1.88 eV, respectively. On the basis of the experimental value ( $1.48 \pm 0.14$  eV), the values of PBE, PBE+D3 and HSE06 are within the standard deviations, while that of RPBE is overestimated.

For 5d element Pt, the computed average aggregation energies of PBE, PBE+D3 and RPBE are 2.77, 2.88 and 3.43 eV for  $\text{Pt}_4$ , and 3.33, 3.41 and 4.04 eV for  $\text{Pt}_6$ , respectively. All these show that the van der Waals dispersion correction does not affect the average aggregation energy significantly, while RPBE greatly overestimates the energy.

### 3.2. Adsorption on $\text{Mo}_2\text{C}(001)$

The most stable adsorption configurations of  $\text{M}_n$  on the  $\text{Mo}_2\text{C}(001)$  surface are calculated at different coverages. In our computation, there are three main modes of growth: (a) a monolayer/two-dimensional dispersion mode (2D); (b) a monolayer/two-dimensional aggregation mode (2D) and (c) a multilayer/3D cluster mode. All stable adsorption configurations are shown in Fig. S1–S7† and the computed energetic parameters are summarized in Tables S2–S7†.

For single metal atoms, adsorption on all possible sites, top, bridge and 3-fold hollow sites, are considered initially (Table S2†). For Co, three stable adsorption configurations are found at the three-fold (3h1–3h3) hollow sites (−4.78, −4.53 and −4.19 eV, respectively). For Ni, four stable adsorption configurations are found at the three-fold (3h1–3h4) hollow sites (−4.78, −4.59, −4.30 and −4.64 eV, respectively). For Cu, three stable adsorption configurations are found at the three-fold (3h1–3h3) hollow sites (−3.46, −3.41 and −3.27 eV, respectively). For Pd, three stable adsorption configurations are found at the three-fold (3h1–3h3) hollow sites (−9.49, −9.39 and −9.03 eV, respectively). For Pt, three stable adsorption configurations are found at the three-fold (3h1–3h3) hollow sites (−11.70, −11.52 and −11.06 eV, respectively). This shows that the most stable adsorption configurations (Fig. 3) for these metal atoms prefer the 3h1 site and the other less stable adsorption configurations also prefer 3-fold hollow sites. The adsorption energy of Pt is the highest, followed by that of Pd, while that of Cu is the lowest, and those of Co and Ni are the same. Based on these results, we computed both dispersion mode, with maximal separation among the adsorbed atoms, and aggregation mode, with as many M–M (or fused triangle) connections as possible.

As shown in Fig. 4 for  $\text{Co}_n$  ( $n = 2-5$ ), the dispersed  $2 \times \text{Co}$ -c mode is more stable than the aggregated mode (−9.70 vs.

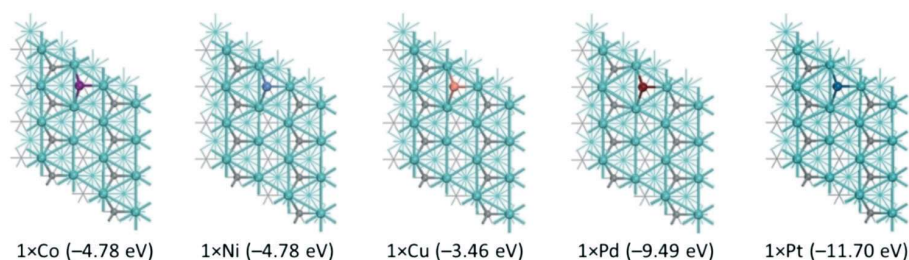


Fig. 3 The most stable adsorption configurations and energies for single Co, Ni, Cu, Pd, and Pt atoms on  $\text{Mo}_2\text{C}(001)$  (Co: purple, Ni: gray blue, Cu: orange, Pd: brown, Pt: blue, C: gray, Mo: cyan).



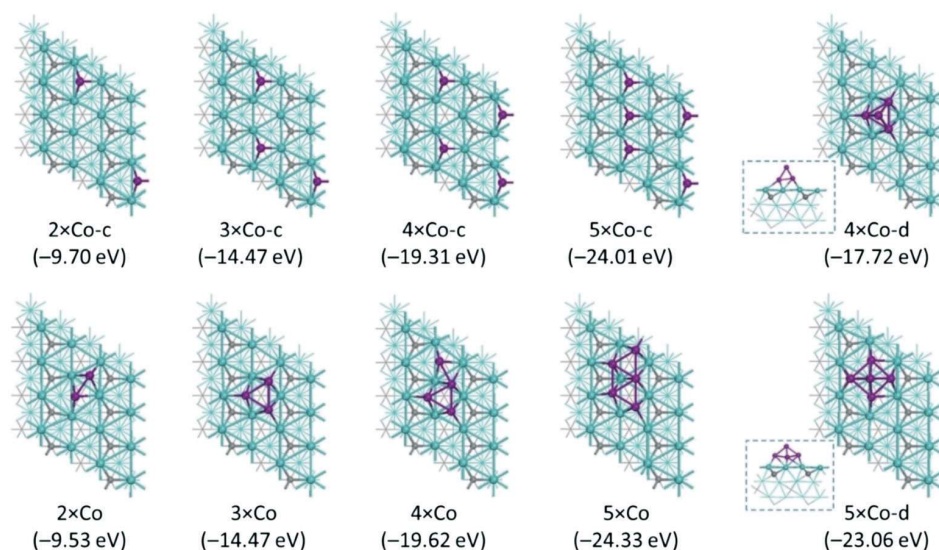


Fig. 4 The most stable adsorption configurations and energies of dispersion, aggregation and 3D (side views inset) modes for  $\text{Co}_n$  ( $n = 2-5$ ) on  $\text{Mo}_2\text{C}(001)$  (Co: purple, C: gray, Mo: cyan).

−9.53 eV), and the dispersed  $3 \times \text{Co-c}$  mode has the same energy as the aggregated mode (−14.47 eV). For  $4 \times \text{Co}$  and  $5 \times \text{Co}$ , the aggregated mode becomes more stable than the dispersed mode (−19.62 vs. −19.31 and −24.33 vs. −24.01 eV, respectively). In addition, the 3D  $4 \times \text{Co-d}$  (tetrahedral) and  $5 \times \text{Co-d}$  (tetragonal pyramidal) cluster modes (−17.72 and −23.06 eV, respectively) are less stable than the aggregated modes, indicating that monolayer modes are more stable. Based on these results, only aggregated modes at high loading are considered. Finally, the saturated monolayer adsorption configuration has  $25 \times \text{Co}$  (Fig. S1†), similar to

the face centered cubic  $\text{Co}(111)$  surface; and the average Co–Co distance of  $25 \times \text{Co}$  is shorter than that in the bulk (2.468 vs. 3.548 Å (ref. 88)).

As shown in Fig. 5 for  $\text{Ni}_n$  ( $n = 2-5$ ), the dispersed  $2 \times \text{Ni-c}$  mode is more stable than the aggregated mode (−9.64 vs. −9.48 eV), while the dispersed  $3 \times \text{Ni-c}$  mode is less stable than the aggregated mode (−14.50 vs. −14.58 eV). The dispersed and aggregated  $4 \times \text{Ni}$  modes are close in energy (−19.34 and −19.33 eV, respectively). For  $5 \times \text{Ni}$ , the aggregated mode is more stable than the dispersed mode (−24.41 and −24.14 eV, respectively). In addition, the 3D  $4 \times$

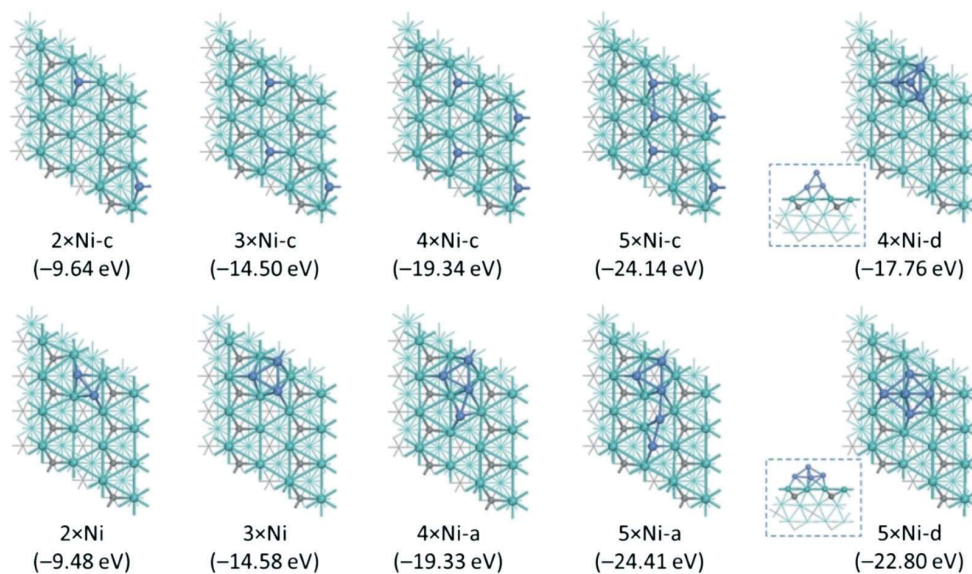


Fig. 5 The most stable adsorption configurations and energies of dispersion, aggregation and 3D (side views inset) modes for  $\text{Ni}_n$  ( $n = 2-5$ ) on  $\text{Mo}_2\text{C}(001)$  (Ni: gray blue, C: gray, Mo: cyan).

Ni (tetrahedral) and  $5 \times \text{Ni}$  (tetragonal pyramidal) cluster modes ( $-17.76$  and  $-22.80$  eV, respectively) are less stable than aggregated modes, indicating that monolayer mode structures are more stable. Based on these results, only aggregated modes at high loading are considered. Finally, the saturated monolayer adsorption configuration has  $25 \times \text{Ni}$  (Fig. S2†), similar to the face centered cubic Ni(111) surface; and the average Ni–Ni distance of  $25 \times \text{Ni}$ -a is  $2.438$  Å, shorter than that ( $3.52$  Å (ref. 89)) in the bulk.

As shown in Fig. 6 for  $\text{Cu}_n$  ( $n = 2-5$ ), the aggregated modes of  $2 \times \text{Cu}$ ,  $3 \times \text{Cu}$ ,  $4 \times \text{Cu}$  and  $5 \times \text{Cu}$  ( $-7.07$ ,  $-10.83$ ,  $-14.49$  and  $-18.29$  eV, respectively) are more stable than the corresponding dispersed modes ( $-6.98$ ,  $-10.67$ ,  $-13.95$  and  $-17.69$  eV, respectively). The 3D  $4 \times \text{Cu}$  (tetrahedral) and  $5 \times \text{Cu}$  (tetragonal pyramidal) cluster modes are less stable ( $-13.21$  and  $-17.05$  eV, respectively). Therefore, only aggregated modes at high loading ( $\text{Cu}_5$  to  $\text{Cu}_{15}$ ) are considered. Finally, the saturated monolayer adsorption configuration has  $25 \times \text{Cu}$  (Fig. S3†), similar to the face centered cubic Cu(111) surface; and the average Cu–Cu distance of  $25 \times \text{Cu}$  is  $2.446$  Å, which is shorter than that ( $2.56$  Å (ref. 90)) in the bulk. As shown in Table S5,† the average adsorption energy ( $-3.72$  eV) and average aggregation energy ( $-0.26$  eV) from  $9 \times \text{Cu}$  to  $12 \times \text{Cu}$  are the same as those of  $25 \times \text{Cu}$ .

As shown in Fig. 7 for  $\text{Pd}_n$  ( $n = 2-7$ ), the dispersed ( $n = 2-4$ ) and linear-shaped ( $n = 5-7$ ) modes ( $-13.96$ ,  $-18.36$ ,  $-22.86$ ,  $-27.26$ ,  $-31.69$ ,  $-36.00$  eV, respectively) are more stable than the corresponding aggregated modes ( $-13.73$ ,  $-18.35$ ,  $-22.76$ ,  $-26.94$ ,  $-31.38$ ,  $-35.83$  eV, respectively). The 3D  $4 \times \text{Pd}$  (tetrahedral) and  $5 \times \text{Pd}$  (tetragonal pyramidal) cluster modes ( $-20.63$  and  $-24.83$  eV, respectively, Fig. S4†) are less stable than the dispersed modes. For  $n = 8$ , the aggregated mode becomes slightly more stable than the linear-shaped mode

( $-40.44$ , vs.  $-40.35$  eV). Therefore, only aggregated modes at high loading ( $\text{Pd}_5$  to  $\text{Pd}_{16}$ ) are considered. The saturated monolayer coverage has sixteen Pd atoms at hollow sites (Fig. S5†), similar to the Pd(111) surface; and the average Pd–Pd distance of  $16 \times \text{Pd}$ -a is  $3.021$  Å, longer than that ( $2.75$  Å (ref. 91)) in the bulk.

As shown in Fig. 7 for  $\text{Pt}_n$  ( $n = 2-8$ ), the dispersed ( $n = 2-4$ ) and linear-shaped ( $n = 5-8$ ) modes ( $-18.35$ ,  $-25.00$ ,  $-31.69$ ,  $-38.01$ ,  $-44.38$ ,  $-50.59$  and  $-56.84$  eV, respectively) are more stable than the corresponding aggregated modes ( $-17.95$ ,  $-24.71$ ,  $-31.07$ ,  $-37.17$ ,  $-43.51$ ,  $-49.77$  and  $-56.30$  eV, respectively). The 3D  $4 \times \text{Pt}$  (tetrahedral) and  $5 \times \text{Pt}$  (tetragonal pyramidal) cluster modes ( $-28.91$  and  $-34.89$  eV, respectively, Fig. S6†) are less stable than the corresponding dispersed modes. Therefore, only aggregated modes at high loading ( $\text{Pt}_5$  to  $\text{Pt}_{16}$ ) are considered. The saturated monolayer coverage has sixteen Pt atoms (Fig. S7†), similar to the Pt(111) surface, and the average Pt–Pt distance ( $2.998$  Å) is longer than that ( $2.78$  Å (ref. 92)) in the bulk.

### 3.3. Adsorption on the $\text{Mo}_2\text{C}(101)$ surface

As shown in Fig. 1b, the  $\text{Mo}_2\text{C}(101)$  surface, which is rugged and terminated by Mo and C atoms in a disordered arrangement, has many more adsorption sites than the metallic  $\text{Mo}_2\text{C}(001)$  surface, and both surfaces should have quite different adsorption structures and energies. The most stable adsorption configurations of  $\text{M}_n$  ( $\text{M} = \text{Co}, \text{Ni}, \text{Cu}, \text{Pd}, \text{Pt}$ ) at different coverages on the  $\text{Mo}_2\text{C}(101)$  surface have been computed.

Initially, the most stable adsorption site for single-atom adsorption was determined and many stable adsorption sites were found. For Co, the first four most stable adsorption configurations are at the **b2**, **3h1**, **b8** and **b3** sites ( $-5.70$ ,

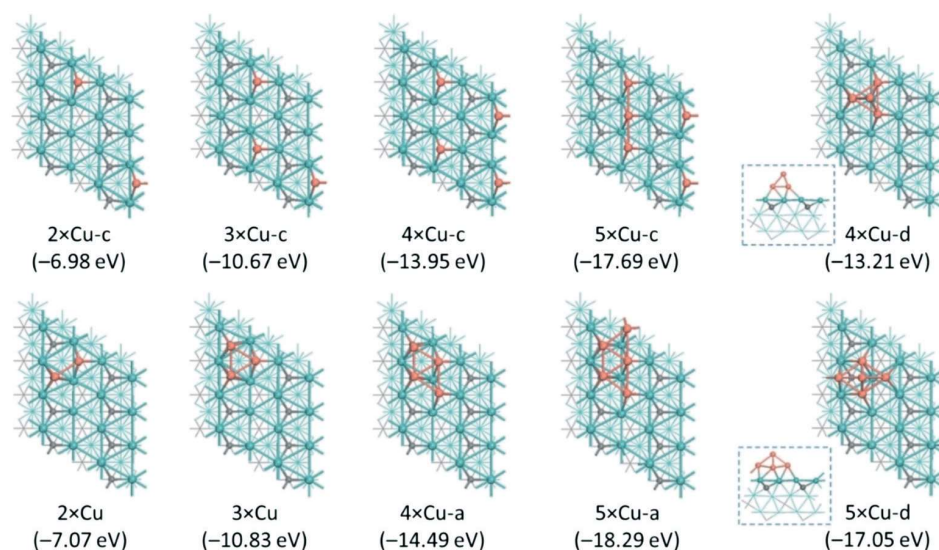


**Fig. 6** The most stable adsorption configurations and energies of dispersion, aggregation and 3D (side views inset) modes for  $\text{Cu}_n$  ( $n = 2-5$ ) on  $\text{Mo}_2\text{C}(001)$  (Cu: orange, C: gray, Mo: cyan).



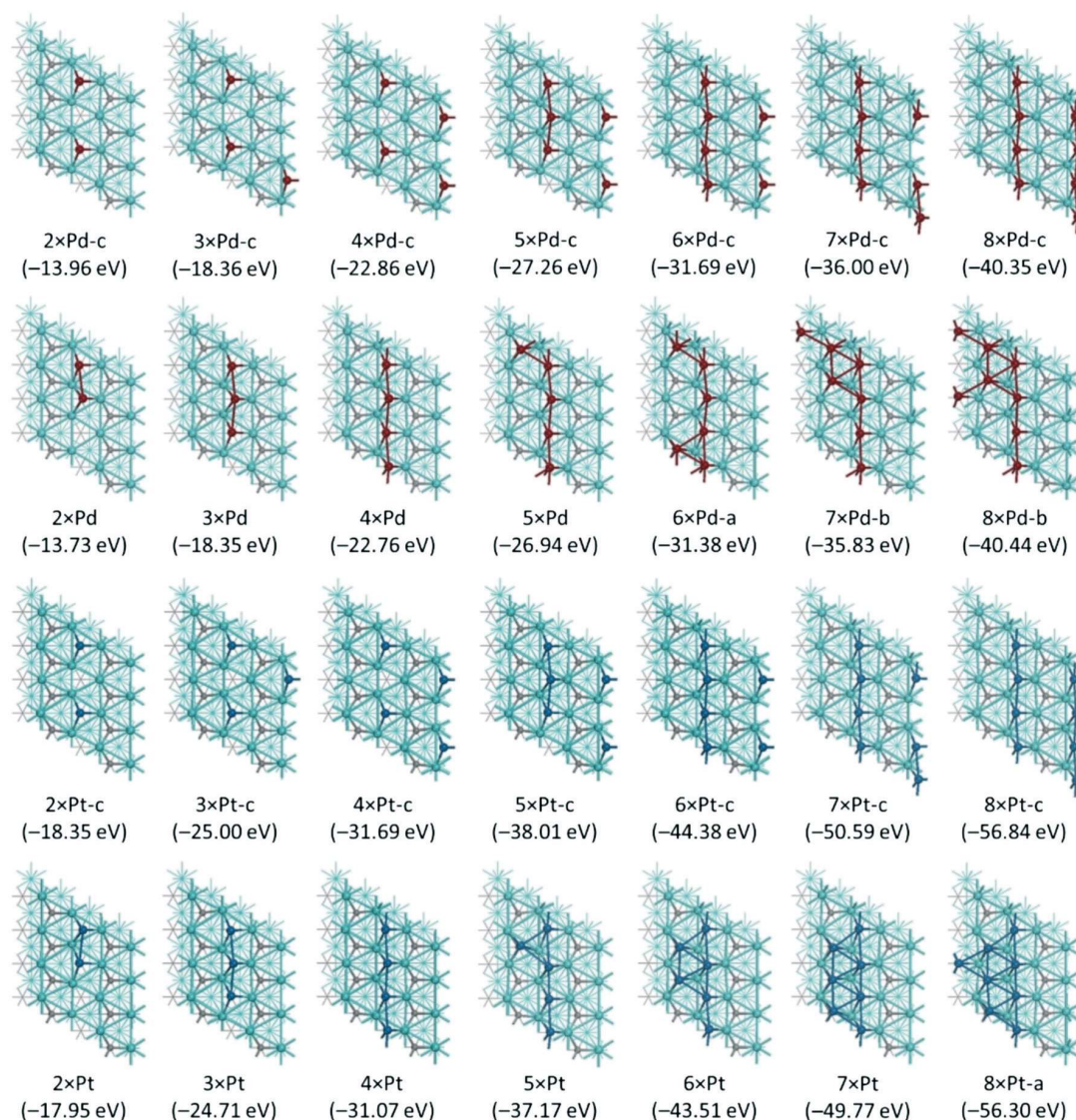


Fig. 7 The most stable adsorption configurations and energies of dispersion and aggregation modes for Pd<sub>n</sub> and Pt<sub>n</sub> (*n* = 2–8) on Mo<sub>2</sub>C(001) (Pd: brown, Pt: blue, C: gray, Mo: cyan).

−3.41, −3.31 and −3.29 eV, respectively). For Ni, the first four most stable adsorption configurations are at the **b2**, **3h1**, **b3** and **3h2** sites (−5.48, −3.55, −3.53 and −3.35 eV, respectively). For Cu, the first four most stable adsorption configurations are at the **b2**, **3h1**, **b7** and **b8** sites (−3.72, −2.30, −2.10 and −1.94 eV, respectively). For Pd, the first four most stable adsorption configurations are at the **b2**, **t1**, **3h1** and **b8** sites (−10.78, −9.81, −9.78 and −9.41 eV, respectively). For Pt, the first four most stable adsorption configurations are at the **b2**, **t1**, **3h1** and **3h3** sites (−12.48, −11.50, −11.42 and −11.17 eV, respectively). For all five metals, the most stable adsorption site for a single metal atom on the Mo<sub>2</sub>C(101) surface is the **b2** site (Fig. S8†), and the second most stable adsorption site for Co, Ni and Cu is the **3h1** site, while that for Pd and Pt is the **t1** site. Based on these results, we computed both the

dispersion modes with maximal separation among the adsorbed atoms and aggregation modes with as many M–M (or fused triangle) connections as possible.

Since the **b2** site is most preferred, and there are eight such equivalent sites, we computed mainly the dispersion adsorption modes (*n* = 2–8, Fig. 8 and S9†). Indeed, it was found that the dispersion modes with remote metal atoms at the **b2** site for Co, Ni and Cu (*n* = 2–4) are much more stable than the aggregation modes with direct M–M connections by 1.84, 3.47 and 3.09 eV for Co, 1.57, 3.11 and 2.69 eV for Ni as well as 1.03, 1.97 and 1.61 eV for Cu, respectively (Fig. S10†).

Starting from *n* = 8, we computed the most stable adsorption configurations up to full monolayer coverage. For M = Co, Ni and Cu with *n* > 8 (Fig. S11–S13†), the next most stable adsorption sites are the 3-fold hollow sites (**3h3**). With an

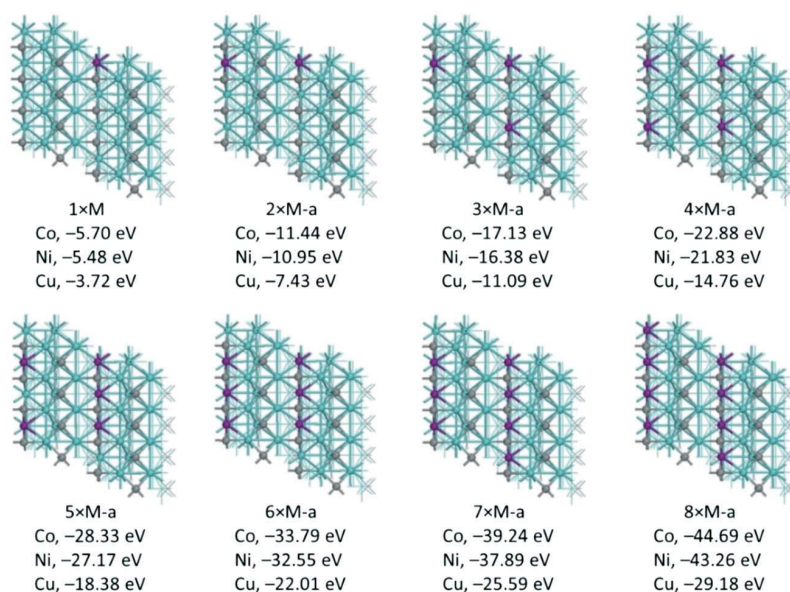


Fig. 8 Structures and adsorption energies of dispersion modes for  $M_n$  ( $M = \text{Co, Ni, Cu}$ ;  $n = 1-8$ ) on  $\text{Mo}_2\text{C}(101)$  (M: purple, C: gray, Mo: cyan).

increase in metal loading, the stable structures have as many triangles as possible. At  $n = 18$ , all these hollow sites are occupied. Finally, we computed the structure for  $n = 28$ , which covers all adsorption sites and represents full monolayer coverage.

For Pd and Pt ( $n = 2-4$ , Fig. 9 and S14†), the linear-shaped dispersion modes are more stable than the aggregation modes by 0.72, 1.50 and 1.25 eV for Pd as well as 0.79, 1.81 and 2.23 eV for Pt, respectively (Fig. S15†). For  $n = 5-8$ , linear-shaped dispersion modes are found. At  $n = 8$ , all eight atoms are located at the **b2** sites and form two parallel lines; and this can be considered to be the first saturation coverage at the **b2** sites.

For  $M = \text{Pd}$  and  $\text{Pt}$  with  $n > 8$  (Fig. S16 and S17†), the next most stable sites are the 3-fold hollow sites (**3h3**). With an increase in metal loading, the stable structures have as many triangles and tetra-angles as possible. At  $n = 16$ , all these hollow or tilted top sites are occupied. Finally, we computed the structure of  $n = 24$  for full monolayer coverage.

### 3.4. Adsorption on the $\text{MoC}(001)$ surface

As shown in Fig. 1c, the  $\text{MoC}(001)$  surface has a roughly planar or slightly waved structure, like  $\text{Mo}_2\text{C}(001)$ , and has  $\text{Mo/C} = 1/1$ , like  $\text{Mo}_2\text{C}(101)$ . Therefore, one should expect different adsorption structures and energy from  $\text{Mo}_2\text{C}(001)$

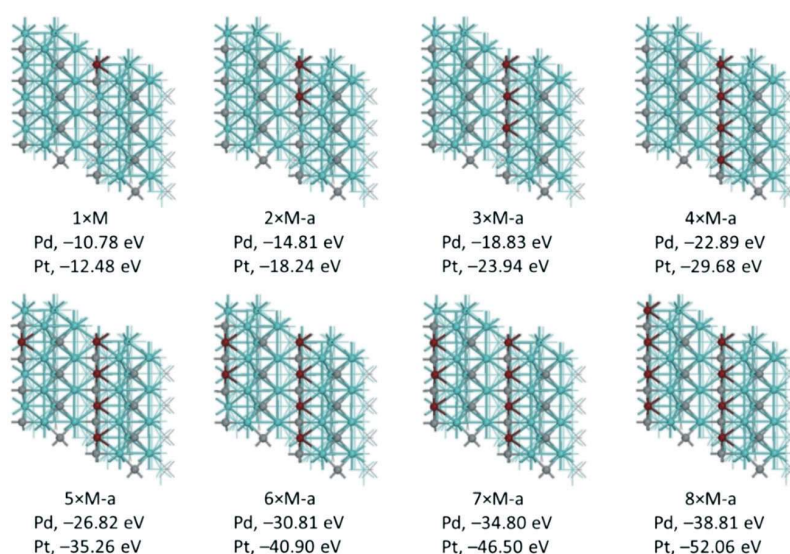


Fig. 9 Structures and adsorption energies of dispersion modes for  $M_n$  ( $M = \text{Pd, Pt}$ ;  $n = 1-8$ ) on  $\text{Mo}_2\text{C}(101)$  (Pd: brown, C: gray, Mo: cyan).



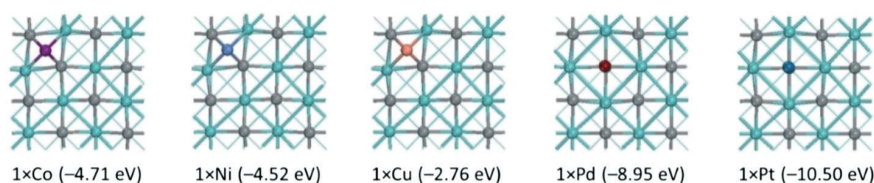


Fig. 10 The most stable adsorption configurations and energies for single Co, Ni, Cu, Pd, and Pt atoms on MoC(001) (Co: purple, Ni: gray blue, Cu: orange, Pd: brown, Pt: blue, C: gray, Mo: cyan).

and Mo<sub>2</sub>C(101). Initially, the most stable adsorption site for a single atom was determined (Fig. 10). For Co and Ni, the stable adsorption configuration is at the **4h** site (−4.71 and −4.52 eV, respectively). For Cu, the stable adsorption configuration is at the **4h** site (−2.76 eV), followed by those at **t1** and **t2** sites (−2.68 and −1.82 eV, respectively). For Pd and Pt, the stable adsorption configuration is at the **t1** site (−8.95 and −10.50 eV, respectively), followed by that at the **4h** site (−8.76 and −10.31 eV, respectively). This shows that the most stable site for Co, Ni and Cu is the **4h** site, while that for Pd and Pt is the **t1** site. Following these results, we computed the most stable adsorption configurations at different coverages.

For the adsorption of Co<sub>n</sub> ( $n = 2-4$ ; Fig. 11), the adsorbed Co atoms prefer the 4-hollow sites; and the aggregation modes with Co–Co bonds are more stable than the dispersion modes without Co–Co bonds (−9.41 vs. −9.00, −14.36 vs. −13.03 and −19.92 vs. −16.94 eV, respectively). This reveals that the greater the number of Co–Co bonds, the more stable the adsorbed structure; and this is further confirmed by the aggregated 5 × Co-b with five Co–Co bonds with respect to the dispersed structure with only two Co–Co bonds (−23.88 vs. −21.22 eV). In addition, the 3D 4 × Co-d (tetrahedral) and 5 × Co-d (tetragonal pyramidal) cluster modes are much less stable (−16.83 and −22.18 eV, respectively) than the aggregation modes. Based on these

results, we computed high Co loading for structures with as many Co–Co bonds as possible, and monolayer structures have been found for  $n = 12$ . It is interesting to note that among these monolayer aggregation structures ( $n = 4-12$ ), all adsorption structures have a common point and the surface carbon atom below the square of four Co atoms at the hollow sites moves over the square and forms a tetragonal pyramidal structure. For  $n = 13-16$ , however, 3D cluster structures become possible (Fig. S18†).

For the adsorption of Ni<sub>n</sub> ( $n = 2-4$ ; Fig. 12), the adsorbed Ni atoms prefer the 4-hollow sites and the aggregation modes with Ni–Ni bonds are more stable than the dispersion modes without Ni–Ni bonds (−8.71 vs. −8.60, −13.22 vs. −12.39 and −17.55 vs. −16.41 eV, respectively). This reveals that the greater the number of Ni–Ni bonds, the more stable the adsorbed structure; and this is further confirmed by the aggregated 5 × Ni with six Ni–Ni bonds with respect to the dispersed structure with two Ni–Ni bonds (−21.68 vs. −20.41 eV). In addition, the 3D 4 × Ni-d (tetrahedral) and 5 × Ni-d (tetragonal pyramidal) cluster structures are less stable (−16.55 and −21.25 eV, respectively) than the aggregation modes. Based on these results, we computed high Ni loading for structures with as many Ni–Ni bonds as possible, and monolayer structures have been found for  $n = 12$ . For  $n = 13-16$ , 3D cluster structures become possible (Fig. S19†). However, it should be noted that the basic unit for Ni

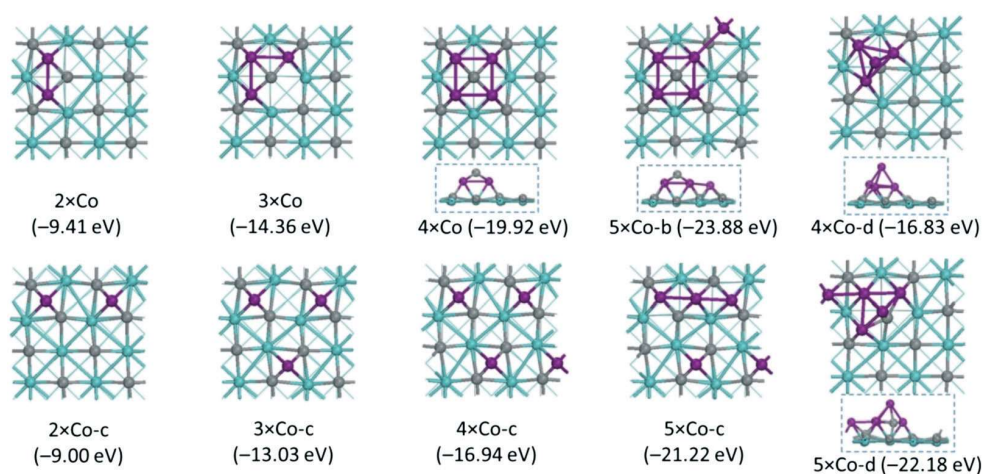


Fig. 11 The most stable adsorption configurations (side views inset) and energies of aggregation, dispersion and 3D modes for Co<sub>n</sub> ( $n = 2-5$ ) on MoC(001) (Co: purple, C: gray, Mo: cyan).



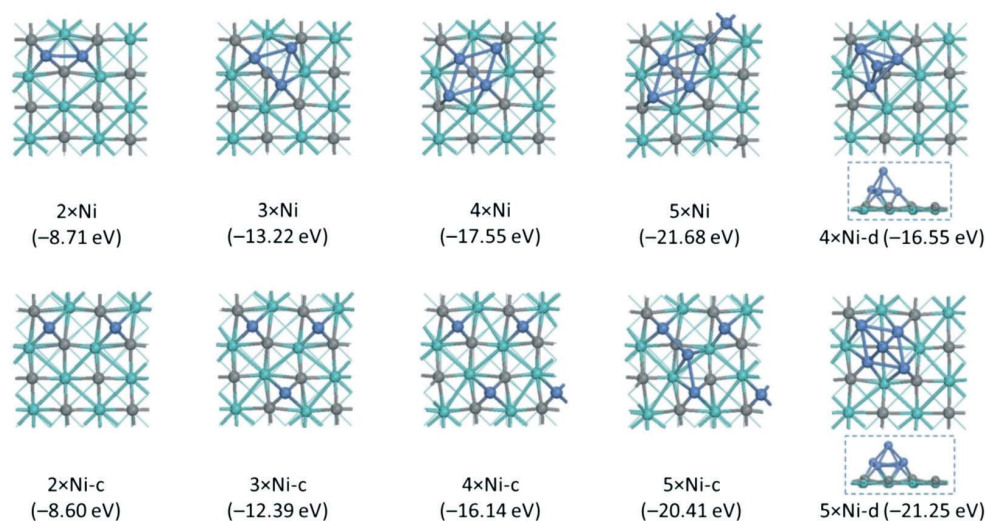


Fig. 12 The most stable adsorption configurations and energies of aggregation, dispersion and 3D (side views inset) modes for  $Ni_n$  ( $n = 2-5$ ) on MoC(001) (Ni: gray blue, C: gray, Mo: cyan).

adsorption is rhombic, while that for Co adsorption is square. In the rhombic form, the surface carbon atom is below the central shorter Ni–Ni bond; and, therefore, the carbon atom cannot stand over the adatoms.

For the adsorption of  $Cu_n$  ( $n = 2-4$ ; Fig. 13), the adsorbed Cu atoms do not prefer the 4-hollow site, and this is in contrast to single Cu atom adsorption or  $Co_n$  and  $Ni_n$  adsorptions. It is interesting to note that for  $Cu_n$  ( $n = 2-4$ ), adsorption configurations in zig-zag form are found; totally different from that of  $Co_n$  (square) or  $Ni_n$  (rhombic). Nevertheless, the aggregation modes with Cu–Cu bonds are more stable than the dispersion modes without Cu–Cu bonds (–5.82 vs. –5.03, –8.63 vs. –6.98 and –11.80 vs. –8.92 eV, respectively). This reveals that the greater the number of Cu–Cu bonds, the more stable the adsorption structure; and this

is further confirmed by the aggregated  $5 \times Cu-a$  with five Cu–Cu bonds with respect to the dispersed one with three Cu–Cu bonds (–14.58 vs. –14.08 eV). In addition, the 3D of  $4 \times Cu-b$  (tetrahedral) and  $5 \times Cu-b$  (tetragonal pyramidal) cluster structures are almost as stable (–11.66 and –14.56 eV, respectively) as the aggregated modes. For  $Cu_n$  ( $n = 2-6$ ), the adsorption configurations prefer monolayer structures, while for  $n = 7-12$ , 3D cluster structures with as many triangles as possible are formed (Fig. S20†).

For the adsorption of  $Pd_2$  (Fig. 14), the adsorbed Pd atoms prefer the top site, and the aggregation mode with a Pd–Pd bond is more stable than the dispersed  $2 \times Pd-c$  mode (–12.59 vs. –11.94 eV). For  $Pd_3$ , the adsorbed Pd atoms also prefer the top site, but the aggregation mode with two Pd–Pd bonds is less stable than the dispersion mode with one Pd–

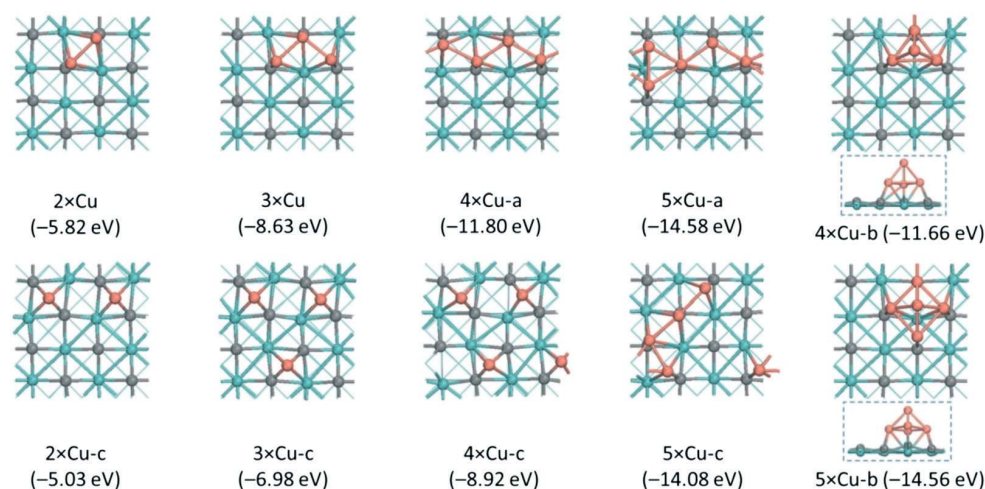


Fig. 13 The most stable adsorption configurations and energies of aggregation, dispersion and 3D (side views inset) modes for  $Cu_n$  ( $n = 2-5$ ) on MoC(001) (Cu: orange, C: gray, Mo: cyan).

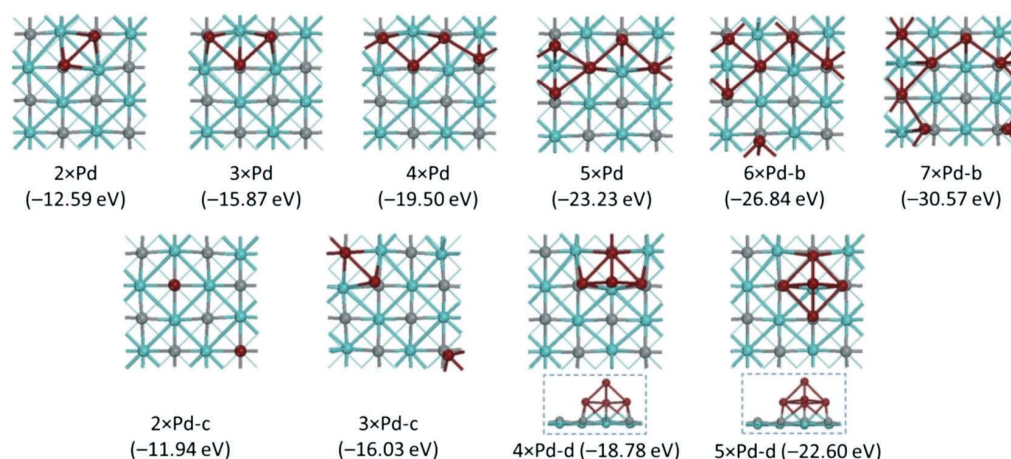


Fig. 14 The most stable adsorption configurations and energies of aggregation, dispersion and 3D (side views inset) modes for  $\text{Pd}_n$  ( $n = 2-7$ ) on  $\text{MoC}(001)$  (Pd: brown, C: gray, Mo: cyan).

Pd bond ( $-15.87$  vs.  $-16.03$  eV). Due to the limited surface size and with an increase in Pd loading, the adsorption configuration becomes zig-zag like ( $n = 4-7$ ) as well as square or rhombic ( $n = 8-10$ ). The monolayer structures of  $4 \times \text{Pd}$  and  $5 \times \text{Pd}$  are more stable than the 3D tetrahedral and tetragonal pyramidal cluster structures ( $-19.50$  vs.  $-18.78$  and  $-23.23$  vs.  $-22.60$  eV, respectively). For  $n = 11-13$ , 3D cluster structures become possible due to the limited surface size (Fig. S21†).

For the adsorption of  $\text{Pt}_2$  (Fig. 15), the adsorbed Pd atoms prefer the top site; and the aggregation mode with the Pd-Pd bond is more stable than the dispersion mode ( $-15.80$  vs.  $-14.84$  eV). For  $\text{Pt}_3$ , the adsorbed Pt atoms also prefer the top site; the aggregated linear mode with two Pd-Pd bonds over three diagonal top sites is more stable than the dispersion mode with one Pt-Pt bond ( $-21.00$  vs.  $-19.62$  eV). Based on the aggregated  $3 \times \text{Pt}$ , we computed aggregated monolayer

structures for  $n = 4-7$  as well as  $n = 8-12$ . For  $n = 12$ , full monolayer coverage is found. The monolayer structures of  $4 \times \text{Pt}$  and  $5 \times \text{Pt}$  are more stable than the 3D tetrahedral and tetragonal pyramidal cluster structures ( $-26.18$  vs.  $-25.66$  and  $-31.42$  vs.  $-30.67$  eV, respectively). For  $n = 13$  and  $14$ , 3D cluster structures are formed (Fig. S22†).

## 4. Discussion

First, it should be noted that the PBE computed average aggregation energy of  $\text{Cu}_n$  ( $n = 2-7$ ) in the gas phase agrees well with the available experimental results; and the same is also true of the results including van der Waals dispersion correction (PBE+D3). In contrast, RPBE greatly overestimates average aggregation energy. This indicates the applicability of the PBE method. For the adsorption of  $\text{Cu}_4/\text{Cu}_6$  as well as  $\text{Pt}_4/\text{Pt}_6$  on these surfaces, PBE+D3 gives lower adsorption than

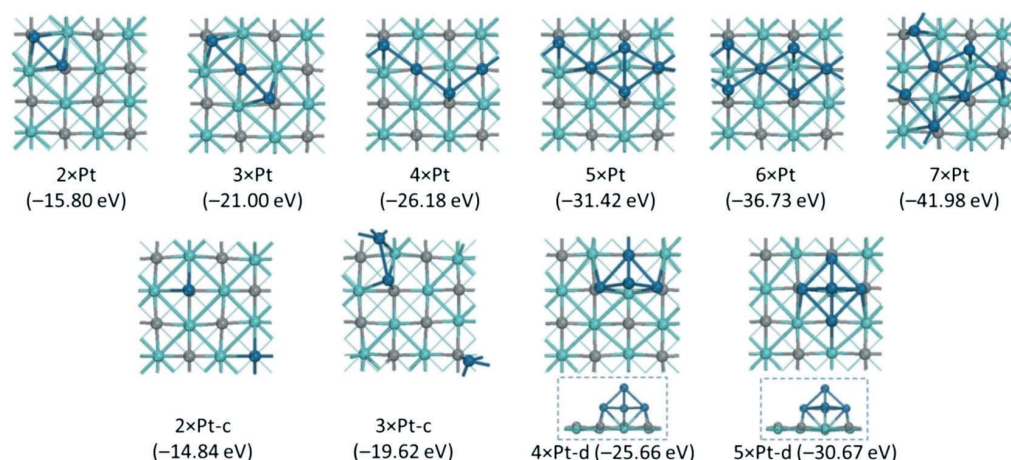


Fig. 15 The most stable adsorption configurations and energies of aggregation, dispersion and 3D (side views inset) modes for  $\text{Pt}_n$  ( $n = 2-7$ ) on  $\text{MoC}(001)$  (Pt: blue, C: gray, Mo: cyan).

only PBE; and both methods show the same relative order of stability of different adsorption modes (Tables S5, S7, S10, S12, S15 and S17†).

All these results discussed above enable a general comparison among these three structurally different surfaces (Table 1). On the metallic Mo<sub>2</sub>C(001) surface, the adsorption of Co and Ni can have dispersion configurations at very low loading, while that of Cu prefers aggregation configurations from low to high loading. For Pd and Pt, dispersion configurations at high loading are possible. Monolayer adsorption modes are more stable than the corresponding 3D cluster modes ( $n = 4$  and  $5$ ); and this should be true for aggregation configurations up to full monolayer coverage. It is to be expected that 3D cluster structures will become possible for metal loading over full monolayer coverage.

On the Mo/C-mixed Mo<sub>2</sub>C(101) surface, all metals prefer dispersion adsorption configurations for  $n = 1-8$ , and aggregation adsorption configurations for  $n = 9-28$  for Co, Ni and Cu, as well as  $n = 9-24$  for Pd and  $9-25$  for Pt; while 3D cluster structures become possible for metal loading over full monolayer coverage.

On the Mo/C-mixed MoC(001) surface, only single-atom adsorption prefers dispersion configuration, and aggregation configurations can be stable from low to medium coverage; and 3D cluster structures become stable over full monolayer coverage.

These results clearly show the surface-dependent adsorption at given metal loading on the one hand; and metal-dependent adsorption on the other hand. With respect to single-atom catalysis for surface-dependent adsorption, the metallic Mo<sub>2</sub>C(001) surface can have single-atom adsorption for Co and Ni at very low loading, and at low to medium loading for Pd and Pt, while the adsorption of Cu prefers aggregation for small clusters at low loading and large clusters or nanoparticles at high and very high loading. On the Mo/C-mixed Mo<sub>2</sub>C(101) surface, single-atom adsorption is favored for all five metals at low and medium loading, while aggregation is favored at high or very high loading. In contrast, it is very hard for the Mo/C-mixed MoC(001) surface to have single-atom adsorption unless at the lowest loading; instead, the MoC(001) surface prefers small clusters at low loading and large clusters or nanoparticles at high and very high loading.

In addition to the surface and metal-dependent adsorption morphology, we compare the general trends in energetic changes up coverage increase (Fig. 16a–c). For  $M_n$  adsorption on

the surface, the total adsorption energy [ $E(M_{n/ads})$ ] is defined according to eqn (3)<sup>36</sup> and the average adsorption energy [ $E(M_{ads/av})$ ] is defined in eqn (4),<sup>36</sup> where  $E(M)_n/slab$  is the energy of the  $M_n$  adsorbed system,  $E(slab)$  is the energy of the clean surface and  $n$  is the number of the adsorbed  $M$  atoms, and  $E(M_{gas})$  is the total energy of an isolated  $M$  atom in the gas phase.

$$E(M_{n/ads}) = [E(M)_n/slab - E(slab) - nE(M_{gas})] \quad (3)$$

$$E(M_{ads/av}) = E(M_{n/ads})/n \quad (4)$$

The stepwise adsorption energy [ $\Delta E(M_{ads})$ ] is defined according to eqn (5).<sup>36</sup>

$$\Delta E(M_{ads}) = E(M_{n/ads}) - E(M_{n-1/ads}) \quad (5)$$

At first, the adsorption energy increases gradually as the coverage increases, indicating the ability for the formation of large clusters on these surfaces due to the enhanced interaction of metal/surface as well as metal/metal. Second, the adsorption energy of Pt is highest, and those of Co, Ni and Pd are in between, while that of Cu is lowest; and this order is only true for adsorption at very low loading, since disorder among Co, Ni and Pd has been found at high loading, indicating the coverage-dependent stability. In contrast to general expectations, it is interesting to note that the more stable Mo/C-mixed Mo<sub>2</sub>C(101) surface has higher adsorption energy at low coverage than the less stable metallic Mo<sub>2</sub>C(001) surface, demonstrating that the adsorption energy depends not only on surface stability but also on local surface structure.

In addition to the adsorption energy for the total interaction, the average adsorption energy shows the trend with the respect to increase in coverage (Fig. 16d–f). For the adsorption of Pd and Pt, the average adsorption energy decreases with the increase in coverage, especially at low coverage on all three surfaces. For Co, Ni and Cu, the average adsorption energy increases marginally on the metallic Mo<sub>2</sub>C(001) and the Mo/C-mixed MoC(001) surfaces, and remains constant with the Mo/C-mixed Mo<sub>2</sub>C(101) surface for  $n = 1-8$  and decreases slightly with increase in coverage. It is interesting to note the crossover between Pd and Co and Ni on all three surfaces, where the adsorption of Pd becomes less stable than that of Co or Ni. On all three surfaces the adsorption of Pt is highest and that of Cu is lowest.

**Table 1** The different coverage ( $n$ ) ranges of Co<sub>*n*</sub>, Ni<sub>*n*</sub>, Cu<sub>*n*</sub>, Pd<sub>*n*</sub>, Pt<sub>*n*</sub> for preferred growth modes on Mo<sub>2</sub>C(001), Mo<sub>2</sub>C(101) and MoC(001)

$M_n$	Mo <sub>2</sub> C(001)		Mo <sub>2</sub> C(101)		MoC(001)		3D cluster
	Dispersion	Aggregation	Dispersion	Aggregation	Dispersion	Aggregation	
Co <sub><i>n</i></sub>	1–3	3–25	1–8	9–28	1	2–13	13–16
Ni <sub><i>n</i></sub>	1–2, 4	3, 5–25	1–8	9–28	1	2–13	13–16
Cu <sub><i>n</i></sub>	1	2–25	1–8	9–28	1	2–6, 12	7–11, 15
Pd <sub><i>n</i></sub>	1–7	8–16	1–8	9–24	1	2–10	11–13
Pt <sub><i>n</i></sub>	1–8	9–16	1–8	9–25	1	2–12	13–14



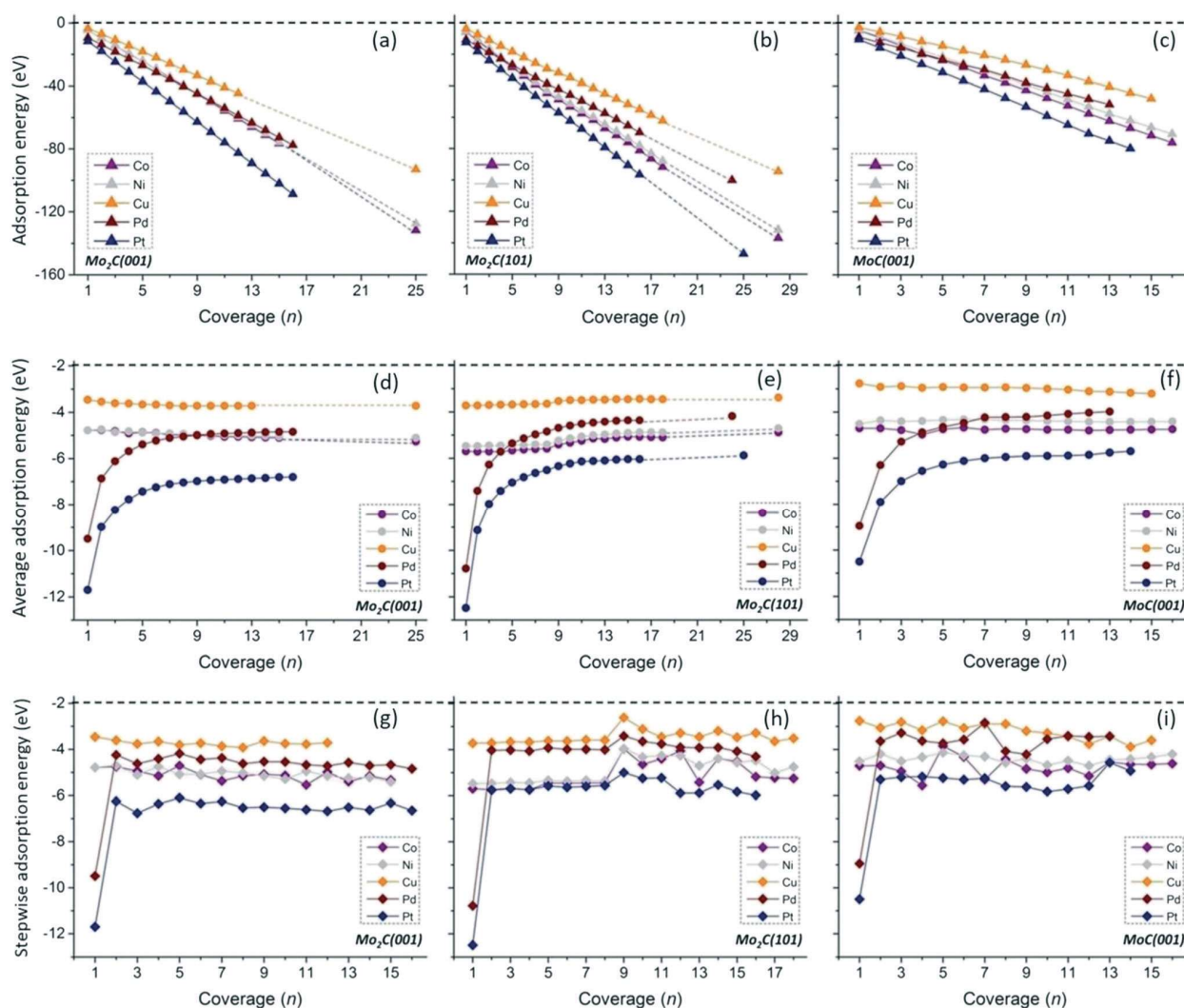


Fig. 16 Adsorption energy (a–c), average adsorption energy (d–f) and stepwise adsorption energy (g–i) values for  $M_n$  ( $M = \text{Co}, \text{Ni}, \text{Cu}, \text{Pd}$ , and  $\text{Pt}$ ) on  $\text{Mo}_2\text{C}(001)$ ,  $\text{Mo}_2\text{C}(101)$  and  $\text{MoC}(001)$ .

The difference in adsorption energy upon increase in coverage can be clearly found from the stepwise adsorption energy (Fig. 16g–i). On all three surfaces, single atoms of Pd and Pt are exceptional due to their rather large adsorption energies. At high coverage on the metallic  $\text{Mo}_2\text{C}(001)$  surface, stepwise adsorption energies are negative on the one hand, and roughly constant up to very high coverage on the other hand due to their more or less regular surface structures. The stepwise adsorption energy of Pt is highest, while that of Cu is lowest. In addition, the stepwise adsorption energy of Pd is lower than those of Co and Ni, and this shows that additional adsorption of the next metal atom is highest for Pt and lowest for Cu; however, the additional adsorption of the next Pd is lower than that of Co or Ni, indicating that the adsorption of Pd becomes weaker than that of Co or Ni despite the fact that single Pd adsorption is much stronger than that of Co or Ni (Fig. 3).

On the Mo/C-mixed  $\text{Mo}_2\text{C}(101)$  surface for  $n = 2-8$ , the stepwise adsorption energy of Pt, Co and Ni are close and constant, and they are higher than that those of Pd or Cu; and all these energies are nearly constant due to their regular adsorption structures. At  $n > 8$ , the stepwise adsorption energy alternates strongly due to their irregular adsorption structure. On the Mo/C-mixed  $\text{MoC}(001)$  surface for  $n > 1$ , however, the stepwise adsorption energies vary strongly due to the change in the surface structures, and this is in sharp contrast to the changes on the  $\text{Mo}_2\text{C}(001)$  and  $\text{Mo}_2\text{C}(101)$  surfaces.

In addition, we also computed the effect of aggregation on all three surfaces on the average aggregation energy and stepwise growth energy. We defined the average aggregation energy [ $E_{\text{agg}}(M_{\text{ads}})$ ] of surface  $M_n$  according to eqn (6),<sup>36</sup> and the more negative the aggregation energy of surface  $M_n$ , the more stable the  $M_n$  on the surface. It should be noted that

surface  $M_n$  in this study includes both aggregated  $M_n$  clusters and  $n$ -dispersed  $M$  atoms on the surface.

$$E_{\text{agg}}(M_{\text{ads}}) = [E(M_{n/\text{ads}}) - nE(M_{\text{ads}})]/n \quad (6)$$

Furthermore, we defined the stepwise growth energy according to eqn (7),<sup>36</sup> and the more negative the stepwise growth energy  $[E_{\text{growth}}(M_{\text{ads}})]$  of the  $M_{n/\text{ads}}$ , the stronger the ability of  $M_{n-1}$  to get one more  $M$  atom from the surface to aggregate. On the other hand, if the  $[E_{\text{growth}}(M_{\text{ads}})]$  is positive, the dispersed structure is thermodynamically more stable.

$$E_{\text{growth}}(M_{\text{ads}}) = E(M_{n/\text{ads}}) - E(M_{n-1/\text{ads}}) - E(M_{\text{ads}}) \quad (7)$$

On all three surfaces, the average aggregation energy for Pd and Pt becomes more positive with an increase in loading, indicating that Pd and Pt prefer dispersion instead of aggregation (Fig. 17a–c); and the stepwise growth energy, which remains constant on the metallic  $\text{Mo}_2\text{C}(001)$  surface and the Mo/C-mixed  $\text{Mo}_2\text{C}(101)$  surface ( $n = 2-8$ ) or becomes negative on the Mo/C-mixed  $\text{MoC}(001)$  surface (Fig. 17d–f), shows that aggregation becomes possible and stable under given conditions. Experimentally, Ma *et al.*<sup>30</sup> have synthesized Pt/ $\alpha$ -MoC catalysts and verified that atomically dispersed Pt species are dominant when the Pt loading is 0.2%, while Pt clusters exist when it reaches 2%. This phenomenon suggested that the dispersion mode is favorable at a low metal loading, while the aggregation mode appears at higher

loading. This is consistent with our study for Pt on the  $\text{Mo}_2\text{C}(001)$  surface (Table 1) which is also an Mo-terminated surface, the same as the surface of  $\alpha$ -MoC in their study.

In contrast, the aggregation of Co, Ni and Cu is thermodynamically favorable with an increase in metal loading on metallic  $\text{Mo}_2\text{C}(001)$ , Mo/C-mixed  $\text{Mo}_2\text{C}(101)$  surfaces ( $n = 2-8$ ) and Mo/C-mixed  $\text{MoC}(001)$  surfaces, while on the Mo/C-mixed  $\text{Mo}_2\text{C}(101)$  surface the average aggregation energy becomes positive with an increase in loading, indicating that dispersion is preferred at low coverage and aggregation at high coverage. With regard to experimental work, atomically dispersed Ni species on  $\beta$ - $\text{Mo}_2\text{C}$  have been synthesized by Tong *et al.*,<sup>32</sup> which evidentially supports our results. To the best of our knowledge, barely atomic scale Co or Ni catalysts supported on  $\text{Mo}_x\text{C}_y$  have been reported. In contrast to Pd and Pt, Co, Ni and Cu find it relatively hard to exist as single atoms on those Mo or Mo/C mixed surfaces according to our results. With respect to single-atom alloys, isolated Pd atoms can remain stable on the Cu(111) surface and Pt is able to disperse atomically on Ni particles.<sup>93,94</sup>

In addition to the adsorption structures and energies, we analyzed the electronic effect of different metal loadings. Table 2 lists the Bader charges of the adsorbed atoms. On the metallic  $\text{Mo}_2\text{C}(001)$  surface, all adsorbed atoms are negatively charged, indicating electron transfer from surfaces to adsorbed metals; and this correlates only qualitatively with the electronegativity of the atoms. According to the Allen scale,<sup>95</sup>

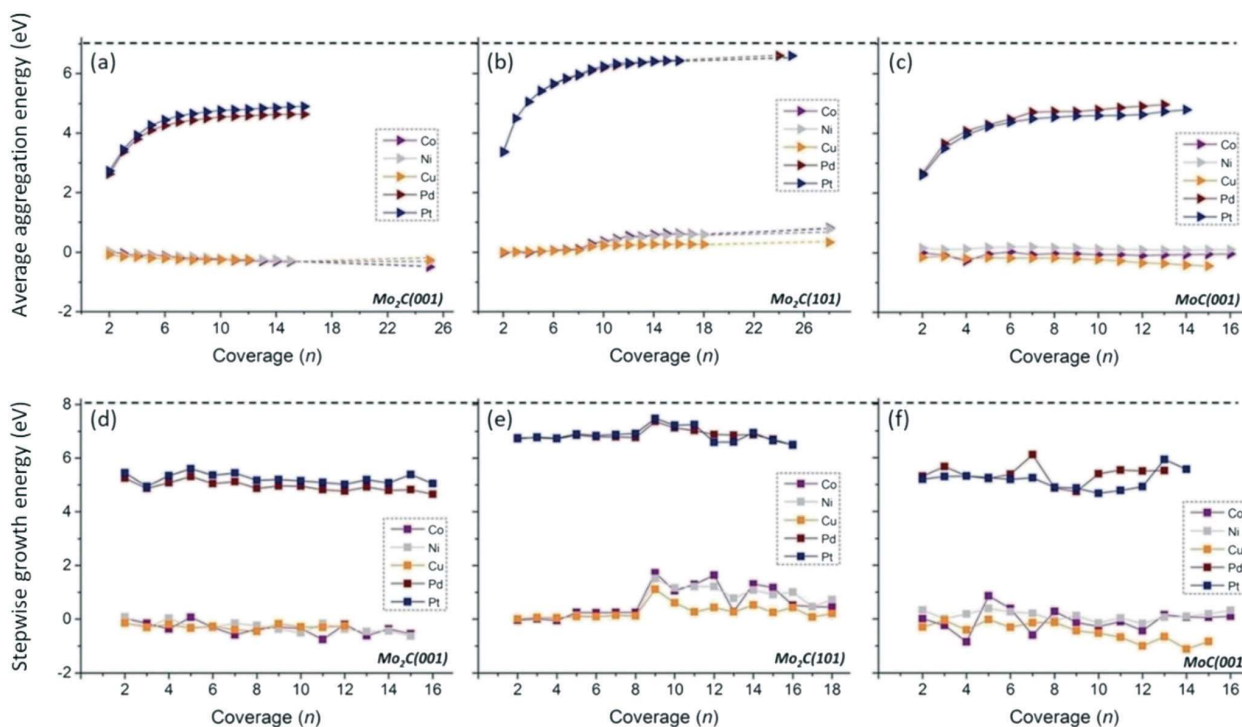


Fig. 17 Average aggregation energy (a–c) and stepwise growth energy (d–f) values for  $M_n$  ( $M = \text{Co}, \text{Ni}, \text{Cu}, \text{Pd}, \text{and Pt}$ ) on  $\text{Mo}_2\text{C}(001)$ ,  $\text{Mo}_2\text{C}(101)$  and  $\text{MoC}(001)$ .

**Table 2** Electronegativity ( $\chi$ ), ionization potential (IP, eV), electro-affinity (EA, eV), and calculated Bader charge ( $q$ ) values for an adsorbed single atom

M	$\chi$ (ref. 95)	IP (ref. 91)	EA	$q$		
				M/Mo <sub>2</sub> C(001)	M/Mo <sub>2</sub> C(101)	M/MoC(001)
Mo	1.47	7.09	0.75 ref. 96	0.45 <sup>a</sup> /Mo <sub>A</sub> ; 0.23 <sup>a</sup> /Mo <sub>B</sub>	0.79 <sup>a</sup> /Mo <sub>A</sub> ; 0.89 <sup>a</sup> /Mo <sub>B</sub>	1.32 <sup>a</sup> /Mo
Co	1.84	7.88	0.66 ref. 97	-0.44	0.20	0.21
Ni	1.88	7.64	1.16 ref. 98	-0.44	0.18	0.18
Cu	1.85	7.73	1.24 ref. 96	-0.32	0.26	0.25
Pd	1.59	8.34	0.56 ref. 98	-0.57	-0.01	-0.05
Pt	1.72	8.96	2.13 ref. 99	-0.79	-0.25	-0.27

<sup>a</sup> The value stands for the average Bader charge of surface Mo atoms on corresponding bare slabs.

the electronegativities of Co, Ni, Cu, Pd and Pt are 1.84, 1.88, 1.85, 1.59 and 1.72, respectively, while that of Mo is 1.47. On Mo<sub>2</sub>C(001) for single-atom adsorption, the charges of the adsorbed Co, Ni, Cu, Pd and Pt are -0.44, -0.44, -0.32, -0.57 and -0.79, respectively, and no quantitative correlation can be found. On the other hand, the negative charge correlates with the adsorption energy (-4.78, -4.78, -3.46, -9.49 and -11.70 eV, respectively); and the more negatively charged the adsorbed atom, the stronger the adsorption energy.

On the Mo/C-mixed Mo<sub>2</sub>C(101) surface, the adsorbed Co, Ni and Cu are positively charged (0.20, 0.18 and 0.26, respectively), while the adsorbed Pd and Pt are negatively charged (-0.01 and -0.25, respectively). The single-atom adsorption energies of Co, Ni, Cu, Pd and Pt are -5.70, -5.48, -3.72, -10.78 and -12.48 eV, respectively. The same trend is also found on the Mo/C-mixed MoC(001) surface: *i.e.*, the adsorbed Co, Ni and Cu are positively charged (0.21, 0.18 and 0.25, respectively), while the adsorbed Pd and Pt are negatively charged (-0.05 and -0.27, respectively); the single-atom adsorption energies of Co, Ni, Cu, Pd and Pt are -4.71, -4.52, -2.76, -8.95 and -10.50 eV, respectively. This might be associated with the larger electronegativity of a surface carbon atom (2.544) and the local structure of the surface molybdenum atoms.

In addition to the surface structures, the electronic state of the single atoms might also play an important role in adsorption energy and electron transfer: *e.g.*, the valence electron configurations of Co, Ni, Cu, Pd and Pt are 3d<sup>7</sup>4s<sup>2</sup>, 3d<sup>8</sup>4s<sup>2</sup>, 3d<sup>10</sup>4s<sup>1</sup>, 4d<sup>10</sup>5s<sup>0</sup> and 5d<sup>9</sup>6s<sup>1</sup>, respectively. However, neither the adsorption energy nor the electron transfer correlates with the ionization potential and electron affinity of the atoms. Next, a comparison of the lattice constants of the supports and the bulk metals also does not give any direct correlation between the structures and energies (Table S18†). Therefore, it is very hard to rationalize adsorption properties by a single parameter; and multi-dimensional parameters are needed to understand the adsorption properties as well as their respective catalytic activities.

## 5. Conclusions

With respect to size- and shape-dependent catalysis involving supported metal catalysts, we systematically computed the adsorption structures and stabilities of M<sub>n</sub> (M = Co, Ni, Cu,

Pd, Pt) on hexagonal Mo<sub>2</sub>C(001) and Mo<sub>2</sub>C(101) surfaces as well as cubic non-polar  $\delta$ -MoC(001) surfaces using a spin-polarized density functional theory method. On all three surfaces, the surface morphologies of monolayer dispersion, monolayer aggregation and three-dimensional clusters were compared and discussed. These results provide a basis for studying catalytic reactions on supported metal catalysts of different sizes and shapes (single atoms, nanoclusters and nanoparticles) and the design of catalysts.

On the Mo-terminated Mo<sub>2</sub>C(001) surface, Co and Ni prefer dispersion at very low loading and aggregation at high coverage. The dispersion of Pd and Pt is possible at relatively higher loading, and Cu prefers aggregation from low to high loading. For all five metals, monolayer adsorption structures are more stable than the corresponding three-dimensional clusters ( $n = 4$  and  $5$ ). On the Mo/C-mixed Mo<sub>2</sub>C(101) surface, all metals prefer dispersion adsorption for  $n = 1-8$  and aggregation appears from  $n = 9$  up to a full monolayer. Three-dimensional clusters become possible for metal loading over full monolayer coverage. On the Mo/C-mixed MoC(001) surface, only single atoms prefer dispersion, and aggregation can be stable from low ( $n = 2$ ) to medium coverage. Three-dimensional clusters become stable at high coverage.

Energetically, on all three surfaces, the adsorption energy of Pt is highest and that of Cu is lowest, while those of Co, Ni and Pd are in between. In addition, the adsorption energies of the metals increase with an increase in metal coverage. The average adsorption energy further verifies the order of adsorption energies. For Pd and Pt, the average adsorption energy decreases dramatically with an increase in coverage from low to medium and decreases marginally up to high coverage. For Co, Ni and Cu, the average adsorption energy increases marginally on the metallic Mo<sub>2</sub>C(001) and Mo/C-mixed MoC(001) surfaces, and is constant on the Mo/C-mixed Mo<sub>2</sub>C(101) surface for  $n = 1-8$ , and it decreases slightly with an increase in coverage. The calculated stepwise adsorption energy can further realize the difference in adsorption energy upon an increase in coverage. Except for single atoms of Pd and Pt, the stepwise adsorption energies of all five metals change regularly, while some exceptional increases or decreases at given coverages appear to be due to surface reconstruction.

In addition to the structures and energies, there is electron transfer between the surface and the adsorbed

atoms. On the Mo-terminated Mo<sub>2</sub>C(001) surface, all adsorbed atoms become negatively charged, indicating electron transfer from the surface to the adsorbed atoms. On Mo/C-mixed Mo<sub>2</sub>C(101) and MoC(001), the adsorbed Co, Ni and Cu atoms are positively charged, and the adsorbed Pt atoms are negatively charged, while the adsorbed Pd atoms are nearly neutral; this demonstrates electron transfer from the adsorbed Co, Ni and Cu atoms to the surface, but from the surface to the adsorbed Pt atoms. For single-atom adsorption, the order of the computed adsorption correlates with the quantity of electron transfer. However, neither the adsorption energy nor the quantity of electron transfer correlates with the electronegativity of the atoms and their respective ionization potential or their electron affinity.

## Conflicts of interest

There are no conflicts to declare.

## Acknowledgements

This work was supported by the China Scholarship Council (F. W.) and the Shandong Provincial Natural Science Foundation, China (grant no. ZR2017MB025), as well as the Leibniz Foundation (Leibniz Competition). We also acknowledge general support from the Federal Ministry of Education and Research Bundesministerium für Bildung und Forschung (BMBF) and the state of Mecklenburg-Vorpommern, Germany.

## References

- 1 Y. Deng, Y. Ge, M. Xu, Q. Yu, D. Xiao, S. Yao and D. Ma, *Acc. Chem. Res.*, 2019, **52**, 3372.
- 2 R. Levy and M. Boudart, *Science*, 1973, **181**, 547.
- 3 N. Ji, T. Zhang, M. Zheng, A. Wang, H. Wang, X. Wang and J. G. Chen, *Angew. Chem., Int. Ed.*, 2008, **47**, 8510.
- 4 S. J. Peppernick, K. D. Gunaratne and A. Castleman, *Proc. Natl. Acad. Sci. U. S. A.*, 2010, **107**, 975.
- 5 T. Hyeon, M. Fang and K. S. Suslick, *J. Am. Chem. Soc.*, 1996, **118**, 5492.
- 6 Q. Gao, C. Zhang, S. Xie, W. Hua, Y. Zhang, N. Ren, H. Xu and Y. Tang, *Chem. Mater.*, 2009, **21**, 5560.
- 7 J. Patt, D. J. Moon, C. Phillips and L. Thompson, *Catal. Letters*, 2000, **65**, 193.
- 8 T. Ferri, D. Gozzi and A. Latini, *Int. J. Hydrogen Energy*, 2007, **32**, 4692.
- 9 S. Wirth, F. Harnisch, M. Weinmann and U. Schröder, *Appl. Catal., B*, 2012, **126**, 225.
- 10 G. Tsirlina and O. Petrii, *Electrochim. Acta*, 1987, **32**, 649.
- 11 H. Vrubel and X. Hu, *Angew. Chem., Int. Ed.*, 2012, **51**, 12703.
- 12 V. Kiran, K. Srinivasu and S. Sampath, *Phys. Chem. Chem. Phys.*, 2013, **15**, 8744.
- 13 L. Liao, X. Bian, J. Xiao, B. Liu, M. D. Scanlon and H. H. Girault, *Phys. Chem. Chem. Phys.*, 2014, **16**, 10088.
- 14 Z. Yan, H. Meng, P. K. Shen, R. Wang, L. Wang, K. Shi and H. Fu, *J. Mater. Chem.*, 2012, **22**, 5072.
- 15 S. Posada-Pérez, R. A. Gutiérrez, Z. Zuo, P. J. Ramírez, F. Viñes, P. Liu, F. Illas and J. A. Rodriguez, *Catal. Sci. Technol.*, 2017, **7**, 5332.
- 16 K. D. Sabnis, Y. Cui, M. C. Akatay, M. Shekhar, W.-S. Lee, J. T. Miller, W. N. Delgass and F. H. Ribeiro, *J. Catal.*, 2015, **331**, 162.
- 17 N. M. Schweitzer, J. A. Schaidle, O. K. Ezekoye, X. Pan, S. Linic and L. T. Thompson, *J. Am. Chem. Soc.*, 2011, **133**, 2378.
- 18 J. A. Rodriguez, P. Liu, F. Viñes, F. Illas, Y. Takahashi and K. Nakamura, *Angew. Chem., Int. Ed.*, 2008, **47**, 6685.
- 19 J. A. Rodriguez, P. Liu, Y. Takahashi, K. Nakamura, F. Vines and F. Illas, *J. Am. Chem. Soc.*, 2009, **131**, 8595.
- 20 L. K. Ono and B. Roldan-Cuenya, *Catal. Lett.*, 2007, **113**, 86.
- 21 J. A. Rodriguez, L. Feria, T. Jirsak, Y. Takahashi, K. Nakamura and F. Illas, *J. Am. Chem. Soc.*, 2010, **132**, 3177.
- 22 S. Posada-Pérez, P. J. Ramírez, J. Evans, F. Viñes, P. Liu, F. Illas and J. A. Rodriguez, *J. Am. Chem. Soc.*, 2016, **138**, 8269.
- 23 J. A. Rodriguez, J. Evans, L. Feria, A. B. Vidal, P. Liu, K. Nakamura and F. Illas, *J. Catal.*, 2013, **307**, 162.
- 24 Y. Chen, S. Choi and L. T. Thompson, *J. Catal.*, 2016, **343**, 147.
- 25 K. T. Jung, W. B. Kim, C. H. Rhee and J. S. Lee, *Chem. Mater.*, 2004, **16**, 307.
- 26 Y. Ma, G. Guan, X. Hao, Z. Zuo, W. Huang, P. Phanthon, K. Kusakabe and A. Abudula, *RSC Adv.*, 2014, **4**, 44175.
- 27 A. Griboval-Constant, J.-M. Giraudon, G. Leclercq and L. Leclercq, *Appl. Catal., A*, 2004, **260**, 35.
- 28 W. Xu, P. J. Ramírez, D. Stacchiola, J. L. Brito and J. A. Rodriguez, *Catal. Lett.*, 2015, **145**, 1365.
- 29 S. Posada-Pérez, P. J. Ramírez, R. A. Gutiérrez, D. J. Stacchiola, F. Viñes, P. Liu, F. Illas and J. A. Rodriguez, *Catal. Sci. Technol.*, 2016, **6**, 6766.
- 30 L. Lin, W. Zhou, R. Gao, S. Yao, X. Zhang, W. Xu, S. Zheng, Z. Jiang, Q. Yu, Y. W. Li, C. Shi, X. D. Wen and D. Ma, *Nature*, 2017, **544**, 80.
- 31 S. Yao, X. Zhang, W. Zhou, R. Gao, W. Xu, Y. Ye, L. Lin, X. Wen, P. Liu, B. Chen, E. Crumlin, J. Guo, Z. Zuo, W. Li, J. Xie, L. Lu, C. J. Kiely, L. Gu, C. Shi, J. A. Rodriguez and D. Ma, *Science*, 2017, **357**, 389.
- 32 T. Ouyang, A.-N. Chen, Z.-Z. He, Z.-Q. Liu and Y. Tong, *Chem. Commun.*, 2018, **54**, 9901.
- 33 T. Gómez, E. Florez, J. A. Rodriguez and F. Illas, *J. Phys. Chem. C*, 2010, **114**, 1622.
- 34 G. G. Asara, F. Viñes, J. M. Ricart, J. A. Rodriguez and F. Illas, *Surf. Sci.*, 2014, **624**, 32.
- 35 S. Posada-Pérez, F. Viñes, J. A. Rodriguez and F. Illas, *J. Chem. Phys.*, 2015, **143**, 114704.
- 36 X. Tian, T. Wang, Y. Yang, Y.-W. Li, J. Wang and H. Jiao, *J. Phys. Chem. C*, 2014, **118**, 21963.
- 37 X. Tian, T. Wang, Y. Yang, Y.-W. Li, J. Wang and H. Jiao, *J. Phys. Chem. C*, 2015, **119**, 7371.
- 38 X. Sun, X. Liu, J. Liu, Y. He, J. Yin, C. Song, Z. Lv, Y. Bai, Y. W. Li and Y. Yang, *ChemCatChem*, 2019, **11**, 715.
- 39 Y. He, P. Zhao, W. Guo, Y. Yang, C.-F. Huo, Y.-W. Li and X.-D. Wen, *Catal. Sci. Technol.*, 2016, **6**, 6726.
- 40 G. Kresse and J. Furthmüller, *Comput. Mater. Sci.*, 1996, **6**, 15.
- 41 G. Kresse and J. Furthmüller, *Phys. Rev. B: Condens. Matter Mater. Phys.*, 1996, **54**, 11169.



- 42 P. E. Blöchl, *Phys. Rev. B: Condens. Matter Mater. Phys.*, 1994, **50**, 17953.
- 43 J. P. Perdew, K. Burke and M. Ernzerhof, *Phys. Rev. Lett.*, 1996, **77**, 3865.
- 44 T. Wang, Y.-W. Li, J. Wang, M. Beller and H. Jiao, *J. Phys. Chem. C*, 2014, **118**, 8079.
- 45 S. Grimme, J. Antony, S. Ehrlich and H. Krieg, *J. Chem. Phys.*, 2010, **132**, 154104.
- 46 S. Grimme, S. Ehrlich and L. Goerigk, *J. Comput. Chem.*, 2011, **32**, 1456.
- 47 A. N. Christensen, *Acta Chem. Scand., Ser. A*, 1977, **31**, 509.
- 48 J. Dubois, T. Epicier, C. Esnouf, G. Fantozzi and P. Convert, *Acta Metall.*, 1988, **36**, 1891.
- 49 T. Epicier, J. Dubois, C. Esnouf, G. Fantozzi and P. Convert, *Acta Metall.*, 1988, **36**, 1903.
- 50 Y. Shi, Y. Yang, Y.-W. Li and H. Jiao, *Catal. Sci. Technol.*, 2016, **6**, 4923.
- 51 Y. Shi, Y. Yang, Y.-W. Li and H. Jiao, *Appl. Catal., A*, 2016, **524**, 223.
- 52 F. Wang, T. Li and H. Jiao, *Surf. Sci.*, 2019, **689**, 121466.
- 53 T. Wang, X. Liu, S. Wang, C. Huo, Y.-W. Li, J. Wang and H. Jiao, *J. Phys. Chem. C*, 2011, **115**, 22360.
- 54 R. Fries and C. P. Kemper, *Anal. Chem.*, 1960, **32**, 1898.
- 55 J. Haines, J. Léger, C. Chateau and J. Lowther, *J. Phys.: Condens. Matter*, 2001, **13**, 2447.
- 56 T. Miyao, I. Shishikura, M. Matsuoka, M. Nagai and S. Oyama, *Appl. Catal., A*, 1997, **165**, 419.
- 57 X.-H. Wang, H.-L. Hao, M.-H. Zhang, W. Li and K.-Y. Tao, *J. Solid State Chem.*, 2006, **179**, 538.
- 58 G. Raghoebar, A. Bell and J. Reimer, *J. Catal.*, 1987, **108**, 40.
- 59 A. Hanif, T. Xiao, A. P. York, J. Sloan and M. L. Green, *Chem. Mater.*, 2002, **14**, 1009.
- 60 A. Fernández Guillermot, J. Häglund and G. Grimvall, *Phys. Rev. B: Condens. Matter Mater. Phys.*, 1992, **45**, 11557.
- 61 A. Vojvodic, *Catal. Lett.*, 2012, **142**, 728.
- 62 J. R. d. S. Politi, F. Viñes, J. A. Rodriguez and F. Illas, *Phys. Chem. Chem. Phys.*, 2013, **15**, 12617.
- 63 M. Castro, C. Jamorski and D. R. Salahub, *Chem. Phys. Lett.*, 1997, **271**, 133.
- 64 M. Michelini, R. P. Diez and A. Jubert, *J. Mol. Struct.*, 1999, **490**, 181.
- 65 M. Michelini, R. P. Diez and A. Jubert, *Int. J. Quantum Chem.*, 1998, **70**, 693.
- 66 M. D. Morse, *Chem. Rev.*, 1986, **86**, 1049.
- 67 M. Morse, G. Hansen, P. Langridge-Smith, L. S. Zheng, M. Geusic, D. Michalopoulos and R. Smalley, *J. Chem. Phys.*, 1984, **80**, 5400.
- 68 J. Bucher, D. Douglass and L. Bloomfield, *Phys. Rev. Lett.*, 1991, **66**, 3052.
- 69 L. M. Russon, S. A. Heidecke, M. K. Birke, J. Conceicao, M. D. Morse and P. Armentrout, *J. Chem. Phys.*, 1994, **100**, 4747.
- 70 S. Datta, M. Kabir, S. Ganguly, B. Sanyal, T. Saha-Dasgupta and A. Mookerjee, *Phys. Rev. B: Condens. Matter Mater. Phys.*, 2007, **76**, 014429.
- 71 X. Xing, A. Hermann, X. Kuang, M. Ju, C. Lu, Y. Jin, X. Xia and G. Maroulis, *Sci. Rep.*, 2016, **6**, 19656.
- 72 M. Kabir, A. Mookerjee and A. Bhattacharya, *Phys. Rev. A: At., Mol., Opt. Phys.*, 2004, **69**, 043203.
- 73 G. H. Guvelioglu, P. Ma, X. He, R. C. Forrey and H. Cheng, *Phys. Rev. Lett.*, 2005, **94**, 026103.
- 74 C. Massobrio, A. Pasquarello and A. Dal Corso, *J. Chem. Phys.*, 1998, **109**, 6626.
- 75 P. Jaque and A. Toro-Labbé, *J. Chem. Phys.*, 2002, **117**, 3208.
- 76 L. Triguero, U. Wahlgren, P. Boussard and P. Siegbahn, *Chem. Phys. Lett.*, 1995, **237**, 550.
- 77 K. Jug, B. Zimmermann, P. Calaminici and A. M. Köster, *J. Chem. Phys.*, 2002, **116**, 4497.
- 78 K. Bhattacharyya and C. Majumder, *Chem. Phys. Lett.*, 2007, **446**, 374.
- 79 X. Tian, T. Wang, Y. Yang, Y.-W. Li, J. Wang and H. Jiao, *Phys. Chem. Chem. Phys.*, 2014, **16**, 26997.
- 80 X.-j. Kuang, X.-q. Wang and G.-b. Liu, *Transition Met. Chem.*, 2010, **35**, 841.
- 81 A. Nie, J. Wu, C. Zhou, S. Yao, C. Luo, R. C. Forrey and H. Cheng, *Int. J. Quantum Chem.*, 2007, **107**, 219.
- 82 L. Xiao and L. Wang, *J. Phys. Chem. A*, 2004, **108**, 8605.
- 83 S. Krüger, S. Vent, F. Nörtemann, M. Staufer and N. Rösch, *J. Chem. Phys.*, 2001, **115**, 2082.
- 84 A. V. Matveev, K. M. Neyman, G. Pacchioni and N. Rösch, *Chem. Phys. Lett.*, 1999, **299**, 603.
- 85 Q. Cui, D. G. Musaev and K. Morokuma, *J. Chem. Phys.*, 1998, **108**, 8418.
- 86 V. A. Spasov, T.-H. Lee and K. M. Ervin, *J. Chem. Phys.*, 2000, **112**, 1713.
- 87 J. Chou, H. Chen, C. Hsing, C. Chang, C. Cheng and C. Wei, *Phys. Rev. B: Condens. Matter Mater. Phys.*, 2009, **80**, 165412.
- 88 J. Cerda, P. De Andres, A. Cebollada, R. Miranda, E. Navas, P. Schuster, C. Schneider and J. Kirschner, *J. Phys.: Condens. Matter*, 1993, **5**, 2055.
- 89 R. T. Downs and M. Hall-Wallace, *Am. Mineral.*, 2003, **88**, 247.
- 90 C. Kittel, *Introduction to Solid State Physics*, John Wiley & Sons, Inc., New York, 2005, p. 21.
- 91 D. R. Lide, *CRC Handbook of Chemistry and Physics*, CRC Press, Boca Raton, Florida, 84th edn, 2003.
- 92 E. Bus, J. T. Miller, A. J. Kropf, R. Prins and J. A. van Bokhoven, *Phys. Chem. Chem. Phys.*, 2006, **8**, 3248.
- 93 G. Kyriakou, M. B. Boucher, A. D. Jewell, E. A. Lewis, T. J. Lawton, A. E. Baber, H. L. Tierney, M. Flytzani-Stephanopoulos and E. C. H. Sykes, *Science*, 2012, **335**, 1209.
- 94 Z. Li, T. He, D. Matsumura, S. Miao, A. Wu, L. Liu, G. Wu and P. Chen, *ACS Catal.*, 2017, **7**, 6762.
- 95 L. C. Allen, *J. Am. Chem. Soc.*, 1989, **111**, 9003.
- 96 R. C. Bilodeau, M. Scheer and H. K. Haugen, *J. Phys. B: At., Mol. Opt. Phys.*, 1998, **31**, 3885.
- 97 X. Chen and C. Ning, *Phys. Rev. A*, 2016, **93**, 052508.
- 98 M. Scheer, C. A. Brodie, R. C. Bilodeau and H. K. Haugen, *Phys. Rev. A: At., Mol., Opt. Phys.*, 1998, **58**, 2051.
- 99 R. C. Bilodeau, M. Scheer, H. K. Haugen and R. L. Brooks, *Phys. Rev. A: At., Mol., Opt. Phys.*, 1999, **61**, 012505.
- 100 E. Y. Zarechnaya, N. V. Skorodumova, S. I. Simak, B. Johansson and E. I. Isaev, *Comput. Mater. Sci.*, 2008, **43**, 522.



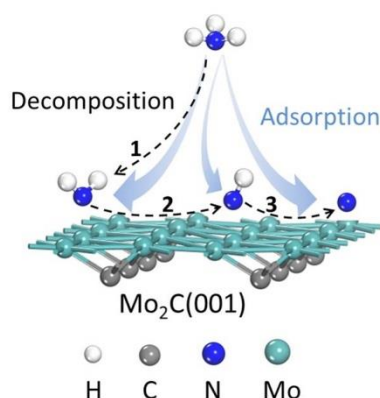
### 3.3 Nitridation of the metallic Mo<sub>2</sub>C(001) surface from NH<sub>3</sub> dissociative adsorption—A DFT study

Fan Wang, Teng Li, Haijun Jiao\*

*Surf. Sci.* **2019**, 689, 121466.

DOI: 10.1016/j.susc.2019.121466

**Summary:** Stepwise dissociative adsorption of ammonia on the hexagonal Mo<sub>2</sub>C(001) surface have been systematically computed using periodic density functional theory under the consideration of van der Waals dispersion correction (PBE-D3). It is found that NH<sub>3</sub> adsorption prefers the top sites from low to saturation coverage. For the adsorption of surface NH<sub>2</sub>, bridge and hollow sites are possible at low coverage and only bridge sites are preferred at high coverage up to saturation. The adsorption of surface NH and N prefers the hollow sites. Sequential dissociation of NH<sub>3</sub> into surface NH<sub>2</sub>, NH and N has low barrier and is highly exothermic. The saturation of coverage for each NH<sub>x</sub> intermediate has been calculated by using gaseous NH<sub>3</sub> as nitridation agent. The saturation coverage of NH<sub>3</sub>, NH<sub>2</sub>, NH and N can have 12, 16, 16 and 8 surface species, respectively or 0.75, 1.0, 1.0 and 0.5 monolayer coverage on the basis of the exposed surface Mo atoms. Our results provide the basis for studying the surface properties and catalytic reaction of nitrided Mo<sub>2</sub>C surfaces.



#### Author contributions

In this work I designed and performed all calculations and analyzed all the results. I completed writing and proofreading based on the suggestions and comments of all co-authors. My scientific contribution as the first author of this paper is more than 95%.



# Nitridation of the metallic Mo<sub>2</sub>C(001) surface from NH<sub>3</sub> dissociative adsorption—A DFT study

Fan Wang<sup>a</sup>, Teng Li<sup>b,c</sup>, Haijun Jiao<sup>a,b,\*</sup>

<sup>a</sup> Leibniz-Institut für Katalyse e.V. an der Universität Rostock, Albert-Einstein Strasse 29a, 18059 Rostock, Germany

<sup>b</sup> State Key Laboratory of Coal Conversion, Institute of Coal Chemistry, Chinese Academy of Sciences, Taiyuan 030001, China

<sup>c</sup> University of Chinese Academy of Sciences, No. 19A Yuquan Road, Beijing 100049, China

## ARTICLE INFO

### Keywords:

Molybdenum carbide  
Ammonia dissociative adsorption  
Nitridation  
Coverage-dependence  
DFT

## ABSTRACT

Adsorption and sequential decomposition of ammonia on the metallic Mo<sub>2</sub>C(001) surface have been systematically computed using periodic density functional theory under the consideration of van der Waals dispersion correction (PBE-D3). It is found that NH<sub>3</sub> adsorption prefers the top sites from low to saturation coverage. For the adsorption of surface NH<sub>2</sub>, bridge and hollow sites are possible at low coverage and only bridge sites are preferred at high coverage up to saturation. The adsorption of surface NH and N prefers the hollow sites. Sequential decomposition of NH<sub>3</sub> into surface NH<sub>2</sub>, NH and N has low barrier and is highly exothermic. On the basis of surface Mo atoms, the saturation coverage of surface NH<sub>3</sub>, NH<sub>2</sub>, NH and N by using NH<sub>3</sub> as nitridation agent is 0.75, 1.0, 1.0 and 0.5 monolayer, respectively. These results provide the basis for the study of surface properties and catalytic reaction of nitrated Mo<sub>2</sub>C surfaces. The dissociative adsorption of ammonia among others metals and molybdenum nitrides has been categorized and compared.

## 1. Introduction

Transition metal carbides have found wide industrial applications due to their extraordinary physical and chemical properties and attracted broad interests in academia and applied research [1–5]. One of the promising applications is transition metal carbides based heterogeneous catalysis and the prominent examples are molybdenum (Mo<sub>2</sub>C) and tungsten (W<sub>2</sub>C) carbides as potential substitutes of noble metals catalysts following the pioneering work of Levy and Boudart in 1973 [6]. It has been demonstrated that Mo<sub>2</sub>C based catalysts are effective in reactions typically catalyzed by noble metals, such as water-gas shift reaction [7,8], CO hydrogenation to alcohols [9,10], hydrodesulfurization [11], hydrodenitrogenation in petroleum refining [12], hydro-treating [13,14], hydrogen production [15] and electro-catalysis and electro-chemistry [16–21].

Catalytic synthesis and decomposition of ammonia are important reactions in science and technology, for example, in producing CO<sub>x</sub>-free hydrogen [22–24], and in purifying fuel from the air-blown gasification of coal [25]. During these reactions, the nature of metal-nitrogen interaction plays a decisive role in determining the catalytic activity [26,27]. Experimentally, Mo<sub>2</sub>C catalyzed ammonia synthesis and decomposition had been reported. For instance, Oyama found the

performance of Mo<sub>2</sub>C and other interstitial alloys to be similar to that of group VIII noble metals in ammonia synthesis [28]. Choi found that Mo<sub>2</sub>C is active in ammonia decomposition and can be used as substitutes for precious metal catalysts in petrochemical processes [29]. Recent study by Schlögl et al. [30], showed the excellent catalytic activity of Mo<sub>2</sub>C in ammonia decomposition and computed molybdenum nitride formation under NH<sub>3</sub> atmosphere. They found that Mo<sub>2</sub>C(0001) (space group *P6<sub>3</sub>/mmc*) having more adsorption sites is more active than MoN(0001) (space group *P6<sub>3</sub>m2*) having less adsorption sites in NH<sub>3</sub> decomposition, although the binding energy of N is stronger over MoN than over Mo<sub>2</sub>C.

In addition to the experimental work, computational studies of the adsorption and decomposition of ammonia on various metals such as Fe, Co and Ni are reported [31–33]. Very recent DFT study focused on the stepwise decomposition of ammonia on the Mo<sub>2</sub>N(100) and Mo<sub>2</sub>N(111) surfaces and illustrated the contributions of individual step to overall process [34]. As one of the most important transition metal carbides, there are no reports about ammonia decomposition on Mo<sub>2</sub>C surfaces. Previously studies mainly focused on surface structures and properties of various Mo<sub>2</sub>C surfaces; [35,36] the adsorption and activation of small molecules [37–41], and the catalytic mechanisms of the dehydrogenation of formic acid [42], and hydrogenation of furfural

Dedicated to Prof. Dr. Jean-François Halet on the occasion of his 60th birthday.

\* Corresponding author at: Leibniz-Institut für Katalyse e.V. an der Universität Rostock, Albert-Einstein Strasse 29a, 18059 Rostock, Germany.

E-mail addresses: [haiju.jiao@catalysis.de](mailto:haiju.jiao@catalysis.de), [haijun.jiao@catalysis.de](mailto:haijun.jiao@catalysis.de) (H. Jiao).

<https://doi.org/10.1016/j.susc.2019.121466>

Received 27 May 2019; Received in revised form 16 July 2019; Accepted 16 July 2019

Available online 17 July 2019

0039-6028/ © 2019 Elsevier B.V. All rights reserved.

[43] and hydrodeoxygenation of carboxylic acid [44]. In this work, we discussed the coverage-dependent dissociative adsorption of ammonia on the Mo<sub>2</sub>C(001) surface and the subsequent nitridation by using NH<sub>3</sub>.

## 2. Method and model

### 2.1. Method

All calculations were done by using the plane-wave based density functional theory (DFT) method implemented in the Vienna *ab initio* simulation package (VASP) [45,46]. The effect of the core electrons was taken into account by the projector augmented wave method (PAW) [47,48]. The electron exchange and correlation energy is treated within the generalized gradient approximation (GGA) in the Perdew-Burke-Ernzerhof functional (PBE) [49]. In this study, we included van der Waals dispersion correction by employing the latest D3 method with Becker-Jonson damping [50,51]. To have accurate energy with errors less than 1 meV per atom, a cutoff energy of 400 eV and the Gaussian electron smearing method with  $\sigma = 0.10$  eV were used. Geometry optimization was converged until forces acting on atoms were smaller than 0.02 eV/Å, whereas the energy threshold-defining self-consistency of electron density was set to  $10^{-4}$  eV. All transition state structures were optimized by using the climbing image nudged elastic band (CI-NEB) method [52], and the frequency analysis was also processed to verify an authentic transition state having only one imaginary frequency and provides zero-point energy (ZPE). For the bulk structure, the lattice parameters of the hexagonal phase were determined by minimizing the total energy of the unit cell by using a conjugated-gradient algorithm to relax the ions and a  $5 \times 5 \times 5$  Monkhorst-Pack k-point grid [39] was used for sampling the Brillouin zone.

### 2.2. Model

Mo<sub>2</sub>C can have orthorhombic [53,54] or hexagonal [55–57] crystalline phase depending on the carburization conditions. In our work, we used the hexagonal Mo<sub>2</sub>C phase with an eclipsed configuration as the unit cell [58]. The calculated lattice parameters of the cell are  $2a = 6.277$  Å,  $2b = 6.070$  Å and  $c = 4.722$  Å, in good agreement with the experimental values ( $a = b = 3.011$  Å,  $c = 4.771$  Å) [59]. We used a periodic  $p(2 \times 2)$  slab with a surface area of  $12.2 \times 12.1$  Å and a six-layer model with the top three layers relaxed and the bottom three layers fixed in the bulk positions. This has been tested in previous studies [37,39].

The adsorption energy ( $E_{\text{ads}}$ ) is defined according to  $E_{\text{ads}} = E(X/\text{slab}) - [E(X) + E(\text{slab})]$ , where  $E(X/\text{slab})$  is the total energy of the slab with one X molecule,  $E(\text{slab})$  is the total energy of the bare slab and  $E(X)$  is the total energy of a free X molecule in gas phase, and therefore the more negative the  $E_{\text{ads}}$  the stronger the adsorption. To get the saturation coverage ( $X = \text{NH}_3$ ), we used the stepwise adsorption energy,  $\Delta E_{\text{ads}} = E(X)n + 1/\text{slab} - [E(X)n/\text{slab} + E(X)]$ , where a positive  $\Delta E_{\text{ads}}$  for  $n + 1$  adsorbed X molecules indicates the saturation adsorption with  $n$  adsorbed X molecules. The barrier ( $E_a$ ) and reaction energy ( $\Delta E_r$ ) are calculated according to  $E_a = E_{\text{TS}} - E_{\text{IS}}$  and  $\Delta E_r = E_{\text{FS}} - E_{\text{IS}}$ , where  $E_{\text{IS}}$ ,  $E_{\text{FS}}$  and  $E_{\text{TS}}$  are the energies of the corresponding initial state (IS), final state (FS), and transition state (TS), respectively. The reaction energies and barriers include the ZPE obtained from frequency analysis [60].

## 3. Results and discussion

Fig. 1 shows the schematic side and top views of the metallic Mo<sub>2</sub>C(001) surface, which has sixteen surface Mo atoms and ten possible adsorption sites (t1, t2, b1–b4 and h1–h4). On t1 site the Mo<sub>1</sub> atom binds two C atoms in the second layer and has one dangling bond (saturated bulk Mo binds three C atoms, saturated bulk C atom binds six Mo atoms); and on t2 site the Mo<sub>2</sub> atom binds with only one C atom in the second layer and has two dangling bonds. The b1 site links two Mo<sub>1</sub>

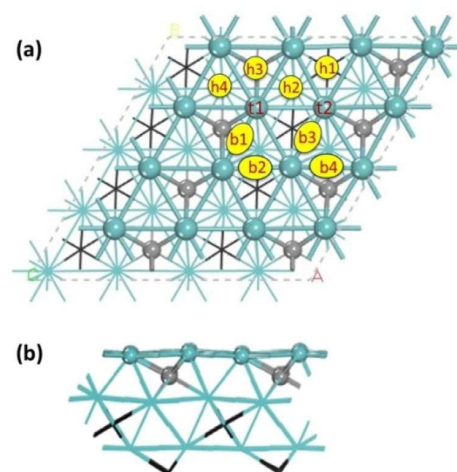


Fig. 1. Top (a) and side (b) views of the metallic Mo<sub>2</sub>C(001) surface with possible adsorption sites (green balls for Mo atoms, gray balls for first layer C atoms and black balls for C atoms in other layers, t for top, b for bridge and h for 3-fold hollow sites). (For interpretation of the references to color in this figure legend, the reader is referred to the web version of this article.)

atoms; the b2 site links one Mo<sub>1</sub> and one Mo<sub>2</sub>; the b3 site links two Mo<sub>2</sub> atoms; the b4 site links one Mo<sub>1</sub> and one Mo<sub>2</sub> sharing one second layer C atom. For the 3-fold hollow sites (h1–h4), they differ in not only surface Mo atoms but also sublayer atoms. The h1 site has one Mo<sub>1</sub> and two Mo<sub>2</sub> as well as one vacancy in the second layer. The h2 site has two Mo<sub>1</sub>, one Mo<sub>2</sub> and one third layer Mo atom. The h3 site has two Mo<sub>1</sub>, one Mo<sub>2</sub> and one second-layer C atom. The h4 site has one Mo<sub>1</sub>, two Mo<sub>2</sub> and one third layer Mo atom.

### 3.1. NH<sub>3</sub> adsorption

The adsorption of one NH<sub>3</sub> on the ten possible adsorption sites was computed, and five stable adsorption configurations are located (Fig. S1). The t1 site has the strongest adsorption energy (−1.30 eV) and the second most stable adsorption configuration is at the t2 site (−1.10 eV); while the adsorption configurations at the bridge (b1; −0.91 and b3; −0.66 eV) and hollow (h2; −0.71 eV) sites are higher in energy and less stable. That the t1 site is more preferred over the t2 site is due to their local difference in electronic property, i.e.; the t1 site with two second layer carbons atoms is more positively charged than the t2 site with only one second layer carbons atom (0.625 vs. 0.419 e) according to Bader charge analysis [61–64]. That NH<sub>3</sub> prefers the top site is due to its electron lone pair at the N center, which represents the highest occupied molecular orbital. Following this energetic order (t1 > t2 > b1 > h2 > b3), we computed NH<sub>3</sub> adsorption at high coverage.

For studying NH<sub>3</sub> adsorption at high coverage we further increased the number of NH<sub>3</sub> molecules one by one at remote sites to minimize the lateral repulsive intermolecular interaction, where we considered the most stable adsorption configuration at individual coverage by considering different possibilities on the basis of the above discussed energetic order, while adsorption configurations with adjacently adsorbed NH<sub>3</sub> molecules are computed for comparison. It is found that the stable adsorption configuration does not exactly follow this energetic order. The more stable adsorption configurations are shown in Fig. 2 and the less stable adsorption configurations are given in Supporting Information (Fig. S2), which shows clearly that the remote adsorption configurations are more stable than the adjacent ones, particularly at low coverage ( $n = 2$ –6). For example, the adsorption configuration of three NH<sub>3</sub> molecules at three adjacent t1 sites in a line is less stable than that at three remote t1 sites by 0.18 eV.



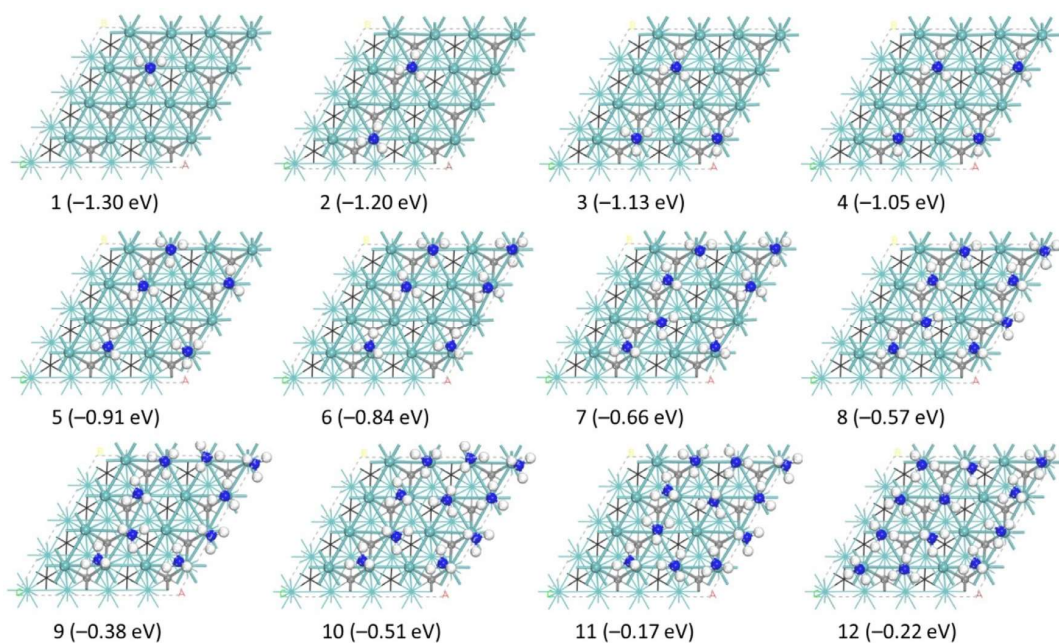


**Fig. 2.** Stepwise adsorption configurations and energies ( $\Delta E_{\text{ads}}$ ) of  $\text{NH}_3$  molecules on the metallic  $\text{Mo}_2\text{C}(001)$  surface (blue balls for N atoms and white balls for H atoms, using gaseous  $\text{NH}_3$  as reference). (For interpretation of the references to color in this figure legend, the reader is referred to the web version of this article.)

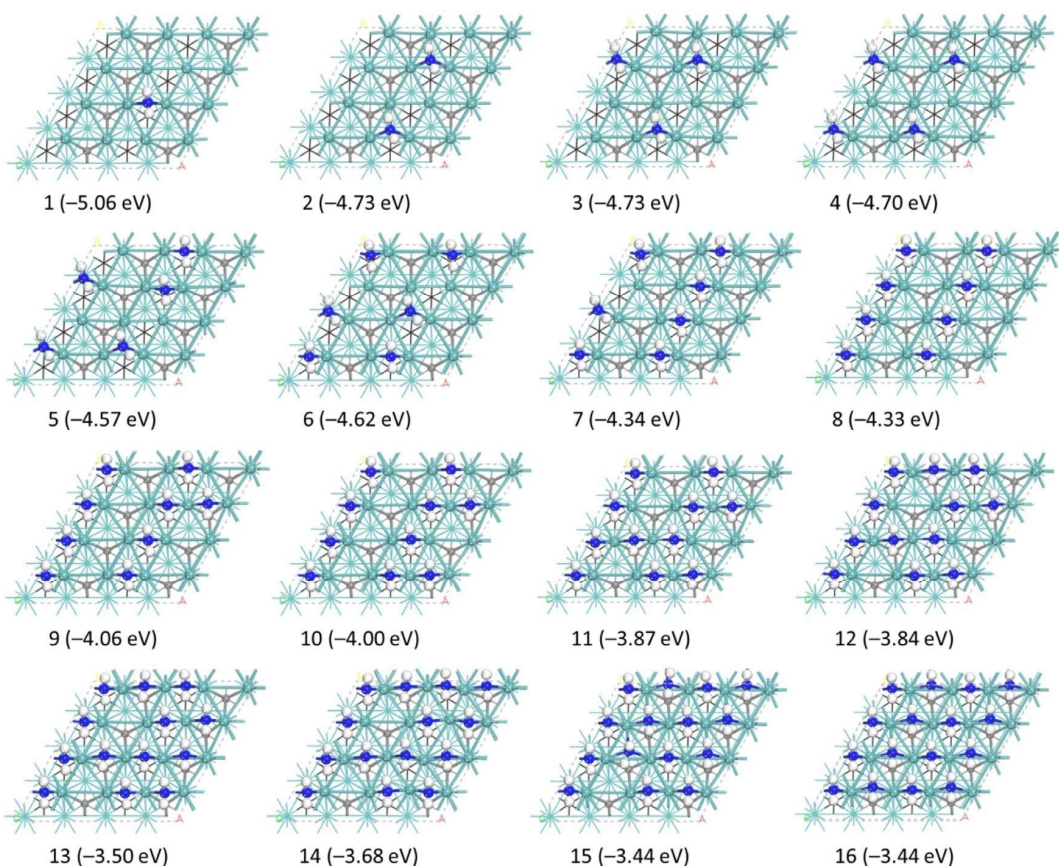


**Fig. 3.** Structures and energies ( $\Delta E_{\text{ads}}$ /eV) of the most stable adsorption sites for stepwise  $\text{NH}_2$  adsorption on  $\text{Mo}_2\text{C}(001)$  surface (blue balls for N atoms and white balls for H atoms; using gaseous  $\text{NH}_2$  radical as reference). (For interpretation of the references to color in this figure legend, the reader is referred to the web version of this article.)

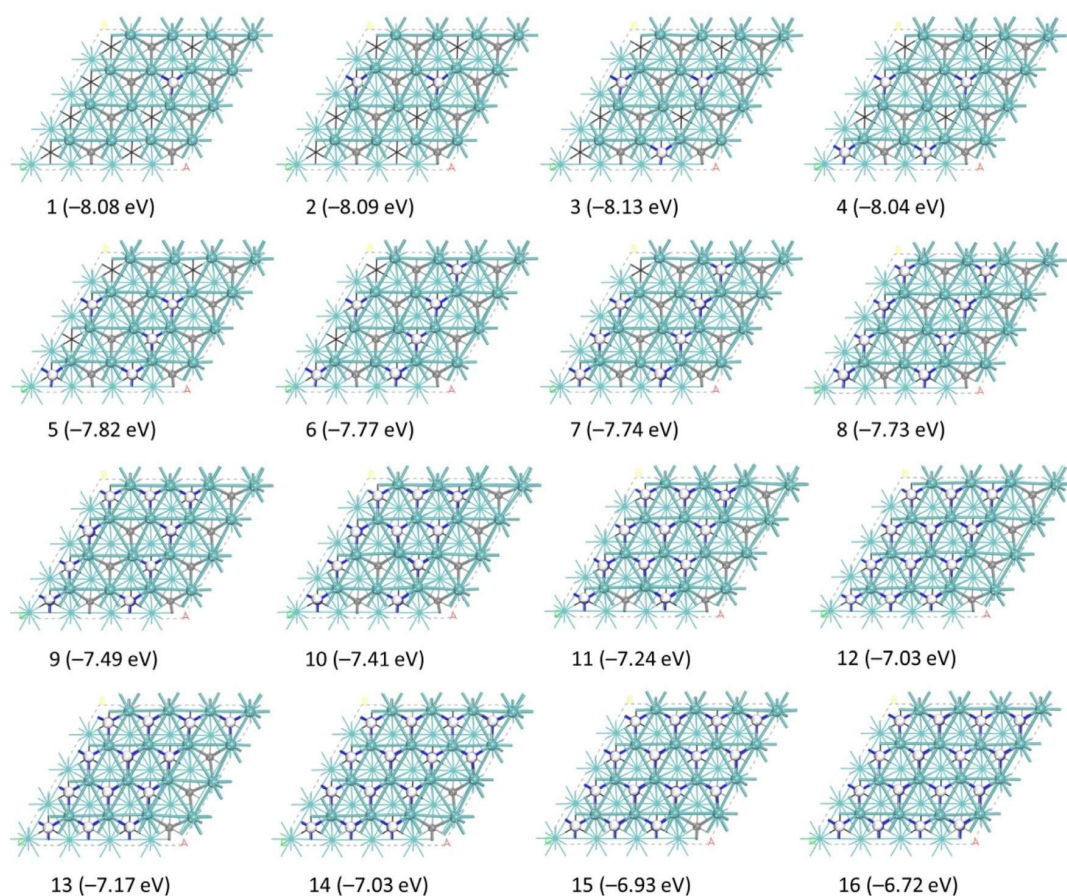


Fig. 4. Structures and energies ( $\Delta E_{\text{ads}}$ /eV) of the most stable adsorption sites for stepwise NH adsorption on  $\text{Mo}_2\text{C}(001)$  surface (blue balls for N atoms and white balls for H atoms; using gaseous NH radical as reference). (For interpretation of the references to color in this figure legend, the reader is referred to the web version of this article.)

For  $n = 1-8$ , the adsorbed  $\text{NH}_3$  molecules are located at **t1** sites and the stepwise adsorption energy decreases gradually, and at the same time, the distance between N-Mo increases gradually (Table S1). For  $n = 8$ , all eight **t1** sites are occupied. On the basis of  $n = 8$ , further  $\text{NH}_3$  molecules are adsorbed one by one. That the **t1** site is more preferred than the **t2** site can also be found at high coverage, for example, for  $n = 7$  with one  $\text{NH}_3$  at the **t2** site is less stable than that with all  $\text{NH}_3$  at the **t1** sites by 0.12 eV; and for  $n = 8$  with two  $\text{NH}_3$  molecules at the **t2** site is less stable than that with all  $\text{NH}_3$  molecules at the **t1** site by 0.19 eV, despite the adjacent  $\text{NH}_3$  in two parallel lines (Fig. S2).

For  $n = 9-12$ , all  $\text{NH}_3$  molecules are located at **t2** site and the stepwise adsorption energy decreases. For  $n = 10$ , however, the stepwise adsorption energy is slightly higher than that of  $n = 9$ ; and this disorder remains despite various variations of the adsorption configurations; and one feature is the head-to-head H-H distance for  $n = 10$  and no such feature can be found in other adsorption configurations. Analysis of charge density does not give any reasonable explanations (Fig. S3). The saturation coverage has twelve adsorbed  $\text{NH}_3$  molecules, since a positive adsorption energy is found for  $n = 13$ , where the added  $\text{NH}_3$  molecule desorb from the surface. For  $n = 12$ , all eight **t1** and four **t2** sites are occupied.

### 3.2. $\text{NH}_2$ adsorption

Different from  $\text{NH}_3$ ,  $\text{NH}_2$  has two electronic configurations [65], the more stable one ( $^2\text{B}_1$ ) has the single electron perpendicular to the molecular plane and the lone pair electron in the molecular plane and

the less stable one ( $^2\text{A}_1$ ) has the single electron in the molecular plane and the lone pair electron perpendicular to the molecular plane. For one  $\text{NH}_2$  adsorption on the ten possible adsorption sites, five stable adsorption configurations were found (Fig. S4). In contrast to  $\text{NH}_3$ , the adsorption configurations at **b2**, **h1** and **h2** sites are very close in energy ( $-5.06$ ,  $-5.04$  and  $-5.05$  eV, respectively) and that at **t2** ( $-4.22$  eV) and **b4** ( $-4.86$  eV) sites are higher in energy and less stable. In these stable adsorption configurations, the  $\text{NH}_2$  plane is nearly perpendicular to the surface. It is also noted that no stable adsorption configuration at **t1** site can be located.

Following this stability order (Fig. S4), we computed  $\text{NH}_2$  adsorption at high coverage, but such negligible energy differences among **b2**, **h1** and **h2** sites make the search for the more or most stable adsorption configurations difficult. Since **h1** and **h2** sites share one **b2** site, small displacement will shift **b2** adsorption either to **h1** or **h2**. For comparison we tentatively computed the adsorption configurations for  $n = 4$  remotely at **h1** and **h2** sites. After structure optimization, the adsorption configuration at **h1** becomes that of **b2**, and that of **h2** is more stable than **b2** by 0.19 eV (Fig. S5). Detailed comparison shows that the adsorption configuration at **h2** site can be considered as tilted **b2** site on the basis of the Ni-Mo distances (2.184, 2.244 and 2.500 Å). For further comparison we computed the adsorption configurations for  $n = 12$  at **h1** and **b4**, **h2** and **b4** as well as **b2** and **b4** sites; and they are very close in energy within 0.03 eV (Fig. S6). This indicates their structure flexibilities. To obtain the most stable configuration at individual coverage, we further calculated and compared different  $\text{NH}_2$  coverage on  $\text{Mo}_2\text{C}(001)$  surface on both **b2** and **h2** sites by considering different possibilities (Figs. S7 and S8). The most stable adsorption



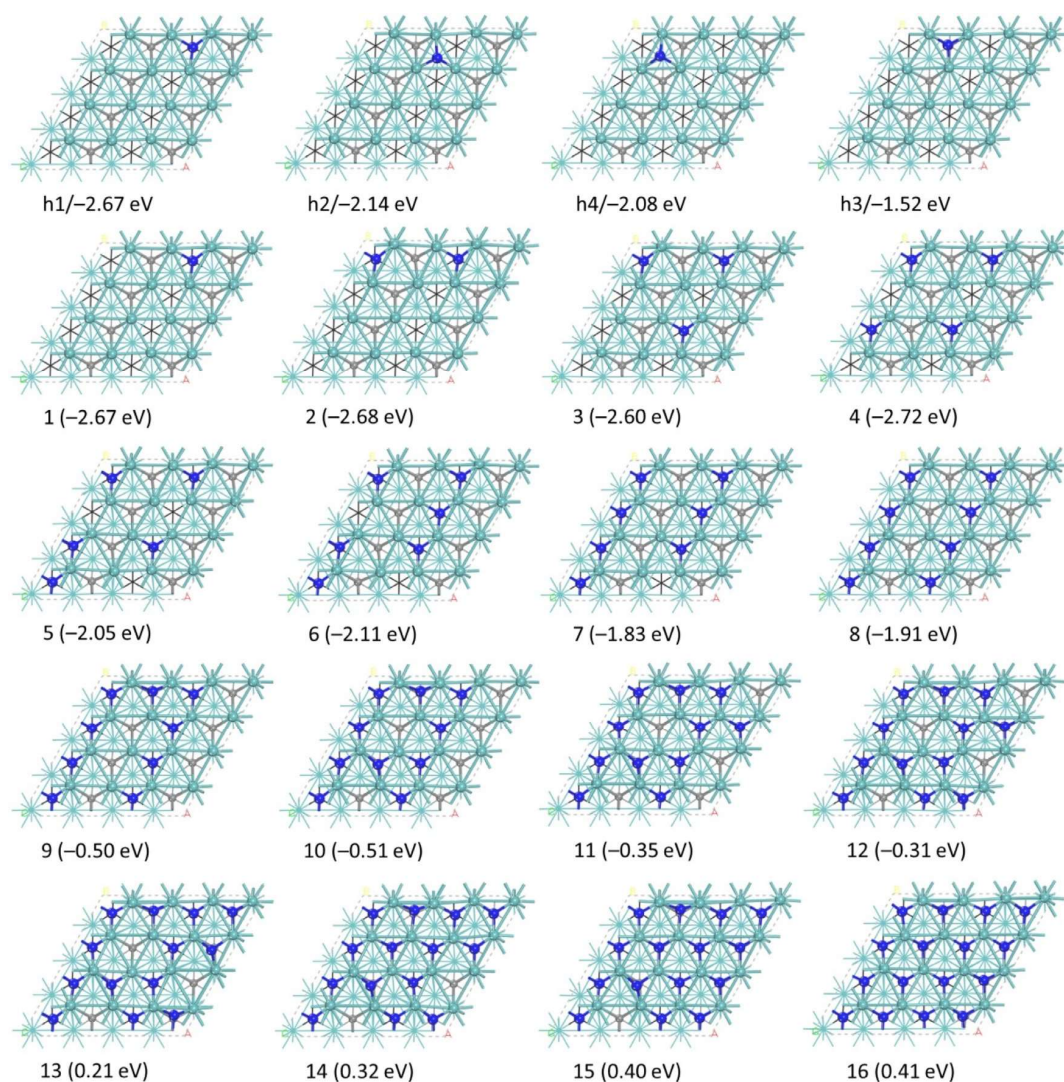


Fig. 5. Structures and energies ( $\Delta E_{\text{ads}}$ /eV) of the most stable adsorption sites for stepwise N adsorption on  $\text{Mo}_2\text{C}(001)$  surface (blue balls for N atoms; using gaseous  $\text{N}_2$  as reference). (For interpretation of the references to color in this figure legend, the reader is referred to the web version of this article.)

configurations at individual coverage with stepwise adsorption energies are summarized in Fig. 3. For  $n = 1-8$ , **h2** sites are preferably adsorbed close to **b2** site, and the stepwise adsorption energies are in close range of  $n = 2-4$ , and that for  $n = 5, 7$  and  $8$  decreases. Apart from  $n = 1$  and  $8$ , where the adsorbed  $\text{NH}_2$  are located at **b2** sites, other adsorption configurations have  $\text{NH}_2$  at **h2** or tilted **b2** sites. On the basis of the adsorption configuration of  $n = 8$ , stepwise  $\text{NH}_2$  adsorption at **b4** sites is computed and the stepwise adsorption decreases from  $n = 9-12$ . At  $n = 16$ , all **b2** and **b4** sites are occupied.

### 3.3. NH adsorption

NH radical can have several electronic configurations [66], and the ground state has a triplet state and the singlet state is much high in energy and less stable. For one NH adsorption (Fig. S9), five stable adsorption configurations were found. The adsorption configuration at **h1** site is most stable ( $-8.08$  eV), followed by that at **h2**, **h3** and **h4** sites ( $-7.91, -7.46$  and  $-7.78$  eV, respectively); and that at **t1** site is much high in energy and less stable ( $-6.57$  eV). In these adsorption configurations, NH is perpendicular to the surface. It is noted that no stable adsorption configurations at the bridge sites can be found.

Having the most stable adsorption configuration at the **h1** site, high coverage NH adsorption in remote sites has been computed (Fig. 4). From  $n = 1-4$ , the stepwise adsorption energies are close and those of  $n = 5-8$  are also close, but somewhat lower than that for  $n = 1-4$ . For  $n = 8$  (Fig. S10), we computed the adsorption configurations at **h2**, **h3** and **h4** sites; and they are higher in energy and less stable than that at **h1** site by  $0.33, 2.68$  and  $5.90$  eV, respectively.

### 3.4. Adsorption of N

For the adsorption of an N atom, only hollow sites adsorption configurations are found (Fig. 5). The most stable one is at **h1** site ( $-2.67$  eV), followed tightly by those at **h2** and **h4** sites ( $-2.14$  and  $-2.08$  eV) and that at **h3** site is least stable ( $-1.52$  eV). Following this energetic order, we computed N adsorption at high coverage. The stepwise adsorption energy for  $n = 1-4$  are close; and that for  $n = 5-8$  decreases with coverage increase. Significant low stepwise adsorption energies are found for  $n = 9-12$ , while those for  $n = 13-16$  are positive, indicating that thermodynamically it is not possible to occupy all hollow site by using molecular  $\text{N}_2$  gas as nitridation agent.

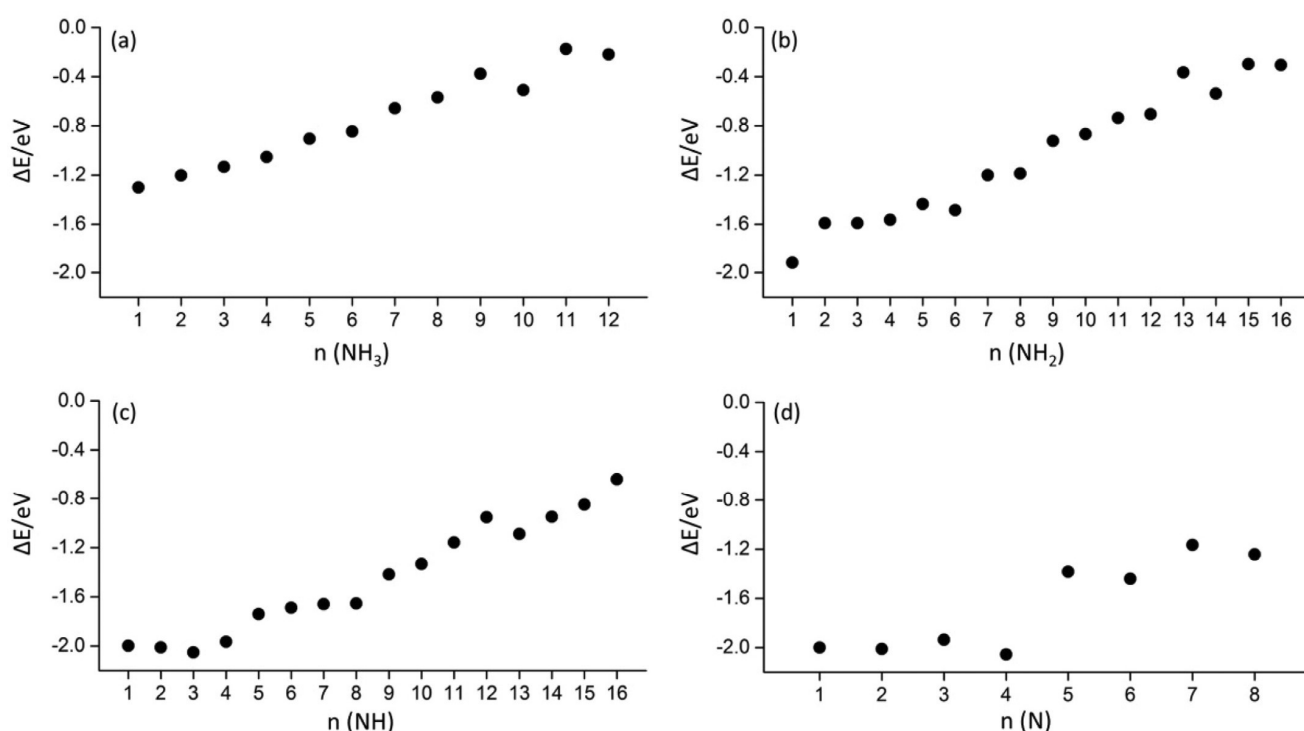
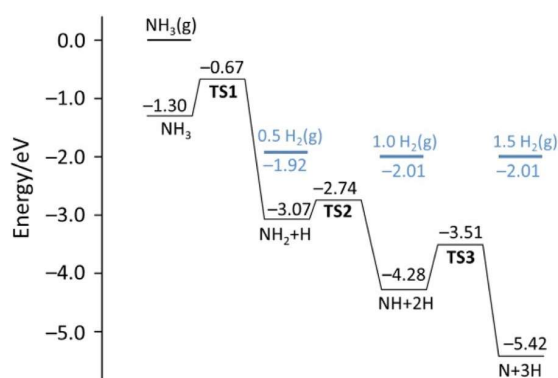


Fig. 6. Stepwise adsorption energies of  $\text{NH}_3$  (a);  $\text{NH}_2$  (b);  $\text{NH}$  (c) and  $\text{N}$  (d) at high coverage by using  $\text{NH}_3$  as nitridation agent. The calculated equation:  $\Delta E(\text{NH}_x) = E[(\text{NH}_x)_n/\text{slab}] - E[(\text{NH}_x)_{n-1}/\text{slab}] - (E[\text{NH}_3] - (3 - x)/2E[\text{H}_2])$ , for  $x = 3, 2, 1, 0$ .



Scheme 1. Potential energy surface of  $\text{NH}_3$  dissociative adsorption on  $\text{Mo}_2\text{C}(001)$  surface.

### 3.5. $\text{NH}_3$ dissociative adsorption

In addition to molecular adsorption,  $\text{NH}_3$  dissociative adsorption on the  $\text{Mo}_2\text{C}(001)$  surface is computed for understanding the nitridation process, where we used the most stable adsorption sites of  $\text{NH}_3$ ,  $\text{NH}_2$ ,  $\text{NH}$  and  $\text{N}$  discussed above, and the most stable adsorption sites of hydrogen were taken from previous report (Fig. S11) [37,39]. The structures of the IS, TS and FS of each step are shown in Fig. S12. The potential energy surface of  $\text{NH}_3$  successive dissociation is shown in Scheme 1.

Starting from  $\text{NH}_3$  at the **t1** site, the first step is  $\text{NH}_3$  dissociation into  $\text{NH}_2$  and  $\text{H}$  ( $\text{NH}_3 = \text{NH}_2 + \text{H}$ ); and this step has barrier of 0.63 eV and is exothermic by 1.13 eV. That the dissociation barrier is lower than the adsorption energy reveals that  $\text{NH}_3$  prefers dissociation. In the transition state (**TS1**, Fig. S12), the breaking N–H distance is 1.543 Å and the forming  $\text{NH}_2$  group is at the **b1** site with N–Mo distances of 2.916 and 2.111 Å; and the H atom is at the **b2** site with N–Mo distance

of 2.621 and 1.645 Å. In the final state (**FS1**, Fig. S12), the  $\text{NH}_2$  group is at the **b1** site and the H atom is at the **h1** site. After the dissociation, both  $\text{NH}_2$  and H migrate to the more stable remote sites, i.e.; the **b2** site for  $\text{NH}_2$  and another **h1** site for the H atom (**IS2**, Fig. S12), and the migration of the  $\text{NH}_2$  and H species is exothermic by 0.64 eV, and the overall first decomposition step of  $\text{NH}_3$  dissociative adsorption at the **t1** site is therefore exothermic by 1.77 eV.

Starting from  $\text{NH}_2$  at the **b2** site, the second dissociation step ( $\text{NH}_2 + \text{H} = \text{NH} + 2\text{H}$ ) is also favorable thermodynamically (−1.17 eV) and has much low barrier of 0.33 eV. The breaking N–H distance in the transition state (**TS2**, Figure S12) is 1.432 Å, and the  $\text{NH}$  group is at the **h1** site with N–Mo distances of 2.180, 2.180 and 2.097 Å; and the H atom is tilted at **b2** site. After the dissociation, the formed H atom at the **h1** site migrates to another **h1** site; and this is exothermic by 0.04 eV (**FS2**, Fig. S12). Totally, the second dissociation step is exothermic by 1.21 eV.

The last step of  $\text{NH}$  dissociation into  $\text{N}$  and  $\text{H}$  ( $\text{NH} + 2\text{H} = \text{N} + 3\text{H}$ ) has barrier of 0.77 eV and is exothermic by 1.01 eV. The higher barrier of this step is due to the perpendicular adsorption configuration of  $\text{NH}$  on the surface. The breaking N–H distance in the transition state (**TS3**, Fig. S12) is 1.314 Å and the N–Mo distances are 2.048, 2.058 and 2.013 Å at **h1** site. The dissociated H atom migrates by exothermic 0.13 eV, and the total reaction is exothermic by 1.14 eV for the last step.

On the basis of the stepwise decomposition, we evaluated the stepwise  $\text{H}_2$  evolution (Scheme 1). The desorption energies of 0.5  $\text{H}_2$ , 1.0  $\text{H}_2$  and 1.5  $\text{H}_2$  is 1.15, 2.27 and 3.41 eV, respectively; and this corresponds to the computed adsorption energy of one H atom on the clean surface (−1.15 eV) [37,39]. This indicates that all these hydrogen atoms are adsorbed on the surface because of the rather low coverage. Therefore, we computed the coverage-dependent  $\text{H}_2$  evolution on the basis of the high coverage adsorbed  $\text{NH}_2$ ,  $\text{NH}$  and  $\text{N}$  reported above; and such coverage-dependent  $\text{H}_2$  evolution can also provide useful information about the nitridation process by using  $\text{NH}_3$ ; and this is particularly interesting since transition-metal nitrides can be used widely as catalysts in hydro-treating reactions [67,68].

**Table 1**Comparison of the calculated barriers ( $E_{\text{ads}}$ , eV) and reaction energy ( $\Delta E_i$ , eV) for each decomposition step of  $\text{NH}_3$ .

surface	$E_{\text{ads}}$ (eV)	$\text{NH}_3 = \text{NH}_2 + \text{H}$ $E_a$ (eV)	$\Delta E_i$ (eV)	$\text{NH}_2 + \text{H} = \text{NH} + 2\text{H}$ $E_a$ (eV)	$\Delta E_i$ (eV)	$\text{NH} + 2\text{H} = \text{N} + 3\text{H}$ $E_a$ (eV)	$\Delta E_i$ (eV)
$\text{Mo}_2\text{C}(001)$	-1.30	0.63	-1.13	0.33	-1.17	0.77	-1.01
$\text{Fe}(110)$ [32]	-0.83	0.72	-0.62	0.24	-1.11	1.16	-0.43
$\text{Fe}(100)$ [69]	-0.92	0.95	-0.29	1.14	-0.32	0.78	-0.52
$\text{Co}(111)$ [32]	-0.68	1.01	-0.14	0.21	-0.44	1.06	0.10
$\text{Ni}(111)$ [32]	-0.75	1.11	-0.28	0.59	-0.57	1.11	0.06
$\text{Ni}(110)$ [70]	-0.80	0.80	-0.25	1.41	0.54	0.70	0.29
$\text{Ir}(100)$ [71]	-0.96	0.86	-0.55	1.02	-0.04	0.96	0.33
$\text{Pd}(111)$ [72]	-0.84	1.71	0.49	1.54	0.15	1.70	0.71
$\text{Cu}(111)$ [73]	-0.46	1.67	0.65	1.35	0.76	1.98	1.55
$\text{CoO}(100)$ [74]	-0.61	3.13	0.89	3.40	1.62	3.03	1.10
$\gamma\text{-Mo}_2\text{N}(100)$ [34]	-0.97	1.20	0.02	1.18	-0.12	1.04	0.40
		1.28	0.30	1.18	0.29	2.05	0.69
		1.31	0.80	—	—	—	—
$\gamma\text{-Mo}_2\text{N}(111)$ [34]	-1.18	0.64	-0.89	0.22	-1.09	1.12	-0.11
		0.78	-0.58	0.46	-0.97	1.14	-0.04

Different from above discussed  $\text{NH}_x$  ( $x = 0, 1, 2, 3$ ) coverages on  $\text{Mo}_2\text{C}(001)$  by using the corresponding gaseous radical as reference, we calculated the saturation of coverage for each  $\text{NH}_x$  intermediate by using gaseous  $\text{NH}_3$  as nitridation agent (Fig. 6). The saturation coverage of  $\text{NH}_3$ ,  $\text{NH}_2$ ,  $\text{NH}$  and  $\text{N}$  can have 12, 16, 16 and 8 surface species, respectively or 0.75, 1.0, 1.0 and 0.5 monolayer coverage on the basis of the exposed surface Mo atoms. The saturation coverage of  $\text{NH}_2$  and  $\text{NH}$  by using gaseous  $\text{NH}_3$  is the same as that by using the  $\text{NH}_2$  and  $\text{NH}$  radical, respectively. The saturation coverage using gaseous  $\text{N}_2$  can have 12 N atoms (0.75 ML) on the surface; while can have 8 N atoms (0.5 ML) using gaseous  $\text{NH}_3$ .

On the basis of these results and the available literature data (Table 1), one can compare the metal and surface dependent  $\text{NH}_3$  decomposition. As listed in Table 1, four types of reactions can be categorized. The first type is the full decomposition, in which all three elementary steps ( $\text{NH}_3 = \text{NH}_2 + \text{H}$ ;  $\text{NH}_2 = \text{NH} + \text{H}$ ;  $\text{NH} = \text{N} + \text{H}$ ) are exothermic, and this can be found on the  $\text{Mo}_2\text{C}(001)$ ,  $\text{Fe}(110)$  and  $\text{Fe}(100)$  surfaces. The second type has partial decomposition, in which the first two elementary steps are exothermic and the last step is endothermic or close to thermal neutral, such as on the  $\text{Co}(111)$  and  $\text{Ni}(111)$  surfaces. The third type has also partial decomposition, but the first step is exothermic and the second and third steps are endothermic, such as on the  $\text{Ni}(110)$  and  $\text{Ir}(100)$ . The clear surface dependence is shown between  $\text{Ni}(111)$  and  $\text{Ni}(110)$  surfaces. The last type shows that all three elementary steps are endothermic, such as on the  $\text{Pd}(111)$  and  $\text{Cu}(111)$  surfaces. On the  $\text{CoO}(100)$  surface,  $\text{NH}_3$  does not decompose and all three elementary steps are endothermic and have extremely high barriers. In addition, surface dependent activity is also found on the  $\gamma\text{-Mo}_2\text{N}(100)$  and  $\gamma\text{-Mo}_2\text{N}(111)$  surfaces, i.e.;  $\text{NH}_3$  decomposes hardly on the  $\gamma\text{-Mo}_2\text{N}(100)$  surface, but very easily and fully on the  $\gamma\text{-Mo}_2\text{N}(111)$  surface, like on the  $\text{Mo}_2\text{C}(001)$ ,  $\text{Fe}(110)$  and  $\text{Fe}(100)$  surfaces.

#### 4. Conclusion

Density functional theory computations were carried out to study the adsorption and sequential decomposition of ammonia on the hexagonal metallic  $\text{Mo}_2\text{C}(001)$  surface. The ultimate goal of this study is the nitridation degree of the  $\text{Mo}_2\text{C}(001)$  surface by using  $\text{NH}_3$  as environment agent. The metallic  $\text{Mo}_2\text{C}(001)$  surface has two types of Mo atoms differentiated by the local carbon environment, the Mo atom with two carbon atoms has higher  $\text{NH}_3$  adsorption energy than that with one carbon atom; and each type has eight expose Mo atoms.

The adsorption of  $\text{NH}_3$  prefers the top site via the nitrogen lone pair electrons in the entire coverage range, and the saturation coverage is 0.75 monolayer on the basis of exposed surface Mo atoms. There is no hydrogen bonding among the adsorbed  $\text{NH}_3$  molecules. It is found that

$\text{NH}_3$  prefers decomposition instead of desorption, and all three elementary decomposition steps have low barriers and are exothermic; and this shows that full decomposition into surface N and H atoms are favored kinetically and thermodynamically.

The adsorption of  $\text{NH}_2$  is coverage-dependent; i.e.; at low coverage  $\text{NH}_3$  adsorption at both bridge and hollow sites have close energies, and bridge sites are preferred at high coverage up to saturation; and the saturation coverage is 1.0 monolayer. In contrast, the adsorption of  $\text{NH}$  and  $\text{N}$  is coverage independent, and only hollow sites are preferred in the entire coverage range. The saturation coverage for  $\text{NH}$  and  $\text{N}$  is 1.0 and 0.5 monolayer, respectively.

The dissociative adsorption of ammonia among others metals and molybdenum nitrides has been categorized and compared. Our results provide the basis for studying the surface properties and catalytic reaction of nitrated  $\text{Mo}_2\text{C}$  surfaces.

#### Acknowledgments

F. Wang thanks the support of the China Scholarship Council (CSC); and the general financial support from the BMBF and the state of Mecklenburg-Vorpommern, Germany, is acknowledged.

#### Supplementary materials

Supplementary material associated with this article can be found, in the online version, at [doi:10.1016/j.susc.2019.121466](https://doi.org/10.1016/j.susc.2019.121466).

#### References

- [1] L.E. Toth, Transition Metal Carbides and Nitrides, Academic Press, New York and London, 1971.
- [2] A.L.I.V.A. Gubanov, V.P. Zhukov, Electronic Structure of Refractory Carbides and Nitrides, Cambridge University Press, 1994.
- [3] S.T. Oyama, The Chemistry of Transition Metal Carbides and Nitrides, Blackie Academic & Professional, an important of Chapman & Hall, Wester Cleddens Road, Bishopbriggs, Glasgow G64 2NZ, 1996.
- [4] J.G. Chen, J. Eng, S.P. Kelty, Catal. Today 43 (1998) 147–158.
- [5] H.H. Hwu, J.G. Chen, Chem. Rev. 105 (2005) 185–212.
- [6] R.B. Levy, M. Boudart, Science 181 (1973) 547.
- [7] M. Nagai, K. Matsuda, J. Catal. 238 (2006) 489–496.
- [8] J.A. Schaidle, A.C. Lausche, L.T. Thompson, J. Catal. 272 (2010) 235–245.
- [9] M. Xiang, D. Li, W. Li, B. Zhong, Y. Sun, Fuel 85 (2006) 2662–2665.
- [10] S. Zaman, K.J. Smith, Catalysis Reviews 54 (2012) 41–132.
- [11] V. Sundaramurthy, A.K. Dalai, J. Adjaye, App. Catal. B: Environ. 68 (2006) 38–48.
- [12] H.A. Al-Megren, S.L. González-Cortés, T. Xiao, M.L.H. Green, Appl. Catal., A 329 (2007) 36–45.
- [13] M.K. Neylon, S. Choi, H. Kwon, K.E. Curry, L.T. Thompson, Appl. Catal., A 183 (1999) 253–263.
- [14] S.J. Ardakani, X. Liu, K.J. Smith, Appl. Catal., A 324 (2007) 9–19.
- [15] R. Barthos, F. Solymosi, J. Catal. 249 (2007) 289–299.
- [16] R. Jiang, J. Fan, L. Hu, Y. Dou, X. Mao, D. Wang, Electrochim. Acta 261 (2018) 578–587.

- [17] C. Wan, B.M. Leonard, *Chem. Mater.* 27 (2015) 4281–4288.
- [18] K. Zhang, Y. Zhao, D. Fu, Y. Chen, *J. Mater. Chem. A* 3 (2015) 5783–5788.
- [19] W.F. Chen, C.H. Wang, K. Sasaki, N. Marinkovic, W. Xu, J.T. Muckerman, Y. Zhu, R.R. Adzic, *Energy Environ. Sci.* 6 (2013) 943–951.
- [20] L. Liao, S. Wang, J. Xiao, X. Bian, Y. Zhang, M.D. Scanlon, X. Hu, Y. Tang, B. Liu, H.H. Girault, *Energy Environ. Sci.* 7 (2014) 387–392.
- [21] S.K. Kim, Y.-J. Zhang, H. Bergstrom, R. Michalsky, A. Peterson, *ACS Catal.* 6 (2016) 2003–2013.
- [22] G. Papapolymerou, V. Bontozoglou, *J. Mol. Catal. A: Chem.* 120 (1997) 165–171.
- [23] T.V. Choudhary, C. Sivadinarayana, D.W. Goodman, *Catal. Lett.* 72 (2001) 197–201.
- [24] R. Lan, J.T.S. Irvine, S. Tao, *Int. J. Hydrogen Energy* 37 (2012) 1482–1494.
- [25] Y. Ozawa, Y. Tochiwara, *Catal. Today* 164 (2011) 528–532.
- [26] R. Schlögl, *Angew. Chem. Int. Ed.* 42 (2003) 2004–2008.
- [27] H.K.G. Ertl, F. Schüth, J. Weitkamp, *Handbook of Heterogeneous Catalysis*, Wiley-VCH, Weinheim, Germany, 2008.
- [28] S.T. Oyama, *Catal. Today* 15 (1992) 179–200.
- [29] J.G. Choi, *J. Ind. Eng. Chem.* 10 (2004) 967–971.
- [30] W. Zheng, T.P. Cotter, P. Kaghazchi, T. Jacob, B. Frank, K. Schlichte, W. Zhang, D.S. Su, F. Schüth, R. Schlögl, *J. Am. Chem. Soc.* 135 (2013) 3458–3464.
- [31] X. Zhang, Z. Lu, D. Ma, Z. Yang, *Int. J. Hydrogen Energy* 40 (2015) 346–352.
- [32] X. Duan, J. Ji, G. Qian, C. Fan, Y. Zhu, X. Zhou, D. Chen, W. Yuan, *J. Mol. Catal. A: Chem.* 357 (2012) 81–86.
- [33] G. Lanzani, K. Laasonen, *Int. J. Hydrogen Energy* 35 (2010) 6571–6577.
- [34] J. Zhao, C. Cui, H. Wang, J. Han, X. Zhu, Q. Ge, *J. Phys. Chem. C* 123 (2019) 554–564.
- [35] T. Wang, X. Liu, S. Wang, C. Huo, Y.-W. Li, J. Wang, H. Jiao, *J. Phys. Chem. C* 115 (2011) 22360–22368.
- [36] T. Wang, S. Wang, Y.-W. Li, J. Wang, H. Jiao, *J. Phys. Chem. C* 116 (2012) 6340–6348.
- [37] Y. Shi, Y. Yang, Y.-W. Li, H. Jiao, *Appl. Catal., A* 524 (2016) 223–236.
- [38] T. Wang, Y.-W. Li, J. Wang, M. Beller, H. Jiao, *J. Phys. Chem. C* 118 (2014) 3162–3171.
- [39] T. Wang, Y.-W. Li, J. Wang, M. Beller, H. Jiao, *J. Phys. Chem. C* 118 (2014) 8079–8089.
- [40] T. Wang, Q. Luo, Y.-W. Li, J. Wang, M. Beller, H. Jiao, *Appl. Catal., A* 478 (2014) 146–156.
- [41] T. Wang, X. Tian, Y. Yang, Y.-W. Li, J. Wang, M. Beller, H. Jiao, *Phys. Chem. Chem. Phys.* 17 (2015) 1907–1917.
- [42] Q. Luo, T. Wang, G. Walther, M. Beller, H. Jiao, *J. Power Sources* 246 (2014) 548–555.
- [43] Y. Shi, Y. Yang, Y.-W. Li, H. Jiao, *ACS Catal.* 6 (2016) 6790–6803.
- [44] Y. Shi, Y. Yang, Y.-W. Li, H. Jiao, *Catal. Sci. Technol.* 6 (2016) 4923–4936.
- [45] G. Kresse, J. Furthmüller, *Comput. Mater. Sci.* 6 (1996) 15–50.
- [46] G. Kresse, J. Furthmüller, *Phys. Rev. B* 54 (1996) 11169–11186.
- [47] P.E. Blöchl, *Phys. Rev. B* 50 (1994) 17953–17979.
- [48] G. Kresse, D. Joubert, *Phys. Rev. B* 59 (1999) 1758–1775.
- [49] J.P. Perdew, K. Burke, M. Ernzerhof, *Phys. Rev. Lett.* 77 (1996) 3865–3868.
- [50] S. Grimme, J. Antony, S. Ehrlich, H. Krieg, *J. Chem. Phys.* 132 (2010) 154104.
- [51] S. Grimme, S. Ehrlich, L. Goerigk, *J. Comput. Chem.* 32 (2011) 1456–1465.
- [52] G. Henkelman, B.P. Uberuaga, H. Jónsson, *J. Chem. Phys.* 113 (2000) 9901–9904.
- [53] T.P. St. Clair, S.T. Oyama, D.F. Cox, S. Otani, Y. Ishizawa, R.-L. Lo, K.-i. Fukui, Y. Iwasawa, *Surf. Sci.* 426 (1999) 187–198.
- [54] A.N. Christensen, *Acta Chem. Scand.*, A 31 (1977) 509–511.
- [55] E. Parthé, V. Sadogopan, *Acta Crystallogr.* 16 (1963) 202–205.
- [56] J. Dubois, T. Epicier, C. Esnouf, G. Fantozzi, P. Convert, *Acta Metall.* 36 (1988) 1891–1901.
- [57] T. Epicier, J. Dubois, C. Esnouf, G. Fantozzi, P. Convert, *Acta Metall.* 36 (1988) 1903–1921.
- [58] J. Haines, J. Leger, C. Chateau, J. Lowther, *J. Phys.: Condens. Matter* 13 (2001) 2447.
- [59] R.J. Fries, C.P. Kempter, *Anal. Chem.* 32 (1960) 1898–1898.
- [60] C.J. Cramer, *Essentials of Computational Chemistry: Theories and Models*, 2nd Edition, Wiley, England, 2004.
- [61] W. Tang, E. Sanville, G. Henkelman, *J. Phys.: Condens. Matter* 21 (2009) 084204.
- [62] E. Sanville, S.D. Kenny, R. Smith, G. Henkelman, *J. Comput. Chem.* 28 (2007) 899–908.
- [63] G. Henkelman, A. Arnaldsson, H. Jónsson, *Comput. Mater. Sci.* 36 (2006) 354–360.
- [64] M. Yu, D.R. Trinkle, *J. Chem. Phys.* 134 (2011) 064111.
- [65] T. Koenig, J.A. Hoobler, C.E. Klopfenstein, G. Hedden, F. Sunderman, B.R. Russell, *J. Am. Chem. Soc.* 96 (1974) 4573–4577.
- [66] T. Fueno, V. Bonacic-Koutecky, J. Koutecky, *J. Am. Chem. Soc.* 105 (1983) 5547–5557.
- [67] R.C.V. McGee, S.K. Bej, L.T. Thompson, *Appl. Catal., A* 284 (2005) 139–146.
- [68] W.-F. Chen, K. Sasaki, C. Ma, A.I. Frenkel, N. Marinkovic, J.T. Muckerman, Y. Zhu, R.R. Adzic, *Angew. Chem. Int. Ed.* 51 (2012) 6131–6135.
- [69] S.C. Yeo, S.S. Han, H.M. Lee, *J. Phys. Chem. C* 118 (2014) 5309–5316.
- [70] X. Duan, G. Qian, C. Fan, Y. Zhu, X. Zhou, D. Chen, W. Yuan, *Surf. Sci.* 606 (2012) 549–553.
- [71] C.-z. He, H. Wang, L.-y. Huai, J.-y. Liu, *J. Phys. Chem. C* 116 (2012) 24035–24045.
- [72] Z. Jiang, Q. Pan, M. Li, T. Yan, T. Fang, *Appl. Surf. Sci.* 292 (2014) 494–499.
- [73] Z. Jiang, P. Qin, T. Fang, *Chem. Phys.* 445 (2014) 59–67.
- [74] K. Shojaei, B.S. Haynes, A. Montoya, *Mater. Chem. Phys.* 156 (2015) 141–149.



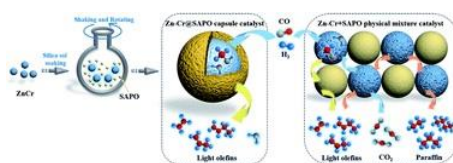
### 3.4 Design of a core-shell catalyst: an effective strategy for suppressing side reactions in syngas for direct selective conversion to light olefins

Li Tan, Fan Wang, Peipei Zhang, Yuichi Suzuki, Yingquan Wu, Jiangang Chen, Guohui Yang\*, Noritatsu Tsubaki\*

*Chem. Sci.* **2020**, *11*, 4097–4105.

DOI: 10.1039/c9sc05544d

**Summary:** An elegant catalyst is designed via the encapsulation of metallic oxide Zn–Cr inside of zeolite SAPO34 as a core-shell structure (Zn–Cr@SAPO) to realize the coupling of methanol-synthesis and methanol-to-olefin reactions. The unique strategy is effective to advance light olefin selectivity and limit CO<sub>2</sub> formation in the STO (syngas to light olefins) synthesis by yielding a light olefin selectivity as high as 64.31% with a CO<sub>2</sub> selectivity at only 36.16%. The different absorption barriers and active phases of the core (Zn–Cr) and shell (SAPO34) play a key role to maximize the catalytic performance. The lower adsorption energy and larger surface area of the SAPO34 shell protect the Zn–Cr core to limit the water gas shift (WGS) reaction, which is demonstrated by DFT calculation. The hierarchical structure and extremely short distance between the two active components allow the Zn–Cr@SAPO capsule catalyst to demonstrate better mass transfer and diffusion for a better synergistic effect. At the same time, the confinement effect of the capsule catalyst also decreases the possibility of side reactions and enhances the light olefin selectivity. This type of catalyst has superior potential since it can be easily scaled up to industrial requirements in the future and it has extensive application prospects for various reactions.



#### Author contributions

In this work I designed and performed all calculations and analyzed all the results. I completed writing and proofreading based on the suggestions and comments of co-authors. My contribution to the computation is 100%.





Cite this: *Chem. Sci.*, 2020, 11, 4097

All publication charges for this article have been paid for by the Royal Society of Chemistry

# Design of a core-shell catalyst: an effective strategy for suppressing side reactions in syngas for direct selective conversion to light olefins†

Li Tan,<sup>a,b</sup> Fan Wang,<sup>c</sup> Peipei Zhang,<sup>b</sup> Yuichi Suzuki,<sup>b</sup> Yingquan Wu,<sup>d</sup> Jiangang Chen,<sup>d</sup> Guohui Yang<sup>b,\*</sup> and Noritatsu Tsubaki<sup>b,\*</sup>

An elegant catalyst is designed via the encapsulation of metallic oxide Zn–Cr inside of zeolite SAPO34 as a core-shell structure (Zn–Cr@SAPO) to realize the coupling of methanol-synthesis and methanol-to-olefin reactions. It can not only break through the limitation of the Anderson–Schulz–Flory distribution but can also overcome the disadvantages of physical mixture catalysts, such as excessive CO<sub>2</sub> formation. The confinement effect, hierarchical structure and extremely short distance between the two active components result in the Zn–Cr@SAPO capsule catalyst having better mass transfer and diffusion with a boosted synergistic effect. Due to the difference between the adsorption energies of the Zn–Cr metallic oxide/SAPO zeolite physical mixture and capsule catalysts, the produced water and light olefins are easily removed from the Zn–Cr@SAPO capsule catalyst after formation, suppressing the side reactions. The light olefin space time yield (STY) of the capsule catalyst is more than twice that of the typical physical mixture catalyst. The designed capsule catalyst has superior potential for scale-up in industrial applications while simultaneously extending the capabilities of hybrid catalysts for other tandem catalysis reactions through this strategy.

Received 3rd November 2019  
Accepted 18th March 2020

DOI: 10.1039/c9sc05544d

rsc.li/chemical-science

## Introduction

C1 chemistry has become a hot research area because one of the most challenging scientific issues is to find alternative energy sources for petroleum in the 21<sup>st</sup> century. With the development of biomass reforming technology and methane mining technology in shale gas and combustible ice, syngas (a CO + H<sub>2</sub> mixture) can be used as a much cheaper stock with larger reserves to synthesize chemicals and energy fuels via a non-petroleum route. Conversion to light olefins (C<sub>2</sub> to C<sub>4</sub>) has attracted immense interest since light olefins are playing more important roles in the chemical industry for a long period.<sup>1–3</sup> Light olefins are widely used in the organic chemicals with the largest production volumes all over the world.<sup>4</sup> Currently, petroleum resources continue to decrease, which raises barriers

for the traditional synthesis of light olefins from naphtha cracking.<sup>5,6</sup>

To solve this problem, considerable studies on the conversion of syngas (synthesis gas, CO + H<sub>2</sub>) to light olefins by the Fischer–Tropsch synthesis have been reported due to the cost-effective feeding stock as compared to crude oil, which is called Fischer–Tropsch to olefins (FTTO).<sup>7–13</sup> CO can be connected to H<sub>2</sub> on the surface of the catalyst and the formation of CH<sub>x</sub> (x = 1, 2, 3) takes place to convert to C<sub>n</sub>H<sub>m</sub> by C–C coupling; finally, the alkane or olefin products are formed by the hydrogenation or dehydrogenation of C<sub>n</sub>H<sub>m</sub>. However, the Anderson–Schulz–Flory distribution affects the selectivity for light olefins, which is a maximum of 58% theoretically.<sup>5</sup>

In another way, light olefins can also be obtained from methanol over a SAPO34 zeolite, namely by the methanol to olefin (MTO) process;<sup>14–19</sup> methanol synthesis from syngas has been a mature industrial product since 1923, which was built by BASF.<sup>20</sup> Using a hybrid catalyst is also a feasible way to realize the tandem catalysis reaction from complex to simple approaches.<sup>21–29</sup> For the above-mentioned findings, a new direct route for syngas to light olefin (STO) synthesis using physical mixture catalysts has been reported.<sup>30–36</sup> The light olefin selectivity breaks through the Anderson–Schulz–Flory distribution, which is beyond 58%. Even though it is a discovery of great importance, the challenges of suppressing highly undesirable CO<sub>2</sub> selectivity of approximately 50% and uneven mixing of

<sup>a</sup>Institute of Molecular Catalysis and Operando Characterization, State Key Laboratory of Photocatalysis on Energy and Environment, College of Chemistry, Fuzhou University, Fuzhou, 350108, China. E-mail: thomas@eng.u-toyama.ac.jp

<sup>b</sup>Department of Applied Chemistry, School of Engineering, University of Toyama, Gofuku 3190, Toyama 930-8555, Japan. E-mail: tsubaki@eng.u-toyama.ac.jp; thomas@eng.u-toyama.ac.jp

<sup>c</sup>Leibniz-Institut für Katalyse e.V. an der Universität Rostock, Albert-Einstein Strasse 29a, 18059 Rostock, Germany

<sup>d</sup>State Key Laboratory of Coal Conversion, Institute of Coal Chemistry, Chinese Academy of Sciences, Taiyuan, 030001, China

† Electronic supplementary information (ESI) available. See DOI: 10.1039/c9sc05544d

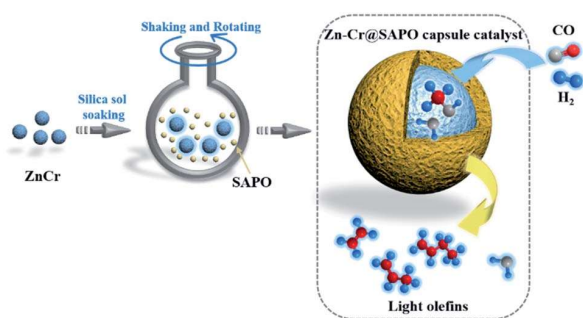


physical mixture catalysts still need to be optimized for its further use in industrialization.

A capsule catalyst with a tailor-made core-shell structure has been designed for several given reactions. Specifically, it can connect two or more consecutive catalytic processes into a direct synthesis. In our previous studies, several successful applications of capsule catalysts have been reported.<sup>37–43</sup> For instance, a Co–Al<sub>2</sub>O<sub>3</sub> (core)@H-β-zeolite (shell) capsule catalyst was designed for the direct synthesis of isoparaffins from syngas *via* the Fischer-Tropsch synthesis. Syngas passes through the zeolite membrane channels to reach the core catalyst, where it forms normal paraffins. These linear hydrocarbons exit by diffusion through the zeolite membrane and those with a straight-chain structure have a chance of being cracked and isomerized at the acidic sites of the zeolite.<sup>39</sup> The capsule catalyst (Cu–ZnO–Al<sub>2</sub>O<sub>3</sub> was encapsulated by an H-ZSM-5 layer) for a syngas to DME (CH<sub>3</sub>OCH<sub>3</sub>) direct synthesis has also been successfully prepared. The formed methanol on the Cu–ZnO–Al<sub>2</sub>O<sub>3</sub> catalyst from syngas can easily be converted to DME *in situ* by the H-ZSM-5 layer.<sup>40</sup>

In this study, the core-shell catalyst comprises metallic oxide Zn–Cr covered by a SAPO34 layer and is used for STO (syngas to light olefins) synthesis. The catalyst is prepared by a modified physical encapsulation method.<sup>41–43</sup> With this tailor-made designed catalyst, methanol can form on the metallic oxide Zn–Cr initially, then the methanol will pass through the SAPO34 membrane to dehydrate to light olefins, as illustrated in Scheme 1.

The SAPO34 shell can also protect the metallic oxide Zn–Cr core to block the contact of the formed light olefins and CO<sub>2</sub>. As a result, the light olefin product has difficulty further hydrogenating into a paraffin on the metallic oxide Zn–Cr. Meanwhile, the water gas shift reaction on Zn–Cr is also limited by SAPO34. A DFT study was performed that clearly shows that the adsorption energies of H<sub>2</sub>O and C<sub>2</sub>–C<sub>4</sub> light olefins on the SAPO34 shell are greater than on the metallic oxide Zn–Cr core, which provides theoretical evidence for illustrating the protective function of the SAPO34 shell. Herein, in contrast to the regular hybrid or physical mixture catalyst, a capsule catalyst can significantly achieve enhanced light olefin selectivity while limiting CO<sub>2</sub> formation successfully.



Scheme 1 The preparation of a Zn–Cr@SAPO catalyst and the strategy for light olefin synthesis from syngas.

## Results and discussion

### Design of active physical mixture catalysts in STO reaction

In our study, we first applied a CO hydrogenation catalyst of Zn–Cr prepared by a co-precipitation method for syngas conversion (Fig. 1A and B). The Zn–Cr metallic oxide catalyst is pre-treated and activated by H<sub>2</sub> to form oxygen vacancies at temperatures below 400 °C, as given in Fig. S1†. In the reaction, the selectivity of methanol is as high as 92.58% at 300 °C under 2.0 MPa (Table S2†). In detail, CO is absorbed at the oxygen vacancies then dissociated and hydrogenated by H<sub>2</sub> gradually to CH<sub>3</sub>O, followed by further hydrogenation to methanol. After the formation of oxygen vacancies, the number of electrons and magnetic moments in the vicinity of Zn increases and there are many electrons located above the highest valence band of the oxide.<sup>49</sup> Thus, the transfer of these energetic electrons to methoxyl promotes its adsorption at the oxygen vacancies. However, by increasing the temperature (300–450 °C) and pressure (2.0–5.0 MPa), light olefin selectivity reached a maximum of 20% with nearly 50% CO<sub>2</sub> produced (Table S1–S3†). It shows that the reaction process has a high barrier to the

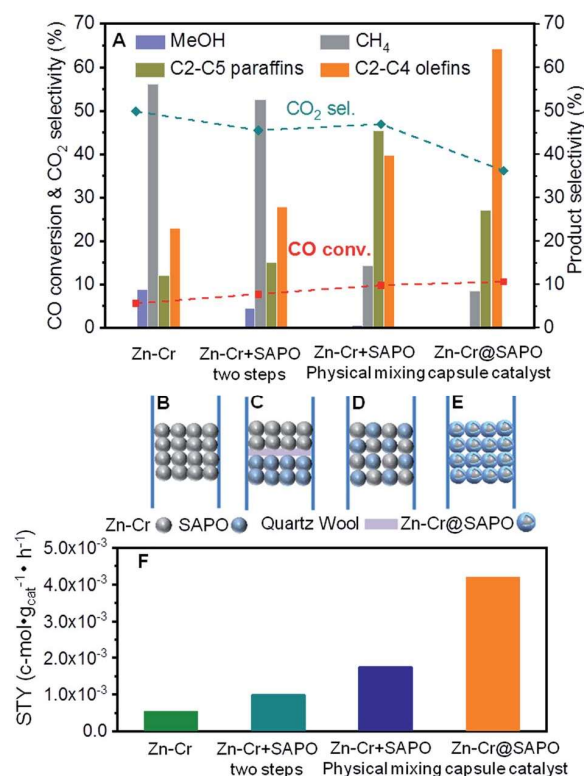


Fig. 1 The catalytic performance over different assembly models of catalysts. Reaction condition: H<sub>2</sub>/CO = 2.0, *P* = 2.0 MPa, *T* = 400 °C, space velocity = 6480 cm<sup>3</sup> h<sup>−1</sup> g<sub>cat</sub><sup>−1</sup>. (A) CO conversion and product selectivity over varied catalysts, CO<sub>2</sub> is excluded in the histogram. (B) Zn–Cr metallic oxide catalyst. (C) Dual bed of Zn–Cr metallic oxide and SAPO34 zeolite catalyst. (D) Physical mixture of Zn–Cr metallic oxide and SAPO34 zeolite catalyst. (E) Capsule catalyst of Zn–Cr metallic oxide and SAPO34 zeolite components. (F) The space time yield of light olefins over different catalysts.



## Edge Article

next MTO step on this sole metallic oxide catalyst. The Zn–Cr metallic oxide does not provide enough active sites for methanol to further dehydrate to light olefins. Thus, the SAPO34 zeolite prepared by a hydrothermal synthesis method was introduced as a C–C coupling catalyst for continuing the light olefin synthesis to realize the STO route. Initially, the SAPO34 zeolite is packed below the Zn–Cr catalyst using a layer of quartz wool to separate these two types of components (Fig. 1A and C). The light olefin selectivity slightly increased to 27.86% but 52.58% of CH<sub>4</sub> and 45.50% of CO<sub>2</sub> are produced, which is far from the target, as given in Fig. 1A and Table S1.† This may be due to the formed methanol and water on the Zn–Cr metallic oxide, which makes it difficult to attach the SAPO34 zeolite for further tandem catalysis reaction and drainage. The methanol and water are involved more readily in further methanation and the WGS reaction with the CO absorbed on the Zn–Cr metallic oxide defects, according to its thermodynamic equilibrium.<sup>50,51</sup>

In order to accelerate the tandem catalysis process as well as mass transfer and diffusion, two kinds of components were physically mixed as a uniform distribution catalyst to shorten the distance between the two different active phases (Fig. 1D). Several reaction conditions were investigated by varying the space velocity (2160–6480 cm<sup>3</sup> h<sup>−1</sup> g<sub>cat</sub><sup>−1</sup>); the light olefin selectivity was boosted to 39.70% at most as the space velocity increased (Fig. 1A and Table S1†). These findings prove that shortening the distance of two different active phases is conducive to the light olefin synthesis. Furthermore, from the investigation of the catalyst acidity, the NH<sub>3</sub>-TPD profiles reveal that the Zn–Cr catalyst has the appropriate acidity to form methanol from CO hydrogenation;<sup>52,53</sup> meanwhile, the acidity of the Zn–Cr metallic oxide and SAPO34 zeolite is not too strong to limit the light olefin synthesis, as given in Fig. S2,† because the strongly acidic catalyst will suppress light olefin formation and favour alkanes in the product distribution.<sup>54</sup>

### Design of powerful capsule catalyst to address the problems of physical mixture catalysts

According to the above results, the capsule catalyst was explored for STO synthesis since it has a unique confinement effect, the ability to regulate a tandem-catalysis reaction sequence, and good mass transfer and diffusion performance (Fig. 1E). The Zn–Cr/SAPO weight ratio of the capsule catalyst is 4 : 1 according to the ICP results (Table S4†). In the reaction, as shown in Fig. 1A, the light olefin selectivity is significantly enhanced to 64.31% with only 36.16% CO<sub>2</sub> formation on the Zn–Cr@SAPO catalyst. Hence, its light olefin space time yield of  $4.2 \times 10^{-3}$  cmol·g<sub>cat</sub><sup>−1</sup>·h<sup>−1</sup> is notably higher than that of any other type of catalyst (Fig. 1F). The reason is that the SAPO34 shell of the Zn–Cr@SAPO catalyst prevents the formed light olefins from further hydrogenating into alkanes on the *in situ* or neighbouring Zn–Cr active sites. At the same time, the SAPO34 shell also protects the Zn–Cr core from further water gas shift (WGS) reactions on the core due to its better water absorbency with larger surface area (Table S4†). It is clear that the capsule catalyst has an advantage over the physical mixture catalyst because of the much higher light olefin selectivity with lower

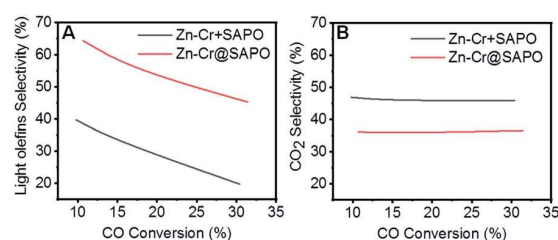


Fig. 2 Relationship curves of CO conversion vs. (A) light olefin selectivity and (B) CO<sub>2</sub> selectivity of physical mixture and capsule catalysts. Reaction conditions: H<sub>2</sub>/CO = 2.0, P = 2.0 MPa, T = 400 °C.

CO<sub>2</sub> selectivity at the same CO conversion level (Fig. 2). Consequently, the product distribution favours light olefins while CO<sub>2</sub> is greatly suppressed by the synergistic effects and confinement effect of this unique core–shell structured catalyst. Meanwhile, CH<sub>4</sub> selectivity is also decreased because the conversion of CH<sub>3</sub>O species to CH<sub>4</sub> is limited in the SAPO34 zeolite shell considering the extremely short distance between the two components, which leads to better mass transfer and MTO-oriented reaction relay.<sup>55</sup>

In particular, the formation of CH<sub>3</sub>OH or CH<sub>4</sub> from intermediate CH<sub>3</sub>O hydrogenation depends on H donor-attaching C or O on the active surface sites of the Zn–Cr metallic oxide. The reaction channel of the Zn–Cr metallic oxide catalyst to CH<sub>3</sub>OH has a reaction barrier of 1.33 eV, which is kinetically much more favourable in comparison to CH<sub>4</sub> formation with a reaction barrier of 2.41 eV.<sup>49</sup> Theoretically, accompanied by CH<sub>3</sub>OH accumulation on the active sites, the product distribution will shift to CH<sub>4</sub> according to the chemical equilibrium between the two competing reactions. Therefore, methane production can be effectively inhibited by the fast scavenging of the accumulated CH<sub>3</sub>OH over the SAPO34 zeolite shell to obtain target products with high selectivity while decreasing CH<sub>4</sub> selectivity.

To clarify the influence of the reaction conditions on the STO synthesis with the Zn–Cr@SAPO capsule catalyst, the effects of the temperature, pressure and space velocity were also investigated (Fig. 3, Table S1–S3 and S5†). Light olefin selectivity ranged from 5.06% to 64.31% within the tested temperature (300–450 °C), pressure (2.0–5.0 MPa) and space velocity (2160–6480 cm<sup>3</sup> h<sup>−1</sup> g<sub>cat</sub><sup>−1</sup>) conditions. The optimum reaction temperature for SAPO34 is 400 °C since more methanol was converted to light olefins as the temperature increased from 300 °C to 400 °C. However, a very high temperature such as 450 °C will drive the products to methane according to the thermodynamics (Fig. 3B). The reaction results also indicate that the hydrogenation ability of the catalyst weakened as the gas flow rate increased. Extending the contact time (decreasing the gas flow rate) for each active site on the catalyst supplies more opportunities for olefin secondary hydrogenation, according to the consecutive reaction kinetics, which alters the product distribution of light olefins (C<sub>2</sub>–C<sub>4</sub> olefins) and paraffins (Fig. 3A). Furthermore, the product distribution profile shifted to light olefins rather than alkanes when the pressure was lower (Fig. 3C), which indicates that the light olefin





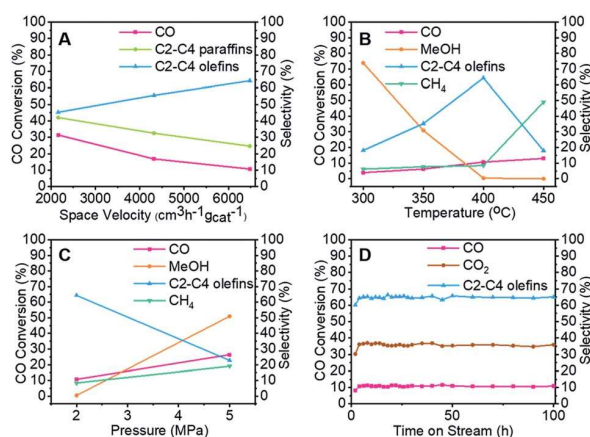


Fig. 3 The specific investigation of catalytic performance for the capsule catalyst. (A) The effect of space velocity. (B) The effect of temperature. (C) The effect of pressure. (D) The stability of the capsule catalyst in the reaction.

synthesis was conducted under the appropriate reaction conditions. The  $\text{H}_2/\text{CO}$  ratio of syngas was also studied, as given in Table S5.† In comparison to the reaction results under syngas ( $\text{H}_2/\text{CO}$  ratio of 2), the methane selectivity increased to 18.45% from 8.39%, partly inhibiting the formation of light olefins at the lower  $\text{H}_2/\text{CO}$  ratio. However, there was no distinct difference in the  $\text{CO}_2$  selectivity. The water formation was inevitable due to the dehydration route for the light olefin synthesis from methanol. It is necessary to synthesize methanol from syngas in the initial stage, which differs from other Fischer-Tropsch routes. To realize methanol synthesis, each CO molecule needs two hydrogen molecules. If there is not enough hydrogen, it is hard to initiate methanol synthesis. As a competitive reaction, more side products will be produced, inhibiting the final light olefin formation. Therefore, it is concluded that the evaluated  $\text{H}_2/\text{CO}$  ratio of 2 is necessary for our catalysts to realize a highly efficient direct synthesis of light olefins from syngas. As known, the strongly acidic catalyst will suppress light olefin formation, favouring alkane formation.<sup>54</sup> Zeolite acidity, the hydrogenation ability of the core catalyst, and hydrogen pressure determine the final olefin selectivity.

Two samples were prepared and studied to verify the effects from the silica sol. The Zn-Cr catalyst and SAPO-34 zeolite were moistened separately by the diluted silica sol, followed by drying and calcining. In Table S6,† the reaction results suggest that trace Si from the silica sol has no effect on the catalysts or their catalytic performance because the Si concentration in both catalysts is extremely low in the induced diluted silica sol during the catalyst preparation. It had a negligible influence on the acidity of the catalysts according to the  $\text{NH}_3$ -TPD results (Fig. S3†).

The capsule catalyst was also used in a syngas conversion reaction for 100 continuous hours to evaluate its catalytic stability (Fig. 3D and S4†). The Zn-Cr@SAPO capsule catalyst had very stable CO conversion and target product selectivity during this period, which reveals that the catalyst possesses

a steady core-shell structure in the STO reaction. To identify whether there were coke deposit species on the catalyst surface, thermogravimetric analysis, Raman and UV-vis spectroscopy were employed to test the used catalysts (Fig. S5 and S7).† All the results suggest that there was no amorphous carbon and graphitic carbon deposition in the spent catalysts. The good catalytic performance of the Zn-Cr@SAPO capsule catalyst also demonstrates its potential for further scale-up in industrial applications.

### In-depth and comparative study of the capsule and physical mixture catalysts

Further studies were performed to understand the unique catalytic functions of the Zn-Cr@SAPO catalyst. Fig. S8† renders the XRD patterns of the catalysts. For the Zn-Cr@SAPO catalyst, the peaks appearing in the range of  $30^{\circ}$ – $45^{\circ}$  are attributed to non-stoichiometric spinel  $\text{Zn}_x\text{Cr}_{2/3(1-x)}\text{O}$ ; the minor peaks appearing in the range of  $5^{\circ}$ – $30^{\circ}$  are attributed to zeolite SAPO34, indicating that the two different components are combined within an integrated catalyst successfully. In the tested samples, the particle size of the catalyst is about 1–2 mm, possessing complete structure. In the tested Zn-Cr@SAPO catalyst, each particle size is about 1–2 mm, possessing an intact core-shell structure. Moreover, the 2D-XRD also shows an obvious thermal signal for non-stoichiometric spinel  $\text{Zn}_x\text{Cr}_{2/3(1-x)}\text{O}$  in the Zn-Cr and SAPO34 physical mixture catalyst (Fig. S9†). However, the signal is much weaker in the Zn-Cr@SAPO capsule catalyst too. This is further evidence that the capsule catalyst with a confined structure was prepared successfully. Meanwhile, the capsule catalyst has the same crystal orientation because of the observed similar Debye rings in both catalysts, which indicates that the Zn-Cr@SAPO catalyst is successfully synthesized without structural damage *via* the encapsulation method.

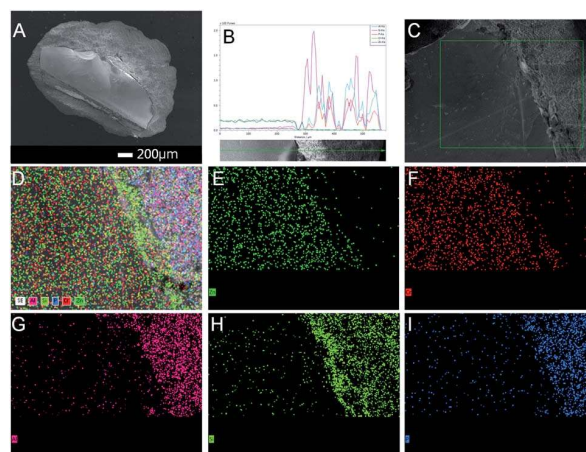


Fig. 4 The surface morphology of the capsule catalyst. (A) FE-SEM images of cut section of Zn-Cr@SAPO capsule catalyst. (B) The EDS analysis by a linear scan of the cut capsule catalyst. (C) The photo of the mapping section. (D) The mapping of all the elements on the above section. (E) Zn elemental map. (F) Cr elemental map. (G) Al elemental map. (H) Si elemental map. (I) P elemental map.



The surface morphology of the Zn–Cr@SAPO capsule catalyst was analyzed by FE-SEM and SEM (Fig. 4, S10 and S11†). The Zn–Cr surface is totally covered by a SAPO34 layer and no signals were observed from Zn and Cr in the EDS of the Zn–Cr@SAPO capsule catalyst, as shown in Fig. 4A and S11(A and C),† which indicates that the shell of the catalyst is encapsulated well over the core. The EDS linear scan of the cut section in the capsule catalyst (Fig. 4B and S11D†) further demonstrates that the Zn–Cr catalyst is encapsulated by SAPO34 evenly. An obvious boundary between the two different components was observed. The different elements clearly show a boundary line between the Zn–Cr metallic oxide and the SAPO34 zeolite in the mapping pictures (Fig. 4C–I). The thickness of the SAPO34 membrane is about 30–45  $\mu\text{m}$ , which is obtained from Fig. S10 (A and B), and S11 (B and D).† In the EDS analysis given by a frontal horizontal incision photo of the capsule catalyst, the signals of Zn and Cr started to increase from 45  $\mu\text{m}$  beneath the catalyst surface with decreasing Si, Al, and P signals, which gives us the thickness of the SAPO34 shell on the capsule catalyst. This is sufficient for the formation of light olefins from methanol on the catalyst shell. The infinitesimal space between Zn–Cr and SAPO34 is beneficial for the mass transfer and diffusion, which leads to the process of MTO (methanol to light olefins) synthesis on SAPO34 using a methanol immediate that forms on the metallic oxide Zn–Cr. Moreover, the surface of the Zn–Cr metallic oxide component is very smooth and clean,

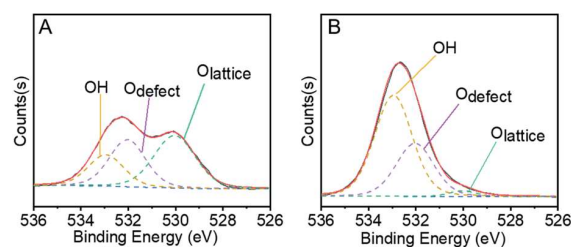


Fig. 6 Active sites in the crucial first methanol synthesis step. (A) XPS O 1s spectrum of fresh Zn–Cr metallic oxide catalyst. (B) XPS O 1s spectra of activated Zn–Cr metallic oxide catalyst in  $\text{H}_2$  at 400  $^\circ\text{C}$ .

which indicates that the core catalyst was not corroded in comparison with the capsule catalyst synthesized by the routine hydrothermal method. In summary, the Zn–Cr@SAPO capsule catalyst prepared by a physical coating method illustrates superior selectivity of light olefins due to its tailor-made core-shell structure.

Other strong evidence for the successful preparation of the Zn–Cr@SAPO capsule catalyst without structural damage is the XRF-CT results, as shown in Fig. 5 and S12.†

The prepared capsule catalyst is scanned by horizontal, angular and vertical triple cycle scanning in 9 random positions at a 100  $\mu\text{m}$  depth (Fig. S13†). The fluorescence intensity of Zn and Cr is easily detected over all the positions. The 3-D images also show an even distribution of Zn and Cr inside the Zn–Cr@SAPO capsule catalyst (Fig. 5A and C).<sup>56,57</sup> More importantly, at the 100  $\mu\text{m}$  depth of the catalyst, there are no signals for SAPO34 (Si, Al, P), which indicates that there is no corrosion occurring. XPS was also performed to investigate the catalyst surface components (Fig. 5E and F). The photoemission features of the Zn 2p spectrum suggest that the binding energies of Zn 2p<sub>1/2</sub> and Zn 2p<sub>3/2</sub> are 1045 eV and 1021.5 eV, respectively (Fig. 5E). However, it is difficult to identify the state of Zn by this approach because the binding energy of metallic Zn and cationic Zn are too close to distinguish.<sup>58</sup> The photoemission features of Cr 2p<sub>3/2</sub> suggest that Cr is only present in the cationic state Cr<sup>3+</sup> since the binding energy of Cr 2p<sub>3/2</sub> is about 576 eV, which differs from the binding energy of metallic Cr or the cationic state Cr<sup>6+</sup> (Fig. 5F).<sup>59,60</sup> After  $\text{H}_2$  activation prior to the STO reaction, the binding energy of Cr 2p<sub>3/2</sub> shows a slight downshift to 575.5 eV, which indicates that the state of Cr is a mixture of Cr<sup>0</sup> and Cr<sup>2+</sup> since the observed binding energy is between the two states (Fig. S14†).

As shown by Fig. S1†, the  $\text{H}_2$ -TPR result has a double overlapping reduction peak in the catalysts, which corresponds to Cr<sup>3+</sup>  $\rightarrow$  Cr<sup>2+</sup> and small quantities of Cr<sup>2+</sup>  $\rightarrow$  Cr<sup>0</sup>. Combined with the XPS results, it is concluded that the catalyst active sites for methanol synthesis are Zn<sup>2+</sup> and Cr<sup>0</sup>/Cr<sup>2+</sup> during the reaction. As a surface-sensitive characterization technique, the signals from the sample in XPS analysis are only detected from the 0–2 nm depth on the catalyst surface. In Fig. 5E and F, no signals of Zn and Cr are observed from the surface of Zn–Cr@SAPO catalyst, which further indicates that the Zn–Cr metallic oxide is covered by a SAPO34 shell.

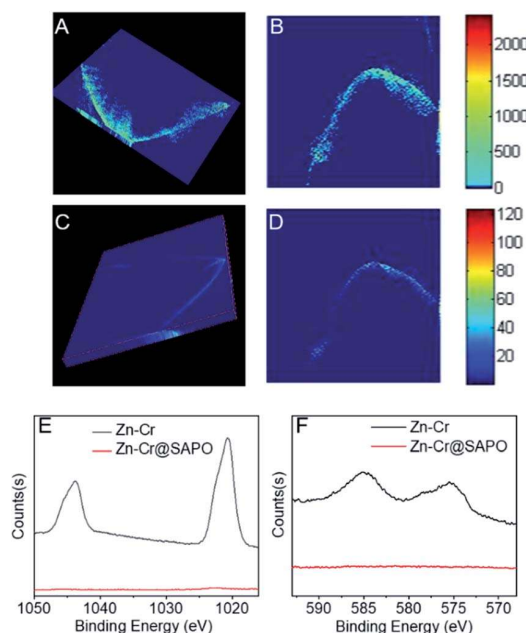


Fig. 5 Demonstrating the synthetic capsule catalyst. (A) The three-dimensional elemental distribution images of Zn in the Zn–Cr@SAPO capsule catalyst. (B) The fluorescence intensity map of Zn in the Zn–Cr@SAPO capsule catalyst. (C) The three-dimensional elemental distribution images of Cr in the Zn–Cr@SAPO capsule catalyst. (D) The fluorescence intensity map of Cr in the Zn–Cr@SAPO capsule catalyst. (E) XPS Zn 2p spectra of Zn–Cr@SAPO capsule catalyst. (F) XPS Cr 2p spectra of Zn–Cr@SAPO capsule catalyst.





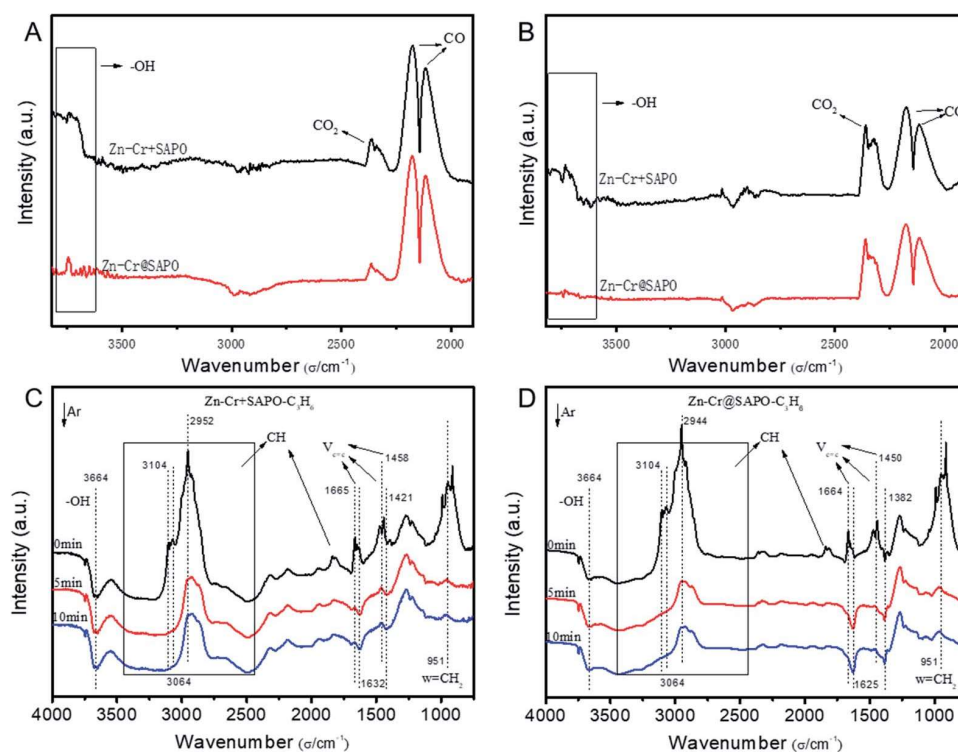
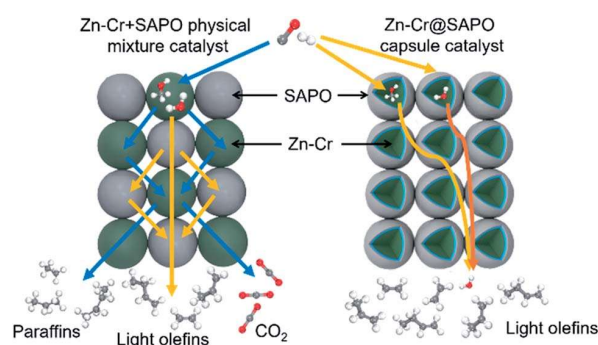


Fig. 7 The adsorption properties over the physical mixture and capsule catalysts. (A) DRIFTS spectra of the physical mixture and capsule catalysts under a flow of syngas at 300 °C; the signals were collected during the syngas conversion process. (B) DRIFTS spectra of the physical mixture and capsule catalysts under a flow of syngas at 400 °C; the signals were collected during the syngas conversion process. (C) *In situ* FT-IR spectra of the Zn-Cr and SAPO34 physical mixture catalyst; the catalyst was absorbed by propylene, then purged under a flow of Ar for 10 min at 400 °C; the signals were collected at 0 min, 5 min, and 10 min, respectively. (D) *In situ* FT-IR spectra of the Zn-Cr@SAPO capsule catalyst; the catalyst was absorbed by propylene, then purged under a flow of Ar for 10 min at 400 °C; the signals were collected at 0 min, 5 min, and 10 min, respectively.

In the first step of STO synthesis, the oxygen vacancy plays a crucial role in the conversion of syngas to methanol. In Fig. 6A, B and Table S7,<sup>†</sup> after  $\text{H}_2$  pre-treating of the catalyst for 10 h at 400 °C, the  $O_{\text{lattice}}$  on the catalyst surface decreased from 43.83% to 2.77%, accompanied with a rapid increase of OH from 21.56% to 63.74%. Simultaneously, the ratio of  $O_{\text{defect}}/O_{\text{lattice}}$  was obviously enhanced from 0.79 to 12.09, which indicates that the sites supplied by oxygen vacancies favour CO adsorption and continuous activation.<sup>44–48</sup> OH increased in the  $\text{H}_2$ -activated Zn-Cr catalyst, which resulted in the adsorption of formed  $\text{H}_2\text{O}$  on the catalyst surface from the process of  $\text{Cr}^{3+}$  reduction. In general, with increasing syngas ( $\text{CO}/\text{H}_2$ ) pressure and reaction temperature in the STO reaction, the oxygen vacancies concentration also increased, which was conducive for the release of surface oxygen on the Zn-Cr catalyst in an anaerobic environment. During the period of sustained syngas feeding, unlike the CO adsorption, the positions for  $\text{H}_2$  adsorption were at the exposed  $O_{\text{lattice}}$  sites nearby the surface oxygen vacancies.<sup>49</sup> Hence, the absorbed CO on the oxygen vacancies can continuously convert into CHO,  $\text{CH}_2\text{O}$ ,  $\text{CH}_3\text{O}$  and  $\text{CH}_3\text{OH}$  by attaching to the adjacent H donor.

The catalytic behaviour of the physical mixture and capsule catalysts in the presence of syngas was studied by diffuse

reflectance infrared Fourier transform spectroscopy (DRIFTS), as illustrated in Fig. 7A and B. The evolution of two peaks at around  $2300\text{ cm}^{-1}$  is attributed to the presence of formed  $\text{CO}_2$ , indicating that the amount of formed  $\text{CO}_2$  on the capsule catalyst was less than that on the physical mixture catalyst, which suggests that the water gas shift (WGS) reaction is limited by the unique core-shell structure of the Zn-Cr@SAPO capsule catalyst during STO synthesis. In comparison to the vibration



Scheme 2 The two different mass transfer routes over the Zn-Cr physical mixture catalyst and capsule catalyst.



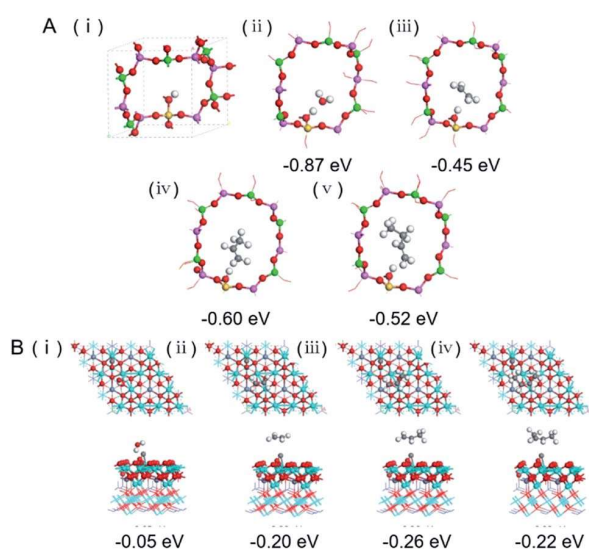


Fig. 8 (A) Optimized periodic structures of SAPO34 (i); H<sub>2</sub>O (ii), C<sub>2</sub>H<sub>4</sub> (iii), C<sub>3</sub>H<sub>6</sub> (iv) and C<sub>4</sub>H<sub>8</sub> (v) are adsorbed on SAPO34 with adsorption energies ( $E_{\text{ads}}$ ). The SAPO34 shell is represented by a SAPO34 12T cell having one acidic site at the O 1 position. Green, red, pink, yellow and white balls represent P, O, Al, Si and H atoms, respectively. (B) Top (above) and side (below) view of optimized configurations for H<sub>2</sub>O (i), C<sub>2</sub>H<sub>4</sub> (ii), C<sub>3</sub>H<sub>6</sub> (iii) and C<sub>4</sub>H<sub>8</sub> (iv) adsorption on CO occupied spinel ZnCr<sub>2</sub>O<sub>4</sub> (111) surface with adsorption energies ( $E_{\text{ads}}$ ). The surface of spinel ZnCr<sub>2</sub>O<sub>4</sub> (111) is presented as CO molecules occupied at the sites of the O vacancies for the syngas first through the Zn–Cr core, the subsequently formed products and by-products were calculated by the adsorption on the CO occupied surface. Red, white, cyan, purple and grey balls represent O, H, Cr, Zn and C atoms, respectively.

peak of the hydroxyl group adsorbed in the two different catalysts, water easily remained in the Zn–Cr phase on the physical mixture catalyst for the continuous WGS reaction. However, the formed water more easily transfers *via* the SAPO34 shell, which prevents the water from attaching to the Zn–Cr core for further WGS reactions, as shown in Scheme 2. High pressure *in situ* IR experiments were also performed under the reaction conditions to support this view, as shown in Fig. S15.† The relative amount of the produced CO<sub>2</sub> was obviously decreased compared to that of CO in the Zn–Cr@SAPO capsule catalyst. In addition, the DFT calculations also indicate that the adsorption energies of water are much higher on the SAPO34 shell (−0.87 eV, Fig. 8A) than on the Zn–Cr core (−0.05 eV, Fig. 8B). This means the SAPO34 shell has better water absorbency to prevent the WGS reaction from occurring on the Zn–Cr core.

The desorption performance of light olefins on the physical mixture and capsule catalysts was simulated under the reaction conditions by DRIFTS, as given in Fig. 7C, D, S16 and S17.† Initially, after the propylene adsorption, the hydrocarbons are more easily adsorbed in the SAPO34 zeolite shell of the Zn–Cr@SAPO capsule catalyst since the  $\pi$  electrons of olefins prefer to be absorbed on the electron-deficient Lewis acid sites of the zeolite. The vibrational peaks of C–H and C=C species are slightly red-shifted, indicating that the vibration energies of C–H and C=C species are lower than that on the physical

mixture catalyst. Therefore, the formed light olefins are more easily adsorbed in the capsule catalyst due to the presence of the zeolite shell. Then, after Ar purging, the intensity of C–H drops rapidly, suggesting the desorption ability is also strong on the capsule catalyst due to the SAPO34 shell in the hierarchical structure. However, desorption is difficult with the Zn–Cr metallic oxide and SAPO34 zeolite physical mixture catalyst during STO synthesis; therefore, parts of the formed propylene were converted into other species (1800 to 2300 cm<sup>−1</sup>) on the active phase of the metallic oxide, which led to a decline of light olefin selectivity. Fig. S16† clearly shows that even though more propylene remain over the Zn–Cr@SAPO capsule catalyst, the adsorbed propylene are more easily removed by Ar purging, which provides strong evidence that the Zn–Cr@SAPO capsule catalyst has a better desorption ability. The variety of vibration peaks of w=CH<sub>2</sub> observed in the ethylene adsorption and desorption IR experiments under the same reaction conditions are similar to the results in the adsorption and desorption of propylene (Fig. S17†). In a continuous mobile phase system, the adsorbed species are more rapidly desorbed in the capsule catalyst, which promotes the mass transfer and diffusion, maintaining a dynamic balance process. The results suggest that the SAPO34 shell can prevent the adsorption of light olefins on the Zn–Cr metallic oxide core, which is consistent with our reaction results, as shown in Scheme 2. In addition, the adsorption energies are also provided by DFT calculation, which are −0.45, −0.60 and −0.52 eV for C<sub>2</sub>H<sub>4</sub>, C<sub>3</sub>H<sub>6</sub> and C<sub>4</sub>H<sub>8</sub> adsorbed on the SAPO34 shell, respectively (Fig. 8A). The adsorption energies of C<sub>2</sub>H<sub>4</sub>, C<sub>3</sub>H<sub>6</sub> and C<sub>4</sub>H<sub>8</sub> on the Zn–Cr core are correspondingly −0.20, −0.26 and −0.22 eV (Fig. 8B), which are all higher than on the SAPO34 shell. According to the difference between the adsorption energies of the Zn–Cr metallic oxide/SAPO zeolite physical mixture and capsule catalysts, the formed water and light olefins are easily removed in the Zn–Cr@SAPO capsule catalyst in the case of side reactions. The complementary DFT study is completely consistent with our experimental results.

## Conclusion

In summary, our study supplies a unique strategy to advance the light olefin selectivity and limit CO<sub>2</sub> formation in the STO (syngas to light olefins) synthesis over a core–shell structured Zn–Cr@SAPO capsule catalyst fabricated from a physical encapsulation method. This catalyst efficiently combines a Zn–Cr metallic oxide with a SAPO34 zeolite membrane, yielding a light olefin selectivity as high as 64.31% with a CO<sub>2</sub> selectivity at only 36.16%. The exquisite structure of the Zn–Cr@SAPO capsule catalyst maximizes its catalytic performance in the STO reaction by utilizing the different absorption barriers and active phases of the two components. The lower adsorption energy and larger surface area of the SAPO34 shell protect the Zn–Cr core to limit the water gas shift (WGS) reaction. The hierarchical structure and extremely short distance between the two active components allow the Zn–Cr@SAPO capsule catalyst to demonstrate better mass transfer and diffusion for a better synergistic effect. At the same time, the confinement effect of



the capsule catalyst also decreases the possibility of side-reactions and enhances the light olefin selectivity.

It should be noted that the confinement structure of the capsule catalyst determines these differences, rather than the random assembly of the physical mixing analogue. All the methanol from the Zn–Cr core must enter the channels of SAPO34 to be regulated for the formation of light olefins under the control of the zeolite acidic and spatial properties. On the other hand, some of the methanol may not enter the narrow channels of SAPO34 in the case of the physical mixture catalyst where most methanol only reacts at the outside surface acidic sites of the SAPO34 zeolite without the zeolite molecule-shape selective regulation, resulting in the formation of many by-products and lower light olefin selectivity. Furthermore, the capsule catalyst structure provides a dense SAPO34 membrane to effectively absorb and collect water and olefins from the Zn–Cr core, reducing CO<sub>2</sub> formation and stopping olefin secondary hydrogenation at the core. The hierarchical structure also provides a zone-separated adsorption difference to control the reaction sequence and avoid side reactions. But all these tools and effects are unavailable or severely weakened for the physical mixture catalyst with random assembly due to its spatially normalized features.

In addition, this type of catalyst has superior potential since it can be easily scaled up to industrial requirements in the future and it has extensive application prospects for various reactions.

## Conflicts of interest

The authors declare no competing interests.

## Acknowledgements

This work was supported by JST CREST (Grant Number 17-141003297), Japan. Dr Tan and Prof. Yang thank the financial support from National Natural Science Foundation of China (21902029, 21978312 and 91645113), Foundation of State Key Laboratory of Coal Conversion (Grant No. J19-20-612) and Foundation of State Key Laboratory of High-Efficiency Utilization of Coal and Green Chemical Engineering (Grant No. 2019-KF-23). The Hard X-ray Micro-focusing Beamline was supported by Shanghai Synchrotron Radiation Facility, BL15U1. The IR experiments was supported by Synfuels China Technology Co., Ltd and East China University of Science and Technology.

## Notes and references

- 1 M. Claeys, *Nature*, 2016, **538**, 44–45.
- 2 K. P. de Jong, *Science*, 2016, **351**, 1030–1031.
- 3 C. Wang, L. Xu and Q. Wang, *J. Nat. Gas Chem.*, 2003, **12**, 10–16.
- 4 L. Zhong, F. Yu, Y. An, Y. Zhao, Y. Sun, Z. Li, T. Lin, Y. Lin, X. Qi, Y. Dai, L. Gu, J. Hu, S. Jin, Q. Shen and H. Wang, *Nature*, 2016, **538**, 84–87.
- 5 H. M. Torres Galvis and K. P. de Jong, *ACS Catal.*, 2013, **3**, 2130–2149.
- 6 B. Hu, S. Frueh, H. F. Garces, L. Zhang, M. Aindow, C. Brooks, E. Kreidler and S. L. Suib, *Appl. Catal., B*, 2013, **132–133**, 54–61.
- 7 H. M. Torres Galvis, J. H. Bitter, C. B. Khare, M. Ruitenbeek, A. I. Dugulan and K. P. de Jong, *Science*, 2012, **335**, 835–838.
- 8 H. M. Torres Galvis, J. H. Bitter, T. Davidian, M. Ruitenbeek, A. I. Dugulan and K. P. de Jong, *J. Am. Chem. Soc.*, 2012, **134**, 16207–16215.
- 9 J. Li, Y. He, L. Tan, P. Zhang, X. Peng, A. Oruganti, G. Yang, H. Abe, Y. Wang and N. Tsubaki, *Nat. Catal.*, 2018, **1**, 787–793.
- 10 X. Chen, D. Deng, X. Pan, Y. Hu and X. Bao, *Chem. Commun.*, 2015, **51**, 217–220.
- 11 Y. Liu, J. Chen, J. Bao and Y. Zhang, *ACS Catal.*, 2015, **5**, 3905–3909.
- 12 W. Gao, R. Gao, Y. Zhao, M. Peng, C. Song, M. Li, S. Li, J. Liu, W. Li, Y. Deng, M. Zhang, J. Xie, G. Hu, Z. Zhang, R. Long, X. Wen and D. Ma, *Chem*, 2018, **4**, 2917–2928.
- 13 W. Gao, *Chem*, 2018, **4**, 2727–2729.
- 14 C. D. Chang and A. J. Silvestri, *J. Catal.*, 1977, **47**, 249–259.
- 15 X. Wu, S. Xu, W. Zhang, J. Huang, J. Li, B. Yu, Y. Wei and Z. Liu, *Angew. Chem., Int. Ed.*, 2017, **129**, 9167–9171.
- 16 P. Tian, Y. Wei, M. Ye and Z. Liu, *ACS Catal.*, 2015, **5**, 1922–1938.
- 17 B. Arstad and S. Kolboe, *J. Am. Chem. Soc.*, 2001, **123**, 8137–8138.
- 18 J. Q. Chen, A. Bozzano, B. Glover, T. Fuglerud and S. Kvisle, *Catal. Today*, 2005, **106**, 103–107.
- 19 H. Koempel and W. Liebner, *Stud. Surf. Sci. Catal.*, 2007, **167**, 261–267.
- 20 D. Sheldon, *Johnson Matthey Technol. Rev.*, 2017, **61**, 172–182.
- 21 P. Zhang, L. Tan, G. Yang and N. Tsubaki, *Chem. Sci.*, 2017, **8**, 7941.
- 22 Y. Wang, L. Tan, M. Tan, P. Zhang, Y. Fang, Y. Yoneyama, G. Yang and N. Tsubaki, *ACS Catal.*, 2019, **9**, 895–901.
- 23 P. Gao, S. Dang, S. Li, X. Bu, Z. Liu, M. Qiu, C. Yang, H. Wang, L. Zhong, Y. Han, Q. Liu, W. Wei and Y. Sun, *ACS Catal.*, 2018, **8**, 571–578.
- 24 Y. Ni, Z. Chen, Y. Fu, Y. Liu, W. Zhu and Z. Liu, *Nat. Commun.*, 2018, **9**, 3457.
- 25 X. Liu, M. Wang, C. Zhou, W. Zhou, K. Cheng, J. Kang, Q. Zhang, W. Deng and Y. Wang, *Chem. Commun.*, 2018, **54**, 140–143.
- 26 Z. Ma and M. Porosoff, *ACS Catal.*, 2019, **9**, 2639–2656.
- 27 B. Zhao, P. Zhai, P. Wang, J. Li, T. Li, M. Peng, M. Zhao, G. Hu, Y. Yang, Y. Li, Q. Zhang, W. Fan and D. Ma, *Chem*, 2017, **3**, 323–333.
- 28 P. Gao, S. Li, X. Bu, S. Dang, Z. Liu, H. Wang, L. Zhong, M. Qiu, C. Yang, J. Cai, W. Wei and Y. Sun, *Nat. Chem.*, 2017, **9**, 1019–1024.
- 29 K. Cheng, W. Zhou, J. Kang, S. He, S. Shi, Q. Zhang, Y. Pan, W. Wen and Y. Wang, *Chem*, 2017, **3**, 33–347.
- 30 F. Jiao, J. Li, X. Pan, J. Xiao, H. Li, H. Ma, M. Wei, Y. Pan, Z. Zhou, M. Li, S. Miao, J. Li, Y. Zhu, D. Xiao, T. He, J. Yang, F. Qi, Q. Fu and X. Bao, *Science*, 2016, **351**, 1065–1068.



- 31 Y. Zhu, X. Pan, F. Jiao, J. Li, J. Yang, M. Ding, Y. Han, Z. Liu and X. Bao, *ACS Catal.*, 2017, **7**, 2800–2804.
- 32 J. Su, H. Zhou, S. Liu, C. Wang, W. Jiao, Y. Wang, C. Liu, Y. Ye, L. Zhang, Y. Zhao, H. Liu, D. Wang, W. Yang, Z. Xie and M. He, *Nat. Commun.*, 2019, **10**, 1–8.
- 33 X. Liu, W. Zhou, Y. Yang, K. Cheng, J. Kang, L. Zhang, G. Zhang, X. Min, Q. Zhang and Y. Wang, *Chem. Sci.*, 2018, **9**, 4708.
- 34 N. Li, F. Jiao, X. Pan, Y. Ding, J. Feng and X. Bao, *ACS Catal.*, 2019, **9**, 960–966.
- 35 F. Jiao, X. Pan, K. Gong, Y. Chen, G. Li and X. Bao, *Angew. Chem., Int. Ed.*, 2018, **57**, 4692–4696.
- 36 K. Cheng, B. Gu, X. Liu, J. Kang, Q. Zhang and Y. Wang, *Angew. Chem., Int. Ed.*, 2016, **55**, 4725–4728.
- 37 J. He, Z. Liu, Y. Yoneyama, N. Nishiyama and N. Tsubaki, *Chem. - Eur. J.*, 2006, **12**, 8296–8304.
- 38 G. Yang, H. Kawata, Q. Lin, J. Wang, Y. Jin, C. Zeng, Y. Yoneyama and N. Tsubaki, *Chem. Sci.*, 2013, **4**, 3958–3964.
- 39 J. Bao, J. He, Y. Zhang, Y. Yoneyama and N. Tsubaki, *Angew. Chem., Int. Ed.*, 2008, **47**, 353–356.
- 40 G. Yang, N. Tsubaki, J. Shamoto, Y. Yoneyama and Y. Zhang, *J. Am. Chem. Soc.*, 2010, **132**, 8129–8136.
- 41 K. Pinkaew, G. Yang, T. Vitidsant, Y. Jin, C. Zeng, Y. Yoneyama and N. Tsubaki, *Fuel*, 2013, **111**, 727–732.
- 42 X. Wang, G. Yang, J. Zhang, S. Chen, Y. Wu, Q. Zhang, J. Wang, Y. Han and Y. Tan, *Chem. Commun.*, 2016, **52**, 7352–7355.
- 43 R. Phienluphon, K. Pinkaew, K. Pinkaew, G. Yang, J. Li, Q. Wei, Y. Yoneyama, T. Vitidsant and N. Tsubaki, *Chem. Eng. J.*, 2015, **270**, 605–611.
- 44 H. Song, D. Laudenschleger, J. Carey, H. Ruland, M. Nolan and M. Muhler, *ACS Catal.*, 2017, **7**, 7610–7622.
- 45 Y. Wu, N. Gong, M. Zhang, W. Zhang, T. Zhang, J. Zhang, L. Wang, H. Xie and Y. Tan, *Catal. Sci. Technol.*, 2019, **9**, 2592–2600.
- 46 X. Gao, Y. Wu, T. Zhang, L. Wang, X. Li, H. Xie and Y. Tan, *Catal. Sci. Technol.*, 2018, **8**, 2975–2986.
- 47 L. Liu, Z. Mei, A. Tang, A. Azarov, A. Kuznetsov, Q. Xue and X. Du, *Phys. Rev. B*, 2016, **93**, 235305.
- 48 M. Chen, P. Wu, Q. Wei, Y. Zhu, S. Yang, L. Ju, N. Zhu and Z. Lin, *Environ. Chem.*, 2018, **15**, 226–235.
- 49 S. Ma, S. Huang and Z. Liu, *Nat. Catal.*, 2019, **2**, 671–677.
- 50 B. Smith R J, M. Loganathan and M. Shantha, *Int. J. Chem. React. Eng.*, 2010, **8**, 1.
- 51 M. Matsukata, T. Hayashi, M. Nishiyama, E. Kikuchi and Y. Morita, *J. Jpn. Petrol. Inst.*, 1987, **30**, 265–272.
- 52 L. Tan, G. Yang, Y. Yoneyama, Y. Kou, Y. Tan, T. Vitidsant and N. Tsubaki, *Appl. Catal. Gen.*, 2015, **505**, 141–149.
- 53 S. Tian, L. Tan, Y. Wu, Y. Kou, H. Xie, N. Tsubaki and Y. Tan, *Appl. Catal. Gen.*, 2017, **536**, 57–66.
- 54 Z. Cui, Q. Liu, W. Song and L. Wan, *Angew. Chem., Int. Ed.*, 2006, **45**, 6512–6515.
- 55 S. Lin, J. Ma, X. Ye, D. Xie and H. Guo, *J. Phys. Chem. C*, 2013, **117**, 14667–14676.
- 56 T. Sheppard, S. Price, F. Benzi, S. Baier, M. Klumpp, R. Dittmeyer, W. Schwieger and J. Grunwaldt, *J. Am. Chem. Soc.*, 2017, **139**, 7855–7863.
- 57 L. Zhang, *et al.*, *Nucl. Sci. Technol.*, 2015, **26**, 060101.
- 58 M. Biesinger, L. Lau, A. Gerson and R. Smart, *Appl. Surf. Sci.*, 2010, **257**, 887–898.
- 59 M. Biesinger, *et al.*, *Appl. Surf. Sci.*, 2011, **257**, 2717–2730.
- 60 M. Aronniemi, *et al.*, *Surf. Sci.*, 2005, **578**, 108–123.





## CURRICULUM VITAE

**Fan WANG**

Leibniz Institute for Catalysis at the University of Rostock (LIKAT)

Room 2.302, Albert-Einstein-Str. 29a, 18059 Rostock, Germany

Phone: +49(381)1281-304

Email: Fan.Wang@catalysis.de

**Personal Data**

<b>Nationality:</b>	Chinese	<b>Gender:</b>	Male
<b>Birth date:</b>	12/03/1990	<b>Marital status:</b>	Married

**Education**

<b>11/2017-Present</b>	Ph.D. candidate
Leibniz Institute for Catalysis at the University of Rostock (LIKAT), Germany.	
Supervisor: Dr. Habil. Haijun Jiao	
<b>07/2014-07/2016</b>	M.S.
Science and Engineering Faculty, Queensland University of Technology (QUT), Australia.	
Master of Applied Science	
Supervisor: Huaiyong Zhu	
<b>09/2009-07/2013</b>	B.S.
Department of Applied Chemistry, Taiyuan University of Technology (TYUT), China	
Degree of Bachelor of Science	

**Research Experience****11/2017-Present**

- (1) Exploring the water gas shift (WGS) reaction on various structures of transition metals modified molybdenum carbide catalysts.
- (2) Investigating the surface properties of transition metals supported and substituted molybdenum carbides.
- (3) Revealing the correlation of electron transfer, adsorption energy and electronegativity of different studied models.

**07/2014-07/2016**

- (4) Visible light photocatalysis with supported metal nanoparticles for organic synthesis.
- (5) Employing supported gold nanoparticles in self-esterification of aliphatic alcohols.
- (6) Applying supported palladium nanoparticle in Heck cross-coupling reaction.

**08/2013-06/2014**

Research Assistant, Institute of Coal Chemistry, Chinese Academy of Sciences, China.  
Synthesis of supported metal nanoparticles and their catalytic applications.



**10/2012-07/2013**

Graduation thesis (B.S.), Department of Applied Chemistry, Taiyuan University of Technology & Institute of Coal Chemistry, Chinese Academy of Science, China.

- (7) Graphene-supported Au-Pd bimetallic nanoparticles with excellent performance for methanol oxidation to methyl formate.

F. Wang prepared Au-Pd bimetallic nanoparticles for the following paper and the contribution was mentioned in the Acknowledgement: R. Y. Wang *et al.*, "Graphene-supported Au-Pd bimetallic nanoparticles with excellent catalytic performance in selective oxidation of methanol to methyl formate", *Chem. Commun.* **2013**, 49, 8250-8252.

- (8) Synthesis of functional carbon microspheres for formic acid and ammonia treatment.

**Publication** (Papers marked with \* are included in this dissertation)

Papers published during PhD Study

- [1] Water-Gas Shift Reaction Mechanisms on the Mo<sub>2</sub>C(101) Surface with Ni Adsorption and Substitution. **F. Wang**, X. X. Tian, H. Jiao. manuscript in preparation.
- [2\*] **F. Wang**, X. X. Tian, H. Jiao. Adsorption of CO, H<sub>2</sub>, H<sub>2</sub>O, and CO<sub>2</sub> on Fe-, Co-, Ni-, Cu-, Pd-, and Pt-Doped Mo<sub>2</sub>C(101) Surfaces. *J. Phys. Chem. C* **2021**, 125, 11419–11431.
- [3\*] **F. Wang**, T. Li, Y. Shi, H. Jiao. Molybdenum carbide supported metal catalysts (M<sub>n</sub>/Mo<sub>x</sub>C; M = Co, Ni, Cu, Pd, Pt) – metal and surface dependent structure and stability. *Catal. Sci. Technol.* **2020**, 10, 3029–3046.
- [4\*] L. Tan, **F. Wang**, P. P. Zhang, Y. Suzuki, Y. Q. Wu, J. G. Chen, G. H. Yang, N. Tsubaki. Design of a core-shell catalyst: an effective strategy for suppressing side reactions in syngas for direct selective conversion to light olefins. *Chem. Sci.* **2020**, 11, 4097–4105.
- [5\*] **F. Wang**, T. Li, H. Jiao. Nitridation of the metallic Mo<sub>2</sub>C(001) surface from NH<sub>3</sub> dissociative adsorption—A DFT study. *Surf. Sci.* **2019**, 689, 121466.

Papers published during Master and Bachelor Studies

- [6] Q. Xiao, Z. Liu, **F. Wang**, S. Sarina, H. Y. Zhu. Tuning the reduction power of visible light photocatalysts of gold nanoparticles for selective reduction of nitroaromatics to azoxy-compounds—Tailoring the catalyst support. *Appl. Catal. B* **2017**, 209, 69–79.
- [7] **F. Wang**, Q. Xiao, P. F. Han, S. Sarina, H. Y. Zhu. Highly efficient self-esterification of aliphatic alcohols using supported gold nanoparticles under mild conditions. *J. Mol. Catal. A Chem.* **2016**, 423, 61–69.
- [8] C. Jin, C. Xing, **F. Wang**, W. Z. Shen. Rapid synthesis of functional carbon microspheres: preparation, forming mechanism and application in formic acid and ammonia treatment, *Sci. Adv. Mater.* **2013**, 5, 1–5.

**Conference Participations**

- (1) At the "2018 CAMD Summer School on Electronic Structure Theory and Materials Design". Copenhagen, Demark, August 12–17, **2018**.

**Poster** "High Coverage NH<sub>3</sub> Dissociative Adsorption on the Hexagonal Mo<sub>2</sub>C(001) and Mo<sub>2</sub>C(101) Surfaces"

- (2) 13th European Congress on Catalysis (EUROPACAT 2017). Florence, Italy. August 27–31, **2017**.

**Oral presentation** “Visible Light Driven Heck Cross-Coupling Reaction using Supported Palladium Nanoparticles”

- (3) 25th biennial North American Meeting of the North American Catalysis Society. Denver. June 4–9, **2017**.

**Oral presentation** “Photocatalytic Heck Cross-Coupling Reaction using Supported Palladium Nanoparticles”

- (4) International Symposium on Green Chemistry (ISGC-2017). La Rochelle, France. May 16–19, **2017**.

**Oral presentation** “Visible Light Driven Heck Cross-Coupling Reaction using Supported Palladium Nanoparticles”

#### **Awards & Scholarship**

**2018** China Scholarship Council (CSC) Scholarship (2018–2021, PhD).

**2014** Equity House Capital Investments Pty Ltd Scholarship (2014–2016, M.S.).

**2012** The winning prize of the second chemistry experiment competition of Shanxi Province, China.

**2012** The third prize of the fifth energy conservation and emission reduction science and technology competition of nationwide.

**2010** Spirit of innovation and ability of practice scholarship (2010, B.S.).

**Doktorandinnen/Doktoranden-Erklärung gemäß § 4 Absatz 1 Buchstaben g und h  
der Promotionsordnung der Mathematisch-Naturwissenschaftlichen Fakultät der  
Universität Rostock**

Name ..... Fan Wang .....  
(Name, Vorname)

Anschrift ..... Albert-Einstein Str. 29A, 18059, Rostock .....  
(Straße, PLZ, Wohnort)

Ich habe eine Dissertation zum Thema

.....  
Surface Structure, Stability and Activity of Molybdenum Carbides Supported Transition  
Metal Catalysts  
.....

an der Mathematisch-Naturwissenschaftlichen Fakultät der Universität Rostock  
angefertigt. Dabei wurde ich von Frau/Herrn

Dr. Habil. Haijun Jiao  
..... betreut.

Ich gebe folgende Erklärung ab:

1. Die Gelegenheit zum vorliegenden Promotionsvorhaben ist mir nicht kommerziell vermittelt worden. Insbesondere habe ich keine Organisation eingeschaltet, die gegen Entgelt Betreuerinnen/Betreuer für die Anfertigung von Dissertationen sucht oder die mir obliegenden Pflichten hinsichtlich der Prüfungsleistungen für mich ganz oder teilweise erledigt.
2. Ich versichere hiermit an Eides statt, dass ich die vorliegende Arbeit selbstständig angefertigt und ohne fremde Hilfe verfasst habe. Dazu habe ich keine außer den von mir angegebenen Hilfsmitteln und Quellen verwendet und die den benutzten Werken inhaltlich und wörtlich entnommenen Stellen habe ich als solche kenntlich gemacht.

Rostock, den 29/10/2021 ..... Fan Wang .....  
(Unterschrift)